AN EXPERIMENTAL AND TIME-DOMAIN NUMERICAL ANALYSIS OF GAP RESONANCE EFFECT OF AN FLNG SYSTEM FOR SIDE-BY-SIDE OFFLOADING OPERATION.

By

JIDEOFOR COLLINS NWAFOR

A thesis submitted for the Degree of Doctor of Philosophy

School of Engineering – Marine Technology

Newcastle University

March 2023

NEWCASTLE UNIVERSITY

School of Engineering

Doctor of Philosophy (PhD)

Academic Year 2017 – 2023

Jideofor Collins Nwafor

AN EXPERIMENTAL AND TIME-DOMAIN NUMERICAL ANALYSIS OF GAP RESONANCE EFFECT OF AN FLNG SYSTEM FOR SIDE-BY-SIDE OFFLOADING OPERATION.

Supervisors: Prof Zhiqiang Hu, Dr Yongchang Pu

March 2023

This thesis is submitted for the Degree of Doctor of Philosophy

ABSTRACT

The side-by-side configuration of an FLNG (Floating Liquefied Natural Gas) facility and LNGC (Liquified Natural Gas Carrier) during LNG offloading operation has become of increasing importance in the offshore gas industry. This side-by-side arrangement brings about the formation of a narrow and long gap region between the two vessels. This PhD project aims to propose a method to predict the occurrence of gap resonance for a side-by side offloading configuration and to analyse the dynamic performance of the FLNG-LNGC system. The FLNG-LNGC system includes the two vessels and the connecting system (hawser, fenders, mooring lines and offloading arms) with the investigation conducted for different loading conditions subjected to a variety of environmental conditions.

Predictive techniques were proposed for the estimation of nonlinear wave elevations based on the parameters of gap distance, vessel draft, wave direction and wave frequency. The numerical analysis was carried out with the potential flow solver, with HydroD in the frequency domain and SIMA in the time domain. To estimate the gap resonance RAOs numerically, a damping lid was introduced into the potential flow solver, to damp the overestimated wave elevation in the gap. The predicted gap resonance RAOs from the potential flow solver is analysed with the addition of a calibrated damping factors and compared with the model test data and show satisfactory agreement for different gap distances. Besides, a gap resonance experiment was conducted in Hydrodynamics Lab at Newcastle University using a new combination of ship sizes with the large model representing the FLNG and smaller model representing the LNGC. The results from the experiment data were used to determine the specific frequencies where resonance occurs. At this resonance frequencies there exist wave elevations in the gap that are extremely higher than that of the incident waves. It was deduced at the resonance frequencies that wave amplification factors can be obtained for the test cases. The generated data from the model test was further analysed to validate the estimated prediction of gap resonance phenomenon. It was indicated that, for the models test at beam sea and oblique sea in regular waves, there are amplification of the surface elevation in the gap at certain specific frequencies which are called resonance frequencies. These frequencies are

related to the scantlings of FLNG and LNGC models. It is possible to estimate the amplitude of gap resonance using the different parameters in the model test analysis.

Another set of numerical analysis was conducted in SIMA, to study the hydrodynamic characteristics of the floating FLNG-LNGC system, with the FLNG moored using a turret mooring system whilst connected to the LNGC via hawsers and fenders. The damping in the gap region was calibrated from the model test and tuned to obtain a suitable damping factor. Various test cases consisting of different loading conditions for the two vessels and environmental factors which combined wind, wave and current was used for the analyses and evaluation. The relative motions and force responses of the mooring system and connecting hawsers and fenders are analysed. The effects of loading conditions and environmental factors on the hydrodynamic performance of the vessels and the forced on the connecting system including the offloading arms are also investigated.

The main in innovation of the research is the provision of an experimental study that better reflects the industry operation by using a new combination of ship sizes for the model test with numerous test cases, because previous gap resonance experiments used models of identical sizes. Secondly, the lack of efficient numerical methods to predict the gap resonance and to guide the operation hence, a novel Artificial Neural Network ANN approach has been proposed and the data from the validated model test and numerical simulation was used for the prediction, Finally, with the limited knowledge on the effect of responses of the FLNG-LNGC mechanical coupling effect, numerical simulation with different test cases such as gap distance, loading conditions and wave direction have been carried out, because FLNG is a relatively new technology the results add to the body of knowledge for improved safety and industry operation during side-by-side offloading.

Keywords:

FLNG, Gap resonance, side-by-side offloading, basin experiment, numerical analysis, predictive modelling, artificial neural network

Dedication

I dedicate this research to Almighty God for guidance and inspiration.

To my lovely and wonderful my mother Edith Nwafor who has always been there to support and encourage me and to my son Malakai Obinna Nwafor who has been a source of inspiration and motivation. I dedicate this work to you as a sign of my love and appreciation throughout the research.

ACKNOWLEDGEMENTS

I would first of all express my sincere gratitude to Almighty God, for the gift of life and for sustaining me through the different challenges I encountered during my research period.

I would also like to acknowledge my supervisor Prof Zhiqiang Hu for his effort, guidance, and contribution towards the success of my research. This would not have been possible without your expertise, knowledge, and experience throughout this program. I am also most grateful to have worked with Dr Yongchang Pu as my second supervisor.

I owe this privileged opportunity to the Federal Republic of Nigeria through the Petroleum Technology Development Fund (PTDF) for sponsoring this research program and ensuring that our yearly progress meet's set targets. I would like to express my appreciation to the Executive secretary and the entire staff of PTDF for meeting up the demands of me and all the other scholars.

I also want to express my deepest and sincere appreciation for the love and support from to my entire family, my mother Edith Nwafor, my Son Malakai Obinna Nwafor, my brothers, Nnanna Nwafor, Chike Nwafor and Emeka Nwafor, my sister-in-law Judith Nwafor, my nephews Nathan Nwafor and Nolan Nwafor, my Uncle Isaac Chuks and my Son's mother Trisha. I am truly grateful for all the motivation and encouragement given to me to see through this PhD research program.

Table of Contents

LIST OF FIGURES

LIST OF TABLES

Nomenclature

ζ	Wave elevation
$\emptyset_z$	free surface condition
$\boldsymbol{\beta}$	Wave direction
ω	Wave frequency
ε	damping factor

List of Publications

1. Nwafor, J.C. and Hu, Z. (2021) 'An Experimental and Numerical Analysis of Gap Resonance Applicable for FLNG Side-by-Side Offloading', *ASME 2021 40th International Conference on Ocean, Offshore and Arctic Engineering*. American Society of Mechanical Engineers Digital Collection.
2. Nwafor, J.C. (2022) 'Numerical Investigation on Coupling Dynamic Performance of FLNG and LNG Carriers ', *The 32nd International Offshore and Polar Engineering Conference*. Shanghai, China. ISOPE: International Society of Offshore and Polar Engineers

List of workshops

- Nwafor, C, J. and Akhil, N. (2020) ‘Numerical Investigation on Coupling Dynamic Performance of FLNG and LNG Carriers’ RINA & IMarEST Southern Joint Branch technical lecture/Workshop.

LIST OF ABBREVIATIONS

LNG	Liquefied Natural Gas
FLNG	Floating Liquefied Natural Gas
LNGC	Liquefied Natural Gas Carrier
SBS	Side by Side
RAO	Response amplitude operator
WG	Wave Gauge
ANN	Artificial Neural Network

Chapter 1. INTRODUCTION

There has been a global increase in the demand for clean energy such as Liquefied Natural Gas (LNG) in the last two decades. In the past, it was considered challenging to exploit the gas reserves located offshore. Previously this operation was in a stable location on land but as we move further into deep waters, the project infrastructure becomes more challenging to construct. To reduce the economic cost and increase the sustainability in bringing the product to market a new type of floating structure was designed which combines the facilities for liquefaction of the natural gas, storage and offloading LNG (Liquefied Natural Gas) to an LNG carrier for export. This structure is called an FLNG (Floating Liquefied Natural Gas) facility.

This new facility might be operating in a severe sea environment and will have to bear various environmental loads. To ensure a safe offloading of LNG from the FLNG to the LNGC, a side-by-side configuration is preferred, and this is to enable the offloading lines to overcome the cryogenic nature which the LNG is stored. The side-by-side arrangement brings the formation of a long narrow gap region between the two vessels during the offloading operation and there is a potential for wave elevations of the fluid in the gap region under the excitation of incident waves propagating in different direction. At specific resonance frequencies these wave elevations are amplified producing large fluid resonance which is higher than the wave amplitude of the surrounding water surface. This highly nonlinear phenomena is referred as “gap resonance” in both offshore industry and academia. The investigation of this phenomenon is important for safe offloading operation while parameters such as vessel hydrodynamics and loads on the connecting system also need to analyse for improved safety during the side-by-side configuration.

The FLNG is a relatively new technology, and this research seeks to fill the gap of existing research due to the lack of reliable gap resonance experimental results for two vessels that are not of identical sizes in side-by-side configuration by using, a new combination of vessel sizes, also there is a lack of an effective numerical modelling for predicting gap resonance, hence the proposition of a novel Artificial Neural Network ANN approach. Finally there is lack of sufficient data on the mechanical coupling effects between the hydrodynamics of the multibody side-by-side configuration and

the connecting system (hawsers, fenders and mooring lines). Thus, numerical simulation using the potential flow software SIMA was done.

1.1 Introduction to Floating Liquefied Natural Gas (FLNG)

The idea to produce LNG offshore has been studied since the beginning of 1970's with significant experimental research starting in the mid-1990s. As the years progressed the concept has strengthened, and technical hurdles and challenges have been addressed to actualise the reality of an FLNG facility. FLNGs are superstructures which provide the ability to access previously stranded gas reserves. This technology was pioneered for the Prelude field in Australia and Petronas for Sarawak Malaysia. Shell's innovative prelude FLNG facility (**Error! Reference source not found.**) was scheduled to be operational in 2018 for offshore Australia. With a total length of 488m, width of 74m and a displacement of 600,000 tonnes the Shell's prelude is the currently the largest floating offshore structure built to date (Zhao et al., 2018a). In 2017, it arrived in Australian waters and was deployed North West coast of Australia to develop the Prelude and Concerto gas discoveries.

Figure 1-1Prelude FLNG on station with LNG carrier alongside – image: Shell

A standard FLNG development is made up of different operations within the supply chain as shown below:

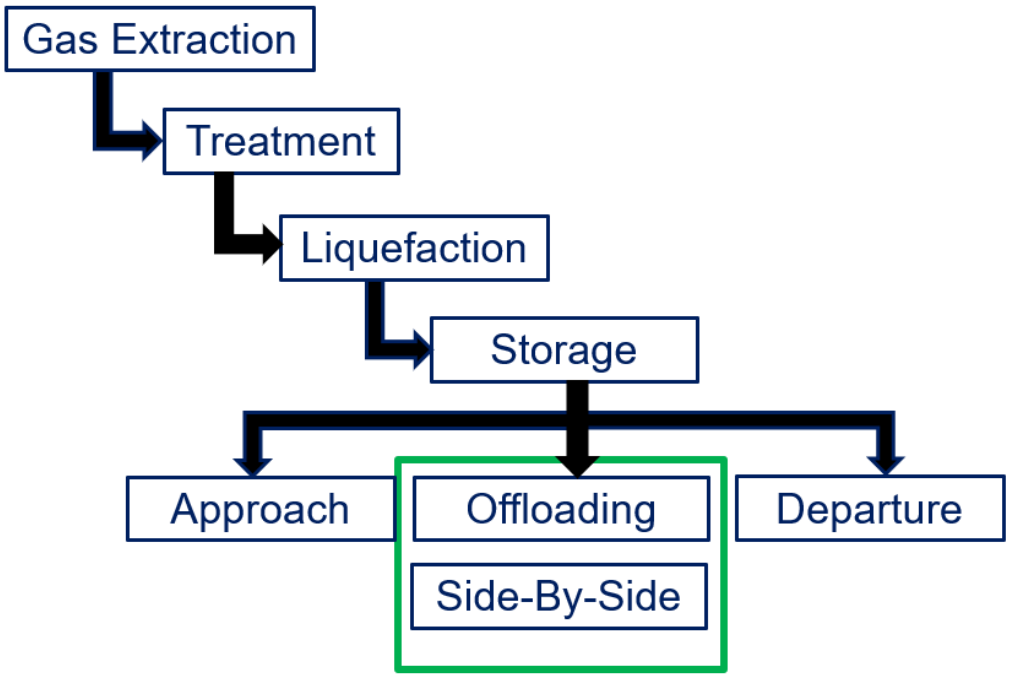

Figure 1-2FLNG supply chain

The FLNG is typically moored close to the gas field using groups of mooring lines, either chain lines or a combination of chain and rope. Flexible multi-layered risers feed gas and condensate via a series of production wells from the reservoirs into the FLNG facility. The liquefaction process of the gas and condensate takes places in modules and the refrigeration process liquefies the gas by cooling it to a cryogenic temperature of -162℃. The liquefied natural gas is initially stored in special containers before the final stage of offloading occurs. The side-by-side offloading configuration is used with the offloading arms specially designed for cryogenic loading onto the LNG carriers (LNGC) for onward delivery directly to market globally. With the adaptability of the FLNG to liquefy, store and offload the LNG right on-site of an offshore gas field either deep-water or shallow water, this reduces the number of operations in the supply chain

and the high cost for long subsea pipelines and constructions onshore. It also has less environmental footprint than the conventional oil and gas processing facilities on land.

1.2 Introduction to offloading operation

A significant part in the supply chain that determines the success of the FLNG concept, is the offloading operation. Which is the ability to transfer cryogenically stored natural gas (LNG) from the FLNG facility to an LNG carrier in the open sea and a high operability of this operation needs to be achieved. The probability of a successful offloading operation within a specific scheduled time is referred to as the operability. For example, the Shell's prelude requires the probability of success to be high at any point in time when the LNG carrier arrives. This is to ensure that the chances of losing the LNG product is reduced due to the inability to offload when the FLNG tank reached full capacity. Loss of this LNG product is a substantial loss of revenue and must be avoided hence the offloading operability is an important aspect to be considered in design.

LNG offloading comes with operational and hydrodynamic challenges and require attention both numerically and experimentally. The weather is also a limiting factor, the possibility of weather downtime impacting on the offloading operation influences the overall economic performance of the facility.

Lastly, offloading operations have a huge influence on safety, because of the involvement of two or more large structures in proximity to one another. The safety of the personnel onboard, the offshore facility and the possibility of environmental impact (pollution) is of great concern for regulatory authorities including the offshore LNG industry itself (Voogt and Brugts, 2010).

1.2.1 Types of Offloading methods

The choice of an offloading method affects the capital cost for the design of the system as well as the operational cost of the offloading operation. There are currently three methods available for offloading form a floating storage vessel as shown in (Figure 1-3).

a) A Catenary anchor leg mooring (CALM) buoy
b) Tandem offloading
c) Side-by-side offloading

(a) Loading at CALM

(b) Tandem offloading from turret moored FPSO

(c) Tandem offloading from spread moored FPSO

(d) Side-by-side offloading from turret moored FSO

Figure 1-3 Offloading configuration (Voogt and Brugts, 2010)

The CALM buoys and tandem offloading methods require a longer distance between the offloading facility and the transport vessel compared to the much shorter and narrow distance in the side-by-side offloading method. The transport vessel in the CALM buoys and tandem offloading configuration are free to weathervane to the prevailing weather (Figure 1-3 (a) and (b)), to position favourably against the wind so

its remnants bow to both wind and weather. This helps to lessen the impact of the external environmental forces on the transport vessel. This weathervane capability is suitable for turret moored vessels but for a spread mooring system shown in (Figure 1-3 (c)) the FPSO is a fixed heading relative to the seabed, where the bow usually heads into the dominant environmental forces which is typically the direction of the largest oncoming wave, in the spread mooring system the vessels cannot weathervane. Hence, due to this the tandem and CALM buoy offloading is widely used in the offshore oil industry for product transfer with limited side-by-side offloading configurations used in the oil industry (Voogt and Brugts, 2010).

However, in the gas industry, LNG can be offloaded in a tandem configuration in theory, with the LNG carrier moored to the stern of the FLNG facility. Tandem offloading arrangement is suitable for harsh environment, but LNG transfer is fairly new and the technology needed to perform this operation e.g. flexible cryogenic pipes is maturing and undergoing qualification. Moreover, the current existing LNG carriers are equipped with only mid-ship cargo transfer setup and for the tandem offloading of LNG to take place further bow loading modifications will need to done (Zhao et al., 2018a), also the incompatibility of cranes with lifting hoses on open sea for tandem arrangement. The typical LNG carrier is usually not fitted with chain stoppers and the LNG carriers that are fitted are not the appropriate size to meet the tandem offloading requirements (Newby and Pauw, 2010). Due to the cryogenic state of the LNG, floating hoses are the preferred option, this floating cryogenic hoses are will underdevelopment for to tandem LNG offloading (Giacosa et al., 2016). Tandem offloading is still in its infancy stage and will require time to improve in its operability, safety and reliability. Hence, the only preferable choice for LNG offloading remains the side-by-side method currently and for some time into the future.

Furthermore, LNG carriers that are usually loaded while berthed at the jetty are typically shielded from the impact of environmental forces such as with the use of breakwaters at a port, this environmental protection is no longer available because the LNGC is now moored to an FLNG in the open seas. Therefore side-by-side offloading of LNG in the open sea is a relatively novel procedure necessitating the need for new hardware development such as cryogenic offloading arms and new analysis methods. It is thus important to conduct research in this area to establish a best practice guideline for side-by-side offloading procedure.

1.2.2 Side-by-side offloading operation

The side-by-side offloading operation typically involves an LNG carrier moored alongside an FLNG vessel (**Error! Reference source not found.**) with temporary mooring lines (hawsers) which are deployed from the LNGC to the FLNG mooring deck to ensure the two vessels are kept together and close to relatively fixed position. Fenders are positioned in-between the offloading vessels to protect the hulls from colliding. A typical gap distance between the offloading vessels is ~4m with the largest available fender having a diameter of 5m. As FLNG projects increases in numbers, larger fenders will need to be developed and this will influence the design of offloading arms. At the import terminals of a quayside, the offloading usually takes 24 hours, with 12 to 16 hours involving actual pumping of LNG (Tusiani and Shearer, 2007). The side-by-side offloading will take a similar duration depending on the size of the LNG carriers which are getting larger, it is expected that the LNG transfer may take up to 30 hours and may be categorised into 3 stages of operation (Zhao et al., 2018a).i.e.

(a) Approach and berthing of the LNG carrier,

(b) LNG offloading

(c) LNG carrier departure/sail away

At the start of berthing stage, the LNG carrier will approach the turret moored FLNG and is positioned parallel to the FLNG vessel at an approximate distance between 100 – 150 m. Tugboats are used to manoeuvre the LNG carrier closer to the FLNG with caution until it impacts on the fender. Thereafter, the hawser lines are used to moor the vessels together with the aid of fasteners, these mooring lines are then pretensioned. Next the offloading arms on the FLNG are connected to the LNG manifold. Once connected, LNG transfer commences. After completion of offloading stage, the loading arms are disconnected individually, and hawser (mooring lines) released. Finally, the LNG carrier can now sail away with the assistance of tugboats where necessary (Poldervaart et al., 2006).

1.2.3 Challenges for side-by-side offloading

The transfer of LNG in a dynamic environment in open sea close to the gas reserve has lots of economic and environmental advantages but also faces numerous challenges and safety is a top priority in the LNG industry. The technology developed for FLNG offloading is relatively new and the data generated in practice are in its early stages, there are various aspects which affect the side-by-side offloading operability. The use of offloading arms requires the LNG carrier to approach very close to the FLNG and to be moored side-by-side. With this proximity of the two vessels they are exposed to external environmental forces such as wind, wave and current which induce vessel motions that limit the operations of the FLNG for example the operation of the onboard plant set acceptable working limits on the pitch or roll motions to one or two degrees to maintain acceptable efficiency level because larger motions can result in the closing down of the process equipment. In addition to the external environmental forces, gap resonance and internal tank slushing also induce multibody hydrodynamic interaction of the two vessels. The relative offloading vessel dynamics are affected by hydrodynamic factors consisting of mean offset due to wind, current, the slow drift motions and wave frequency notion of the two connected floating system. The vessel connecting systems consist of mooring lines, hawsers, and fenders. When the two vessels are moored side-by-side, the relative motions induce high tension in the hawsers between the vessels, a compressing force on the fenders and large angles in the offloading arms. The combination of the external and internal forces limits LNG offloading, which is crucial in the supply chain, if offloading is not taking place, production will have to shut down when the storage tanks of the FLNG are full. With the limited vessel motion which the FLNG operates the suitable weather is a calm or benign condition which has limited weather windows that to allow sufficient production and offloading to work safely and efficiently.

1.3 Connecting systems

The side-by-side mechanical connecting system offer nonlinear dynamic coupling of the two vessel and consist of

- Hawsers lines
- Mooring lines
- Fenders
- Offloading arm

1.3.1 Hawser Lines

A hawser is a heavy rope or cable used for towing or mooring a ship. The hawser goes through a component of the vessel called the hawsehole.
. The hawsehole can either be a single or pair of openings located at the waterproof section of the hull which is situated at the front and the side of the vessel. The hawseholes are typically referred to as hawse. The long-established method of making hawsers was to braid together three fibrous strands to ensure the rope is thick and strong enough to secure or move the vessel. Recently, hawsers are made of steel, which is less susceptible to wear and breakage than ropes. The thickness of most hawsers ranges from 0.02 inches (0.5mm) to 0.4 inches (10mm). The level of toughness and the thickness of the hawser signifies how effective it will be in towing or mooring the vessels. The hawser rope lines must be strong enough for the crew to pull the ship. The reliable hawser should be able to keep the vessel in a specific position, usually at a dock or for loading and unloading during the side-by-side configuration without allowing the transport vessel to go a drift or cause damage. Safe mooring of the FLNG and LNGC SBS comprise of environmental forces applied to the two vessels, general principles are used to determine how the applied forces are distributed to the hawser lines.

Figure 1-4 Hawser rope (Mooring Hawser-pekasis company)

The Hawser for the FLNG LNGC side-by-side offloading can be grouped into nine groups: the bow lines, forward bow spring, forward breast line, aft bow spring, waist breast line, forward quarter spring, aft breast line, aft quarter spring and the stern line.

- **Bow lines:** Usually runs through the bull nose on the bow and down to the dock, leading ahead of the ship. These lines help to bring the ship towards the dock.
- **Forward bow spring:** From the aft part of the bow leading forward, these lines help to stop the ship from surging backward should a wind wave force the ship astern.
- **Forward Breast line:** Typically put out from the bow, these lines hold the ship along the dock. The lines do not stop surge but prevent sway away from the other vessel of dock.
- **Aft bow spring:** From the bow leading aft, these hawser lines help to stop forward surging of the ship in a wind wave force in heading sea. Also, when

run forward against, the lines help to kick the ship stern out away from the dock.

- **Waist breast line:** They are pulled out from midship to hold the ship alongside another ship or dock. They do not prevent surging but sway away from the dock and are typically the last lines sent out and first brought in.
- **Forward quarter spring:** These lines stop the ship from surging aft and run from the stern forward. When pulled astern against, the lines aid in pushing the bow out away from the other ship or dock.
- **Aft breast line:** Usually put out from the stern, these lines hold the ship alongside another ship or dock. The lines do not stop surging but sway away from the other ship or dick.
- **After quarter spring:** These lines stop the ship from surging and run from the quarter aft. These lines help to pull the ship in towards another ship or dock when pulled astern against.
- **Stern lines:** The line runs from the stern and typically run through the centreline chock. It run aft of the ship. The lines help to bring the ship alongside another ship or the dock when pulled forward against.

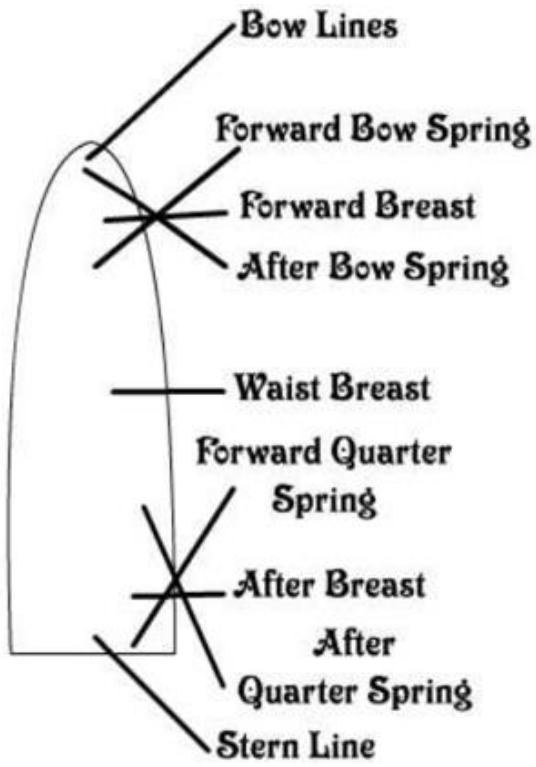

Figure 1-5 Hawser Lines (https://deckskills.tripod.com/cadetsite/id131.html)

1.3.2 Mooring Lines

The key function of a mooring system is to ensure the FLNG facility station-keeping characteristics. The line has various design challenges [Offset + lifetime + installation + positioning]. During the design stage, the mooring lines have to maintain the vessel & subsea operation safety in extreme & accidental condition, to size mooring line components (length & strength) vs extreme tension and to determine extreme & mean tension level to size deck equipment & hull structure.

Types of mooring systems: We have two main groups

- **Spread mooring:** The spread mooring is a passive system and is used for platforms such as Floating Production Storage and Offloading (FPSO), Semi-submersibles and SPARs. This mooring system is typically used in offshore operations in West Africa & Gulf of Mexico (GoM). Mooring lines are typically made from a combination of chain and wire or synthetic rope, they are in a fixed position on the platform as shown in Figure 1-6. This mooring system is best suited for benign environment (wave) and may be cost effective. The main drawback of the spread mooring system is the low availability for the offloading operation with a shuttle tanker or LNG carrier this can be overcome by making use of a catenary anchor leg mooring (CALM) buoy for the export operation.

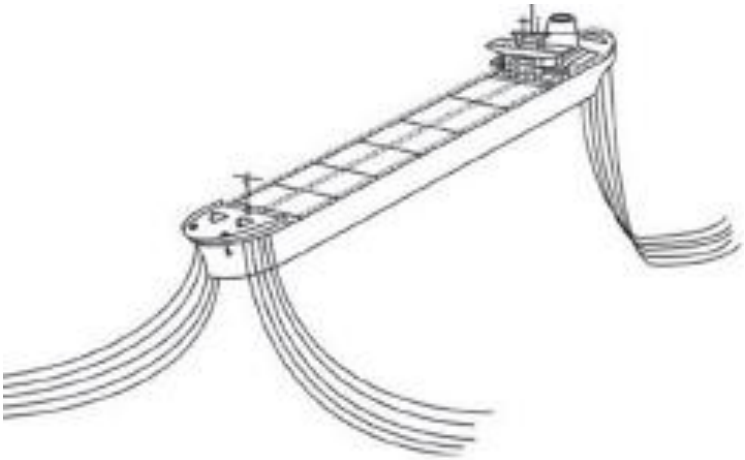

Figure 1-6 Spread mooring system
(Jenis mooring system Pada FPSO SSO)

- **Single-point mooring (SPM)** such as a turret and a buoy: The turret mooring is an active system. It has weathervane capability to keep the mooring forces and vessel roll motion to a minimal. The turret mooring systems are either be permanently fixed or disconnectable. It can be fitted with thrusters or Directional Position (DP) systems. This mooring system is typically used in offshore operations in the North Sea, offshore Canada, and offshore Australia.

  The turret is a device which can be built into a vessel with a bearing arrangement for weathervane. An internal turret has more than 20 risers while an external turret has up to 20 risers. The internal turret is with FPSO and is adapted for the FLNG.

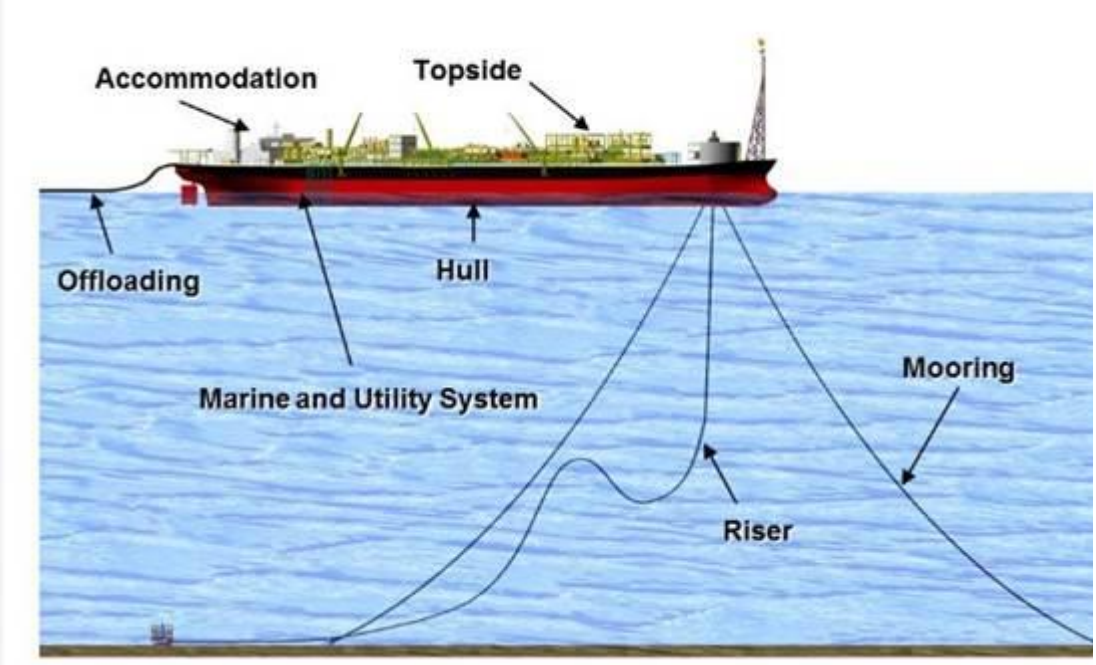

Figure 1-7 turret mooring system
(Offshore Tech, LLC)

Mooring Line Configuration: There are four main types of mooring line configurations

- **Catenary mooring:** This mooring configuration has part of the chain running on the seabed this makes a large anchor radius. There are small vertical loads on the anchors.

- **Semi-taut mooring:** These moorings consist of partial chains on the seabed and the anchor is subjected to vertical loads.
- **Taut mooring:** There are no chains touching the seabed and the anchor radius is approximately the same as the water depth.
- **Hybrid mooring:** This mooring configuration are designed with buoyancy modules. It is normally avoided due to interference issue.

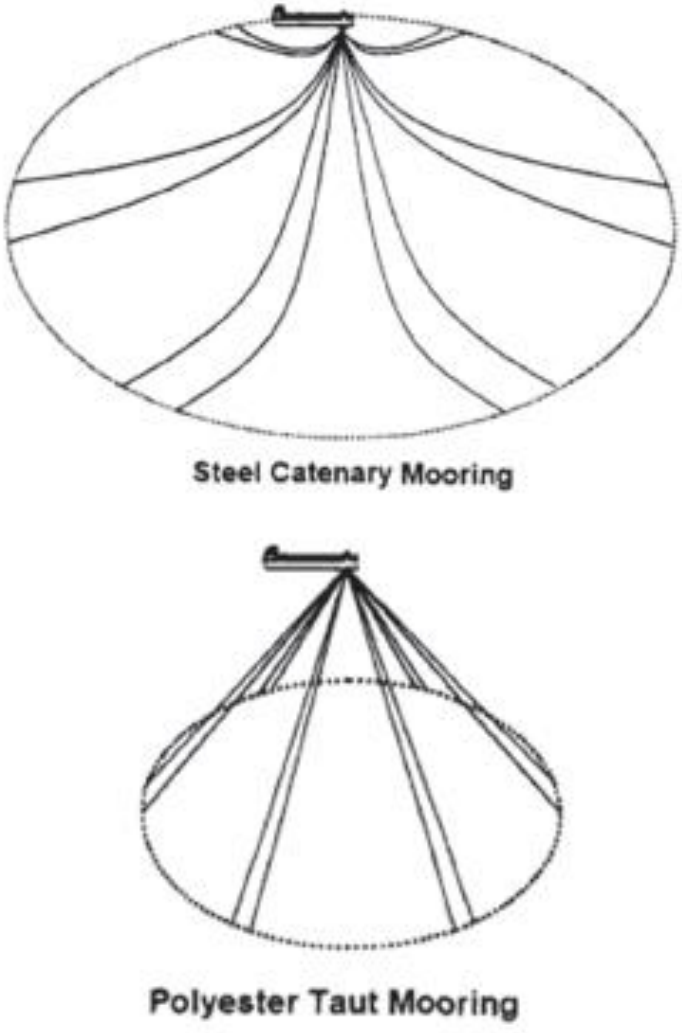

Figure 1-8 Mooring configuration
(https://www.esru.strath.ac.uk//eande/web_sites/11-12/more/mooring/types.html)

For the pattern of the mooring system there are no specific rules for the number of lines, headings, or anchor distances. Although the arrangement must be as much symmetrical as possible, and the vessel is usually moored facing the main weather incidence. This combination of patterns depends on the subsea & field layout,

geotechnical survey (soil condition), weather directionality, water depth, risk of collision, offset limitation, lifetime before replacement etc.

Mooring Line Component: The mooring lines are composed the anchor, ground chain segment, Lighter segments (Spiral strands or synthetic fibre rope), the top chain segment and the mooring connectors.

- Mooring line chain: The chain is typically heavy, has high-breaking strength, high young modulus (E) and no bending. An all chain line is used for water depth less than 100-200m. The studs provide stability for shallow waters.
- Metallic Wire: The most popular materials are carbon or stainless steel. It is lighter than chain, slightly bending. 6 strand are used for temporary operations while the spiral are for permanent operation. Sheathing provides corrosion resistance
- Synthetic fibres: These non-metallic ropes are used for their good corrosion resistance properties and have a high strength-to-weight ratio. Fibre ropes are made of a number of strands twisted together.

(a)

(b)

Figure 1-9 Mooring Line components (a) Chain (b) rope (Garware Fibres)

1.3.3 Fenders

Marine Fenders are used to absorb kinetic energy generated during collision of a berthing vessel and help to stop any damage to the vessel (LNGC) or the berthing structure (FLNG). They are like bumpers but for ports/ships to ensure efficient berthing. For side by side offloading operation floating fenders such as pneumatic or foam elastomer fenders are typically used. There are different shapes and sizes of fenders used for a variety of functions and applications.

a. **Cylindrical fenders:** These fenders are commonly used to ensure safe and linear berthing of various types of vessels. Cylindrical or extruded fenders offer an economical solution to protect most berthing structures and provides ease of installation.
b. **Pneumatic fenders:** Pneumatic fenders are widely used for side-by-side, ship to ship transfer in open sea, double banking operations and as vessel-to-berth at dock or jetties. This fender has an exceptional property of having a low reactionary force at low deflection which makes the pneumatic fender appropriate for liquid cargo vessels and protects vessels with delicate equipment. The energy absorption and linear load-deflection characteristics of this fender is very good. The pneumatic fender can also be called floating fender or yokohama fender. There are four types of Pneumatic fenders (i) Chain

and tyre Net type (ii) Sling type (iii) Rib type (iv) Rope Net type. This fender is extensively used as a sheep protection medium by large tankers, ocean platforms, LPG vessels, etc.

Figure 1-10 Pneumatic fenders (https://www.y-yokohama.com/global/product/mb/pneumatic)

c. **Foam elastomer fenders:** The foam elastomer fenders are usually made up of a closed-cell Polyethylene foam core, that is encased in Kevlar or nylon reinforced Polyurethane skin. The pneumatic fender and the foam elastomer fenders have comparable performance, but this fender will sustain their functionality in the event of the skin getting punctured. It is not possible to deflate the foam elastomer fenders.

Figure 1-11 Foam fenders
(*http://trelleborg.tecs1.com/smarter-foam-theory-foam-fender-behaviours*)

d. **Square fenders:** These fenders are used on vessels and small jetties. The square fenders are compression-molded and commonly used on tugs, boats and ship
e. **Roller fenders:** Roller fenders are used to guide floating structures and pontoons gently and quietly up & down their guide piles.

Figure 1-12 Roller fenders (https://www.trelleborg.com/en/marine-and-infrastructure/products-solutions-and-services/marine/marine-fenders/rubber-fenders/cushion-rollers)

some popular ones are cell fenders, cone fenders, Arch fenders, D-shape fenders, Tugboat fender, Hydro-pneumatic fenders, Corner fenders, Keyhole fenders, Solid rubber fender, Floating rubber fender etc. It is important to consider the design and berthing data to determine the most suitable fender. Quality fenders are needed to keep for safe offloading during side-by-side configuration.

Fender design: There are several standards used globally to design a fender system. The most widely used standard is the PIANC " Guidelines for the design of fenders, 2002" (Pianc, 2002). The Industrial Standards (JIS) are mostly used in Japan, while both the United States of America and the United Kingdom use the British Standard BS 6349:part 4 (Standard, 1991).

In the design of the fender system the berthing energy of a different vessels are analysed to determine what size of fender can be able to absorb the kinetic energy generated and lastly finding a way to minimise the reaction force generated from causing excessive pressure on the hull.

1.3.4 Loading arms

As discussed earlier the side-by-side offloading operation has different stages: the approach or berthing stage, the offloading stage and the departure stage. The

offloading stage has the longest duration with the use of offloading arms in the side-by-side moored configuration and this process takes about 20~29 hours. The tip of the loading arm is connected to the manifold of the LNGC, thereby increasing the interdependence between the two vessels in the LNG offloading systems. It is important to identify and reduce cascading failures across the system. This is a significant challenge to maintain reliability and safety during operation of the LNG offloading process (Hu et al., 2021). A proper loading arrangement is necessary for any ship that loads liquid cargo. The conventional Tankers typically make use of flexible rubber hoses or reinforced composite hoses. LNG are loaded only through loading arms.

a. Loading Arrangement

Due to the cryogenic temperature (-159) degree Celsius which the LNG is stored and usually loaded rubber flexible hoses or normal steel loading arms cannot cope with such temperatures. Hence, these are generally made using expensive special low temperature alloy, that possess very good thermal expansion and contraction properties. Figure 1-13 shows some of the main parts of the loading arm. The FLNG loading terminal typically have 4 or 5 arms as shown in Figure 1-14 which are used for different purposes. Loading arms are mainly used because of their flexibility and ability to accommodate vessel movement, trim or list during the offloading operation. The loading arms are operated hydraulically with emergency release coupling and emergency release system also fitted. A vital point is the fitting of strainers in-between the loading arms and the LNGC manifold. There are two swivel joints at the top and at the bottom of the loading arm. The top swivel and sheave are connected to the inboard and outboard arms. The assembly for slewing and shore side docking piping are formed by the bottom swivel and sheave. The bottom sheave and swivel integrate the use of counterweights to decrease the amount of dead weight of the arm on the LNGC manifold connection, this reduces the power needed to guide the arm into position. The main design for the use of loading arm is to allow sufficient operating envelope

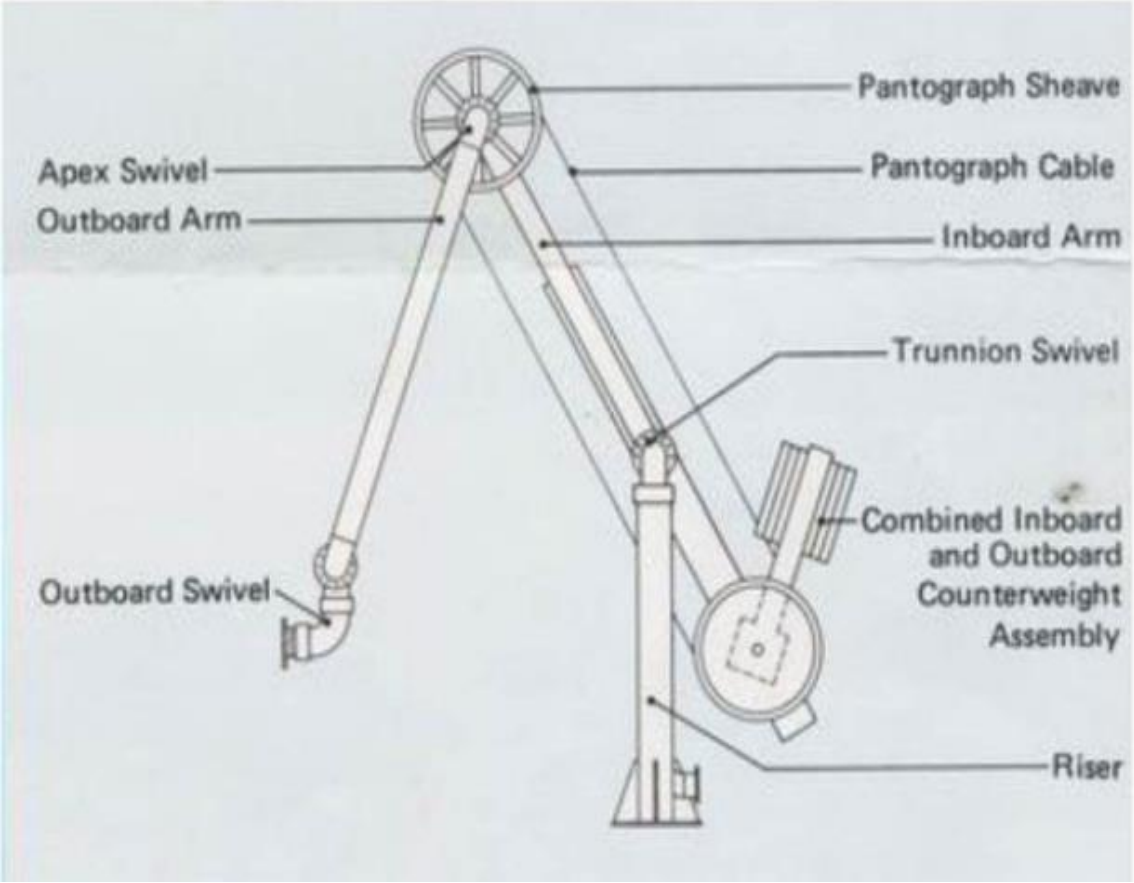

Figure 1-13 Loading Arm Schematic Picture (Marine insight)

b. The Inner Connections

There are two types of connection between the loading arm and the shore side pipe flange which is the simple bolted flange connections and the QCDC (Quick Connect/Disconnect Couplings). LNG terminals usually use the QCDC for fast connections. The couplings are operated hydraulically and controlled manually. The vessel and shore flanges are mechanically locked and independent of hydraulic power supply. The major benefit of the loading arm QCDC connection is the addition of the ESD (Emergency Shutdown). During a loading operation the ESD can be activated in an emergency from multiple points, that may cause the loading arm to breakaway immediately in a safe way to prevent further damage. There are typically two ball valves linked remotely to the emergency shutdown system. Anytime ESD is activated, the two valves instantly shut without any further damage to the vessel cargo and shore pipe works.

TechnipFMC loading arms
onboard Petronas FLNG satu

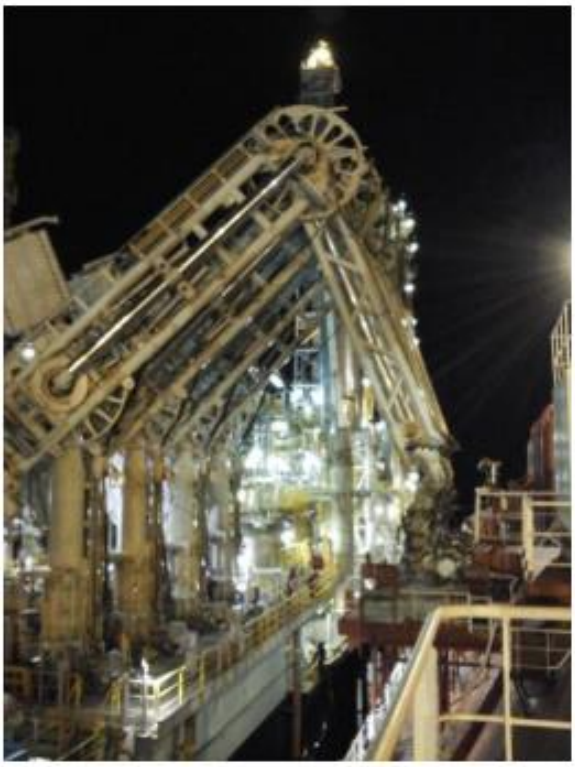

TechnipFMC loading arms

Figure 1-14 FLNG loading arms

Several challenges were identified for the loading arms during the installation on the prelude FLNG (Morilhat, 2019)

- Extreme hydrodynamic conditions of 2.5m significant wave height (Hs), with two moving bodies (FLNG and LNGC) require new nonlinear dynamic stress analysis to highlight both the inertia and frequential loads applied to the offloading arms and to the LNGC manifold.

- Due to the different levels of vessel elevation between the FLNG and LNGC, the development of a new loading arm kinematic, the OLAF (Offshore Loading Arm Footless) is required to reduce the weight of articulated assembly of the loading arm that results in dynamic load transfer to the LNGC manifold.
- The safety and integrity level expectation are increased from SIL2 to SIL3, which has a significant impact in the control systems architecture and Emergency Shut Down (ESD) philosophy.

With offshore access limited, the maintenance process was reviewed and modified, to take into account that the offloading arm needed to be readily available an average of every 4 days for offloading.

1.4 Introduction to gap resonance

Gap resonance is an important phenomenon which needs to be taken into consideration in the design phase for the side-by-side offloading operation. Gap resonance has some similarity to the features of a moonpool resonance. A moonpool is a typical feature of marine drilling vessels, drilling platforms and diving support vessels, It is an opening through the base of a hull or platform that enables researchers or technicians to have access to the sea to easily lower tools and instruments into the sea as shown in (

Figure 1-15(a)). Moonpools have a significant effect on the seakeeping performance of a ship in the area of resonance frequency. At certain frequencies when external waves and the structure interact this dramatic resonance fluid motion occur which mostly happens at the natural frequency. The moonpool drillship acts differently at different resonance modes called the sloshing and piston mode, in the sloshing mode, the water moves from side to side, back and forth between the vertical walls, while in the piston the water moves in a heave motion up and down like a rigid body(Molin, 2001)

In the FLNG side-by-side offloading configuration the formation of a long narrow gap with open ends is formed and the first harmonics (mode) which is equivalent to the piston mode in the moonpool is non flat along the gap. Due to the proximity of the vessels the side-by-side offloading should only be carried out in calm sea condition. Although, we have long period swells every time on the ocean surface from distance storms. In practice, the water surface in the gap region does not posses significant

surface motion linearly from these swells, because of the low frequencies of long period to couple to the lowest gap mode. Nevertheless, it has been demonstrated that it is possible to show in model test that quadratic frequency doubling can occur and couple to the gap resonance (Zhao et al., 2017b).

(a) Moonpool

(b) Float over operation

(c) Transhipment of iron ore

(d) Wind turbine

Figure 1-15: Hydrodynamic resonance in marine operations. Figure (a) JOIDES Resolution, (b) Aasat Hansteen (c) Almeida (d) Groizeleau.

The occurrence of gap resonance is significant importance. The wave elevation of the trapped water in the gap region will be much larger than that of the surrounding water which can induce vessel motion, thereby increasing the risk of collision, increasing the impact on the fenders, tension on the hawsers and exceeding the safety limits pitch or roll motion for the offloading arms. This may increase downtime for the offloading operation and thereafter affect the economic performance of the project. This phenomenon may also threaten the safety of both the vessel and crew members.

Hydrodynamic resonance such as the moonpool or gap occur is numerous other offshore operations, which cause a large water elevation at resonance frequency to occur as shown in Figure 1-15 which include an offshore wind turbine damping pool, the gap between two barges transporting topsides or the transhipment of bulk dry cargo respectively. All these forms of hydrodynamic resonance affect the vessel and cargo motions causing operational challenges if the necessary safety measures are not taken into consideration.

To provide engineering guidelines for improved safety and reliability of the FLNG side-by-side offloading and to gain a better understanding of the effects of gap resonance on the vessels, connecting system and offloading arms adequate research has to be conducted.

1.5 Introduction to Multi-body floating systems

1.5.1 Multibody structure

When we have more than one floating structure that are in water, we have a multi-body system such as the side-by-side arrangement of an FLNG and LNGC. When the vessels are in motion, the interaction of one body (FLNG) close to the other body (LNGC) is very important, particularly if they are in proximity to each other as shown in **Error! Reference source not found.**. The presence of one body influences the forces acting on the other body. The hydrodynamic coefficients of one body depends on the other body moving in unison. In this case, all the floating bodies of structures have to be included in the diffraction and radiation analysis (Chakrabarti and Cotter, 1979). An illustration is of this example is presented by Kokkinowrachos and Zibell (1984b) Figure 1-16. A three-cylinder configuration added mass and damping coefficients for heave motion are plotted for two-dimensional cylinders case. The corresponding values for a single body cylinder case is also shown. It is observed that the coefficient values are sensitive to the presence of the neighbouring cylinder. As a matter of fact, this interaction makes the coefficient have negative values at certain *ka* values.

One of the widely seen multi-body structures that come across this type of interaction problems is the semi-submersibles. The twin-hull pontoon of the semi-submersibles are parallel and have vertical columns that are connected to the platform. This structure is a common type of floating drilling rig. The submerged vertical members of the twin hull semi-submersible vary in size from the Morison force regime to the diffraction regime. The strip theory method is occasionally, coupled with the former. The arrangement of the vertical and horizontal submerged members are in such a way that the two neighbouring members have interaction which is inevitably present irrespective of the method used for the wave force calculation.

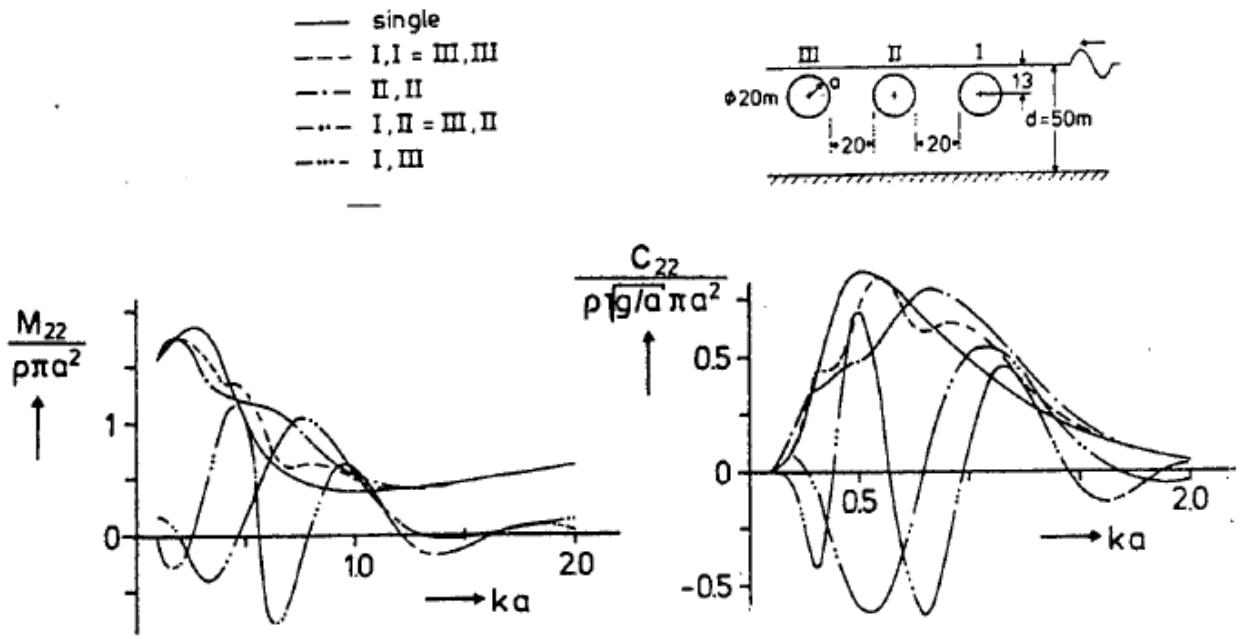

Figure 1-16 Added mass (M_{22}) and damping coefficients (C_{22}) in heave for three circular cylinders in unison (Kokkinowrachos and Zibell, 1984a)

1.5.2 Two Floating vessels

For the FLNG and LNGC vessels in side-by-side configuration, that are allowed to move independently, this poses a more complexed interaction problem. When the two floating large displacement vessels are in proximity to each other linked together with connecting systems (hawsers, fenders & mooring lines), the motion of one vessel is influenced by the motion of the other floating vessel. This multibody interaction is gotten from the fact that when an incident wave impacts on one vessel and scatters, this scattered waves incident on the second floating vessel. Furthermore, radiated waves produced from one vessel are experienced by the other vessel. Besides the hydrodynamic interaction, the elastic coupling between the FLNG and LNGC through the connecting system also influences the responses of the two. Vessels which are moored side-by-side particularly experience this kind of interaction challenges. The LNGC, which is the smaller vessel, is influenced more by the presence of the larger FLNG vessel. To compute the hydrodynamic coefficients associated with one of the vessels, the second vessel is assumed to be fixed in a first order solution and only the former one under consideration is in simple harmonic motion. Hence, the body surface boundary conditions on the two structures are as follows. The velocity potential on the vessel motion should satisfy the radiation condition. This brings about an added mass

and damping coefficient for the first vessel because of its motion and a cross term of added mass and damping coefficients on the second vessel because of the motion of one vessel only. Consequently, many cross terms occur in that each motion of one vessel gives rise to, up to six pairs of coefficients for the other vessel. The boundary value problem is also a bit complexed to solve due to the fixed boundaries including the contour of the fixed structure. The hydrodynamic forces are computed in a relatively straightforward way by the linear diffraction/strip theory in which the boundary conditions on both the fixed vessels are satisfied simultaneously. In this case the same numerical analysis as fixed multibody structure discussed earlier is applicable. The hydrodynamic and mechanical interaction between the two vessels (FLNG and LNGC) is computed from the potential theory as used for a single vessel with principal extension that the degrees of freedom is increased from 6 (six) to 6N where the N is the total number of structure. For the case of side-by-side arrangement we have 2 floating vessels therefore there are 12 degrees of freedom.

1.6 Predictive modelling

1.6.1 Nonlinear Curve fitting

The curve-fitting data analysis is run in MATLAB coding software and uses the least square method of when fitting data. The fitting processes involves a model that relates the response data to that of the predictor data with one or more coefficients. The result of the fitting process is an approximate of the “true” but unknown coefficients of the model. To get the estimated coefficients, the least square method minimizes the summed square of the residuals.

The curve-fitting toolbox is a collection of GUI graphical user interfaces and M-files functions developed on MATLAB technical computing environment. It offers numerous features, such as parametric fit, which is used in this section. A custom equation that can be defined to suit our specific curve fitting requirements and be used to perform the parametric fit.

Algorithms of different methods can be chosen in the curve-fitting Toolbox such as Trust-region, Levenberg-Marquardt, and Gauss-Newton.

a. *For Trust-region:* This algorithm is set as default and is used if you specify a coefficient constraint. It can solves difficult nonlinear problems more efficiently than other algorithms and represents an advancement over the popular.
b. *Levenberg-Marquardt:* This algorithm has been proven to work for a wide range of nonlinear models and starting values. If the trust-region doesn't generate a reasonable fit, and there is no coefficient constraints the Levenberg-Marquardt algorithm can be used.
c. Gauss-*Newton:* This is potentially faster than other algorithms but has the assumption that the residuals are close to zero. It is included in the toolbox for pedagogical reasons and is usually the last choice for most models and data sets (Motulsky and Christopoulos, 2004)

1.6.2 Artificial Neural Networks

ANN was initially presented as a simplified model of brain-function. The human brain is made of billions of interconnected neurons. These cells have specialized members which allow the transmission of signals to neighbouring neurons (Cha et al., 2011).

The theory of neural network concepts can be found in different studies including books (Kubat, 1995). Neural network application in engineering prediction have been studied by Kasperkiewicz et al. (1995), Grubert (1995), Thirumalaiah and Deo (1998), and Thirumalaiah and Deo (1998) with its application for prediction of concrete strength, rainfall and waves in offshore and onshore structural parts.

Furthermore, ANN modelling has been applied for wave equations based on hydraulic data by Dibike (2002), prediction of water quality parameters Maier and Dandy (1997), tidal prediction by Lee et al. (2002), dynamic amplification of soil analyses prediction by Hurtado et al. (2001). In this paper, the ANN will be further applied to the prediction of gap resonance for different vessel configuration and environmental condition.

1.7 Aims & Objectives

This research aims to propose a useful method to predict the gap resonance amplitudes for engineering application guidance and improve the understanding its effects on vessel motion, connecting system and the offloading arm.

1.8 Objectives of the research

- To analyse the hydrodynamic behaviours of gap resonance between side-by-side configured FLNG and an LNG carrier.
- To perform experimental model test to investigate the wave elevation in the gap region between two closely spaced models with different incident waves frequencies, wave directions, gap distances and vessel draft for a new combination of model sizes.
- To apply numerical computation for analysis of the coupling effects between the gap resonance, the motions of the vessels and the connection systems.
- To develop a model to predict the occurrence of gap resonance based on the model test and numerical simulation data.
- To summarize a hydrodynamic law/conclusion from the research outcomes related to effect of gap resonance on multi-body systems during side-by-side configured offloading.

1.9 Thesis outline

Chapter 1 details the background of the research with an increase in demand for greener and an overview of the LNG industry trends leading to the demand for the production, storage and offloading of LNG in the open sea from the relatively new FLNG facilities to an LNG carrier. It also presents the challenges associated with the offloading stage, the areas this research intends to explore which is the phenomenon of gap resonance, and effect of external forces on the vessel motion and connecting systems (hawser, fenders, turret mooring and loading arms). This chapter also contains aims and objectives of the research.

Chapter 2 is literature review chapter. It expands on the characteristics of the gap resonance phenomenon, as it relates to FLNG side-by-side offloading scenario, safe

LNG offloading and an in-depth literature review of gap resonance, experimental model test for analysing gap resonance, hydrodynamics of multibody floating system and the connecting system. Also state of the art SIMA model features for the analysis. Also, in this chapter is the broad overview of the use of semi-empirical method and artificial neural network for predicting gap resonance occurrence.

Chapter 3 details the theoretical background for gap resonance phenomenon and addition of artificial damping term.

Chapter 4 discusses modelling process for the numerical simulation using potential flow theory and state of the art SIMO code in SIMA, for analysing the effects of gap distance and wave direction on the vessel motion, the hawser, fenders and offloading arms.

Chapter 5 discussed the experimental model test specification to conduct the gap resonance investigation based on different vessel sizes, different gap distances, wave frequencies, wave directions and vessel draft. The wave elevations of the incident wave in front of the models, the wave elevation in the gap and the diffracted wave behind the models were recorded with wave gauges position at strategic locations.

Chapter 5 details the verification of the experimental model test with the potential flow theory analysis to get the damping lid factor. It also highlights gap distance and wave direction on the vessel motion, also the sway and surge motion data was used to carry out calculations for the relative motions of the offloading arm position. As well as the parametric study on the vessel hydrodynamic and connecting system a comparative study was conducted between the semi-empirical analysis and Artificial Neural Network (ANN) to predict the occurrence of gap resonance.

Chapter 6 is the conclusion chapter. It Presents the research outcomes as well as the limitations associated with the current study and suggestions for future work was also captured within this chapter.

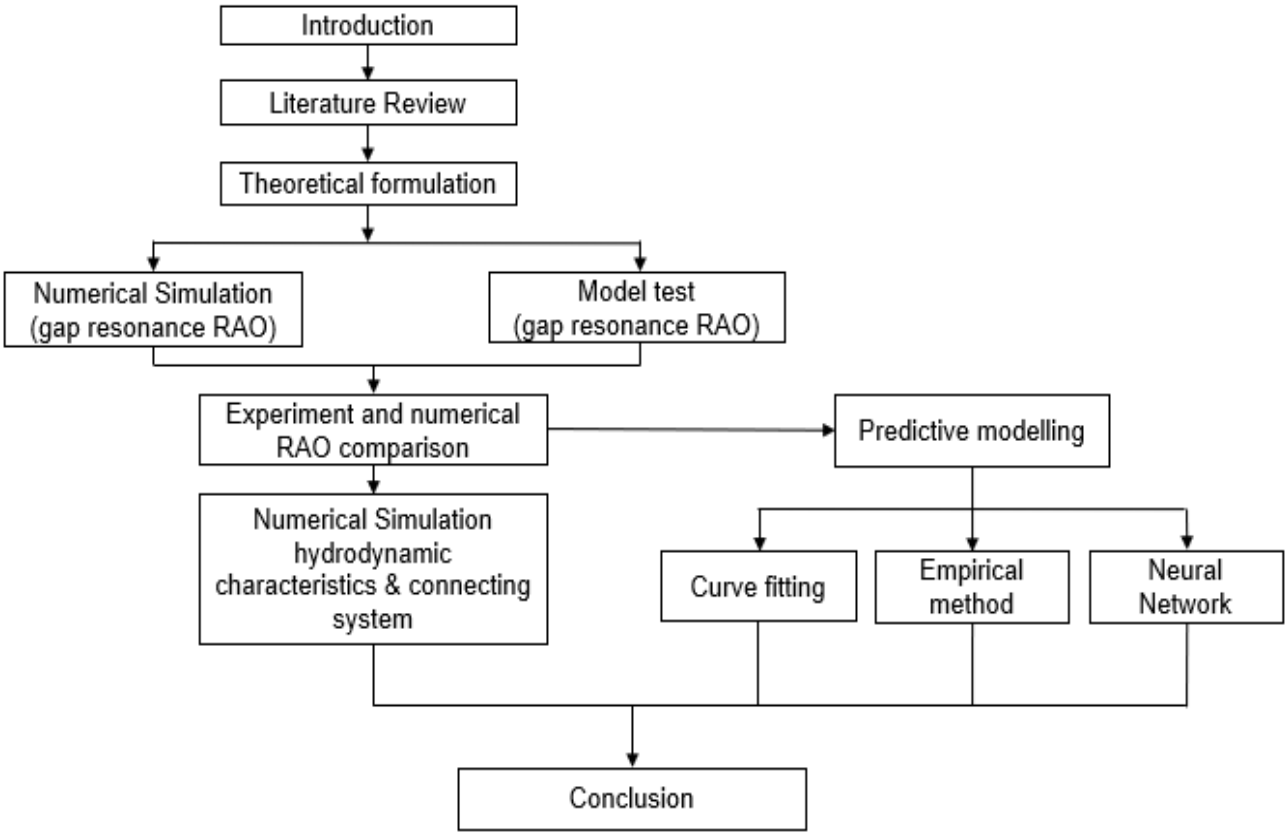

Figure 1-17 Thesis Structure

Chapter 2. LITERATURE REVIEW

2.1 General Description of trapped modes

Gap resonances are related to a category of trapped modes and their associated structures called trapped structures. Trapped modes can be described as oscillations of the free surface around a body which are not connected to the free surface in the far field. Initial research on trapped modes made use of fixed structures in a small area for instance horizontal by Ursell (1951) or vertical by Callan et al. (1991) cylinders in a channel, whereas subsequent authors built more complexed shapes that enclosed a section of the otherwise unbounded free surface in 2D by McIver (1996) and 3D by McIver and McIver (2007). A phenomenon related to near trapping where the local oscillation gradually decays because of the weak energy radiation to the far field, was discovered for fixed bottom-mounted cylinders in a finite row by Maniar and Newman (1997) or circles by Evans and Porter (1997).

A new nomenclature occurred when trapped modes around floating structures were discovered by McIver and McIver (2006) called sloshing trapped modes which happens in fixed structures and motion trapped modes which occurs around floating bodies. Structures that are motion-trapping and have part of the free surface enclosed with an axisymmetric shapes of complex vertical cross-section were studied by McIver and McIver (2007) and a simple rectangular cross-section was used later by Porter and Evans (2008). The incident regular waves at the trapping frequency, cannot excite motion-trapping structures as shown by McIver (2005) and experimentally researched by Kyozuka and Yoshida (1981), but given appropriate initial conditions, they can be excited.

The mathematical problem of the interaction of water waves and freely floating structures in open water was linearised and solved by firstly taking the Fourier transform in time and decomposing the result of the frequency domain problem into scattering and radiation problems. For a specific type of geometry, the non-uniqueness of the solutions water-wave problem correlates to the occurrence of the trapped mode and vice-versa. John (1950) showed the uniqueness for a distinct class of geometry and subsequently numerous other partial results have been found (e.g. Simon and Ursell (1984). At that time, most researchers in this field believed that it was only a

question of time before a general uniqueness proof would be obtained for any geometrical structure and for all frequencies.

Clarification on the reason why there was no general uniqueness proof was explained by McIver (1996) showing how to fixed structures that support trapped modes are constructed at a specific frequency. Thereafter, different structures for trapping were found. All those discovered are categorised by one or more holes that basically separate a portion of the free surface. The motion of the fluid is made up of sloshing supported by the hole, and the fluid motion decays to zero at the areas away from the structure. The trapped mode that are supported by fixed structures are called “sloshing modes”. McIver (1996) built a potential for sources of waves in the free surface with a gap of half a wavelength, which represents a trap mode oscillation between two surface piercing bodies. Subsequently, numerous trapping structures have been found in both 2D and 3D wave water problems. For example the trapped modes construction in axisymmetric toroidal structures (Kuznetsov and McIver, 1997, McIver and McIver, 2007), elliptical toroidal structures (McIver and Porter, 2002) two concentric surface piercing circular cylinders with no thickness (Shipway and Evans, 2003) and non-axisymmetric trapping structures with no vertical symmetry axis (McIver and Newman, 2003).A hydrodynamic analysis of surface piercing toroidal structure was carried out by Newman (1999) using potential flow solving software WAMIT and gave numerical evidence for the presence of trap modes: i.e. the added mass, free surface elevation and damping coefficients all exhibit singular behaviours in the area of the trapped mode frequency. The existence of a trap mode shows that finding accurate numerical solutions to radiation and diffraction problems close to the trap mode frequency is difficult. According to McIver (2005) we have “sloshing trapped structures” which are structures that are either fixed or have a prescribed motion. Additionally, we have “motion trapped structures”, which are free floating structures that respond to various hydrodynamic forces.

Though numerous kinds of trapping structures have been made, they take careful construction. Generally trapping are unlikely to happen but for offshore structures where large resonance effects occurs, neat trapping is highly likely. Wolgamot et al. (2016) constructed, experimentally a near motion trapping structure made up of rings of eight truncated cylinders.

This thesis mains aim is the slosh near trapped mode associated with two fixed boxes with a narrow gap between then and the motion trapped mode for two floating vessels and the effects on the vessel hydrodynamic and connecting system.

2.2 Literature review on gap resonance

There have been different studies on the gap resonance phenomenon, which shares some similarities to the moonpool resonance. FLNG is a relatively new type of offshore structure and side-by-side offloading operation increases the likelihood of gap resonance occurring thus research on the effect of this phenomenon is important and the side-by-side offloading from an FLNG to an LNGC should be carried in a calm sea state. Zhao et al. (2017b) observed that though, almost everywhere in the open ocean there is the possibility for the existence of long period swells from distance storms. In practice, these long period swells are of low frequency and produce surface wave excitation linearly in the gap region between the two vessels to couple with the lowest gap mode. Nevertheless, it has been demonstrated that it is possible to show experimentally that quadratic frequency doubling can happen and couple to the gap resonance. Frequency doubling is a phase sensitive process, that requires phase matching. Hence, this interaction are significant and should be investigated for safe and reliable planning of the offloading operation (Zhao et al., 2017b). One of the critical challenges which can take place in the long narrow gap region during the parallel configuration is the phenomenon of gap resonance. The resonance response occurs at specific frequencies which are associated with different motions and vessel response (Feng et al., 2017).

Molin et al. (2002), expanded on an earlier approach by Molin (2001) for predicting the frequencies and mode shapes for different gap resonant modes in a moonpool. An extensive investigation using two fixed boxes to study the frequencies, mode shapes and response amplitude using potential flow theory was carried out by Sun et al. (2010).

To obtain a better agreement of the potential flow results and the experimental data, different approaches have been introduced. One important approach for studying gap resonance problem is basin testing, and it is commonly known that potential flow theory tends to over predict the response amplitude than what is observed in the model

test experiment, despite having a good prediction of the resonant frequencies. There have been lots of attempts made to determine the cause of the difference between the linear potential flow theory and the model test data. For example it is widely stated that a major cause of difference is brought about from the viscous effects related to flow separation (Chua et al., 2016, Kristiansen and Faltinsen, 2012, Kristiansen and Faltinsen, 2008). A nonlinear numerical simulation using potential flow theory, was conducted by Feng and Bai (2015) and it was observed that the nonlinearity in the free surface conditions may instigate a small change in the resonance frequency (comparable to the recognised resonance frequency shift detected for a non-linear spring), but with limited effects on the resonance frequency amplitudes.

Various studies have found that during side-by-side offloading operation, low frequency motion is influenced by fluid in the long narrow gap in-between the vessels (Nam et al., 2015, Lu et al., 2010, Chakrabarti, 2001, Buchner et al., 2001). It was found that the gap resonance response for two identical fixed models takes many periods to reach steady state in the gap region and once this gap resonance is excited the decay time is lengthy (Zhao et al., 2018c). There is a strong connection between the gap distance and hydrodynamic interaction for advancing ships, the smaller the gap distance the larger the hydrodynamic interaction will be as stated by Islam and Murai (2013).

While research have been conducted with a focus on the study of the resonance amplitude at steady state in regular wave, though waves in the ocean are not regular in nature, and to achieve steady state is not straightforward in a wave tank because of the duration it takes for the gap resonance response to reach maximum amplitude, where wave reflection from the tank edges may interfere with experiment (Zhao et al., 2018c). Steady state resonance response was investigated in 2 dimension by Lu et al. (2011), Faltinsen et al. (2007) and in 3 dimensions by Molin et al. (2009), Pauw et al. (2007).

The estimation of the response amplitude operator (RAOs) of resonant fluid motion in the narrow gap (gap resonance RAOs), for different gap width can be carried out when a parametric fit to potential flow response transfer function is used with a scaled viscous damping. The predicted response amplitude has satisfactory agreement with the experimental data. At lab scale, it was observed that there was a non-zero gap

distance that produced the maximum wave amplitude in the gap region (Zhao et al., 2018b).

Investigations was carried out using a fixed and a floating vessel, taking the nonlinear wave excitation, the results show that at certain frequencies resonance amplification occurs, even if the fluid motion is first or second harmonic. It was also observed that hydrodynamic interaction occurs notwithstanding if the incident wave is a regular wave random wave (Perić and Swan, 2015).

There are specific frequencies that correspond with the resonance frequencies of the water surface in the gap region, this gap resonance frequencies producing maximum wave elevation, and this can induce an increased motion of the vessels which increase the likelihood of vessel collision and increased load on the connecting system. Also, at these specific frequencies the resonance response of the wave elevation on the kinematic free surface becomes extreme and the simulation model using potential flow theory, these wave amplitude in the gap become unrealistically high due to the low damping in the narrow gap. Many authors have introduced a various type of damping mechanisms to take this viscous damping effect into consideration. A rigid lid was introduced in the long narrow gap to reduce the free surface elevation under the lid by Huijsmans et al. (2001). The rigid lid was used to study multi-body vessel hydrodynamics to supress the unrealistic fluid velocity in the gap region, the potential flow solver according to Buchner et al. (2001) reduced the fluid velocity from 90m/s to acceptable limits of 9m/s. An alternative approach to the rigid lid was proposed for reducing the gap resonance responses by introducing a dissipation term to the kinematic free surface boundary condition. Numerous researchers have named this dissipation term epsilon (ε) or damping lid method. Many scholars have used the epsilon (ε) damping lid method to bring the gap region flow to an acceptable level.

Based on the 3D frequency domain green function, the damping lid method has been used to successfully reducing irregular frequencies present in the numerical solution Chen (2005b). The rigid lid and damping lid methods were compared an the widely recommended preference is the damping lid method on the fess surface region and a better alternative due the ability of due to its ability to reduce extreme free surface motion and reduce the irregular frequency in the narrow gap region (Bunnik et al., 2009).

The epsilon (ε) term used in the damping lid method has a challenge of choosing a suitable value for epsilon (ε). The selection of a suitable epsilon (ε) damping lid value has significant effect on the free surface kinematic wave elevation and forces at the specific resonance frequencies, but the response across the other frequency range is not considerably affected (Chen, 2005b). To select an acceptable value for epsilon (ε) damping lid term it recommended to use a calibration of the numerical simulation results with that of the experimental result in a wave tank (Jean-Robert et al., 2006).

A different study proposed that no exact value can be set for the epsilon (ε) damping lid term. It was shown that calibrating the value for epsilon (ε) based on the gap wave elevation for first order motion had effect on the second order quantities more significantly than the first order response (Pauw et al., 2007).

CFD (computational fluid dynamics) method and potential flow theory method have both been used to analyse the gap resonance motion of multi-bodies in proximity under the influence of water waves with a three-body configuration in 2D with a range of damping lid values (comparable to epsilon (ε) term) used in the potential flow method only and obtained satisfactory result similar to Chen (2005a) in terms of the damping effects across the frequency range. The specific frequency where gap resonance occurs are affected by viscosity, but the other range of frequencies are not significantly affected. Furthermore, combining the potential flow theory with damping lid, produces results that are of satisfactory agreement with the CFD results for acceptable wide range of damping coefficient terms.

CFD analysis have been utilized to study 2D gap resonance by Lu et al. (2008), Moradi et al. (2015) taking into account the viscosity and nonlinear effect, and the results have been shown to have satisfactory agreement with experimental data, demonstrating that CFD can be used to adequately predict the extreme free-surface oscillation at the fluid resonance. Compared with 2D gap resonance analysis, 3D gap resonance computation is much more complicated, because multiple modes can be excited. Additionally, Kristiansen and Faltinsen (2012) proposed a new domain decomposition method using a combination of potential and viscous flow to improve the efficiency of computation

A research making use of two identical barges of different draft in incident wave was carried out and it was observed that the frequency associated with the largest wave elevation in the gap reduces as either barge draft increases (Ning et al., 2018).

To integrate the effect of viscous damping, this research conducted a parametric fit to the frequency response transfer function gotten from a linear potential flow analysis in combination to with a novel experiment using a new combination of model sizes with test cases including 10 wave frequencies, 2 vessel drafts, 2 wave directions and 3 gap widths. With the inclusion of an approximated viscous damping within the parametric fit based on stokes laminar boundary layer assumption, we obtain predictions for the gap resonance response RAOs for the test cases and new combination of vessel sizes and shows an acceptable agreement with the experimental data (Nwafor and Hu, 2021).

Model testing is a useful method for investigating the nonlinear effect of incident waves on the resonance response in the gap region for a multibody side-by-side configuration.

There has been various model test carried out to study gap resonance and hydrodynamic of the multibody system over the last decades with most investigations focused of these two key areas (Inoue and Islam, 1999). Experiments was conducted for moored tankers arranged parallel to each other, with the tankers subjected to incident regular waves. The motion response of the vessels, drift forces and wave structure interaction results investigated. From the model test, it was found that the global level of longitudinal wave drift forces larger for the multibody system than for the single body system for heading sea, for beam sea case the wave drift usually acts on the weathered side of the vessel. The vessel motion and mean wave drift forces for the side-by-side moored tankers in irregular waves can be calculated using linear superposition principle according to Hong et al. (2002). Quite a few model tests in wave basins have been carried out with the models subjected to waves propagating from different directions for side-by-side arrangement. It was observed from these experiments that mooring option for side-by-side offloading would not be appropriate for harsh sea conditions. A practicable solution of using weathervane barge moored to an LNGC on extreme sea environment with a full dynamic positioning system

without and physical mooring between the unit was suggested by Van der Valk and Watson (2005).

Model testing is important to obtain required damping parameter value and verification of estimations made which are not directly available in the numerical solutions (Pauw et al., 2007). First order wave loads motion RAOs and the gap region free surface elevation can be gotten from experimentally (Naciri et al., 2007)

Model testing in a towing tank or basin are important in investigating gap resonance. Numerous of model test have been carried out in towing tanks for 2D observation and fewer numbers in 3D because of the need to use a wave basin. A series of 2D model test was conducted by Saitoh et al. (2006) to investigate the wave elevation response in the gap of two identical fixed boxes with regular waves and different gap width and draft. A 2D model test analysis was carried out by Faltinsen et al. (2007) to investigate the piston modes resonance frequencies and amplitude for a moonpool with wave excitation using a small heave. Another 2D model test was conducted by Kristiansen and Faltinsen (2008) in shallow water to investigate the resonance water surface excitation between a fixed gravity based structure and a ship with round corners.

3D model test has also been conducted using different gap distanced, these gap distances can affect the behaviour of the resonance response differently in terms of the relative influence of viscous and radiation damping, the smaller the gap distance the greater the importance of viscous damping. 3D model test was carried out by Molin et al. (2009) to investigate gap resonance in-between two fixed rectangular barges with square and round bilges connected side-by-side with incident irregular waves propagating from different direction. At full scale the minimum gap width was 9m with an LNGC width of 46m. A free surface wave elevation analysis was carried out a 3D model test by Clauss et al. (2013) using transient wave groups in heading sea. The model test set up had a gap of 4m at full scale in-between a fixed terminal barge and an LNGC. Perić and Swan (2015) performed a study in a 3D wave basin with an experimental setup of one floating model and gravity-based structure (GBS) in the form of a fixed box at full depth, both in proximity and a gap distance of 6m at full scale. Zhao et al. (2017b) carried out a 3D experiment with two identical rectangular boxes with round and square bilges which were fixed and rigidly mounted on a gantry at the centre of the wave basin to investigate gap resonance response of the fluid between

the models with transient wave groups. The full-scale gap width was 4m which is close to the operational gap width for FLNG LNGC offloading. In both cases considerable damping together with radiation damping was observed and for the cases with round bilge, it was stated that the damping was majorly due to laminar boundary layer. Chua et al. (2018) carried out a 3D model test to study gap resonance responses for two identical boxes under the influence of different irregular sea states and bilge geometry, with the full-scale gap width at 8m. Nwafor and Hu (2021) conducted an 3D model test using a new combination of boxes of different sized both with round bilge to study the gap responses under the excitation of incident regular and irregular waves propagating in beam and oblique seas for 3 gap distances 4m, 5.5m and 6m at full scale and at different drafts.

2.3 Investigations on multi-body system

The hydrodynamic interaction between the floating multibody systems in proximity such as FLNG and LNGC in side-by-side configuration, when gap resonance occurs can result in increased risk of vessel collision, maximum tension and compression loads on the hawsers and fenders, and an exceeding of the set limits of motions for the offloading arms.

Investigations on the hydrodynamic wave structure interactions of floating vessels in side-by-side arrangement have been conducted in the past. Kodan (1984) conducted model test and showed the occurrence of a nonlinear hydrodynamic interaction in following sea, and the significance of maintaining a constant gap between two vessels. A study on the motion of moored vessel was carried out by Van Oortmerssen (1976) and showed that resonance sway motion of a floating vessel the quayside experience hydrodynamic interactions. As detailed by Kim et al. (2003), Huijsmans et al. (2001), Chen and Fang (2001) an analytical method for investigating the hydrodynamic interaction and motion in different heading waves, for a single floating body which is symmetrical in the vertical plane along the vessels centre line will experience no sway or roll motion due to the force in the athwart ship. However, for a floating multi body analysis, the sway and roll motions can be observed in heading sea conditions. The presence of large sway motion in multibody investigation can be ascribed to the increase in the mean wave force produced due to a frequency shift with a reduction in the gap width in-between the vessels as shown by Bunnik et al. (2009), Jean-Robert

et al. (2006).A further study conducted by Zhu et al. (2008) stated that added mass and damping have and important role to play. In addition to the hydrodynamics of the vessels studies have been done on the existence of a substantial increase in the free surface elevation due to trapped water in the gap at Helmholtz resonance. Also Yan et al. (2009) stated than a decrease in the gap width resulted in a production of large second-order hydrodynamic coefficients compared to the first-order because of the presence of nonlinear effects.

The simulation of an offshore lifting operation in the frequency domain was carried out by van Oortmerssen (1977) without consideration of the dynamic cross coupling motion involving the floating bodies, due to this, the motion of one vessel did not affect the second body gotten from radiation wave. Lee (1995) stated that radiation potential, has different components that correspond to modes of the rigid body motion, and this can be applied to multibody interactions. It was carried out by defining the velocity potential which corresponds to a specific mode of one vessel, whilst the second vessel is kept stationary. Using this method, the total radiation potential consists of *"6N"* components, where *N* is the number of bodies. The theory on the hydrodynamic interaction effects of adjacent floating bodies with incident oblique waves obtained from two dimension wave diffraction theory was described by Kodan (1984). The research studied the wave excitation forces, moments and dynamics for certain test cases made up of a ship and a rectangular barge with a satisfactory agreement between the numerical simulation and experimental results. Hong et al. (2002) used a perturbation scheme with higher order boundary method to analyse hydrodynamics of floating systems. Tajali and Shafieefar (2011) investigated hydrodynamic interaction between floating piers under the influence of different wave frequencies and directions in the frequency domain. For estimating the effect of hydrodynamics on an array of hinged floating structures, a numerical simulation method was used for that function. A research was carried out by Harichandan and Roy (2012) on characterises of flow past single body and multi-bodies. It was noted from various research that the flow with the gap region of two side-by-side vessels show complex vorticities that are affected by varying gap widths. The study has now been done using time domain method, to investigate the nonlinear effects gotten from mooring forces and viscous flow, where retardation functions are used to transform the results obtained from the frequency domain. The hydrodynamic response of side-by-side configured vessels

was analysed by Buchner et al. (2001) with the coupling between the motions of the two vessels taken into consideration. Furthermore, to reduce the extreme resonance wave elevation in the gap region, a surface lid was applied between the multibody diffraction which is an improvement from previous approach. A similar free surface lid method was used by Naciri et al. (2007) to study gap resonance wave oscillations in the time domain and or validating the numerical simulation with experimental results. Hydrodynamic responses and wave drift forces for multibody systems was analysis investigation was conducted by Kashiwagi et al. (2005), Hong et al. (2005) taking into consideration the viscous roll damping and the results was compared to the model test data. A 3 dimension sink-source technique was used by Inoue and Kamruzzaman (2005) in the time domain to analyse hydrodynamic radiation and diffraction forces, which also involved the study of the nonlinear moorings and connecting system forces. Koo and Kim (2005) Conducted numerical simulations on floating multibody, taking account the hydrodynamic interaction between the two vessels. Investigation carried out by Chitrapu et al. (2007) to evaluate the sea-keeping performance and manoeuvrability of vessels in proximity that are advancing forward in waves using simulations in the time domain, with nonlinear effect of the mooring lines and fenders considered and effects of viscous roll-damping was also included. Numerical analysis was carried out by Xu et al. (2013) to calculate the hydrodynamic performance of multi net cases subjected to currents and waves with illustrations made to the directions of the currents and waves. The motion of floating multibody in shallow water was conducted by Lee et al. (2010) and it was recommended that the effects of shallow waters should be considered in the studies of floating bodies in shallow water locations. Ship to ship LNG offloading in artic waters was researched by Berg and Bakke (2008) and recommendations made, that caution should be taken when using historic environmental; data obtained from studies of complex marine operations. A comparison between single and multi-body response was carried out by Yu et al. (2009) and a distance variation between the two responses was observed. The importance of slowly varying nonlinear motion for vessels operating in proximity was illustrated by Newman (2001). A study carried out by Islam and Murai (2013) found that ship at higher speed have increased hydrodynamic interaction between the vessels, therefore static vessels have less hydrodynamic interaction when compared to advancing vessels. Nevertheless, static floating vessels can be compared against

current speed. The hydrodynamic interaction increases with current speed, thus considering the current is also important.

2.4 Linear Potential flow model

Linear potential flow theory has shown to give reliable estimates for resonance frequencies of trapped fluids such as moonpools or gap for side-by-side configured vessels by allowing the free surface boundary condition to be linearized by dropping wave height terms which are beyond first order.. Newman and Sclavounos (1988) probably analysed the first linear 3D problem with linear potential flow theory to model two rectangular barges in a catamaran configuration separated by a small gap. A theoretical approximation method was proposed by Molin (2001) using linear potential flow theory, to compute in both 2D and 3D, the piston mode resonance frequencies along with the sloshing modes in a rectangular moonpool with the assumption of an infinite water depth and length and an infinite beam of the barges containing the moonpool. Molin et al. (2002) expanded on the theoretical method to derive the approximate natural modes of an open-ended gap or moonpool by applying Dirichlet conditions rather than Neumann condition at the gap ends. Molin (2017) estimated the natural frequencies and modal shapes of the piston in moonpools with one or two recesses. A modified theoretical model was derived by Molin et al. (2018) by releasing the assumption of infinite water depth and infinite horizontal extent of the support. An analytical oriented method was proposed by Faltinsen et al. (2007) which is based on linear potential flow theory for predicting 2D piston mode steady-state motions of a fluid in a moonpool formed by two rectangular hulls with excitation using vertical harmonics of a partly submerged structure in calm water with infinite depth. Their analytical oriented method produced a more satisfactory agreement with resonant frequencies from 2D experiment when compared to Molin's method Molin (2001), which is dependent on selecting a location for an artificial sink or source for a fixed support. the differences between the to methods increases when the draught is relatively small in comparison to the moonpool width. Linear potential flow model (Sun et al., 2010) to calculate resonance frequencies of free surface wave elevations in the gap region between two parallel arranged barges in 3D, with the results obtained similar to the predictions when using Molin's method (Molin et al., 2002).

While linear potential flow theory can predict gap resonance, but it tends to overestimate the wave elevation in the gap region, model tests are used to determine resonant amplitudes responses in the gap, Pauw et al. (2007), Buchner et al. (2001) conducted experiments with a wide gap width which made radiation damping relatively important, while the investigations carried out by Clauss et al. (2013), Molin et al. (2009) observed that the undamped linear potential flow model had a reasonable agreement with the model test results for round bilge cases, transient wave groups was used to determine resonance response amplitude operators RAOs. The free surface amplification becomes unrealistically large closer to the resonant frequency, when radiation damping is minimal. To supress the extreme surface elevation in the gap some researchers proposed a numerous solutions, a rigid lid method (Huijsmans et al., 2001), a flexible lid method by Newman (2004) or using a linear dissipation term Chen (2005b) to introduce artificial damping in a linear potential flow model.

2.5 Nonlinear potential flow model

Investigations of problems involving gap resonance have been studied using weakly nonlinear potential flow models. Teigen and Niedzwecki (2006) analysed the wave amplifications between two identical barges up to second order with results showing strong sum frequency, second order waves, with remarkable diffractions taking place, calculations was performed using WAMIT potential flow code.Sun et al. (2010) computed water wave diffraction between parallel close identical rectangular barges, with second order diffraction analysed based on quadratic boundary element method using second-order potential flow cod DIFFRACT. It was observed that quadratic excitation at half gap resonance frequency is significant to the wave amplitude of the response in the gap rather than the second order terms coming from linear excitation of gap resonance.

Viscous effects are believed to be the main source of the discrepancies noted above (between the experimental results and the unmodified linear potential flow results) the and also possibly the effects related to nonlinear free surface condition. Kristiansen and Faltinsen (2008) carried out numerical simulations using a fully nonlinear numerical wavetank based on sou's 2nd identity (Eularian phase) combined with inviscid vortex tracking method (Lagrangian phase) applied to a moonpool problem. The fully nonlinear potential flow (FNPF) model is based on a 2D standard mixed

Eulerian and Lagrangian approach (MEL). An analysis by Feng and Bai (2015) also used the fully nonlinear potential flow FNPF for a numerical study in 3D and observed that there was a for the first resonance frequency, there was a shift but the peak value had a minimal change even with an increase in the steepness of the incoming waves. Thus, viscous dissipation needs to be focused on more.

2.6 Connection system models

2.6.1 Hawsers

In the side-by-side configuration for offloading operation, hydrodynamic interaction between the vessels is a challenge due to how it can significantly affect vessel motion and needs to be taken into consideration. The FLNG and LNCG are in close proximity and are connected with hawsers and fenders. This connecting system arrangement reduces the distance and relative motion to some degree and also provides conveniences for offloading operation (Zhao et al., 2017a). Simultaneous changes in the loading levels of the tanks in the FLNG and LNGC during offloading operations and sloshing of internal liquids also contribute to complex coupling effects of the FLNG connection system (Graczyk and Moan, 2008, Zhao et al., 2012).

In order to mitigate against vessel collisions, offloading arm cracks and other potential offloading operational risk, connecting systems, such as hawsers and fenders have an important role to play in limiting relative vessel motion to within certain range. For a connection system to be reliable, the hawsers length, diameter, minimum breaking load (MBL) and stiffness properties should be adequate to reduce relative vessel motion and avoid breakage. The load distribution along each hawser line should be analysed to avoid any overloading of the hawsers. Thus, an optimum hawser and fender arrangement is required with regards to safety and economic efficiency standards of side-by-side offloading operations (Zhao et al., 2017a).

The features of connection systems are very complex, it is highly unlikely to accurately predict extreme conditions accurately using normal numerical calculations. The tension force levels in connection systems are usually assumed to be quasi-static in numerical simulations. Lee (2002), Zhao et al. (2012) noted that during the computational coupling process, hawser tensions are directly proportional to the

relative vessel displacements and is subsequently transmitted to the hull. Nevertheless, the calculation may be inaccurate because for parts that have not considered the damping and inertia terms of the hawsers, and the snap loads can be produced when changing from a slack position to a taut state. Ablow and Schechter (1983), Cai and Chen (1994) carried out several numerical methods while, Perkins (1992) used the analytical method to proffer dynamic solutions, but apparent impulsive properties of the hawser lines cannot be used in the solution. A series of model test was carried out by Vassalos et al. (2004) showing that snap loads can substantially increase the maximum tension amplitude and the excitation amplitude is nonlinear. An investigation on side-by-side offloading of LNG from a Floating storage and regasification unit (FSRU) onto an LNGC through a benchmark study was conducted by Naciri et al. (2007). Nevertheless, no agreement between the large loads on the hawser was found after comparison of results for three numerical programs. Zhao et al. (2013) also observes similar unsatisfactory agreements between the experimental and numerical data, stating complication associated with producing a full mechanism for transient snap loads. Additionally Koo and Kim (2005) incorporated the coupling effects of hawsers between two floating platforms although it was difficult to get the accurate impulsive force properties on the connecting system. Currently, to accurately predict the snap loading mechanism involving analytical and numerical methods is limited to simplified models. It is therefore recognized that experimental research is an effective method for evaluating the connection system loads for safety levels.

Model test approaches are some of the reliable methods available for studying hydrodynamic problems e.g., side-by-side offloading configuration. Hong et al. (2005) conducted experiments on multibodies with the use of two hawsers and two fenders installed in-between an FPSO and LNGC. Horizontal mooring lines was used to moor the FPSO model and subjected to regular waves. Buchner et al. (2001) also carried out a similar model test and numerical simulation. The main focus of these model test are the hydrodynamic interactions and relative motions patterns of the two vessels of their coupling effects with mooring lines and risers (Kim, 2003). few considerations have been made to the connecting system and in practice a very limited data exist for the loads on connection systems in real environmental conditions. A Classic design of connecting system configuration in a side-by-side arrangement comprises of spring and breast lines as presented by Van der Valk and Watson (2005) with features of

different model configurations also presented. Model test and numerical analysis was carried out by Lee et al. (2013) on the level of performance of the Hyundai LNG-FPSO. Hawsers in this configuration had 4×3 breast lines and 2×2 spring lines. The offloading estimations were given based on global performance data. Experimental and numerical investigation was conducted by Zhao et al. (2012) on an FLNG system in side-by-side configuration, with a simplified connection system used with no detailed presentation on the connecting system results discussed. In the researches stated above there isn't adequate investigations on the connecting system, thus more experimental and numerical studies illustrating the characteristics dynamic response of side-by-side FLNG connection system is required.

2.6.2 Fenders

In numerous marine operations such as berthing or loading operations, the demand on the performance of fenders have become more stringent. Traditional fenders have poor capability for energy absorptions and cannot guarantee tile safety, thus a new type of fender with a high performance is recommended. Hydropneumatics fenders has good shock absorbing qualities and obtains its restoring force from a combination of water and compressed air in a flexible sealed vessel. A comparison of the hydropneumatics fender with the traditional rubber fender shows that the former performed better in energy absorption and reduction of reaction force per unit area. (Bai et al., 2001, Dong-ying, 2009) carried out some studies on traditional rubber fenders, the hydropneumatics fender investigations have not been reported extensively. Therefore, the investigation into hydropneumatics fender has significant importance for side-by-side offloading operation.

The energy absorption and reaction force are the primary performance indicator of fenders. Compressed air and water are used to generate the reaction force while the capabilities of energy absorption is denoted by energy accumulated in the fender when maximum deformation take place. The energy absorbed by the fender should be higher than the berthing energy of the ship, and the rection force should not be more than the maximal allowable force of a port (Hong et al., 2000).

2.7 Artificial neural networks (ANN) application in engineering

There have been several applications of ANN in the last five decades for engineering prediction. These application include wave height and period forecasting by Deo et al. (2001), wave reflection prediction from coastal structures in design condition by Zanuttigh and van der Meer (2008), and prediction of water level by Patrick et al. (2003). Some earlier studies related to Artificial Neural Networks application in engineering and science will be summarized under water resources, geotechnical engineering, structural engineering, and coastal engineering.

Makarynskyy et al. (2004) studied using ANN method to the problem of improving wave predictions using two approaches. Firstly, an initial simulation of the wave parameters with leading times from 1 to 24 hours. Secondly, the merger of the measurements and initial predictions. The results showed that ANN models can give an accurate simulation and demonstrated the ability of ANN to improve the initial outlooks, It is estimated in terms of the correlation coefficients, root mean square error and scatter index.

Deo et al. (2001) analysed the presentation of practical methods doe designing better ANN architectures for wave predictions. The paper demonstrated an improvement between the actual observations and prediction results which shown by an increase of the correlation coefficient (R^2) OF 68%. The conclusions made was that smaller differences in wind characteristics at a certain location coupled with the single location wind and wave measurement brought about an improvement in predictions.

Lee et al. (2001) developed an ANN model to predict stub-girder system behaviour in structural analysis. In their paper they stated that it was a challenging task to model stub girder involving complex material behaviour by conventional numerical modelling computationally. It was concluded that many uncertainties and empirical problem within an approximated structural analysis can be successfully solved by the ANN model that involve both fast calculation with acceptable margin of error in structural engineering.

Kim et al. (2001) presented the usage of accumulated database for evaluating particular tunnel sites and prediction od ground surface settlement because of tunnelling using ANN modelling. The ANN model was based on past tunnel records

that was used as a reliable database which led to prediction of the settlement of ground surface. It was suggested that the ability to predict an accurate result is entirely dependent on the quality and quantity of data used in training ANNs.

French et al. (1992) in water engineering made use of an ANN model to predict rainfall intensity. The back-propagation neural network was used for training, and comparison made with natural rainfall history with an ANN predicted field model. Their results showed that ANN has the capability of learning the complex relationships describing the space-time evolution of rainfall that is characteristic of a complex rainfall simulation model.

Maier and Dandy (2000) applied ANN for predicting water quality parameters. The authors made reviews between the ANN and other traditional prediction methods. Such as timeseries, physical based models, and applied ANN model to predict salinity in the River Murray at Murray bridge, southern Australia. It was concluded that ANN models are a useful tool for predicting salinity in rivers, even though it was challenging to determine the appropriate model inputs. Further investigations on the relative performances of various training algorithms were carried out using feed-forward ANNs for salinity predictions.

There are other machine learning algorithm for predicting outcomes from a group of dataset such an Support Vector Machine (SVM) but ANN has numerous advantages over SVM. ANN produces different number of outputs while SVM can produce only one output, Hence ANN can train models in one go while SVM is restricted to trained one at a time. ANN is one whole system while SVM is an isolated system, finally ANN is a parametric model while SVM is a non-parametric model. These are some of the reasons why ANN method was chosen for the prediction of gap resonance in this research.

In recent years, there has been developments of computer-technology, deep learning of artificial neural networks (ANN) has become an essential topic research in artificial intelligence (AI) Fu (1999). There are data sets that have complex attribute relationship which are difficult to quantify using the traditional method of analysis (Shanmuganathan, 2016). Modelling using ANN is nonlinear and a multilayer mathematical technique, which describes the relationship that exist between user defined inputs and outputs (Deboeck and Kohonen, 2013). Research on ANN for

predictive analysis of gap resonance for FLNG side-by-side offloading has not been conducted to the knowledge of the author. It brings about an innovative and alternative way of using AI technology to improve the accuracy of predicting wave excitation responses in the gap region for different offloading configurations from the validated model test and numerical simulation data Figure 6-1 and Figure 6-2.

2.8 Conclusion on Literature Review

Although experiments in the field for a prototype scale to study gap resonance are ideal such large-scale experiments are quite challenging to obtain data to date, in this area of research in general. Model test has thus provided the readily accessible data source for design and development. This enables us to better understand gap resonance phenomenon at lab scale and to highlight the implications for full scale. The fluid motion in narrow gap problems is overpredicted at resonance frequency. The potential theory analysis for this thesis focuses on the wave response taking place at first resonance frequency, also known as piston response mode. The gap resonance numerical analysis is done with the potential flow solver Boundary Element Method (BEM) which is currently the industry standard for wave-body analysis. Our experiment is focused on a rigidly connected rectangular models, using a new combination of model sizes separated with three different gap widths. The model test cases also include 10 wave frequencies, two vessel drafts, two wave directions and irregular waves. We validate our experiments with our potential flow solver to calibrate the damping lid term (ε) which is used to correct the linearly overestimated fluid motion response at resonance frequencies in the long narrow gap. We investigate a method using artificial neural network to predict the occurrence of gap resonance based on the results obtained from the experiment test cases.

Furthermore, the literature review on previous studies and current developments on side-by-side offloading operations, shows specific additional areas of concerns besides the phenomenon of gap resonance such as complex hydrodynamic interaction, and effect of nonlinear dynamic coupling on vessel motion and loads on the connection system (hawser and fender) and offloading arms which we carried out investigations using numerical simulations. Low frequency motion estimation is important for moored vessel. However, wave frequency motion should also be focused on, such as roll motion due to the heave topside of the FLNG. A significantly high roll

acceleration may lead to heavier sea fasteners needed and the dynamic stability will also be a cause of concern. Additional literature on applicable methodology recommends the hydrodynamic analysis in the frequency domain be carried out to obtain response amplitude operators (RAOs) of the vessels, subsequently an integrated time domain hydrodynamic analysis to investigate the loads on the hawsers, fenders, offloading arms and mooring lines. Analysing loads on the connection system and relative vessel motion for a combination of environmental factors of wind, wave, current and different tank filling level is vital for the dangerous cryogenic offloading operation.

Chapter 3. MODEL TEST SPECIFICATION

The main purpose of the model tests is to investigate the nonlinear behaviour of gap resonance for a side-by-side offloading configuration. The focus of the model test will be to analyse the influence of wave excitation related to four parameters: wave frequencies, wave directions, gap distances and vessel drafts at the different locations in the gap, for new combination of ship sizes.

3.1 Scaling Ratios

Froude similitude scaling law will be used. The model is scaled following Froude's Law. In (Zhao et al., 2018c, Zhao et al., 2017b) the viscous damping was found to have a linear form for the range of waves tested (which, scaled according to Froude scaling, would be at the upper limit of practical interest for operations). It was reported that this behaviour is consistent with damping by Stokes oscillatory laminar boundary layers. (Wei et al., 2015) In normal wave condition, Froude scaling can be adopted for scaling up the model test results with any width, the scaling factor can be up to 100.

The Froude number has a dimension corresponding to the ratio.

$$Fr = \frac{u}{\sqrt{gD}} \tag{3-1}$$

Where u is fluid velocity, g is gravitational acceleration and D is the characteristic dimension of the structure. Let a full scale of λ and geometric similarities, the Froude full scale will satisfy.

$$\frac{u_M^2}{gD_M} = \frac{u_F^2}{gD_F} \tag{3-2}$$

Where the subscript M and F stand for model and full scale respectively.

The quantity 0.975 is the ratio between the fresh water and sea water density

Table 3-1. Scaling ratio

Description	Definition
Length	$l_M = \lambda l_F$
Velocity	$u_M = \sqrt{\lambda} u_F$
Mass	$m_M = \lambda^3 m_F$
Force	$F_M = \frac{\lambda^3}{0.975} F_F$
Fluid acceleration	$\dot{u}_M = \dot{U}_F$
Time	$t_M = \sqrt{\lambda} t_F$
Stress/Pressure	$S_M = \lambda S_F$
Frequency	$f_M = \frac{f_F}{\sqrt{\lambda}}$

3.2 Experimental set-up

The experiments were carried out in the Hydrodynamic Laboratory, Newcastle University. The investigation made use of a towing tank with a plan area of 37m × 3.7m and depth of 1.25m. Figure 3-1 shows the towing tank, wave gauges and data collector. The towing tank is equipped with 8 wave paddles shown in Figure 3-1(a) and wave absorbers at the end shown in Figure 3-1(b) for reduce reflection. The wave maker can be generate regular waves and irregular wave periods ranging from 0.5 to 2 seconds.

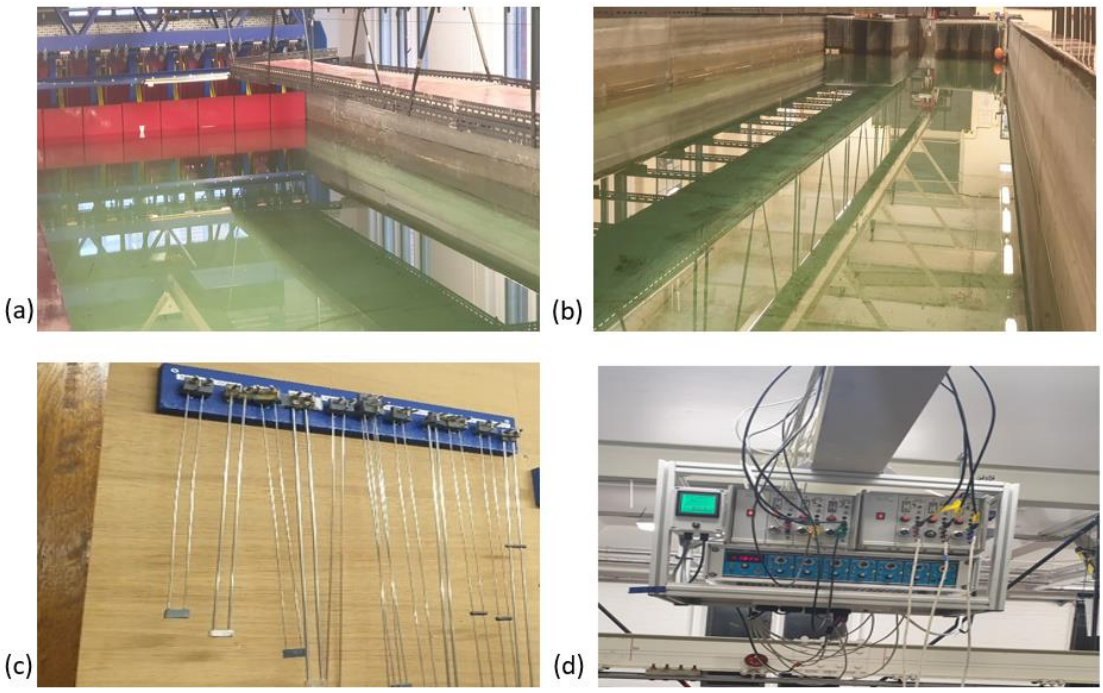

Figure 3-1 Facilities of model experiments: (a) towing tank wave makers; (b) towing tank beach; (c) wave gauges; (d) data collector.

Figure 3-2. Shows the plan view for the positions of the experimental models in the towing tank for beam sea cases and oblique sea case. Two rectangular boxes of different geometries representing a side-by-side multibody system with the FLNG as the larger model and the LNGC as the smaller model. The larger model has a dimensions of 1.5 m length, 0.4m width and 0.25m height, with a bilge radius of curvature of 0.03m while the smaller model is dimensions are 1.2m length, 0.3m width and 0.174m height with a bilge radius of curvature of 0.02m as shown in Table 3-2. The gap sizes between the models are set as 0.033m, 0.053m and 0.067m, respectively. At full scale it represents vessels of 150m length, 40m width and 25m high while the other vessel is 120m long, 30m wide and 17.4m high. The gap widths are 3.3m, 5.3m and 6.7m.

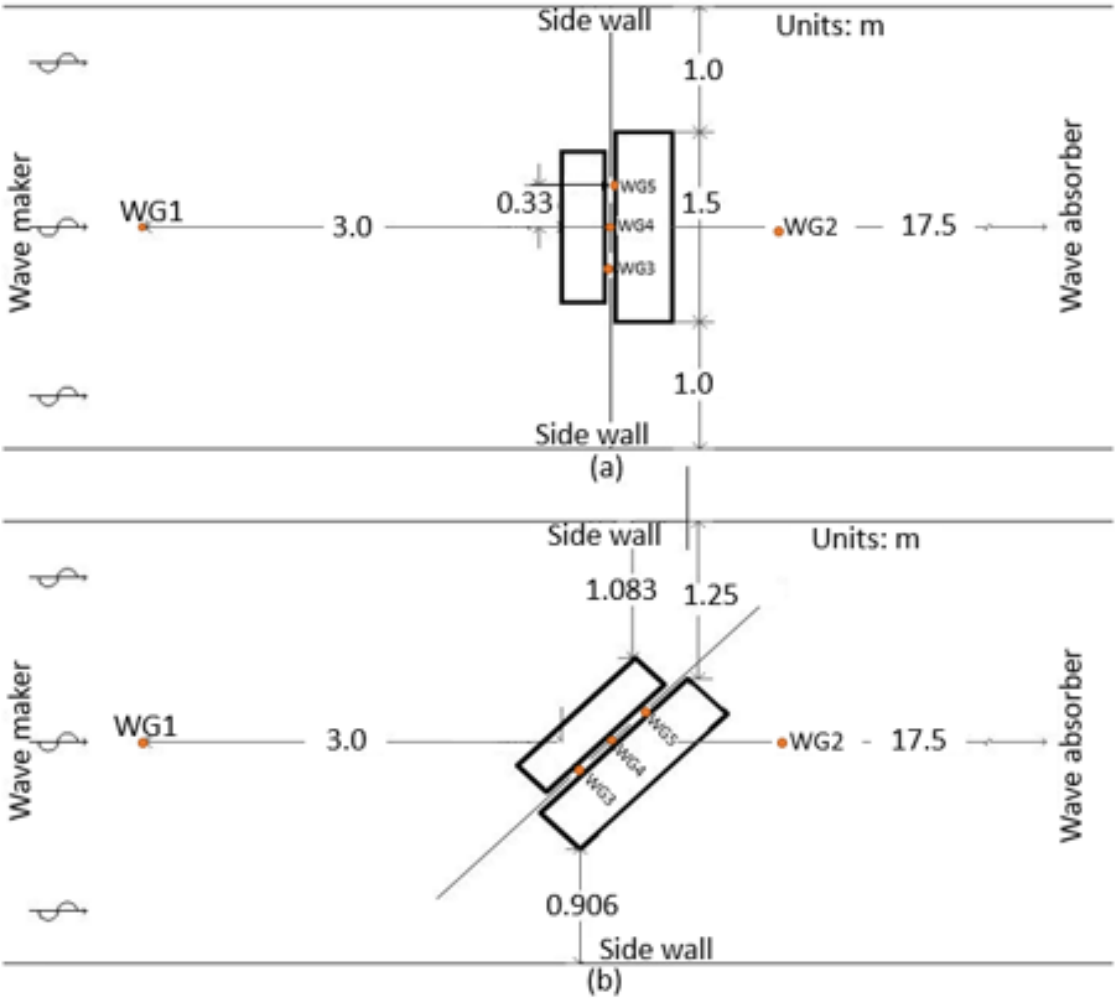

Figure 3-2 (a) Plan view beam sea (b) Plan view oblique sea

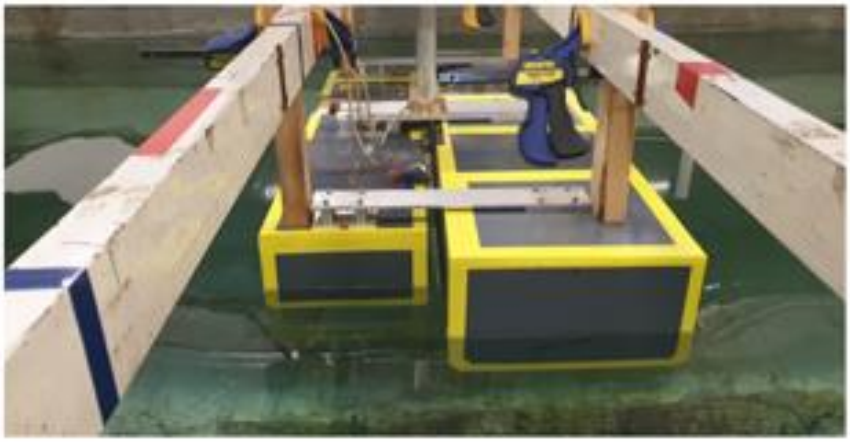

(a)

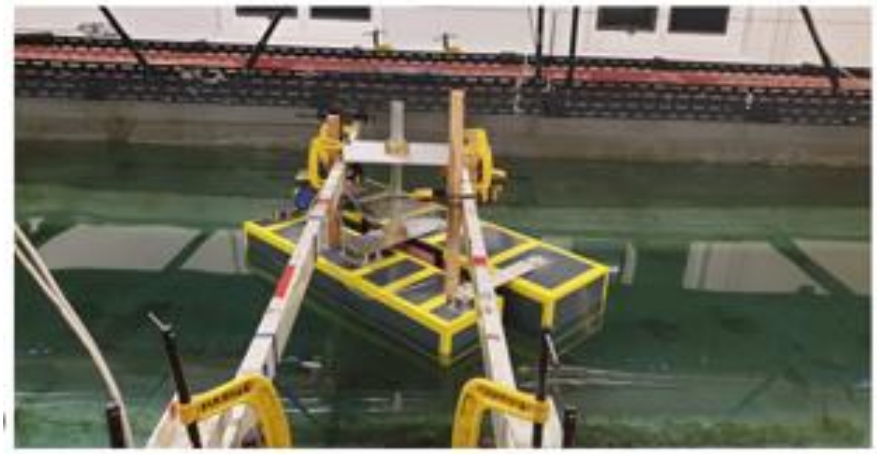

(b)

Figure 3-3 (a) Beam Sea, (b) Oblique sea.

Table 3-2. Dimensions of the models

Parameter	Model scale		Full scale	
	Box 1 (m)	Box 2(m)	Box 1 (m)	Box 2(m)
Length	1.5	1.2	150	120
Breadth	0.4	0.3	40	30
height	0.25	0.174	25	17.4
Blige radius	0.03	0.02	3	2
Draft 1	0.12	0.074	12	7.4
Draft 2	0.12	0.064	12	6.4

The two models are fixed to steel beam across the wave tank and clamped down with vices to provide extra stiffness to keep them firmly in place restricting movement and preventing vibrations of the box models at wave frequencies. The photo of the model during experimental set up is shown in Figure 3-3. The two models have an initial draft of 0.12m and 0.074m. The oblique sea configuration was setup by turning the models 45 degrees as shown in Figure 3-3(C).

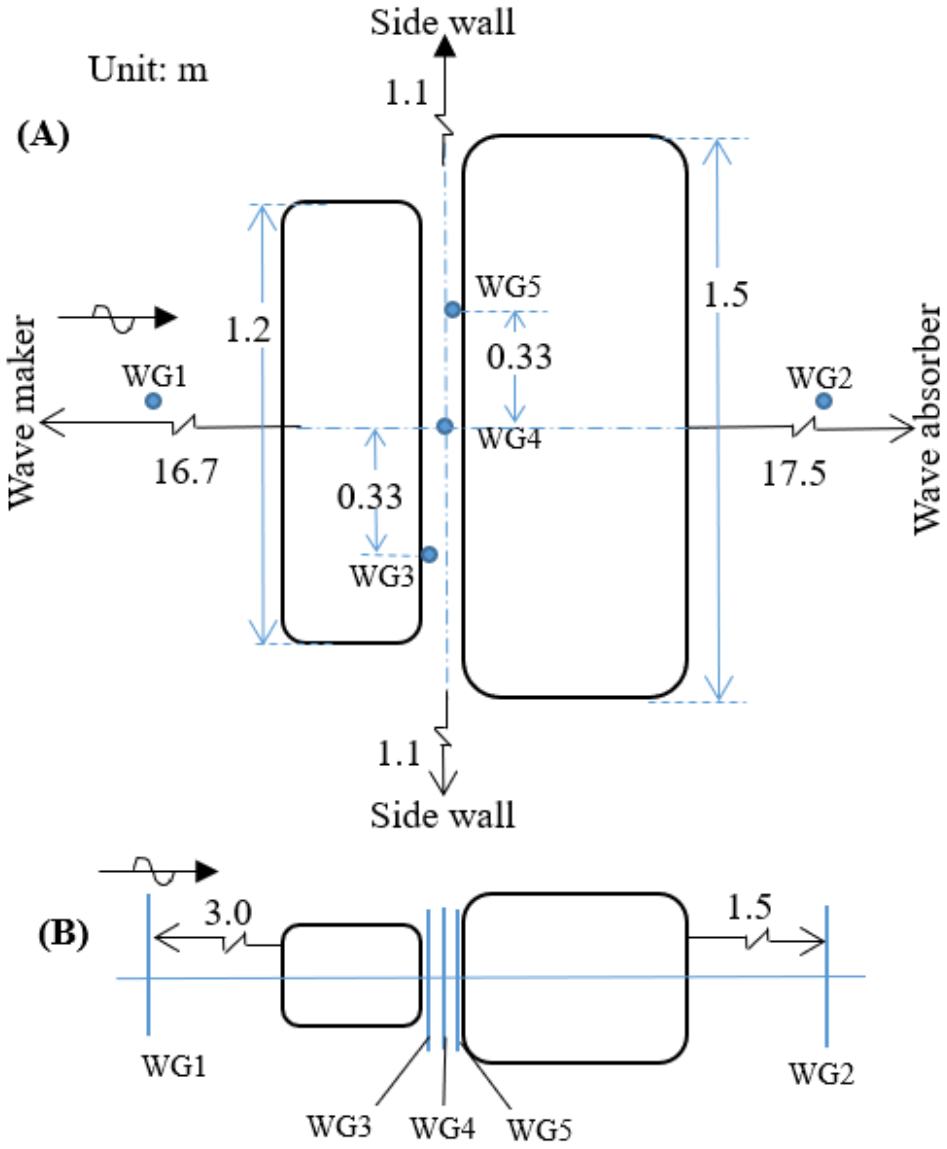

Figure 3-4 Schematic drawing of the models in the wave tank showing the location of the wave gauges (a) plan view (b) front view.

The measuring instrumentation used for data collection consist of standard resistance wave gauges to record the time-history of the water surface elevation. We make use of five wave gauges in total for the experiment as shown in Figure 3-4, wave gauge 1 (WG1) is 3m in front of the model set-up and is used as the reference gauge to measure the incident surface wave elevation, wave gauge 2 (WG2) is 1.5m behind the models and measured the diffracted wave elevation, wave gauge 3 (WG3) is 0.33m from the centre of the gap and closer to the smaller box model (leeward side), wave gauge 5 (WG5) is 0.33m from the gap centre and closer to the larger box model

(weather side) and gauge 4 is central as shown in Figure 3-4. Each wave gauge is made up of parallel free-standing stainless-steel rods with a diameter of 1.5mm and 12mm apart in Figure 3-1(c). These wave gauges have a measurement error of ±0.5 mm and create very negligible disturbance of the wave field. The wave gauges are calibrated by changing the immersion depth.

The models were subjected of incident wave types, of regular waves and irregular waves. The regular waves consist of 120 cases with 10 incident wave frequencies ranging from 0.3 – 1.6 rad/s full scale and the incident wave amplitude of 4mm for all frequencies. The irregular waves consist of Pierson-Moskowitz spectra having a peak period of 0.707s and significant wave height of 0.004m For the wide range if incident wave cases, observations were made for beam-sea and oblique sea configuration according to Table 3-4.

Table 3-3 the frequency range for the analysis

S/n	Frequency (rad/s)
1	0.337
2	0.478
3	0.615
4	0.759
5	0.901
6	1.045
7	1.18
8	1.331
9	1.475
10	1.618

Table 3-4. Beam and Oblique sea observations

	FLNG Box		LNGC Box	
	Beam	Oblique	Beam	Oblique
Regular	✓	✓	✓	✓
Random	✓	✓	✓	✓

Test Case overview

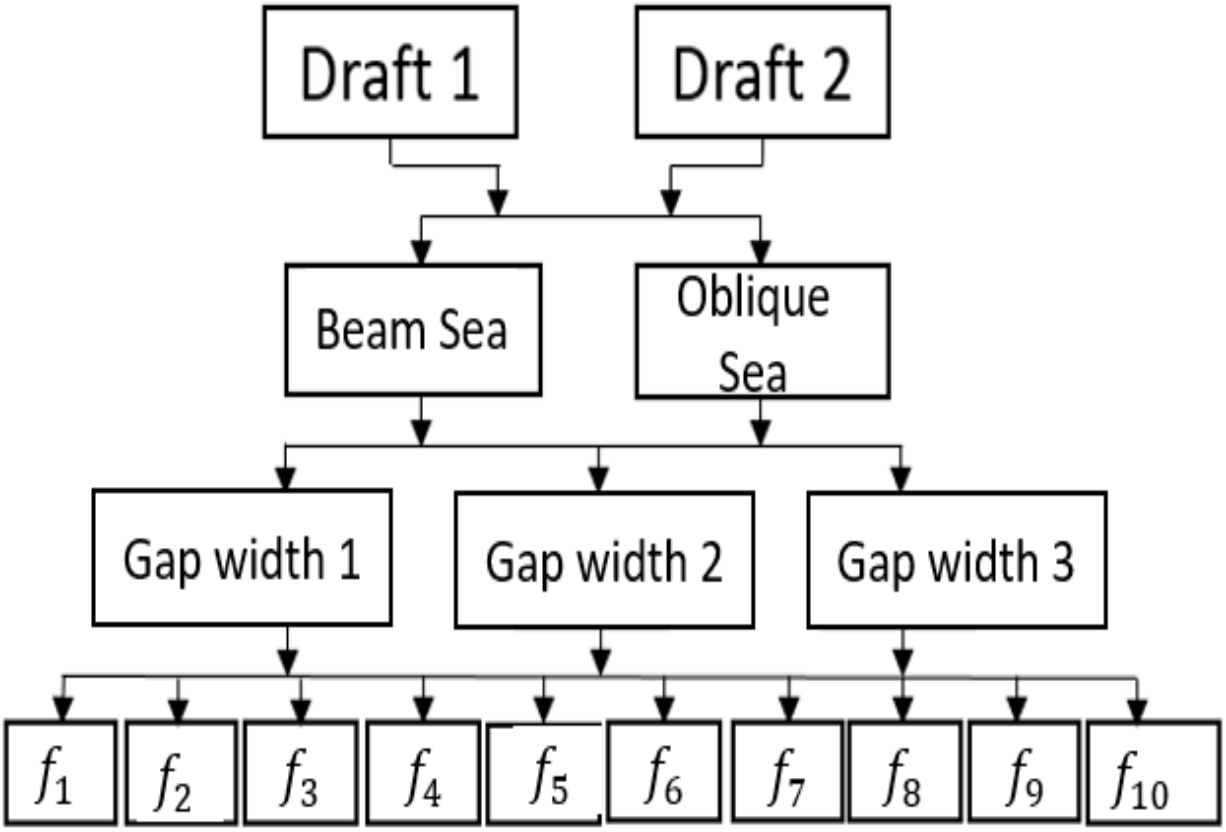

Figure 3-5. Chart of experiment cases

Total number of test cases (regular waves) = 2 ×2×3×10= 120

Wave Gauge (WG) = 1, 2, 3, 4, 5

Wave Direction (WD) = 90 deg , 135 deg

Gap width = 0.33m, 0.55m, 0.67m

Wave Frequency (f_n) = 0.05, 0.1, 0.15 ….n rad/s

Table 3-5. Test cases regular waves draught 1 & 2.

Cases	Wave Height (mm)	Wave Frequency (rad/s)	Wave Direction (deg)	Gap Distances (mm)	Draft
1	40	0.33652	90	33	Draft 1
2	40	0.47745	90	33	Draft 1
3	40	0.61551	90	33	Draft 1
4	40	0.75836	90	33	Draft 1
5	40	0.90121	90	33	Draft 1
6	40	1.045	90	33	Draft 1
7	40	1.1879	90	33	Draft 1
8	40	1.3307	90	33	Draft 1
9	40	1.4745	90	33	Draft 1
10	40	1.6174	90	33	Draft 1
11	40	0.33652	90	53	Draft 1
12	40	0.47745	90	53	Draft 1
13	40	0.61551	90	53	Draft 1
14	40	0.75836	90	53	Draft 1
15	40	0.90121	90	53	Draft 1
16	40	1.045	90	53	Draft 1
17	40	1.1879	90	53	Draft 1
18	40	1.3307	90	53	Draft 1
19	40	1.4745	90	53	Draft 1
20	40	1.6174	90	53	Draft 1
21	40	0.33652	90	67	Draft 1
22	40	0.47745	90	67	Draft 1
23	40	0.61551	90	67	Draft 1
24	40	0.75836	90	67	Draft 1
25	40	0.90121	90	67	Draft 1
26	40	1.045	90	67	Draft 1

27	40	1.1879	90	67	Draft 1
28	40	1.3307	90	67	Draft 1
29	40	1.4745	90	67	Draft 1
30	40	1.6174	90	67	Draft 1
31	40	0.33652	145	33	Draft 1
32	40	0.47745	145	33	Draft 1
33	40	0.61551	145	33	Draft 1
34	40	0.75836	145	33	Draft 1
35	40	0.90121	145	33	Draft 1
36	40	1.045	145	33	Draft 1
37	40	1.1879	145	33	Draft 1
38	40	1.3307	145	33	Draft 1
39	40	1.4745	145	33	Draft 1
40	40	1.6174	145	33	Draft 1
41	40	0.33652	145	53	Draft 1
42	40	0.47745	145	53	Draft 1
43	40	0.61551	145	53	Draft 1
44	40	0.75836	145	53	Draft 1
45	40	0.90121	145	53	Draft 1
46	40	1.045	145	53	Draft 1
47	40	1.1879	145	53	Draft 1
48	40	1.3307	145	53	Draft 1
49	40	1.4745	145	53	Draft 1
50	40	1.6174	145	53	Draft 1
51	40	0.33652	145	67	Draft 1
52	40	0.47745	145	67	Draft 1
53	40	0.61551	145	67	Draft 1
54	40	0.75836	145	67	Draft 1
55	40	0.90121	145	67	Draft 1
56	40	1.045	145	67	Draft 1
57	40	1.1879	145	67	Draft 1

58	40	1.3307	145	67	Draft 1
59	40	1.4745	145	67	Draft 1
60	40	1.6174	145	67	Draft 1
61	40	0.33652	90	33	Draft 2
62	40	0.47745	90	33	Draft 2
63	40	0.61551	90	33	Draft 2
64	40	0.75836	90	33	Draft 2
65	40	0.90121	90	33	Draft 2
66	40	1.045	90	33	Draft 2
67	40	1.1879	90	33	Draft 2
68	40	1.3307	90	33	Draft 2
69	40	1.4745	90	33	Draft 2
70	40	1.6174	90	33	Draft 2
71	40	0.33652	90	53	Draft 2
72	40	0.47745	90	53	Draft 2
73	40	0.61551	90	53	Draft 2
74	40	0.75836	90	53	Draft 2
75	40	0.90121	90	53	Draft 2
76	40	1.045	90	53	Draft 2
77	40	1.1879	90	53	Draft 2
78	40	1.3307	90	53	Draft 2
79	40	1.4745	90	53	Draft 2
80	40	1.6174	90	53	Draft 2
81	40	0.33652	90	67	Draft 2
82	40	0.47745	90	67	Draft 2
83	40	0.61551	90	67	Draft 2
84	40	0.75836	90	67	Draft 2
85	40	0.90121	90	67	Draft 2
86	40	1.045	90	67	Draft 2
87	40	1.1879	90	67	Draft 2
88	40	1.3307	90	67	Draft 2

89	40	1.4745	90	67	Draft 2
90	40	1.6174	90	67	Draft 2
91	40	0.33652	145	33	Draft 2
92	40	0.47745	145	33	Draft 2
93	40	0.61551	145	33	Draft 2
94	40	0.75836	145	33	Draft 2
95	40	0.90121	145	33	Draft 2
96	40	1.045	145	33	Draft 2
97	40	1.1879	145	33	Draft 2
98	40	1.3307	145	33	Draft 2
99	40	1.4745	145	33	Draft 2
100	40	1.6174	145	33	Draft 2
101	40	0.33652	145	53	Draft 2
102	40	0.47745	145	53	Draft 2
103	40	0.61551	145	53	Draft 2
104	40	0.75836	145	53	Draft 2
105	40	0.90121	145	53	Draft 2
106	40	1.045	145	53	Draft 2
107	40	1.1879	145	53	Draft 2
108	40	1.3307	145	53	Draft 2
109	40	1.4745	145	53	Draft 2
110	40	1.6174	145	53	Draft 2
111	40	0.33652	145	67	Draft 2
112	40	0.47745	145	67	Draft 2
113	40	0.61551	145	67	Draft 2
114	40	0.75836	145	67	Draft 2
115	40	0.90121	145	67	Draft 2
116	40	1.045	145	67	Draft 2
117	40	1.1879	145	67	Draft 2
118	40	1.3307	145	67	Draft 2
119	40	1.4745	145	67	Draft 2
120	40	1.6174	145	67	Draft 2

Video shots were taken to visualise the wave elevation in the gap region and compared to the wave gauge measurements to provide additional substantiation of the excellent quality of the measured data. In the smaller model a video camera was fixed inside the box to provide an internal view of the wave elevation at the water surface in the centre of the gap through a transparent window. A red and white chessboard grid with 1cm squares attached to the side of the larger box is provided to reference for visualization as shown in Figure 3-6.

The geometry is simplified and are focused for data collection for validation of numerical models and to allow for the development of a fundamental understanding of gap resonance phenomenon. The study will analyse the gap resonance response with the models subjected to regular waves and irregular waves with three different gap widths and two draughts.

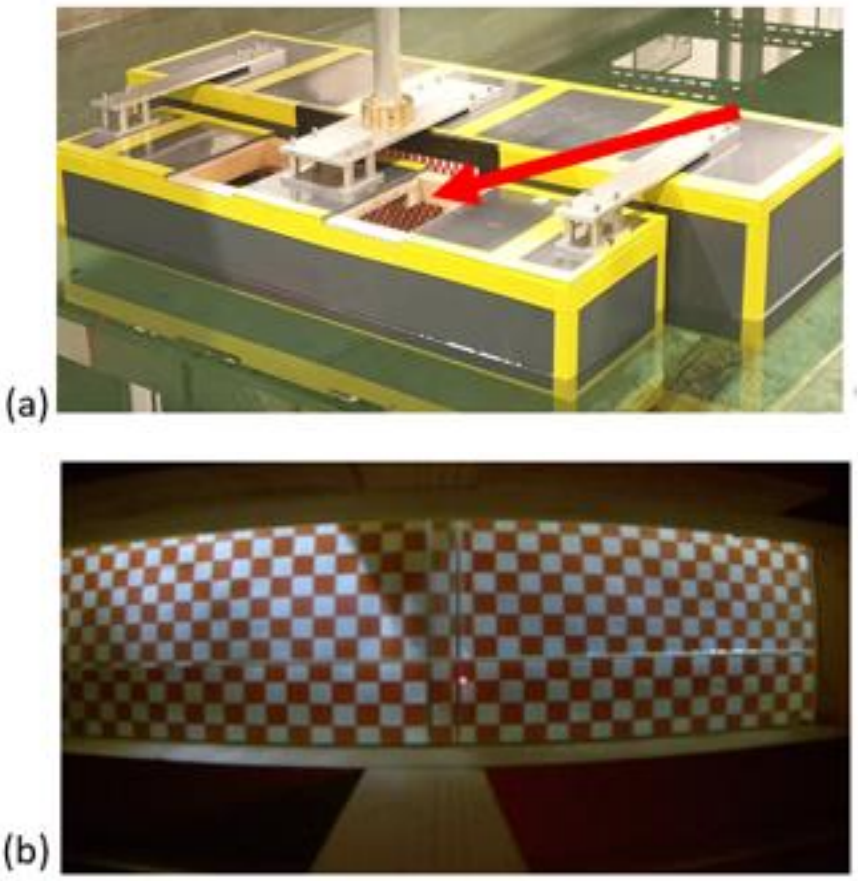

Figure 3-6 (a) Internal access for video camera, (b) Internal view of gap centre with chessboard grid, (c) incident regular waves.

3.3 Model Test results and discussions

This section focuses on the gap resonance result at lab scale, for which experimental comparisons can be used for validation of the potential flow solver hydrodynamic model. The configuration consists of a narrow gap with three gap distances Figure 3-5, formed by two fixed boxes with a new combination of model sizes arranged side-by-side, and is representative of a side-by-side offloading system consisting of an FLNG and LNG carrier under beam and oblique sea condition (the boxes of different sizes are used for simplicity). The models have two different drafts and are subjected to irregular waves and regular waves with 10 wave frequencies Table 3-3.

The amplitude of the gap oscillation based on the above-mentioned parameters are discussed in this section

3.3.1 Amplitude of gap resonance

Regular wave test with incident wave amplitude 4mm was carried out for beam and oblique sea, to analyse the maximum gap resonance response at steady state. The time history of free surface elevation for beam sea cases with varied gap widths are shown in Figure 3-7. The regular wave results shown below, is a comparison of the surface elevation time history between the incident wave in blue and the corresponding free surface gap response in red, for the beam sea case with the maximum amplification highlighted.A harmonic analysis using Fast Fourier Transform (FFT) is carried out on the steady state part of the time history in Figure 3-7 to obtain the surface elevation RAOs in Figure 6-1.

The accuracy of the numerical model is dependent on the value of the damping coefficient, modelled to introduce a viscous damping effect, as in the Newtonian cooling method on the free surface boundary condition (Kim et al., 2003), which can be inserted into the (linear) kinematic free surface condition, with the dynamic condition remaining the same in Equation(5-2).

It was observed that the amplification factor reduces with an increase in the gap distance for our test cases as shown in Table 3-6. This may be due to the larger size of the of the free surface in the gap region when the vessels are further apart. This increase in gap width comes with limitations in practice, because of the maximum allowable length of the offloading arms during operation.

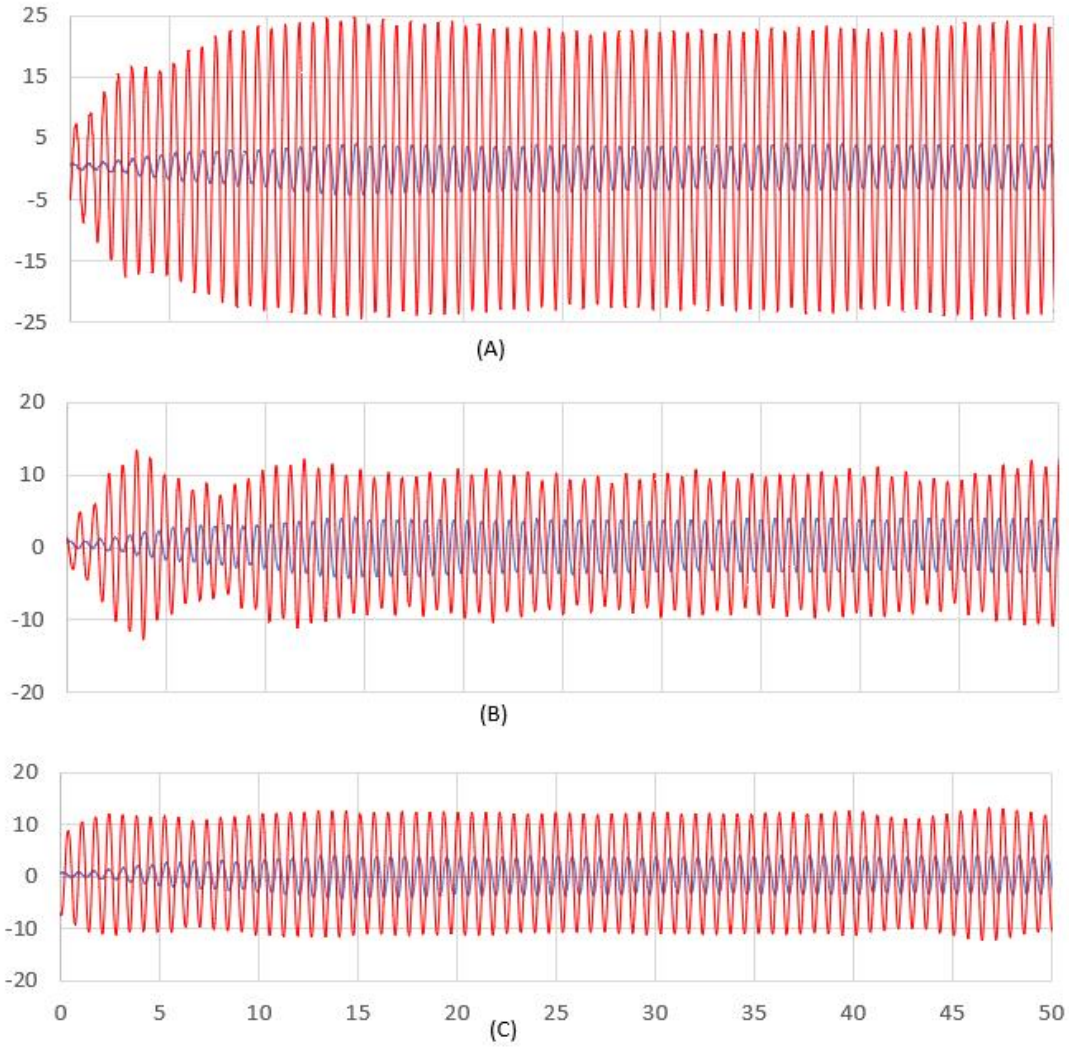

Figure 3-7: Regular wave model test: time history of incident wave in $BLUE$ and wave elevation in the gap region in red for (a) 33mm, (b) 53mm, (c) 67mm gap width respectively for wave gauge 4 at midship at 1.18rad/s.

3.3.2 *Effects of wave direction on surface elevation in the gap region (Model test)*

In this section, we consider test cases when the vessels are subjected to incident waves propagating from different wave directions. The beam-sea case and oblique sea case model setup are shown in Table 3-4. In the wave direction analysis, the undisturbed wave frequencies and amplitude were kept the same for both cases. Figure 3-8 shows the free surface elevation of incident wave and the wave elevation in the gap region for the two wave directions. The frequencies and corresponding amplification factors where gap resonance occur are shown in Table 3-6.

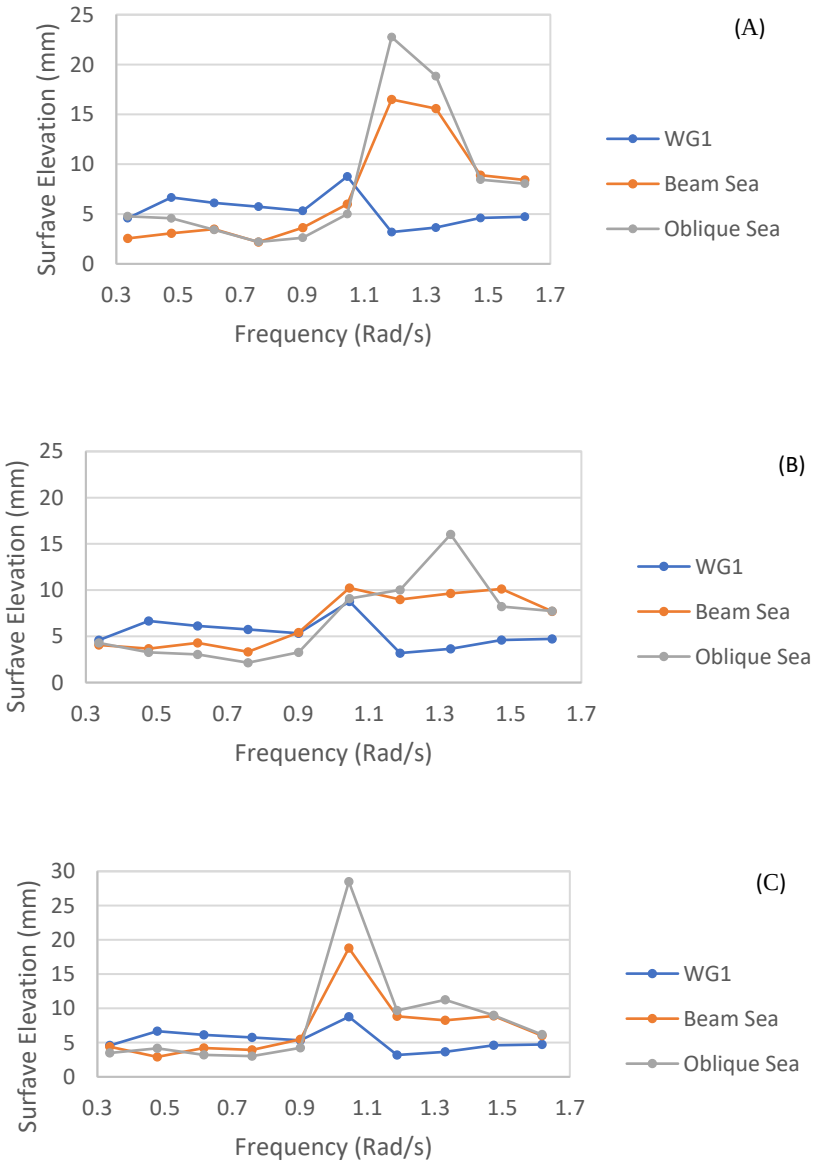

Figure 3-8: Variation of the first harmonic gap surface elevation with incident wave frequency for beam and oblique sea at gap distance (a) 33mm (b) 53mm (c) 67mm.

Table 3-6: Regular wave amplification factor

Resonant Frequency (rad/s)	Beam Sea			Oblique Sea		
	33mm	53mm	67mm	33mm	53mm	67mm
1.045	-	-	2.4	-	-	3.6
1.18	5.7	2.9	3.1	6.7	3.1	3.0
1.331	4.3	2.7	2.3	5.1	4.4	3.1
1.475	1.8	2.2	2.0	1.8	1.8	2.0

For the effect of wave direction on gap resonance, it can be observed that the oblique sea test case produced larger amplification factors. This could be due to the slamming effect of the propagating incident wave as it approaches the entrance of the long narrow gap and impacts the big vessel which is boxed shaped and has a longer length and larger draft. It was also observed that the gap resonance occurred at the same frequencies for both the beam sea and oblique sea test cases. These results suggest that the wave elevation in the gap region can be affected by the direction of wave propagation, for vessels with different sizes, drafts, and length.

3.3.3 Irregular waves (Model test)

Figure 3-10 shows the time history of the incident wave in blue and the free surface response at the centre of the gap in red, for gap widths 33mm, 53mm and 67mm. The wave kinematics including diffraction effects are calculated using Equation(5-5) by relating wave particle velocities in x, y and z-directions.

Figure 3-12 shows the spectra describing the magnitude (or amplitude) of frequency components of the incident wave and at the centre of the gap.

The objective of Figure 3-12I s to identify the occurrence of significant wave amplification of the incident spectrum when compared with a variation of gap distances for irregular waves. There is an observable amplification at frequencies 1.047 rad/s and 1.331 rad/s for the three gap distances. It is also observed that the gap distance of 67mm experiences the largest resonance amplification as shown in Table 5. The

two resonant frequencies for the irregular wave analysis are also similar with two of the resonance frequencies in the regular wave analysis.

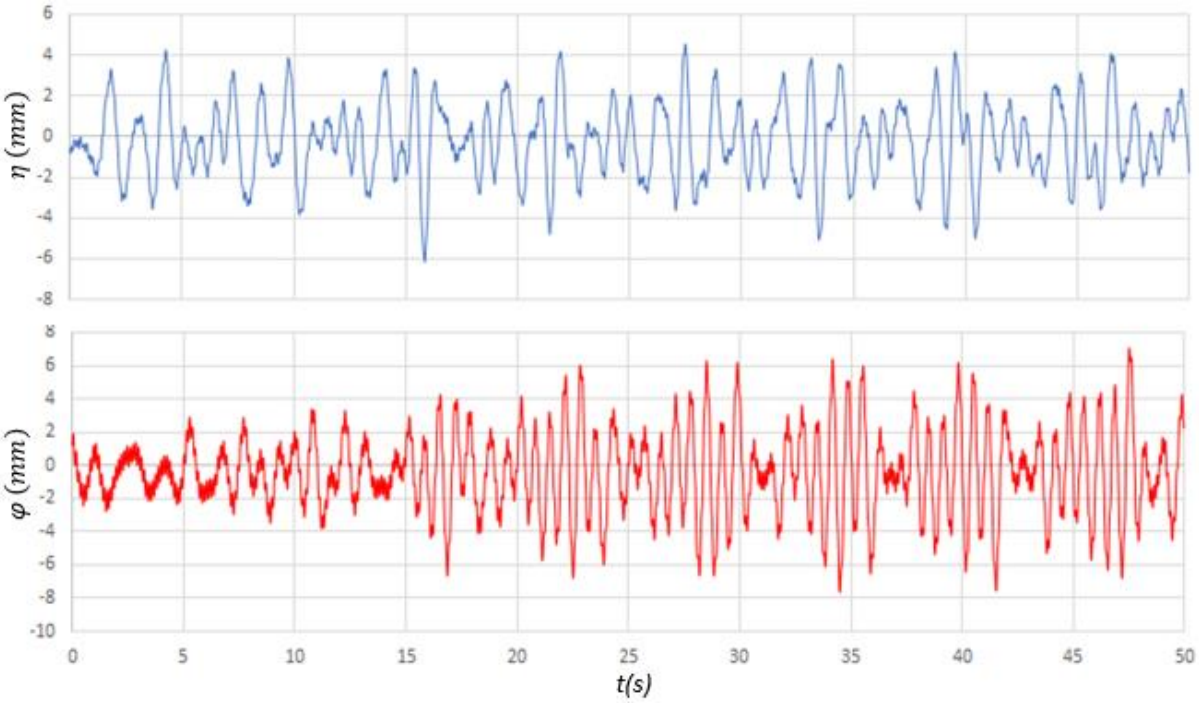

Figure 3-9 Time history of the surface elevation measured at the centre of the gap (33mm gap width): the top plot is the surface elevation of the reference incident

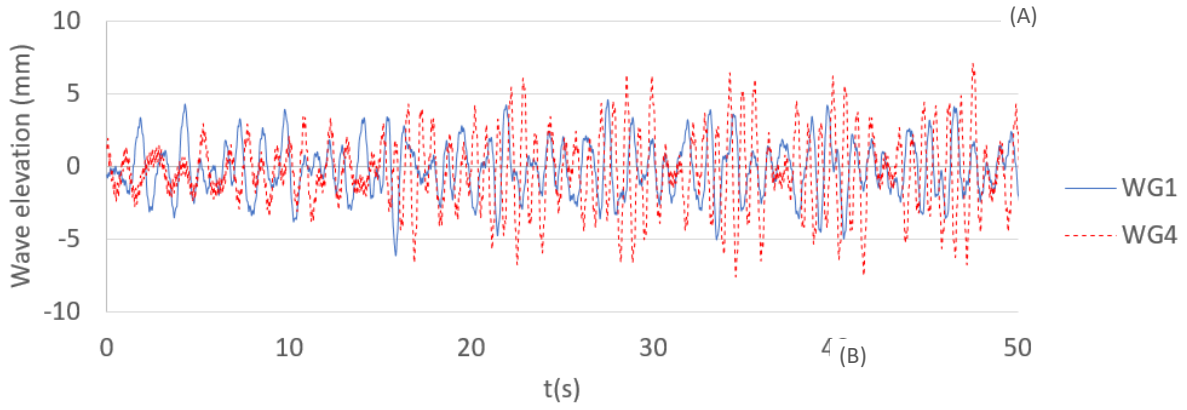

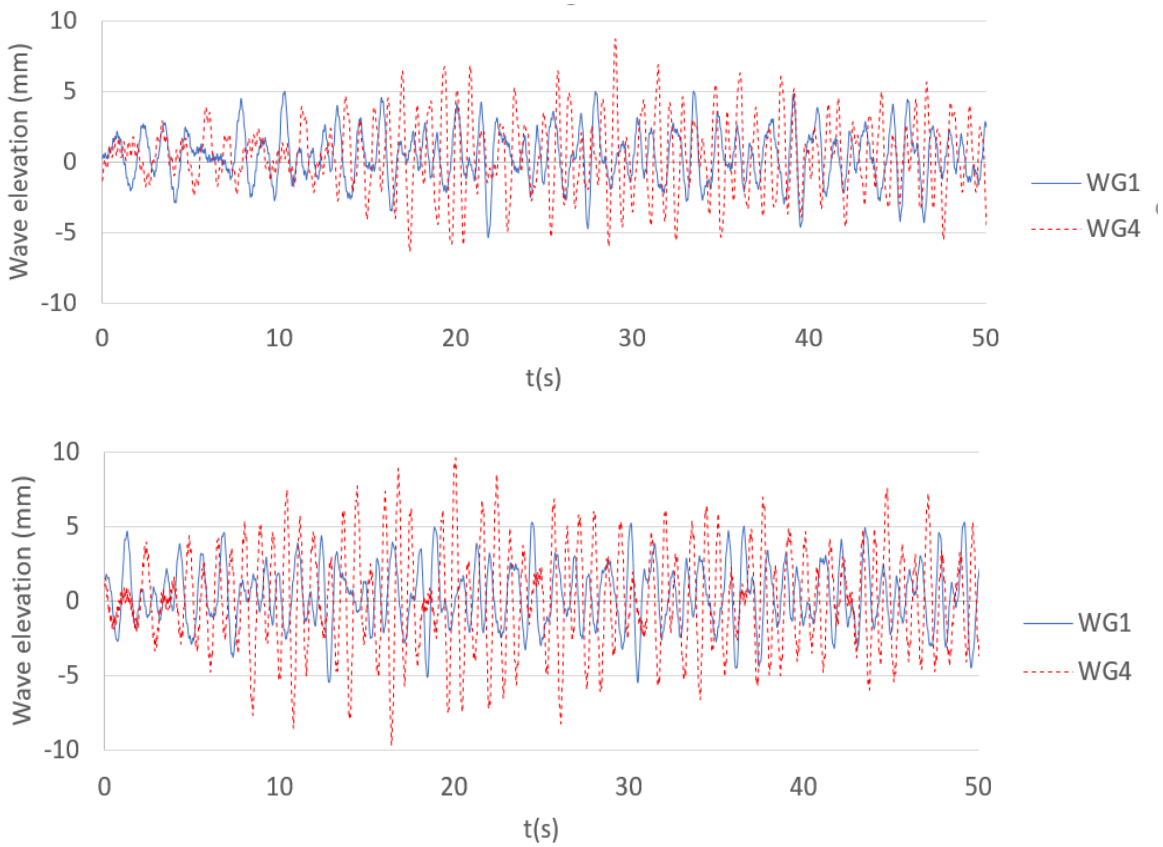

Figure 3-10: Comparison of irregular wave elevation for beam sea with incident wave gauge (wg1) and wave gauge 4 (wg4) at midship at the centre of the gap for (a) 33mm, (b) 53mm and (c) 67mm lab scale

Table 3-7 Statistical data for irregular waves for gap 33mm

	Max	Min	Mean	STD
WG1 (incident wave)	4.0545	-4.6676	0.0658	1.4534
WG4	5.6822	-5.597947	0.004227747	2.072466208

Table 3-8 Statistical data for irregular waves for gap 53mm

	Max	Min	Mean	STD
WG1 (incident wave)	4.0545	-4.6676	0.0658	1.4534
WG4	5.597654	-5.512321	-0.00736603	1.865529385

Table 3-9 Statistical data for irregular waves for gap 67mm

	Max	Min	Mean	STD
WG1 (incident wave)	4.0545	-4.6676	0.0658	1.4534
WG4	7.22E+00	-7.48E+00	-1.62E-01	2.770795681

In this section of the study several irregular waves were produced, an upcrossing analysis was conducted on the time-history of the water surface elevation $\eta(t)$, recorded at each wave gauge location and for each successive upcrossing the wave height was gotten. The generated data was categorized and given a probability of exceedance. The varying wave heights with probability of exceedance for $f_p = 1.047\ Hz$ is plotted in Figure 3-11, for each wave gauge location in the gap region as well as the incident wave gauge (WG1) recording used as the reference. For the three cases below and all other subsequent cases, the probability of exceedance lines are seen to be comparable but of different magnitudes.

In other to put Figure 3-11. Into a practical interpretation, consideration of the return period, T_r, of the maximum incident wave height ($H_{max} = 10mm$) at each wave gauge location. At first the wave period, Δt, at each wave gauge location was calculated. This is done by dividing the experimental run duration, here 120s, by the number of upcrossing at each wave gauge location; the number of upcrossing varying from gauge to gauge. Next the probability of exceedance value corresponding to $H_{max} = 10mm$ is read off Figure 3-11 for each wave gauge location. Finally, the return period T_r is defined by

$$T_r = \frac{\Delta t}{probability\ of\ exceedence}$$

The result of this approach is presented in Table 3-10. For gap distance 33mm at y = -3.3m at wave gauge 3 at the leeside of the smaller vessel, a wave height larger than $2H_s = 14mm$ has a return period 10s, whereas at y = 3.3m location at wave gauge 5 at the weathered side of the larger vessel it is almost 6 times more frequent. In this way the Table 3-10 indicates the location based on wave gauge position where extreme wave excitation is likely to occur which are the more dangerous areas within the gap to place equipment like fenders, etc. (Perić and Swan, 2015).

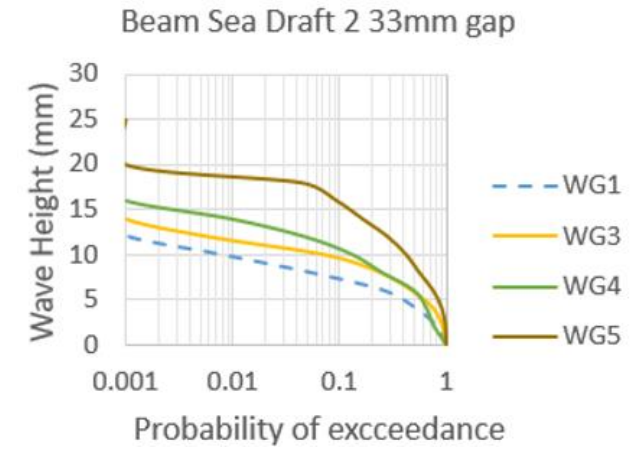

(a)

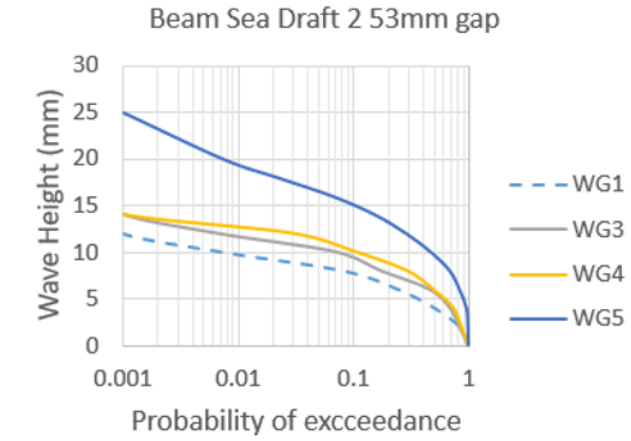

(b)

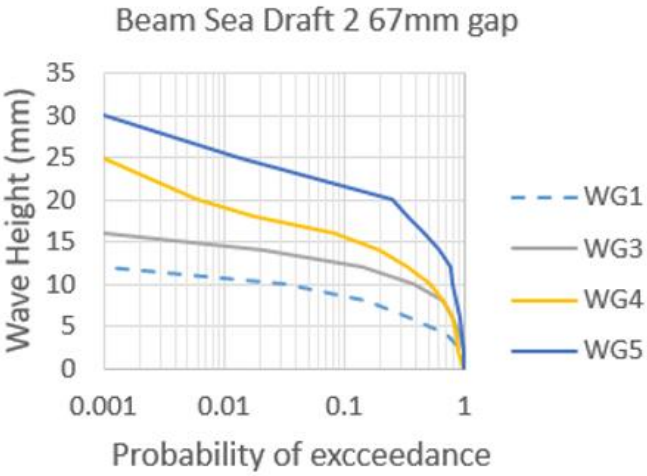

Figure 3-11 Probability of exceedance of wave height in the gap subjected to random sea

Table 3-10. Return period T_r, for wave gauge locations for different gap distances

	Location(m)	33 mm	53mm	67mm
WG3	3.3	10.0s	10.9s	4.8s
WG4	0	4.1s	6.7s	2.0s
WG5	-3.3	1.8s	1.9s	1.1s

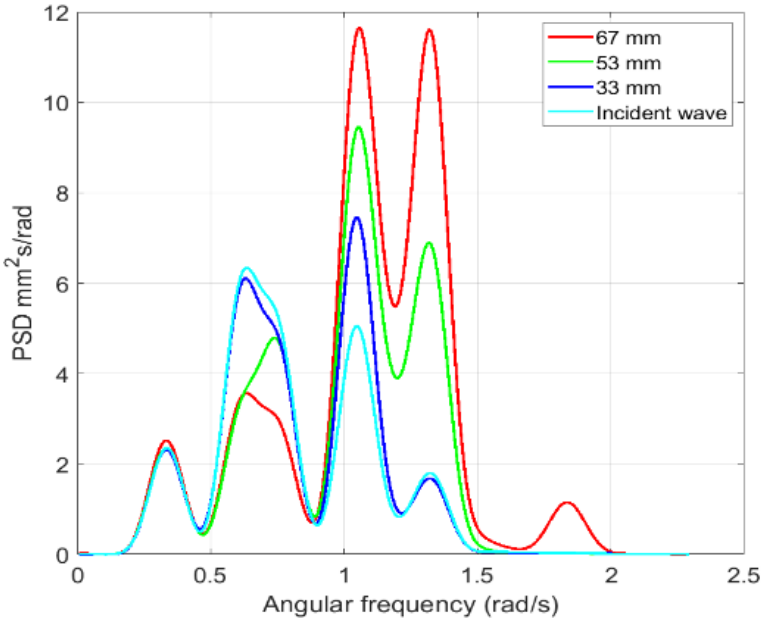

Figure 3-12: Amplitude power spectra density (PSD) of wave gauge located in the gap with comparison of incident wave and other lines denoting gap distances of 33mm, 53mm, and 67mm

Table 3-11: Irregular wave amplification factor

Resonant Frequency (rad/s)	33mm	53mm	67mm
1.045	1.5	1.9	2.3
1.331	-	3.7	6.1

3.3.4 Regular Wave Beam Sea Case

Regular wave with incident wave amplitude A=0.04 m was carried for different gap distances and wave directions. A frequency content analysis was carried out for the regular wave results, making use of Fast Fourier Transform (FFT) applied to the time history of the wave elevation at the water surface and recorded at each wave gauge

location; the data record corresponds to a fully developed wave condition. The time series of the incident wave for the regular wave test cases is shown in Figure 3-13 In the analysis of regular waves, the input of waves is sufficiently close to sinusoidal and the waves is stable, stationary and long enough to obtain steady state. The result in frequency spectra describing the magnitude |η| of the wave elevation at each wave gauge position. The models are subjected to 10 regular wave frequencies with wave amplitude of 4mm.

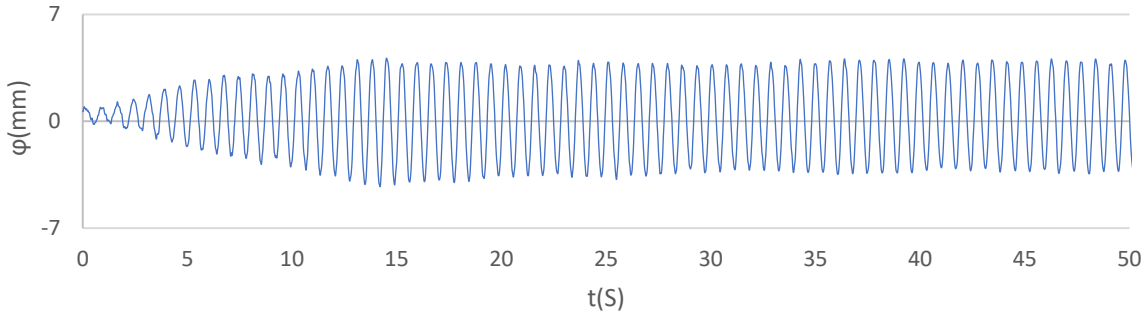

Figure 3-13 Time series of incident wave for regular wave test cases A=0.04m

3.3.4.1 Variation of Gap Distance for Beam Sea Case

Table 3-12 Beam Sea regular wave case with gap distance 33mm

33mm Beam Sea Draft 1					
frequency (rad/s)	WG1	WG2	WG3	WG4	WG5
0.33652	27.6925	17.2286	17.3624	23.8213	71.8812
0.47745	81.9227	31.5378	23.0575	23.7992	82.7501
0.61551	66.3256	48.2988	20.7429	26.077	78.5889
0.75836	53.4214	0.75836	30.1482	19.5602	104.2467
0.90121	44.944	9.7137	29.003	43.0763	92.7574
1.045	56.2138	2.7344	46.9985	47.0691	199.4951
1.1879	7.8914	5.6171	247.0584	317.2715	686.3886
1.3307	22.4402	1.1814	55.6293	138.6136	458.7861
1.4745	36.0858	1.5263	115.0381	245.6289	213.3592
1.6174	27.7035	0.87891	15.9793	214.7334	171.8889

53mm Beam Sea Draft 1					
frequency (rad/s)	WG1	WG2	WG3	WG4	WG5
0.33652	30.1756	16.9255	25.3653	26.8965	70.8243
0.47745	81.9354	31.4016	34.7279	29.4866	85.452
0.61551	66.5548	45.3399	31.4789	33.0554	85.8975
0.75836	50.3548	11.4326	52.8663	29.9915	132.9859
0.90121	43.4141	8.2273	65.4109	78.1476	154.3668
1.045	130.75	4.0385	282.5177	258.9958	816.0103
1.1879	10.366	8.4244	58.0046	94.9122	97.9649
1.3307	15.4301	0.5	88.4545	150.3837	225.4038
1.4745	19.4036	1.0386	115.5192	271.4788	147.8386
1.6174	20.5906	1.3976	12.5589	105.9669	123.7047

67mm Beam Sea Draft 1					
frequency (rad/s)	WG1	WG2	WG3	WG4	WG5
0.33652	28.8275	16.9146	26.0494	26.6109	77.6231
0.47745	84.3309	31.1997	36.6802	30.2404	93.8508
0.61551	65.1599	46.2408	33.8937	34.8389	101.4777
0.75836	52.6009	11.0915	60.0732	33.4244	160.1172
0.90121	37.8747	7.9486	81.8064	99.4498	200.2906
1.045	149.0913	3.1953	583.846	631.51	1660.2059
1.1879	6.0571	4.5398	40.3056	44.7863	60.0338
1.3307	17.2839	0.47007	49.8286	75.789	124.1298
1.4745	20.8393	1.0368	90.7426	280.1994	94.8773
1.6174	15.7056	0.99635	11.5819	79.0679	219.6771

3.4 Focused wave group

Figure 3-14 shows the test results for the focused wave group with the first plot the incident wave surface elevation marked in blue η measured with the absent of the model. The second plot ‘b’ measured the same location but with the presence of the models marked in red φ. T=60s is the instant when the wave group focused at the location of the centre in the absence of the model is measured, i.e. the travel time it takes the focused wave to travel from the wave maker to the wave gauge. The third ‘c’ graph shows the comparison between the incident wave and the wave excitation in the gap response.

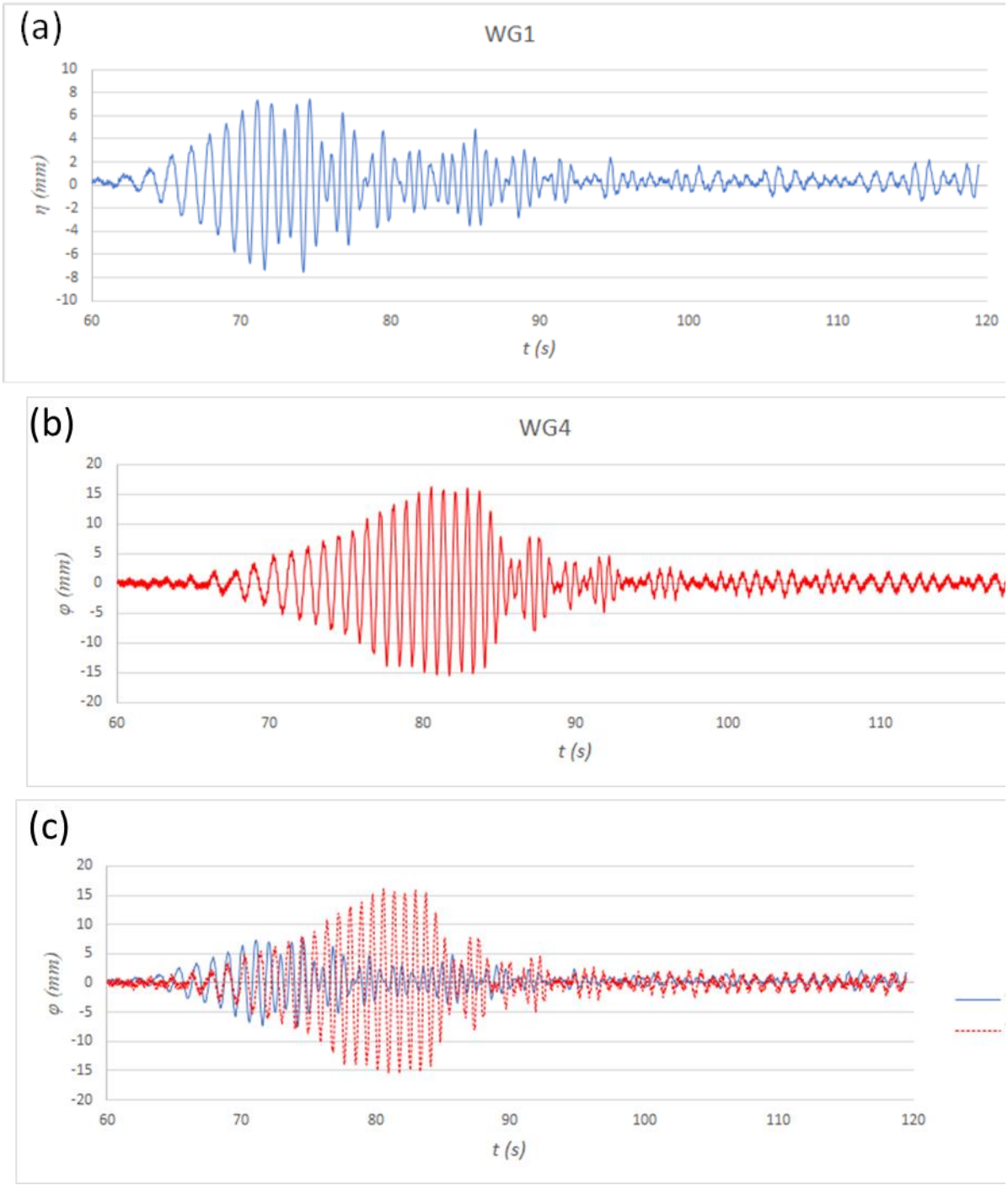

Figure 3-14 Focused wave group time history of surface elevation **blue** incident wave **Red** gap response

Chapter 4. THEORETICAL FORMULATION

4.1 Introduction

This chapter describes the numerical methods in this thesis. For the potential flow theory modelling in this thesis, the DNV SESAM module SIMA (Simulation and engineering analysis of marine operations) was used to analysis the flexible modelling of multibodies, nonlinear time-domain simulations and environmental forces due to wind, wave and current. The following subsections present an introduction to the numerical methods involved Potential flow theory including governing equations, gap resonance problems and potential damping model. The fundamental theories about the damping factor, with the introduction of a free surface lid to obtain different damping coefficients are considered in this chapter.

4.2 The Gap Resonance Problem

Gap resonance problems occurs in various marine operations in situations where one or more structures surrounded by a free surface in any arrangement. There are several typical examples where this is happens in marine operations such as construction with moonpool, multi-hull vessels, ships beside a terminal and side-by-side offloading operation.

Once a free surface is enclosed and bounded by structures there is usually an extreme elevated motion at some frequencies of oscillation. In the side-by-side offloading configuration we shall refer to the long narrow gap as the *gap region* or *gap surface*. For fixed structures the gap surface excitation is triggered by the incident wave and is treated as a purely diffraction problem. The gap surface excitation can also occur for an oscillating body, this is treated as a diffraction and radiation problem. Notwithstanding, if the excitation of the gap surface motion is by the incident wave or forced body motion, there are an infinite number of frequencies where resonance occurs, and these are referred to as *gap resonance* frequencies. At these specific frequencies the free surface in the gap region will experience large motions with a variety of shapes and *modes* of the gap surface, for each gap resonance frequency. The frequency location depends on the geometry of the body surrounding the free surface. At the very start, the gap surface oscillates at the same frequency as the

incident waves. Once the incident wave passes through, the gap surface begins to oscillate at a higher frequency, which are combination of different gap resonance modes.

In moonpools and long narrow gaps, the Newtonian cooling method is used to add external damping to the fluid motion. The damping coefficient is made constant and kinematic free surface condition is modified to include a damping term which is applied in the gap region's free surface or moonpool. In a potential theory solver this method is relatively easy to implement. The introduction of this external damping is easy to control and calibrate. However, this additional damping is a purely mathematical character and doesn't have any foundation in physics. The actual physical damping has different variations corresponding to the free surface geometry and sea state involved, thus the damping is usually calibrated to match the model test.

4.3 Potential flow theory

4.3.1 Potential Damping

Potential damping corresponds with wave-generation. At specific gap resonance frequencies, the response of resonance piston mode elevation in the gap is triggered and the amplitude of oscillation will stay finite. This is because of the interaction between gap fluid and the surrounding external fluid. Energy will be dissipated away from the bodies with the outgoing wave. The wave generation is captured using potential theory, and it is the only damping source when there is no introduction of any external damping mechanism.

4.3.2 The Green function and Green's theorem

Green's theorem is used to formulate integral equations for unknown potentials.

The potential theory as described in Newman (1977) is applied, for the frequency domain evaluation of the first-order radiation and diffraction effects on large displacement structures. The implementation of the numerical simulation is based on WAMIT (Wave Analysis MIT) (Lee, 1995), which utilizes 3D panel methods shown in Figure 5-2 to calculate velocity potentials and hydrodynamic potentials. The radiation and diffraction velocity potentials on the wet part of the body surface are obtained from

the solution of an integral equation gotten using green's theorem with the free-surface source potentials as the green function. The source strengths estimated based on the source distribution method using the same source potential. The source distribution method is approximated with linear combination of radial based function. The integral equation is solved by "panel" method for the unknown potentials and/or the source strength on the body surface.

The Green function $G(X; \xi)$, defined as the wave source potential, is the velocity potential at the point x, due to the point source strength -4π positioned at point ξ. The free surface condition and the radiation condition are both satisfied and the green function is introduced for infinite depth in two-dimensions (Wehausen and Laitone, 1960).

$$G(X,\xi) = In\, r_1 - In\, r_2 - 2PV \int_0^{\infty} \frac{1}{k - v}\, e^{k(z+\eta)} cos\,(k(x - \xi))dk + 2\pi i e^{v(z+\eta)}\, cos(v(x - \xi)), \tag{4-1}$$

Where $r_1 = \sqrt{(x - \xi)^2 + (z - \zeta)^2}$, $r_2 = \sqrt{(x - \xi)^2 + (z + \zeta)^2}$, and **x** = *(x, z)*, $\boldsymbol{\xi} = (\xi, \eta)$ are coordinates in the two dimension plane. The Green function equation (4-1) is defined as a pulsating source potential at point ***ξ*,** calculated at point **x**, and satisfies the free surface boundary condition at equation (8-9) and the radiation condition equation (8-20).In Figure 4-1 below shows a diagram of the fluid domain. Green's theorem is applied on the fluid domain to an unknown potential φ and G produces an integral equation for unknown potential φ,(Liang et al., 2021)

$$\int_S \left(\varphi(\xi) \frac{\partial G(\boldsymbol{\xi}: \boldsymbol{x})}{\partial n_\xi} - G(\xi; x) \frac{\partial \varphi(\xi)}{\partial n_\xi}\right) d\xi = \begin{cases} 0, & Outside\ the\ fluid\ domain \\ \pi\varphi(x) & on\ the\ boundary \\ 2\pi\varphi(x), & inside\ the\ fluid\ domain \end{cases} \tag{4-2}$$

The integral is taken only over the fluid surface due to the face that (4-1) satisfies the free surface boundary conditions. This is an important characteristic of Green function.

The unknown radiation and scattering potentials form integral equations using (4-2). Then $\frac{\partial \varphi}{\partial n}$ is identified from the boundary conditions, and the equation is arranged as

$$\int_S \varphi(\xi) \frac{\partial G(\boldsymbol{\xi}:\boldsymbol{x})}{\partial n_\xi} d\xi \quad - \binom{\pi}{2\pi} \varphi(x) = \int_{S_w} G(\xi; x) \frac{\partial \varphi(\xi)}{\partial n_\xi} \, d\xi \tag{4-3}$$

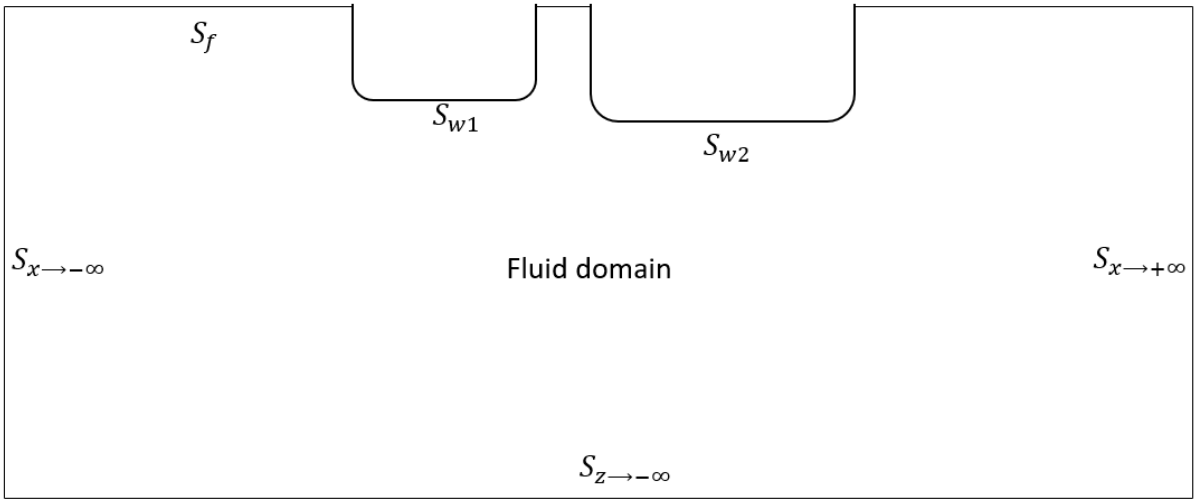

Figure 4-1. Description of fluid domain with boundaries S. S_f is free surface, S_{w1} and S_{w2} are the rigid bodies (FLNG and LNGC). $S = S_f + S_{W1} + S_{w2} + S_{x\to\infty} + S_{x\to-\infty} + S_{z\to-\infty}$.

4.4 Zeroth order mode (piston mode)

As previously stated, individual gap resonance frequencies have their associated free surface gap modes. One mode of has a particular distinction from the other modes in numerous ways. This unique mode is the first mode, and it occurs at the first gap resonance frequency, which is also known as the *piston mode* or *zeroth mode*. In this mode, the gap region free surface oscillates without variation throughout the gap. Thus, the fluid in the gap moves with an almost uniform velocity, hence acting practically like a rigid body. The piston mode has an amplitude referred to as the piston mode amplitude A_g. Where the subscript g represents the word gap. We express $A_g = \frac{H}{2}$, with H_g referred to as the average trough-to-crest height of the free surface along the gap region. Following the description of piston-mode amplitude, there is also an occurrence of a nonlinear case where there might be a slight difference in between

the magnitude of the trough and the magnitude of the crest. There is a resonance frequency associated with the piston mode, which can be called the piston mode resonance frequency ω_p (Kristiansen and Faltinsen, 2010).

The natural period of the piston mode exists because of the mass-spring type behaviour of the piston mode motion. If we take into consideration two fixed models and denote the volume of the fluid between the two ships Ω_p. Assuming that the fluid in the gap region is uniform (vertical), the undamped natural period of the piston is

$$\tilde{T}_p = \frac{1}{2\pi} \times \sqrt{\frac{\rho D b + \tilde{A}_p}{\rho g b}} \tag{4-4}$$

Where, g is acceleration due to gravity, ρ is water density, $\tilde{A}_p$ is added mass of $\Omega_p$at the natural period. We observe that there is an increase in the natural frequency with the square root of the draft D. Which depends on the added mass term $\tilde{A}_p$. The added mass term and thus the resonance frequency will depend on the geometry of the model e.g. water height H, draft D, breath B, gap distance b A n explicit approximate formular for T_p for a moonpool in deep water and small b/B ratio is given by Molin (2001)

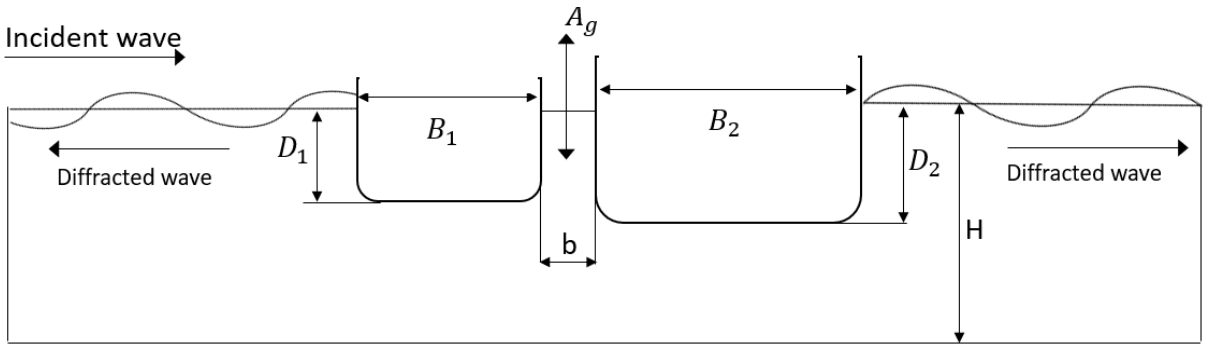

Figure 4-2 Schematic dimension of two rectangular models in a side-by-side configuration, Transverse view: Water height H, breath B, draft D, gap distance b.

The zeroth or piston mode may not always be the first resonance mode that takes place. For instant, when a rigid body with a gap is made to oscillates in sway, it is expected that the first encounter of resonance phenomenon is at the second and third resonance frequency. The first resonance that occurs in forced heave is constantly resonance in the piston mode. Examples of heave and sway induced free surface

motion in the gap region are shown in Figure 4-3 and Figure 4-4 (Markeng et al., 2017)
.

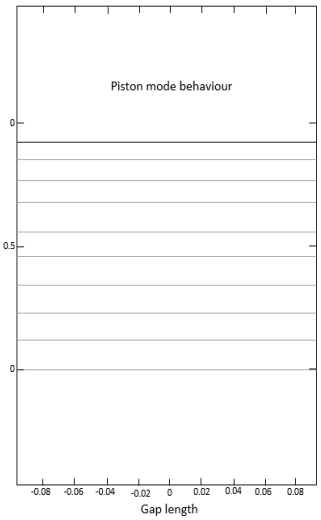

Figure 4-3 Heave generated piston mode (Markeng et al., 2017)

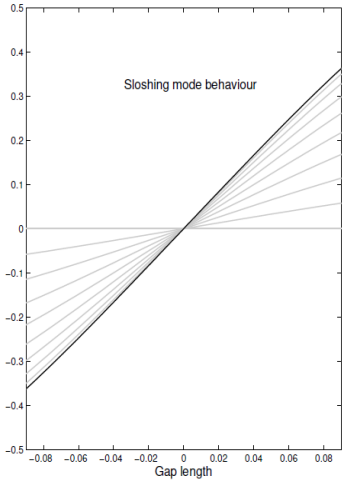

Figure 4-4 Sway generated sloshing behaviour (Markeng et al., 2017)

4.5 Viscous Damping Contribution

Artificial damping is useful when analysing wave water problems to include a realistic damping and in the application of radiation condition at the far field. Potential flow theory assumes an ideal fluid; hence a proper mechanism is usually required to consider energy dissipation by viscosity or alternative damping mechanisms. Numerous marine hydrodynamics applications consider viscous effect to be minor, hence codes based on potential theory have proven to be very useful tools. Although, experimental model test suggest that for narrow gap scenarios this is not the case (Kristiansen and Faltinsen, 2012). A comparison of the of experimental data with data from potential theory calculations, shows there is a clear tendency to overpredict fluid velocities. Studies have been carried out to investigate the effects of non-linear potential damping with conclusions stating that the effects are negligible for piston mode motions (Sun et al., 2010, Kristiansen and Faltinsen, 2012). The difference between the experimental data and potential flow theory calculation is due to the absence of viscous damping in the potential calculation. Viscous damping is considered to have a non-linear characteristic. As the wave elevation in the gap

increases, viscous damping will be a major contributor to the total damping. The viscosity force will dissipate the energy, consequently the surface elevation in the gap and the motion of the body should be reduced. Accurate numerical models of viscous effects are very time-consuming, and not practicable for large marine structures. Hence, empirical formulars, that can approximate viscous effects are very useful.

For hydrodynamics in marine operations where viscous effects are significant, the viscous drag on moving bodies is usually estimated. For the side-by-side offloading configuration the focus is on viscous damping for piston mode elevation. Then again, when the viscous drag force acts on the body, an equal but opposite force is acted on the fluid.

A general expression for viscous drag force acting on an oscillating body in an unbounded fluid is.

$$F_D = \frac{1}{2}\rho L^2 C_D |v| v, \tag{4-5}$$

Where ρ is density of the fluid, L is the characteristic length, v the relative velocity between the body and the fluid and C_D is a problem specific drag coefficient. The drag coefficient will usually be a function of Reynolds number given by

$$R_e = \frac{vL}{\nu}, \tag{4-6}$$

where ν is the kinematic viscosity. The drag coefficient is determined empirically. Many experimental studies have been dedicated for this purpose, with reliable valued for drag coefficients obtained for different applications.

As stated above in Equation (4-5) the assumption is based on the fluid being unbounded. However, we assume that presence of the free surface has little effect on the viscous force. These assumptions are not uncommon, Equation (4-5) is regularly used to calculate viscous forces on Jackets, risers and roll damping of ships or other offshore structures that have the presence of a free surface.

Three different contributors to the viscous damping force acting on the piston behaved gap fluid motion will be considered. These are the effect of viscous damping from skin friction, vortex shedding at bilge (eddy-making damping) and vortex shedding from bilge keel. The total viscous force is expressed as

$$F_{viscous} = F_s + F_e + F_{bk}, \tag{4-7}$$

Where F_s is viscous force due to skin, F_e is viscous force due to eddy making and F_{bk} is viscous force due to bilge keel, respectively. The overall damping is calibrated against experimental results (Tan et al., 2019).

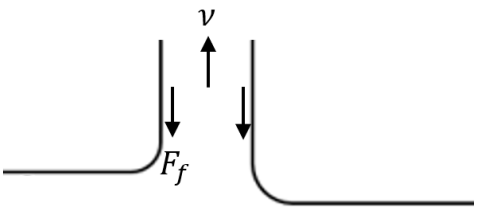

Figure 4-5: Diagram of friction force in the gap

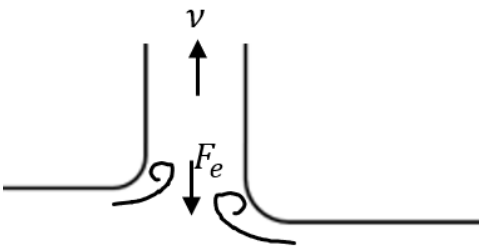

Figure 4-6: Diagram of vortex shedding at the bilge

4.5.1 Viscous damping from Skin Friction of the hull

As the fluid flows over the surface of the body a skin friction stress is generated. The stress is because of the internal forces acting between particles. The viscous effect happens primarily on the surface of the body. The fluid stress effect is a frictional tangential force acting in the opposite direction of the relative velocity between the body surface and the fluid flow. The frictional force on acting generated on a small part of the body is given by Markeng et al. (2017)

$$dF = \frac{1}{2}\rho C_F |v| v dS, \tag{4-8}$$

Where C_F is the frictional drag coefficient. Friction force is only considered on the wetted surface which surrounds the narrow gap. With this inner part of the hull denoted as S_{wg}. Due to the relatively small velocities elsewhere, the frictional forces will be negligible. Total friction force per unit depth is defined integrally as

$$F_f = -\frac{\rho}{2} C_F \int_{S_{wg}} |v| v dS. \tag{4-9}$$

v is not a function of space, under the piston mode assumption and thus can be moved outside the integral sign. We concentration on the rectangular hulls and evaluated integral is over the draft of the body where the gap is defined.

$$F_f = -\rho C_f |v| v. \tag{4-10}$$

From experimental studies of flow over flat plates, drag coefficients as function of Reynolds number and plate measurements has been proposed by Shoenherr (Newman, 1977).

4.5.2 Viscous damping from Eddy-making

Eddy-making is associated with vortex shedding at the bilge. This is important when analysing roll damping, It is considered to be a major contributor of large piston-mode motion in narrow gap analysis. The value of the drag coefficient associated to vortex shedding is based on experiments with cylinders of varying shapes and sizes (Bearman, 1984). The geometries are fully submerged in his experiments. The findings in the report are given as

$$\begin{array}{ll} C_e \approx 8.0KC^{-1/3} & (flatplate) \\ C_e \approx 5.0 & (diagonal\ square) \\ C_e \approx 3.0 & (facing\ \ square) \\ C_e \approx 0.2KC & (circular\ cylinder), \end{array} \tag{4-11}$$

Where KC is Keulegan-Carpenter number given as

$$KC = \frac{V_{max}T}{L_e}. \tag{4-12}$$

Where V_{max} is the maximum velocity, T is the period of oscillation.

The expression for the eddy-making force per unit depth is given by:

$$F_e = -\frac{1}{2}B\frac{C_e}{2}|v|v. \tag{4-13}$$

4.5.3 Free Surface Damping Model

There is energy conservation in the typical potential theory formulation. Which is an unphysical characteristics and usually justified by the assumption of small dissipative effects. There will be energy dissipation if it is a viscous fluid. Heo et al. (2014), Kristiansen and Faltinsen (2010) stated that in a narrow gap the viscous effects should not be neglected. As discusses previously the force due to viscous effect will result in a reduction of the free surface elevation in the gap. The methods formulated to provide

added damping to the free surface in the gap region is the *Newtonian Cooling* damping model. The method is based on potential theory and an external damping lid is introduces on the free surface boundary condition in the gap. This method is designed to dissipate energy from the system, with Newtonian cooling damping model of empirical character.

4.5.4 Damping lid formulation

The modification of the kinematic free surface condition introduces a viscous damping effect (damping term) as in the Newtonian cooling method, with the dynamic condition in equation (4-14) retained (Zhao et al., 2018b).

$$\frac{\partial \Phi}{\partial t} + g\eta = 0\,, \tag{4-14}$$

$$\frac{\partial \eta}{\partial t} = \frac{\partial \Phi}{\partial z} - \mu_1 \eta - \frac{\mu_2}{g}\Phi, \tag{4-15}$$

The two terms μ_1 and μ_2 are additional damping terms. Due to the form of equation (4-15), the additional damping has a linear form Eq. (4-14) which can have further modifications. The kinematic and dynamic conditions are combined to give the free surface boundary condition.

$$-\frac{\partial^2 \Phi}{\partial t^2} - g\left(\frac{\partial \Phi}{\partial z} + \frac{\mu_1}{g}\frac{\partial \Phi}{\partial t} - \frac{\mu_2}{g}\Phi\right) = 0, \tag{4-16}$$

Note, that the free surface condition is not satisfied by the Green function, thus an integral for the free surface is required.

$$\binom{\pi}{2\pi}\varphi(x) = \int_{S_w+S_g}\left(\varphi(\xi)\frac{\partial G(\xi;x)}{\partial n_\xi} - G(\xi;x)\frac{\partial \varphi(\xi)}{\partial n\xi}\right)d\xi \tag{4-17}$$

The term Φ from equation (4-16) is re-written in the form $\Phi = \phi e^{i\omega t}$, we thus obtain $\frac{\partial^2 \Phi}{\partial t^2} = -\omega^2\Phi$, $\frac{\partial \Phi}{\partial t} = i\omega\Phi$ and $\frac{\partial \Phi}{\partial z} = k\Phi$ where k is the wavenumber. Equation (4-16) can be re-written as (Liang et al., 2021)

$$\omega^2 - gk - i\mu_1\omega + \mu_2 = 0, \tag{4-18}$$

We are given the solution as

$$\omega = \pm\sqrt{gk\left(1 - \frac{\mu_2}{gk} - \frac{\mu_1^2}{4gk}\right)} + i\frac{\mu_1}{2} \tag{4-19}$$

To maintain the linear dispersion relationship for the real part of the frequency, we make $4\mu_2 + \mu_1^2 = 0$. In this situation, μ_2 would be a negative number, denoted as $\mu_2 = -\varepsilon_1^2$, thus equation (4-15) can be written as,

$$\frac{\partial \eta}{\partial t} = \frac{\partial \Phi}{\partial z} - 2\varepsilon_1 \eta - \frac{\varepsilon_1^2}{g}\Phi, \tag{4-20}$$

Where the additional damping term is used to give damping of the free surface elevations in the gap, while the second damping term ensures that that the linear dispersion relation is unchanged as in Eq. (4-19). This artificial damping is of purely mathematical character and has no foundation in physics. The epsilon ε_1 coefficient will determine the damping level and shall be obtained through experimental model test.

We introduce our dynamic Eq. (4-14) into Eq. (4-20) (Kinematic), then the free surface boundary condition can be expressed in terms of the time independent potential

$$\frac{\partial \phi}{\partial z} = \frac{\omega^2}{g}\phi - 2\varepsilon_1 \frac{i\omega}{g}\phi - \frac{\varepsilon_1^2}{g}\phi, \tag{4-21}$$

Which is further written as follows

$$\frac{\partial \phi}{\partial z} = K\phi(1 - i2\mu - \mu^2), \tag{4-22}$$

Where $\mu = \frac{\varepsilon_1}{\omega}$ and $K = \frac{\omega^2}{g}$, Eq. (4-22) is used for the free surface in the gap region. μ is tuneable.

4.6 Frequency Domain Analysis

Hydrodynamic problems in regular waves are considered as a combination of diffraction and radiation problems. The radiation part enables the computation of the frequency dependent added mass and damping.

The potential function formulation can be written as

$$\emptyset(x,y,z) = \emptyset_I(x,y,z) + \emptyset_S(x,y,z) \tag{4-23}$$

Where $\emptyset_1(x,y,z)$ and $\emptyset_s(x,y,z)$ are the incident potential and scattering potential respectively.

The scattering potential is subdivided into diffraction and radiation parts

$$\emptyset(x,y,z) = \emptyset_1(x,y,z) + \emptyset_D(x,y,z) + \emptyset_R(x,y,z) \tag{4-24}$$

The necessary boundary conditions can be solved from each part of the equations. The wave forces acting on the floating body are calculated using the incident and diffraction potential. While the radiation part calculates the hydrodynamic coefficients added mass and potential damping from the body oscillation.

$$A_{mn} = Re\left(\rho \iint_{S_O} \Phi_m \frac{\partial \emptyset}{\partial n_j} ds\right)(m,n = 1,2,\ldots.6) \tag{4-25}$$

$$B_{mn} = Im\left(\rho\omega \iint_{S_O} \Phi_m \frac{\partial \emptyset}{\partial n} ds\right)(m,n = 1,2,\ldots.6) \tag{4-26}$$

Where A_{mn} is the added mass and B_{mn} is the potential damping in the *m* direction induced from the body oscillating in direction *n*. ω is the oscillating frequency and n_j is generalized normal vector.

The equation of motion based on Newton's second law

$$\sum_{n=1}^{6}[(M_{mn} + A_{mn})]\ddot{\eta}_n + B_{mn}\dot{\eta}_n + C_{mn}\eta_n] = F_m e^{-i\omega_e t} \quad (m=1,2,\ldots.,6) \tag{4-27}$$

Where M_{mn}, C_{mn} are the mass matrix and hydro static stiffness matrix respectively while F_m is the complex amplitude of the excitation force and moments.

The heave, roll and pitch hydrostatic stiffness are defined as and C_{33}, C_{44}, and C_{55}.

$$C_{33} = \rho g A_{WP} \tag{4-28}$$

$$C_{44} = \rho g V G M_T \tag{4-29}$$

$$C_{55} = \rho g V G M_L \tag{4-30}$$

A_{WP} is the water plane area, V is volume of displaced water, while GM_T and GM_L are the transverse and longitudinal metacentric heights respectively.

In this current calculation structure, which has no forward speed is considered according to the distribution's second identity the symmetric relations $A_{mn} = A_{nm}$ and $B_{mn} = B_{nm}$

Solving the equation of motion we can obtain the kinematics of the body in frequency.

4.7 Time Domain Analysis

The frequency domain is not capable of effectively analyzing the nonlinear coupling effects between the FLNG, LNCG and connecting system, the investigation of the multibody system in side-by-side arrangement is therefore important. The formulation of the coupled analysis time domain analysis for the FLNG facility and LNGC is given below (Rho et al., 2007).

$$[M + A(\infty)]\{\ddot{\xi}\} + D_1\{\dot{\xi}\}\, D_2 f(\{\dot{\xi}\}) + C\{\xi\} + \int_0^t [h(t-\tau)]\{\dot{\xi}\} d\tau = F^{wave} + F^{current} + F^{wind} + F^{ext} \tag{4-31}$$

M is generalised mass matrix for the ship hull

$\mathbf{A}(\infty)$is added mass matrix at infinite frequency

K Hydrostatic restoring stiffness matrix,

$\boldsymbol{D_1}$ and $\boldsymbol{D_2}$ are linear and quadratic damping matrix respectively,

$\{\ddot{\boldsymbol{\xi}}\}$ Indicates, the displacement vector of the vessel,

$\mathbf{F^{wave}}$, $\mathbf{F^{current}}$ $\mathbf{F^{wind}}$ denotes the wave force and force and the current force OCIMF (1994) data

$\boldsymbol{F^{ext}}$ any other force (specified forces and forces from station keeping and coupling elements.

$\boldsymbol{h}(\boldsymbol{\tau})$ is the retardation function matrix

$$\boldsymbol{h}(\boldsymbol{\tau}) = \frac{1}{2\pi}\int_{-\infty}^{\infty}[c(\omega) + i\omega a(\omega)]e^{i\omega t}d\omega, \tag{4-32}$$

c is the radiation damping matrix, **a** is the added mass matrix calculated in the frequency-domain analysis respectively, ω is the frequency. The 2 parts in equation 1 must be opposite for $\tau < 0$ and identical for, namely:

$$\boldsymbol{h}(\boldsymbol{\tau}) = \frac{1}{2\pi}\int_{0}^{\infty} c(\omega)\cos\omega\tau\, d\omega = -\frac{2}{\pi}\int_{0}^{\infty}\omega a(\omega)\sin\omega\tau\ d\omega. \tag{4-33}$$

The calculation of the retardation functions are done using the frequency dependent damping. This is because, during very low and very high frequencies damping is zero which affects the accuracy of computation of the retardation function.

From equation (1) the frequency dependent added mass and damping forces are influenced by the hydrodynamic interaction and are introduces in the coupled added-mass and coupled

Retardation functions at infinite frequency. In such a situation, the inertia term $[M + a(\infty)]\{\ddot{\xi}\}$ in Equation (1) is written as

$$\begin{bmatrix}(M + a(\infty))_{i,j} & (a(\infty))_{i,j}\\ (a(\infty))_{j,i} & (M + a(\infty))_{j,i}\end{bmatrix}\begin{Bmatrix}\ddot{\xi}_i\\ \ddot{\xi}_j\end{Bmatrix}. \tag{4-34}$$

The subscripts *i* and *j* represent body *i* and body *j.* The retardation function term $\int_0^t [h(t-\tau)]\{\dot{\xi}\}d\tau$ in Equation 1 can be written as

$$\int_0^t \begin{bmatrix} h(t-\tau)_{i,j} & h(t-\tau)_{i,j} \\ h(t-\tau)_{j,i} & h(t-\tau)_{j,j} \end{bmatrix} \begin{Bmatrix} \ddot{\xi}_i \\ \ddot{\xi}_j \end{Bmatrix} d\tau \tag{4-35}$$

The analysis of the hydrodynamic coupling is carried out with the state-of-the-art code SIMO, with time step of 0.2 s based on the convergence test and proposed in the research conducted by Zhao et al. (2014). The wind and current forces $\mathbf{F}^{\mathbf{wind}}$ and $\mathbf{F}^{\mathbf{current}}$ on the two vessels are evaluated with the standardized (OCIMF, 1994).

The mooring lines are modelled to adopt a catenary form using the nonlinear catenary equations. A simplified dynamic model is adopted, with the assumption that only the tangential component of the line motion has effects on the dynamic tension and elastic line elongation predicted by quasi-static analysis. Equation (6) describes the line motion, *u*.

$$c^* \dot{u}|\dot{u}| + k^* u = k^E x \tag{4-36}$$

Where

c^* Generalized line damping

k^* Generalized line stiffness

k^E Axial line stiffness, assumed to be constant

k^G Geometric catenary stiffness

u displacement of the line

$\dot{u}$ Velocity of the line

x Tangential motion excitation of the line end

To maintain a constant side-be-side offloading configuration, the hawser and fenders are used. They are hardly subjected to drag forces, so the hawser are modelled as force elongation coupling while the fender are defined with compressive forces.

$$F_n = -\left(f(R) + c\left|\dot{R}\right|^{\epsilon}.\frac{\dot{R}}{\left|\dot{R}\right|}\right).n \qquad (4\text{-}37)$$

Where

$f(R)$ Fender characteristics

c damping constant

$\dot{R}$ deformation velocity

ϵ specified exponent

Chapter 5. NUMERICAL SIMULATION METHOD

This section describes the numerical method used for the simulation. The calculation methods for the wave loads uses potential flow theory as described in (Newman, 1977) is applied to calculate the radiation and diffraction effects on large displacement structures.

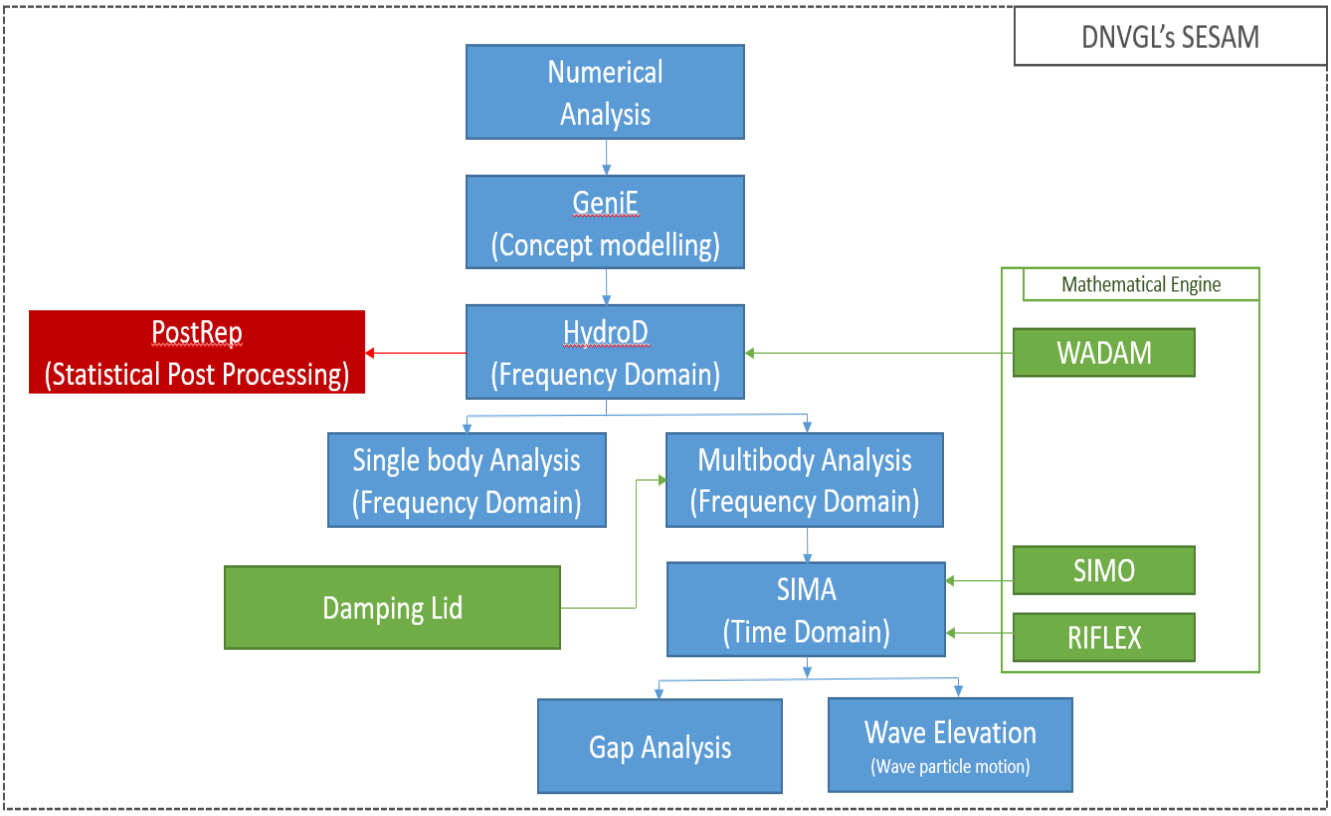

Figure 5-1 SESAM Workflow

5.1 Hydrodynamic Modelling

The model test numerical simulation analysis involves using SIMA module of DNVGL SESAM software. The HydroD module computes the wave loads and motion via WADAM (Wave Analysis by Diffraction and Morison Theory) which uses first and second order 3D potential theory for wave load calculation in the frequency domain. The frequency domain results are imported into SIMA software which uses SIMO

state-of-the art code. SIMO supports analyses of nonlinear time-domain simulation of wave frequency as well as low frequency forces for multibody system. The numerical procedure utilizes the Runge Kutta integration method and Fast Fourier Transform is applied for the wave method.

The two vessels of different sizes were fixed during the model test, consequently we have a pure diffraction problem. For the numerical simulation, the same damping coefficient are applied for the different gap resonance mode for simplicity to allow a fundamental understanding of gap resonance to be developed and showed satisfactory agreement with the model test for the various test cases.

5.2 Damping free surface lid in WADAM

The linear potential flow theory is known to over-predict the water surface elevation in narrowed spaces such as the gap in side-by-side offloading configurations. For potential flow theory the gradient of the velocity potential Φ must satisfy the Laplace equation and a series of boundary conditions. The linearized form of the boundary value formulation free surface condition is:

$$\phi_z - k\phi \ = 0 \ \ on \ z \ = 0 \tag{5-1}$$

From Equation (5-1) a linear damping factor ε is introduced on the exterior free surface area S_e.

$$\phi_z = K\phi(1 - 2i\varepsilon - \varepsilon^2) \quad on \ \ S_e \tag{5-2}$$

The option of removal of irregular frequencies from the diffraction solution is provided in WADAM by adding panels in the free surface interior to the body with an imposed homogeneous Neumann (or Dirichlet) condition. The total diffraction velocity potential ϕ_D is (Korsmeyer et al., 1988).

$$2\pi\phi_D(x) + \iint_{S_b} \phi_D(\xi) \frac{\partial G(\xi; x)}{\partial n_\xi} d\xi = 4\pi\phi_0(x) \tag{5-3}$$

The same equation system is used for both internal and external solutions (WADAM, 2017). The panel model for the two vessels is shown in Figure 5-2(a). For the study

we stick to a fine mesh of 3m, for the large and small vessels we have 1328 and 862 quadrilateral panels generated respectively while the free surface mesh panels are 2950 shown in Figure 5-2(b).

The numerical simulation was analysed as a pure diffraction problem to isolate the gap resonance response and study how the different setup variations influence the wave excitation in the long narrow gap region. Hence, the two vessels were fixed. The artificial damping coefficient in the potential flow solver were introduced with the addition of calibrated damping and showed satisfactory agreement with the model test. This simplification of the hydrodynamic model geometry was for a suitable comparison with the model test, to obtain the damping lid factor.

(a)

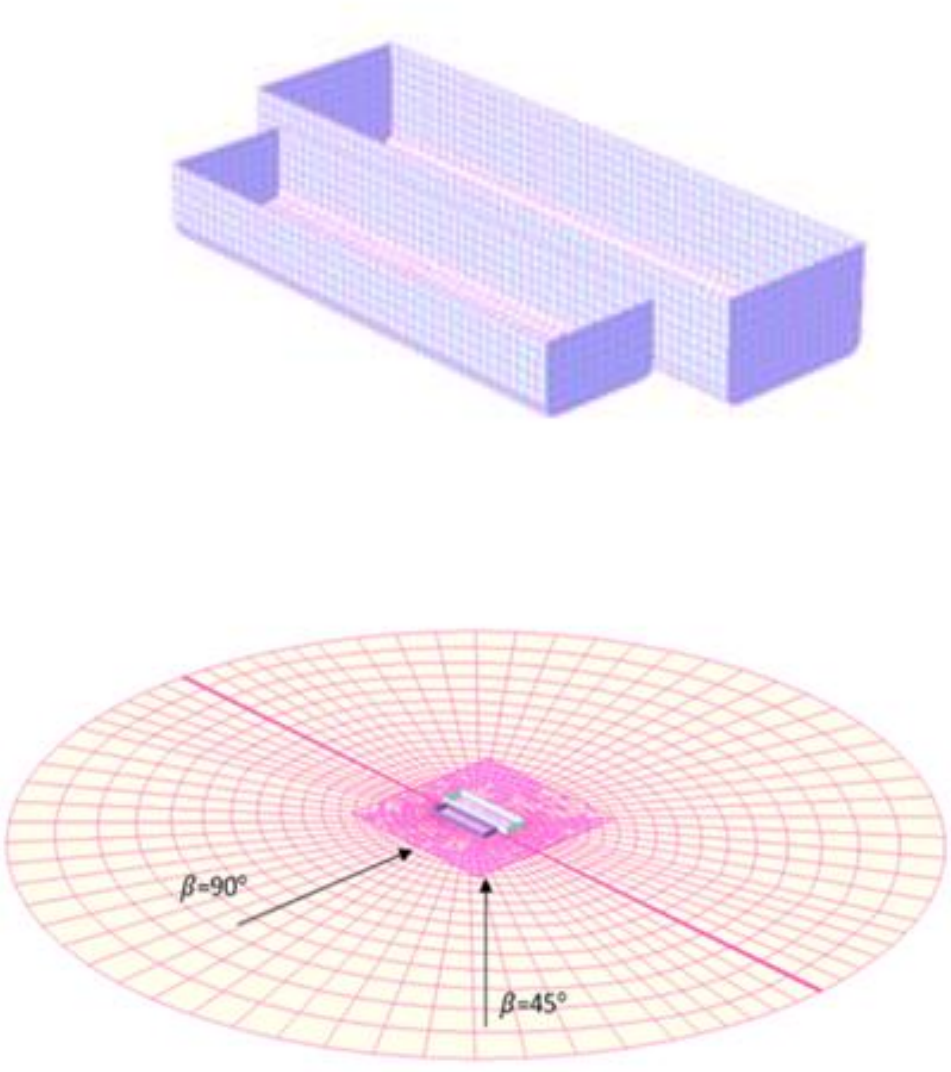

(b)

Figure 5-2 (a) The panel model in the potential flow solver WADAM, (b) Free surface panel mesh

Table 5-1 Model scantlings

Parameter	**Box 1 (m)**	**Box 2(m)**
Length	150	120
Breadth	40	30
height	25	17.4
Blige radius	3	2
Draft 1	12	7.4
Draft 2	12	6.4

5.3 SIMA Simulation

The full scale model test formulation for the fixed model is conducted with the SIMA time-domain program which is used to visualize the simulation calculation, while the SIMO (Simulation of marine operation) code analyses the nonlinear time domain simulation of complex systems such as calculating the wave excitation in the gap between the two vessels using Froude-Krylov and diffraction force.

To measure the time dependent wave elevation at specific points on the vessels as shown in Figure 5-3. The wave gauges are places at certain points to obtain different data sets. Three wave gauges were placed in the gap symmetrically with respect to the centre of the gap. The reference gauge (WG1) is used to measure the incident surface wave elevation hence it is places Infront of the models. The position behind the model has a wave gauge (WG2) placed there to enable the measurement of the diffracted wave. Wave gauge 3 (WG3) is 0.33m from the centre of the gap and closer to the smaller box model (leeward side), wave gauge 5 (WG5) is 0.33m from the gap centre and closer to the larger box model (weather side) and gauge 4 is central. The 3 wave gauges are places in between the two vessels to measure then wave elevation and comparisons made with the incident wave and diffracted wave are made.

The wave gauges are created as slender elements and positioned accordingly as shown in Figure 5-3 with the mass and volume coefficients set to zero and only one strip element used. The time history of surface elevation at the projected point are computed using the wave particle motion distribution.

To generate the time history of surface elevation, water particle velocities and acceleration, the short crested irregular sea is discretized into a set of harmonic components (Nwafor and Hu, 2021)

The surface elevation in complex notation is given by

$$Z_\zeta = \sum_{J=1}^{N_\beta}\sum_{k=1}^{N_\infty} Z_{jk} = \sum_{J=1}^{N_\beta}\sum_{k=1}^{N_\infty} A_{jk}^{e^{i\left(\omega_k t+\emptyset_{jk}^{p}+\emptyset_{jk}\right)}}$$

$$A_{jk} = \left|Z_{jk}\right| = \sqrt{2S_\zeta\left(\beta_j,\omega_k\right)\Delta\beta\Delta\omega} \qquad (5\text{-}4)$$

$$arg\left(Z_{jk}\right) = \omega_k t + \emptyset_{jk}^{p} + \emptyset_{jk}$$

is direction of wave propagation, ω is frequency, and $\emptyset_{jk}$ is random phase angle

The surface elevation can be expressed as:

$$\zeta(t) = Im\left(Z_\zeta\right) = Re\left(Z_\zeta \cdot e^{\frac{-i\pi}{2}}\right) = \sum_{j=1}^{N_\beta}\sum_{K=1}^{N_\infty} A_{JK}\sin\left(\omega_k t + \emptyset_{jk}^{p} + \emptyset_{jk}\right) \qquad (5\text{-}5)$$

The velocity and acceleration components are derived from the surface elevation components .

$$\dot{Z}_{jk} = i\omega_k Z_{jk}$$
$$\ddot{Z}_{jk} = -\omega_k^2 Z_{jk} \qquad (5\text{-}6)$$

The time series are obtained by adding the harmonic components by performing a Fourier Transformation algorithm (SINTEF, 2017).

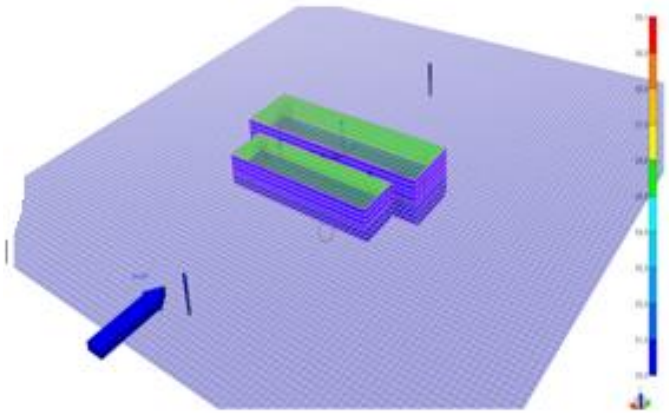

(a)

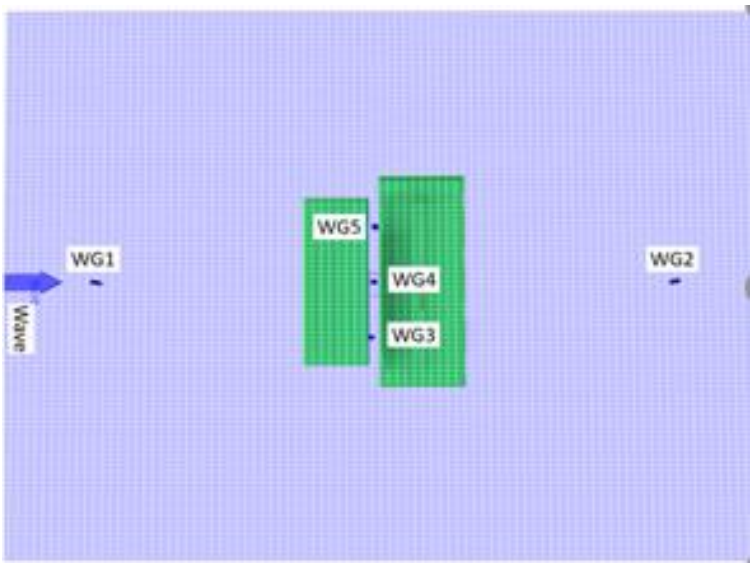

(b)

Figure 5-3 The hydrodynamic models in the time domain sima software with wave direction at beam sea and slender elements positioned to measure water particle wave elevation.

5.4 Hydrodynamics of the FLNG and LNGC system in side-by-side configuration

5.4.1 Features of the FLNG vessel and LNG Carrier

The side-by-side offloading operation of the FLNG-LNG system consist of gap distance of 4.5m with connecting systems such as mooring lines, hawser and fender. The operational area has a water depth of 1500 meter. The main particulars of the

FLNG and LNGC are given in Table 5-2and Table 5-3. The outline of the two vessels is shown in Figure 5-4. The FLNG outline shows it has a fuller geometry because its operational function does not involve voyages. While, the LNGC has a slender geometry to enable cruising for LNG transportation. There is a steady change in the draft of the system as LNG transfer progresses. The FLNG draft decreases, while the LNGC arrives in a ballast condition with a larger draft and decreases as the loading condition is at 50 percent. There is a difference in the 100% and 50% loading condition for the LNGC.

Table 5-2 General parameters of FLNG vessel

Designation	unit	Filling level 1(full loading)	Filling level 2 (50% loading)	Filling level 3 (10% loading)
Length over all LOA	m	340	340	340
Breadth, B	m	61	61	61
Depth, D	m	37	37	37
Draft, T	m	17.844	15.599	14.261
Displacement Δ	t	323251	278805	252826
Centre of gravity above base, KG	m	23.977	22.265	23.147
Centre of gravity from midship, LCG	m	-5.613	-4.075	-0.562

Table 5-3 General parameters of LNG carrier

Designation	unit	Filling level 1 (full loading)	Filling level 2 (50% loading)	Filling level 3 (10% loading)
Length over all LOA	m	291	291	291
Breadth, B	m	45.8	45.8	45.8
Depth, D	m	26.5	26.5	26.5
Draft, T	m	9.646	9.688	11.717
Displacement Δ	t	99100.5	99546.3	122671
Centre of gravity above base, KG	m	12.059	12.298	16.501
Centre of gravity from midship, LCG	m	0.036	0.392	-0.68

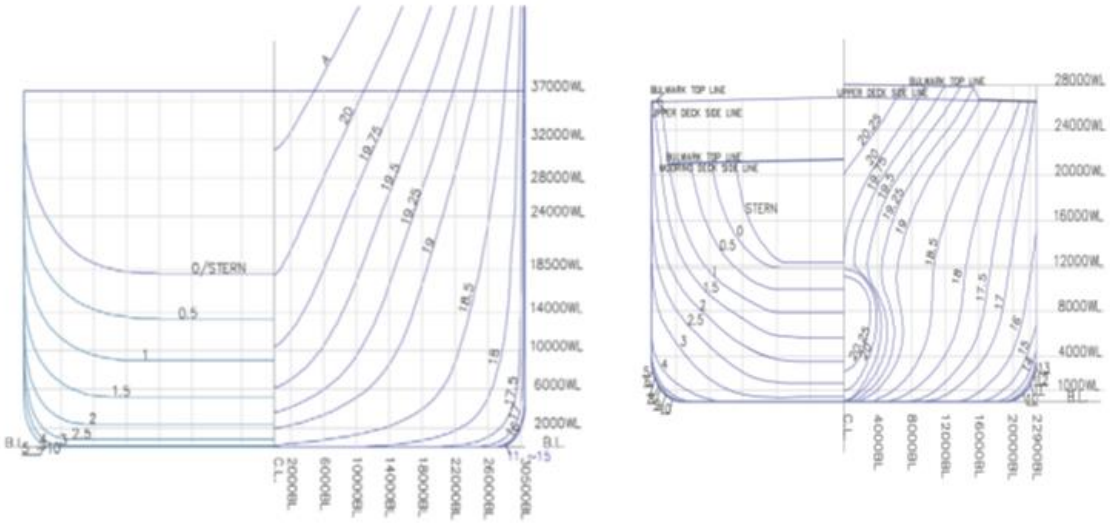

Figure 5-4 FLNG and LNGC Outline

5.4.2 Hydrodynamic Modelling

The panel models for the FLNG and LNGC are shown in Figure 5-6. The FLNG is given a mesh density of 3 m with 3728 panels generated and the LNGC also has a mesh density of 3 m with 2252 panels generated, this is satisfactory enough to have a nice balance between computational time and result accuracy according to the mesh sensitivity study shown in Figure 5-5 where three different mesh sizes of 5.0 meter, 4.0 meters and 3.0 meters. A notable reduction in the sway drift force transfer function is observed as the mesh size reduces. Indicating the importance of using a fine mesh for multibody problem. Moreover multibody analysis can suffer from inaccuracies when calculated using diffraction code because of insufficient number of panels (Huijsmans et al., 2001) . The mesh size on the free surface should be comparable to that on the wet hull.

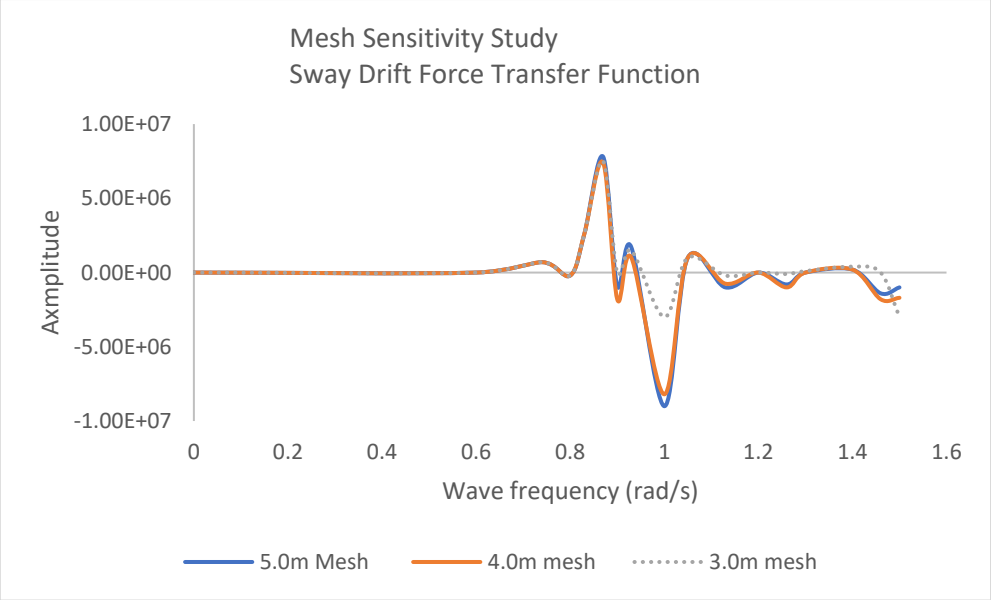

Figure 5-5 Mesh Sensitivity Analysis

5.4.3 Mass Modelling

The Mass model is used to obtain the appropriate vessel displacement, Center of gravity from mid ship LCG (Longitudinal Centre of Gravity), Center of gravity above base (KG) and radius of gyration which corresponds to the different loading conditions. It is created by using a number of beams of varying densities and combining them to get the LCG of the vessel. A total of 20 beams were used for building the mass model. The total mass of the beams is equal to the total displacement of the vessel based in the loading condition. Table 8-1 is the mass model for the FLNG full loading condition shown in Table 5-2 with a total displacement of 323251 tons and longitudinal center of gravity (LCG) from midship of -5.613 m.

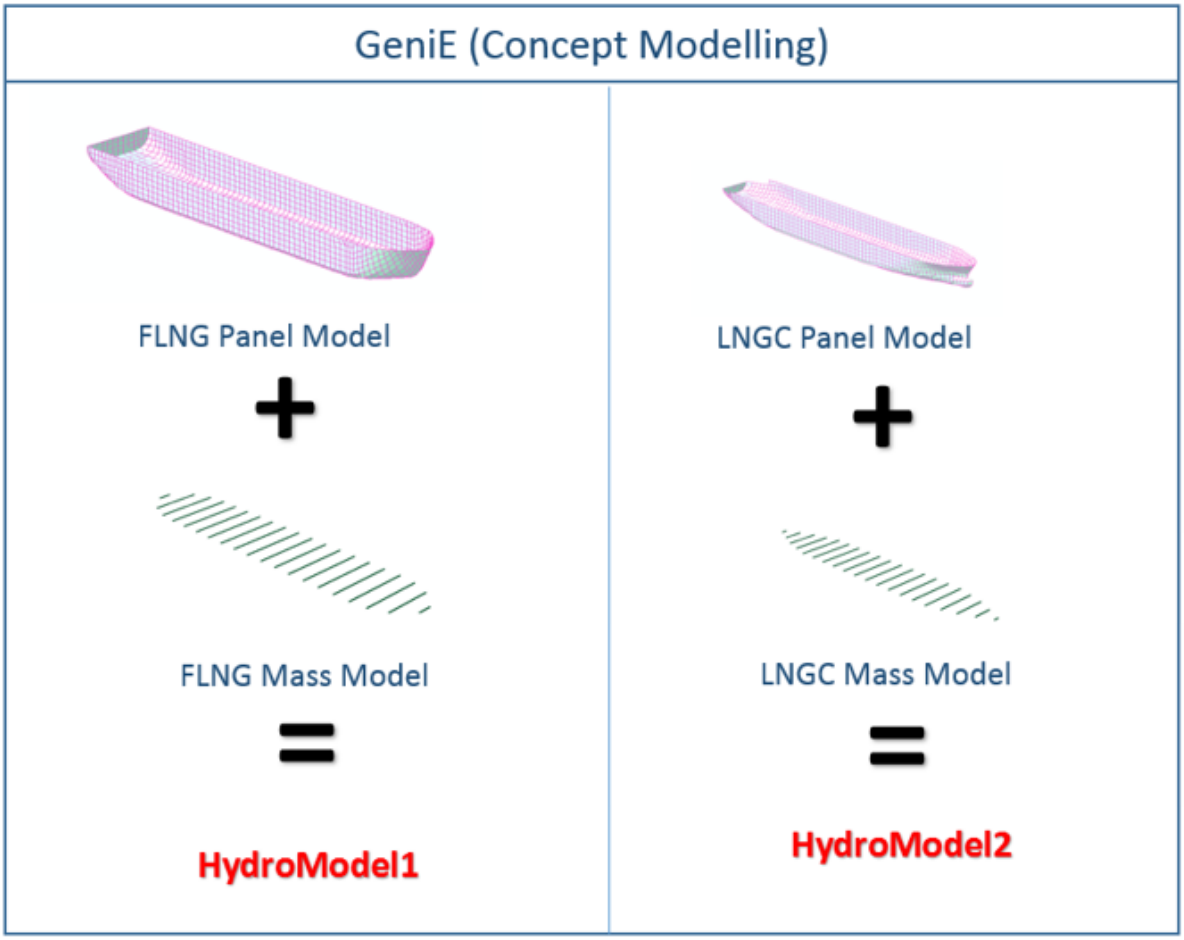

Figure 5-6 Hydrodynamic model of FLNG and LNGC

5.4.4 Single Body Analysis

The single body analysis is carried out for FLNG and LNGC. The analysis is done for a series of wave directions and frequencies. The set of frequencies are selected to contain the maximum wave spectrum energy. The wave directions are 0 degree~360 degree with direction interval of 45 degree and the wave frequency range (wave period range) 0.05rads/s~1.50rad/s. The potential function is be based on a deep water problem with water depth of 1500 meter. Nevertheless, for the side-by-side configuration the operation requires the incorporation of hydrodynamic coupling. Therefore, multibody analysis is also carried out subsequently. The free surface boundary condition is linearized for the first order potential flow theory computation Equ (8-7) whereas the non-linear free surface boundary condition is used for the second order potential computation to obtain the wave drift forces and quadratic transfer function (Difference frequency) using Newman's approximation method.

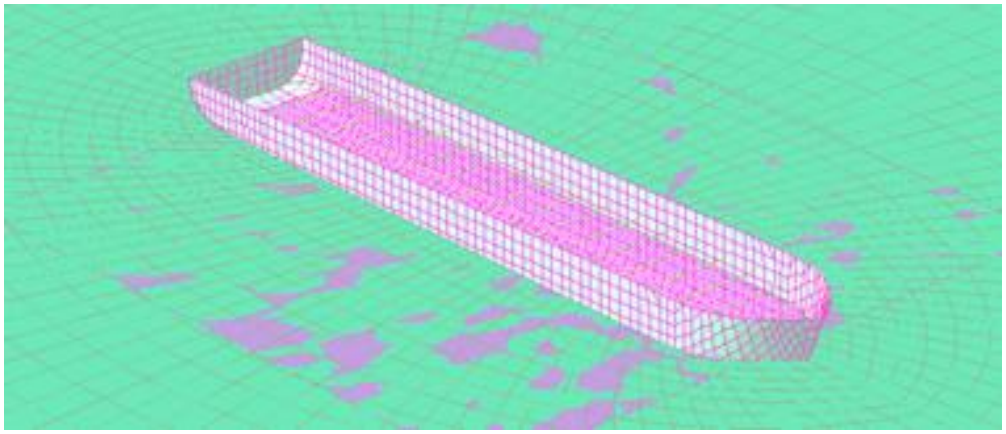

Figure 5-7 : Free water Surface

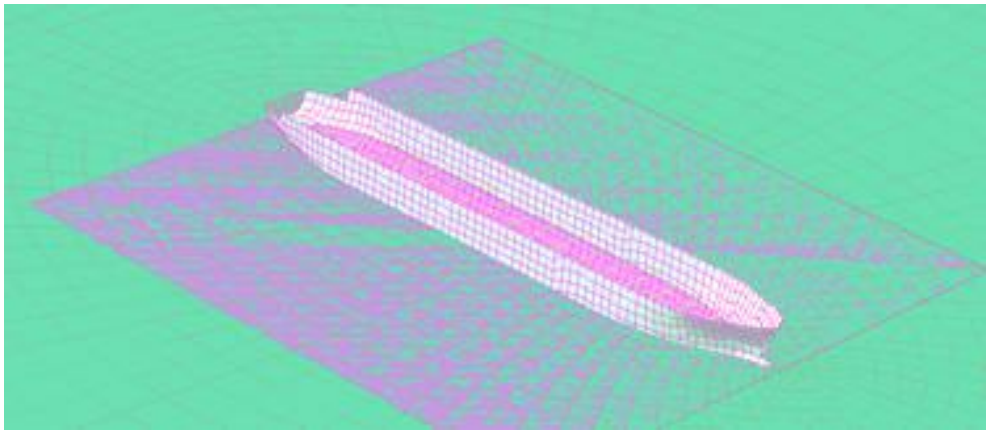

Figure 5-8 Free water surface LNGC

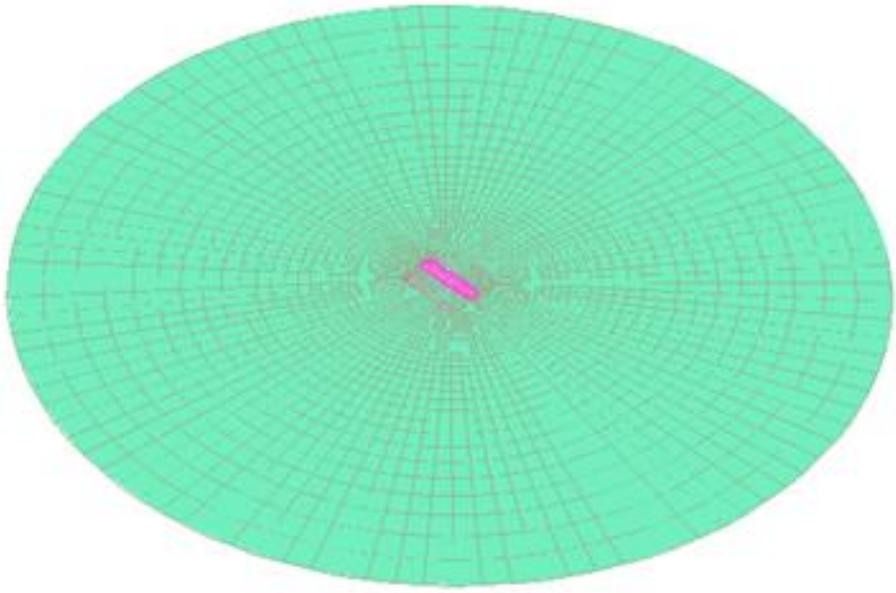

Figure 5-9 Circular free surface

5.4.5 Turret mooring system

The FLNG is in water depth of 1500m and an internal turret with a catenary mooring system is modelled in SIMA simulation, comprising of fifteen (15) mooring lines that enable the FLNG to weathervane around freely under different environmental loading conditions. Each mooring line is 3351m long. The identical mooring lines are made up of three segments which are, chain-wire-chain and a horizontal distance between anchor and fairlead of 2815m. The pre-tension at the top of each mooring line is 5101.8 KN for the fully loaded condition, details of the mooring configuration are listed in Table 5-4.

Table 5-4 Configuration of mooing lines

	Length (m)	Diameter (mm)	Weight in air (kg/m)	Submerged weight (kg/m)	Breaking loads (kN)	Axial stiffness (kN)
Chain	100	146.05	427.10	371.58	18908	1607180
Wire rope	1859	139.7	102.40	81.40	19186	1822670
Chain	1392	146.05	427.10	371.58	18908	1607180

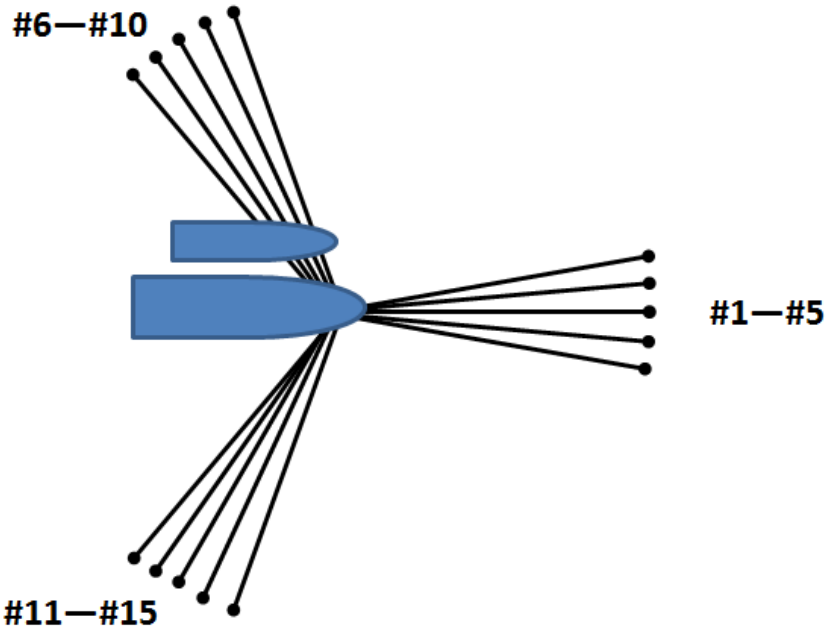

Figure 5-10 General arrangement of mooring system

5.4.6 Connecting System

Figure 5-11 and Figure 5-12 shows the connecting system. A total of sixteen hawsers and six fenders are used to limit relative vessel motion and prevent collisions. One hawser and fender each from the afterward and forward of the vessels are chosen for the result presentation. The physical properties of the hawser lines are given in

Table 5-5 the graphical representation of the stiffness property is described in Figure 5-15, the fender properties are nonlinear and is depicted in,Figure 5-15

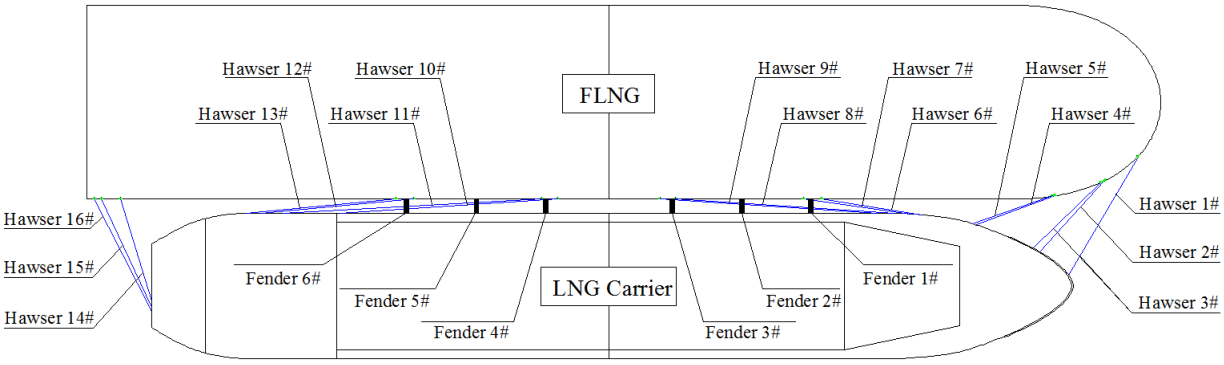

Figure 5-11 Connecting lines distribution between two vessels

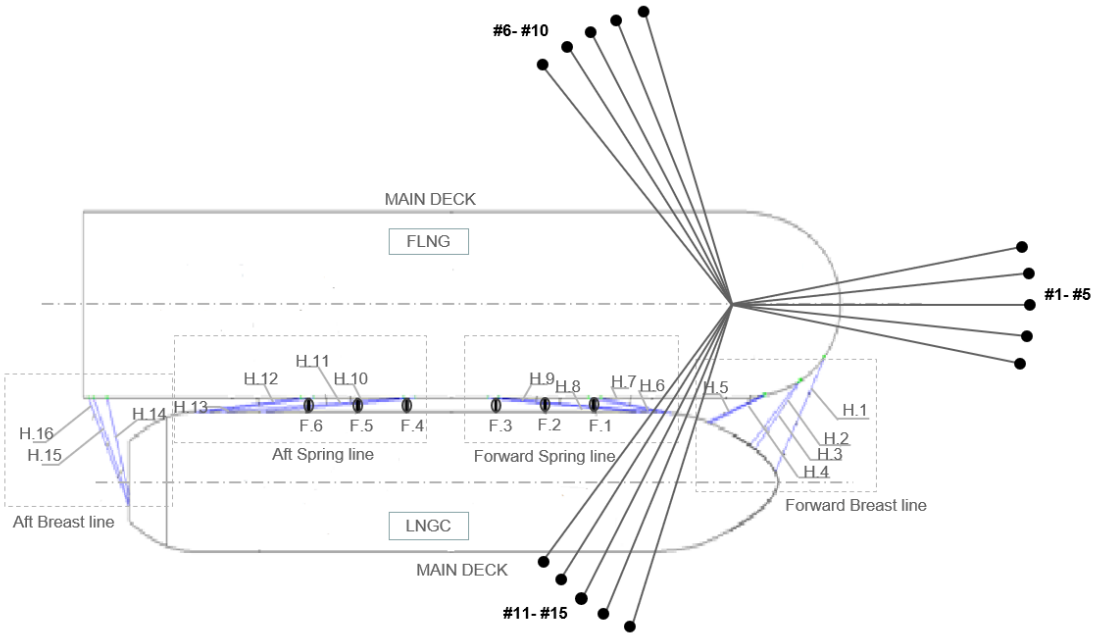

Figure 5-12 Connection system arrangement

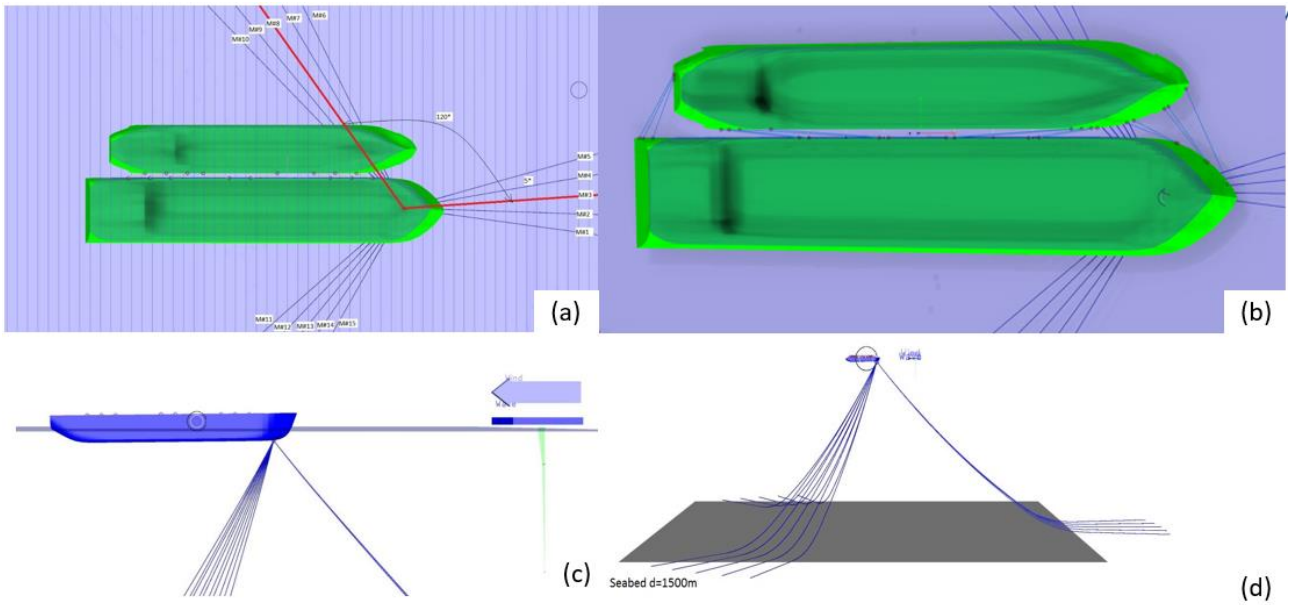

Figure 5-13 (a) Plan view of the turret mooring, (b) hawser and fender system, (c) side view with wind wave and current directions. (d) Overview of operational depth.

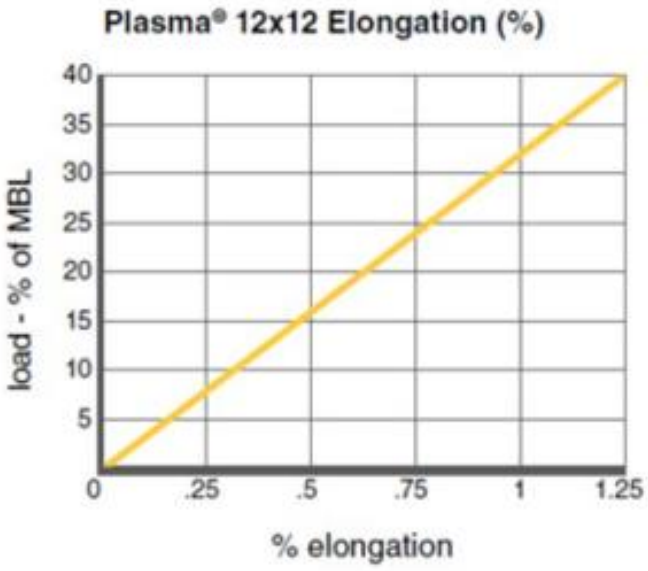

Figure 5-14 Stiffness property of hawser

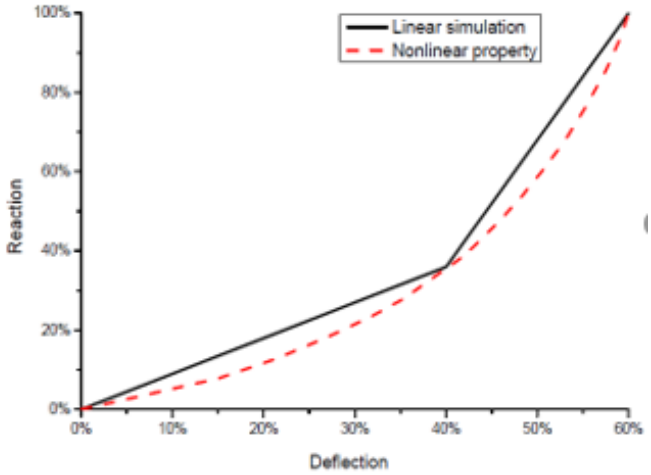

Figure 5-15 Stiffness property of Fender

Table 5-5. Configuration of hawser

Diameter (mm)	Density (kg/m^3)	MBL (kN)
72	319	3469.2

Table 5-6. Configuration of fender

Diameter (m)	Length (m)	Design deformation	Maximum reaction force (kN)
4.5	10.5	60%	5690

5.5 Test Cases

The definition of the sea condition and the three loading conditions are defined for the side-by-side offloading operation is given in Figure 5-16.

Table 5-7. Parameters of test cases

Test Cases	FLNG Filling Level	LNGC Filling Level	Sea condition	Hs (m)	Tp (s)	Wave direction (deg)	Wind Speed (m/s)	Wind direction (deg)	Current speed (m/s)	Current direction (deg)
1	100%	10%	1	2.5	8.25	180	14.1	180	0.48	180
2	100%	10%	2	2.5	8.25	135	14.1	180	0.48	180
3	50%	50%	1	2.5	8.25	180	14.1	180	0.48	180
4	50%	50%	2	2.5	8.25	135	14.1	180	0.48	180
5	10%	100%	1	2.5	8.25	180	14.1	180	0.48	180
6	10%	100%	2	2.5	8.25	135	14.1	180	0.48	180

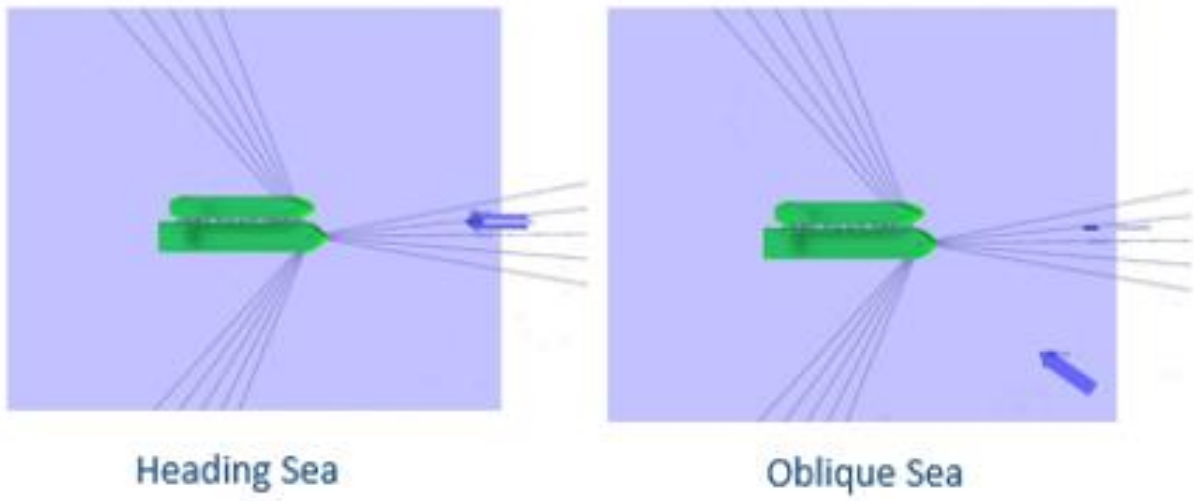

Figure 5-16. Environmental condition

5.6 Numerical Simulation results and discussions

5.6.1 First Order Forces

The principle of superposition is used to arrive at the first order RAO's for the frequency domain analysis. The loading conditions for each of the vessels are:

a) FLNG-100% b) FLNG-50% c) FLNG-10%

d) LNGC-100% e) LNGC-50% f) LNGC-10%

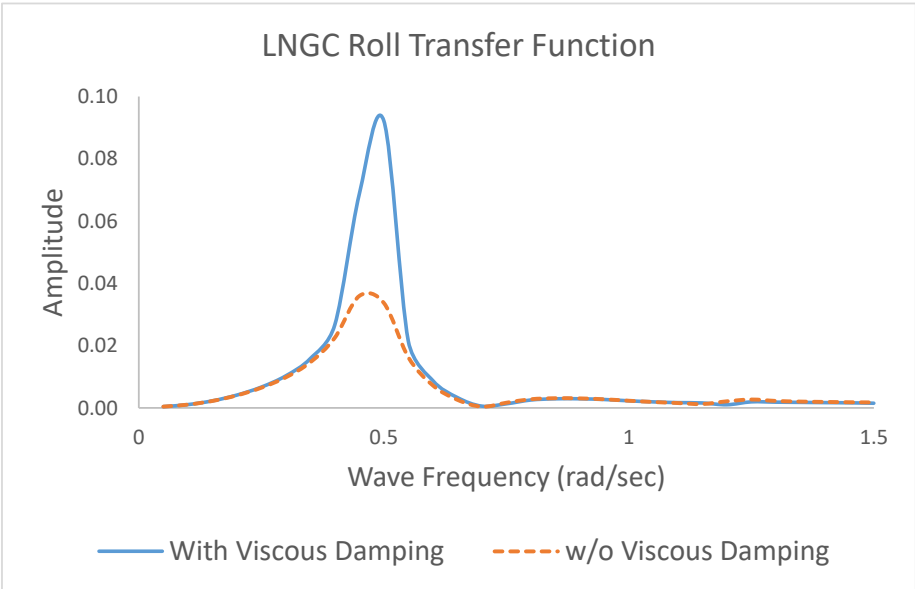

Figure 5-17 Viscous damping comparison

Potential theory is unable to directly address the issue of viscous damping. Consequently, the introduction of critical damping matrix was included. The damping term is very important in resonance amplitude. Figure 5-17 compares the roll RAO of the LNGC with viscous damping and without viscous damping. The resonance frequency at 0.48rad/sec is reduced.

In the frequency domain for multi-bodies analysis, WADAM does not take into account the viscous damping for both bodies, hence, to reduce the unrealistic motion of multibody, linear damping will be included in the time domain to reduce the unrealistic motion. However, the challenge of accurately predicting the value for linear damping should be obtained from model test.

For the single body analysis the RAO's of the FLNG and LNGC are compared and the vessel with more significant motion response is the LNGC. This can be observed from the main particulars of both vessels in Table 5-2 and Table 5-3. The FLNG is much heavier than the LNGC, therefore the LNGC has a lower inertia. Also, the geometry outlines the LNGC has a much lower block coefficient than the FLNG so the narrower vessel will experience more motion. The resonance frequency are also slightly different. The LNGC's resonance frequency is into higher frequency region compared to FLNG. For the same set of frequencies there are different transfer functions, and this will produce different motion spectrum and thus, the relative motion is evident. Observations of the heave motion shows that the RAO tends to unity at low frequency, therefore the vessel will follow the wave.

It can be observed from general plot, the motion mode, frequency, and vessel geometry dependence of the RAOs.

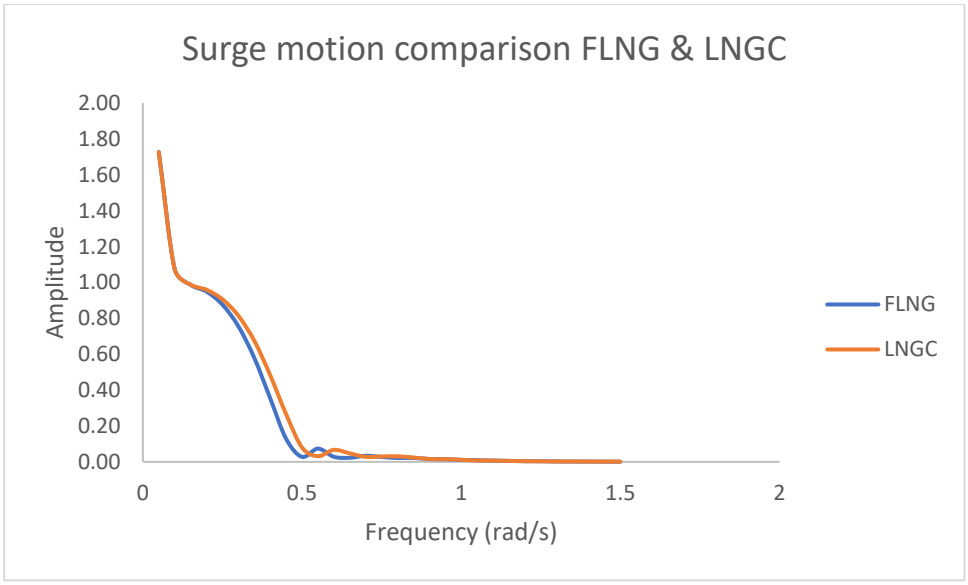
Surge motion comparison FLNG & LNGC
2.00
1.80
1.60
1.40
1.20
1.00
0.80
0.60
0.40
0.20
0.00
Amplitude
0
0.5
1
1.5
2
Frequency (rad/s)
FLNG
LNGC

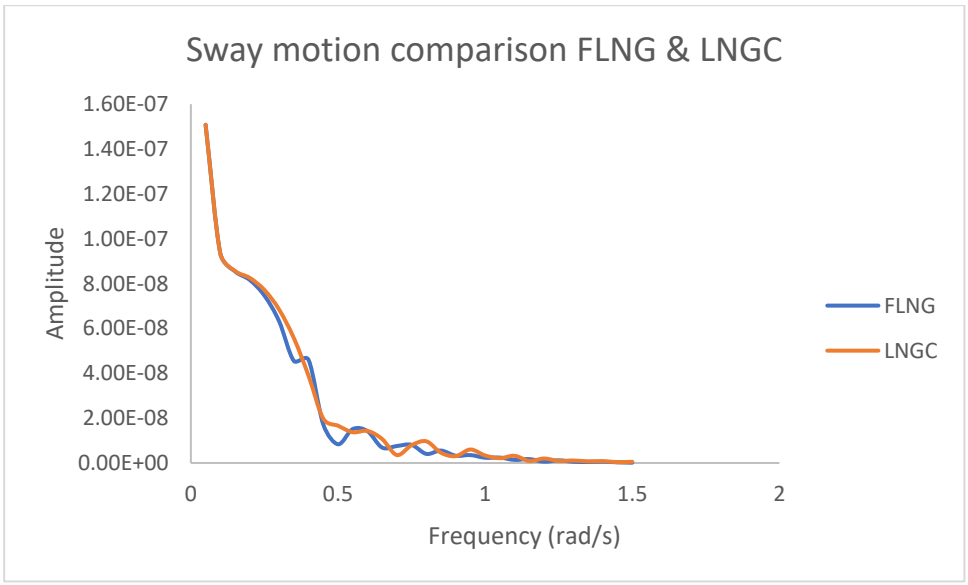
Sway motion comparison FLNG & LNGC
1.60E-07
1.40E-07
1.20E-07
1.00E-07
8.00E-08
6.00E-08
4.00E-08
2.00E-08
0.00E+00
Amplitude
0
0.5
1
1.5
2
Frequency (rad/s)
FLNG
LNGC

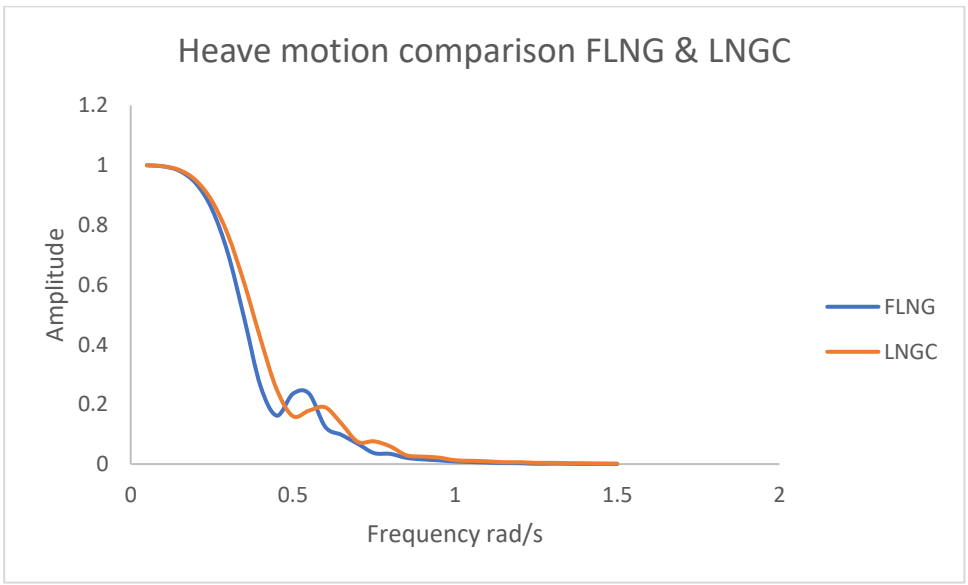
Heave motion comparison FLNG & LNGC
1.2
1
0.8
0.6
0.4
0.2
0
Amplitude
0
0.5
1
1.5
2
Frequency rad/s
FLNG
LNGC

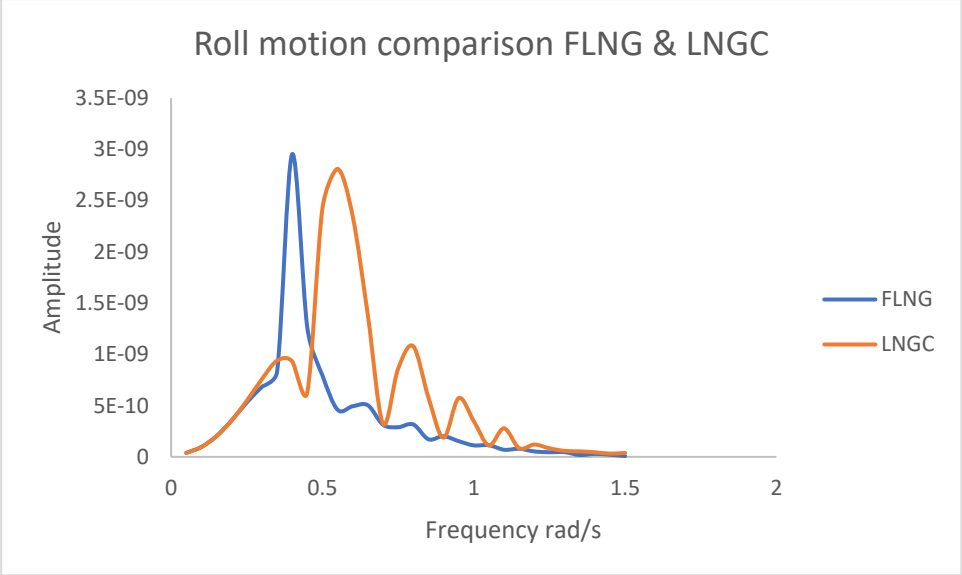

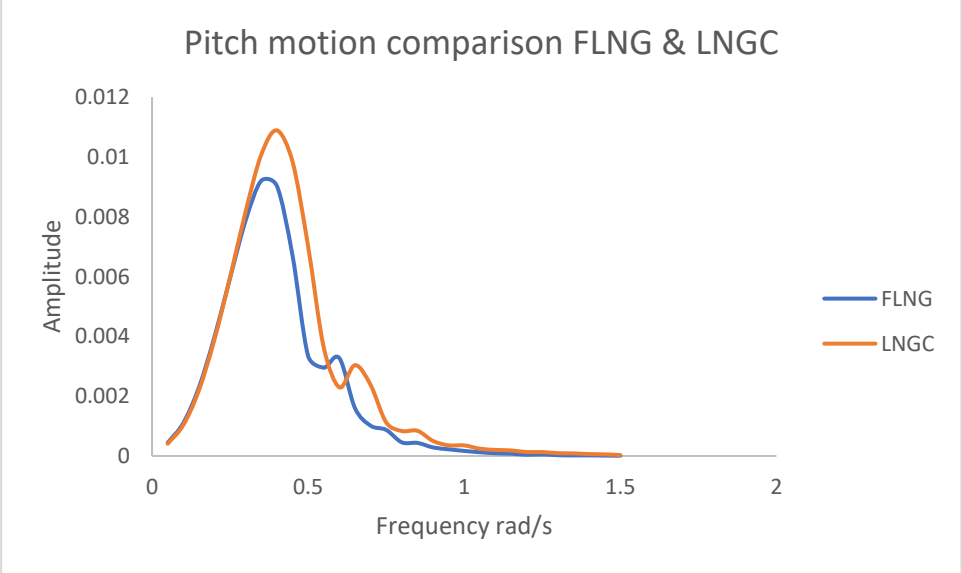

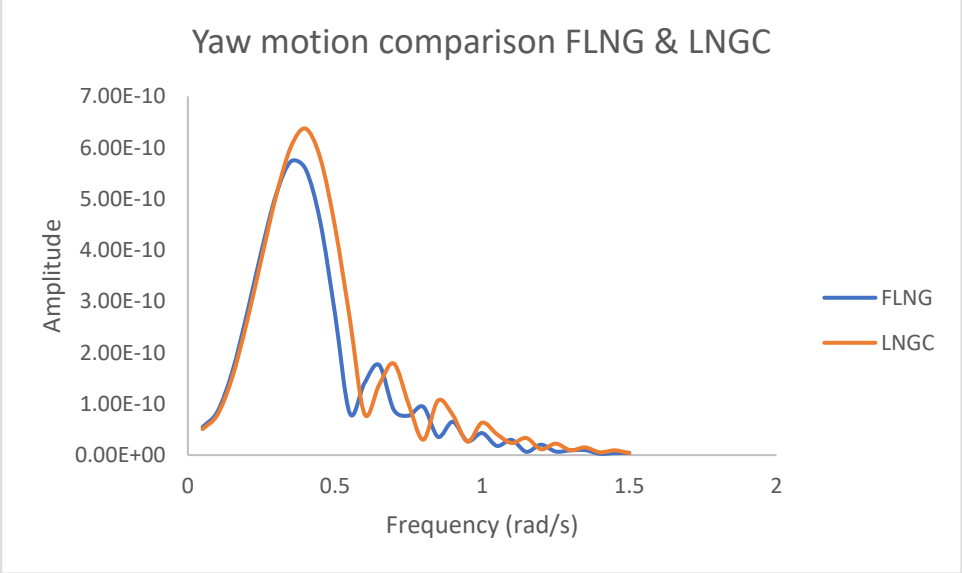

Figure 5-18 *First order RAO*

5.6.2 Second Order Forces

a) Wave Drift Forces

The wave drift force is calculated for the FLNG and LNGC is done using near field method/Pressure integration method because the current version of SIMA only allows the import from near field method. The results for the surge, sway and yaw drift motions are shown in Figure 5-19. It can be observed that the wave drift force for the FLNG is greater than that of the LNGC. The amplitude peaks show a phase shift. Due to the ability of the FLNG to make larger waves than the LNGC, the FLNG has a higher amplitude of drift motion. The reason for lower amplitude of sway drift motion is because of the wave direction in in heading sea, whilst the surge and yaw drift motions consider wave direction at 180 and 135 degree respectively, therefore the larger amplitude expected.

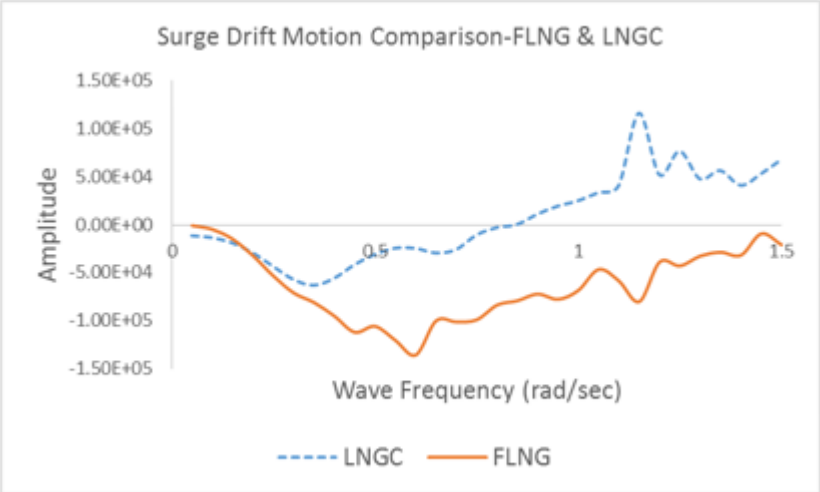

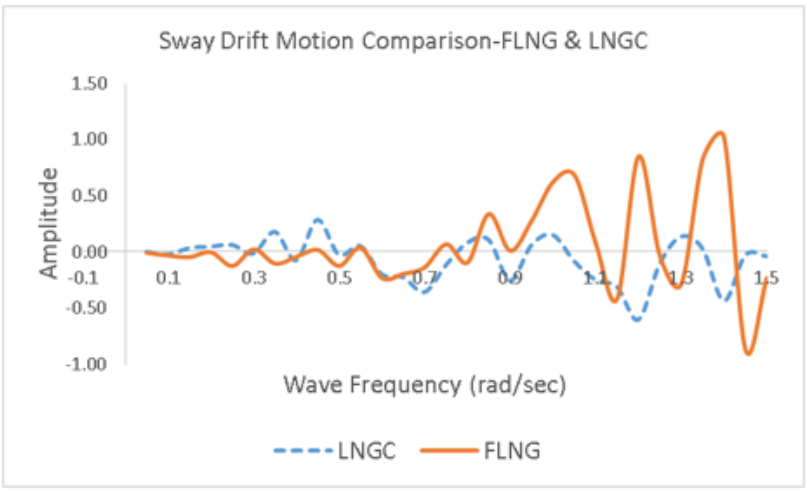

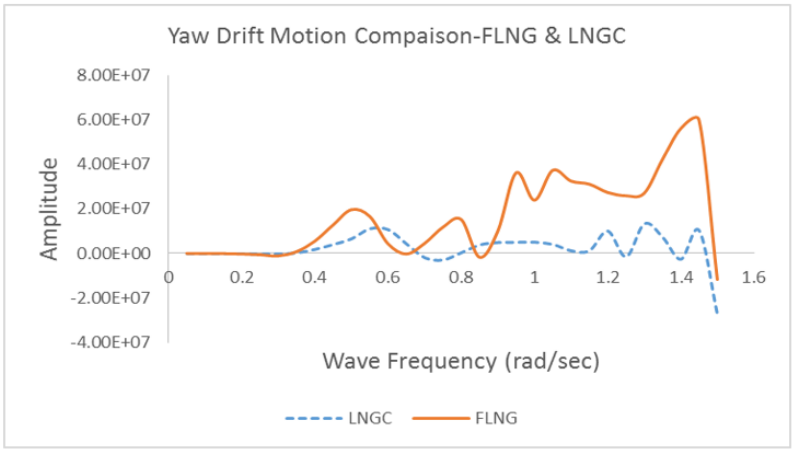

Figure 5-19 The second order wave drift motion

b) Second Order Quadratic Transfer Function (Difference Frequency)

The Newman's Approximation method is used to calculate the Quadratic transfer function. Figure 5-20 and Figure 5-21 shows the amplitude of the second order response variable for surge motion. It can be observed from the surface graph below, the amplitude which corresponds to $(\omega_1 - \omega_2)$ and $(\omega_2 - \omega_1)$ are the same, Newman's Approximation is used for the calculation. Furthermore, when the difference between ω_1 & ω_2 is very small the amplitude of the transfer function is negligible as indicated in the graph using the red arrow. As the difference in frequency increases the amplitude also increases. At the end of the diagonals the peaks can be observed at frequencies corresponding to (1.5rad/s – 0.05rad/s) and (0.05rad/s – 1.5rad/s).

From the surge second order response variable for FLNG and LNGC, observations can be made that the maximum amplitude of the FLNG is 2.5 times that of the LNGC. This is evident because the mean drift force of the FLNG is greater than that of the LNGC. Moreover, for other low frequency motions, similar results can be observed. Therefore, due to the higher displacement of the FLNG the second order difference frequency is more significant for the FLNG compared to the LNGC.

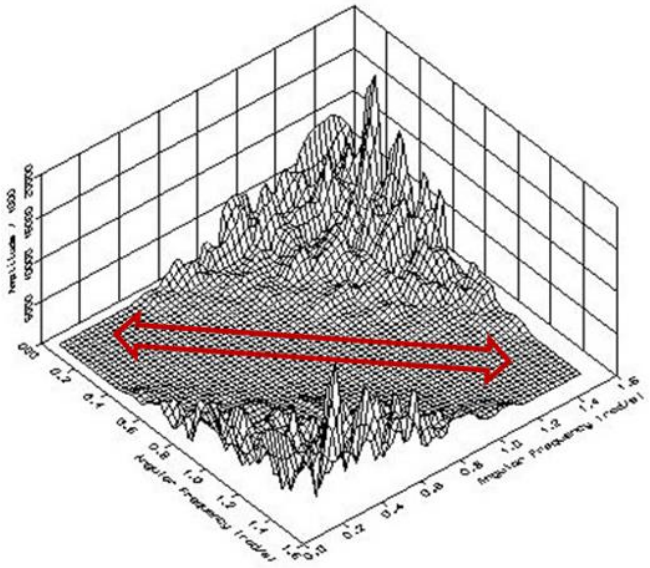

Figure 5-20 LNGC Surge QTF (difference frequency)

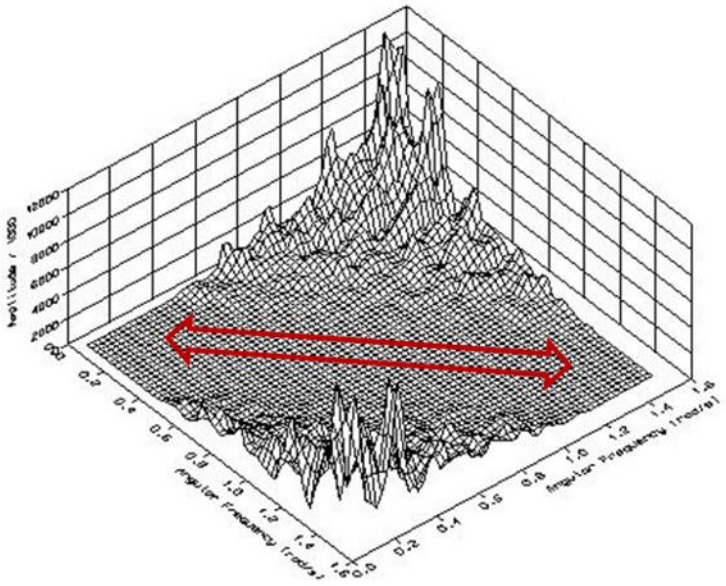

Figure 5-21 FLNG Surge QTF (difference frequency)

The Post-processing is carried out through SESAM's statistical analysis tool POSTRESP to present RAO's, potential damping, hydrostatic stiffness, added mass, wave drift force and QTF for difference frequency.

5.6.3 Multibody Analysis

Multibody analysis is conducted for a combination of the following loading conditions

1) FLNG 100%, LNGC 10 %
2) FLNG 50%, LNGC 50 %
3) FLNG 10%, LNGC 100 %

The frequency domain the multibody analysis is carried out for the FLNG and LNGC without the mechanical connecting system to include the hydrodynamic coupling. A comparison of the hydrodynamic loads and coefficient for the multibody and single body results was carried out to demonstrate the hydrodynamic interaction when two vessels are in close proximity.

A comparison of the multi-body analysis results with the single body analysis results is plotted in Figure 5-22 below. It shows the hydrodynamic interaction for heave, surge and sway drift motion. For the heading sea there is no amplitude for the single body FLNG and LNGC due to the symmetry of the vessels, but for the multibody analysis there is the presence of sway drift motion due to the multibody interaction in the small gap. Furthermore, there is more hydrodynamic interaction for the surge drift transfer function where peaks are observed at 0.95rad/sec and 1.18rad/sec. Additional gap analysis will be carried out in the frequency domain to study the relationship between the hydrodynamic interaction and gap width.

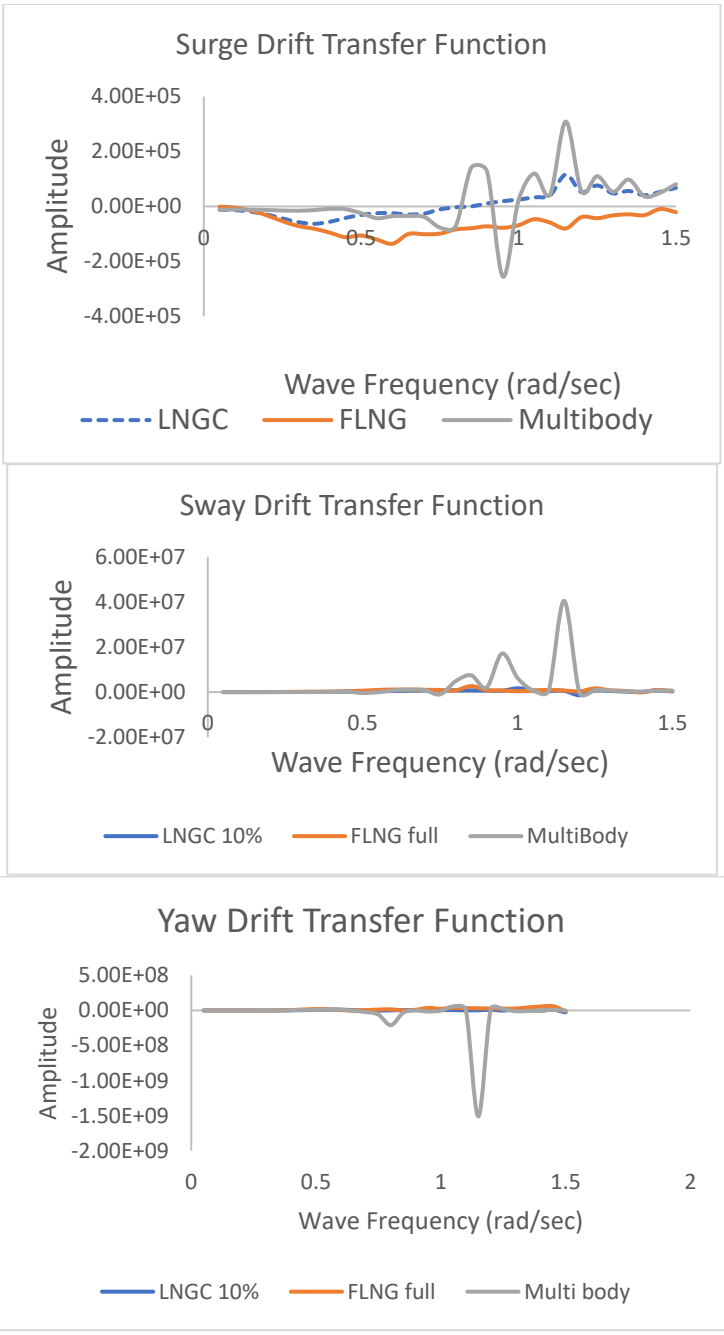

Figure 5-22 Hydrodynamic interaction

To further analyse the hydrodynamic interaction the frequency dependent hydrodynamic coefficients such as potential damping and added mass matrix is shown in Figure 5-23. The frequency dependent added mass, and potential damping is observed to be negative in case of multibody interaction at a resonance frequency of 0.75 rad/sec. The added mass is the capacity of a structure to accelerate the associated water. Notwithstanding, a negative added mass suggest that the motion of

one body affects the other body. Additionally, Faltinsen (1990)stated that the negative added mass relates to the wave elevation between hulls.

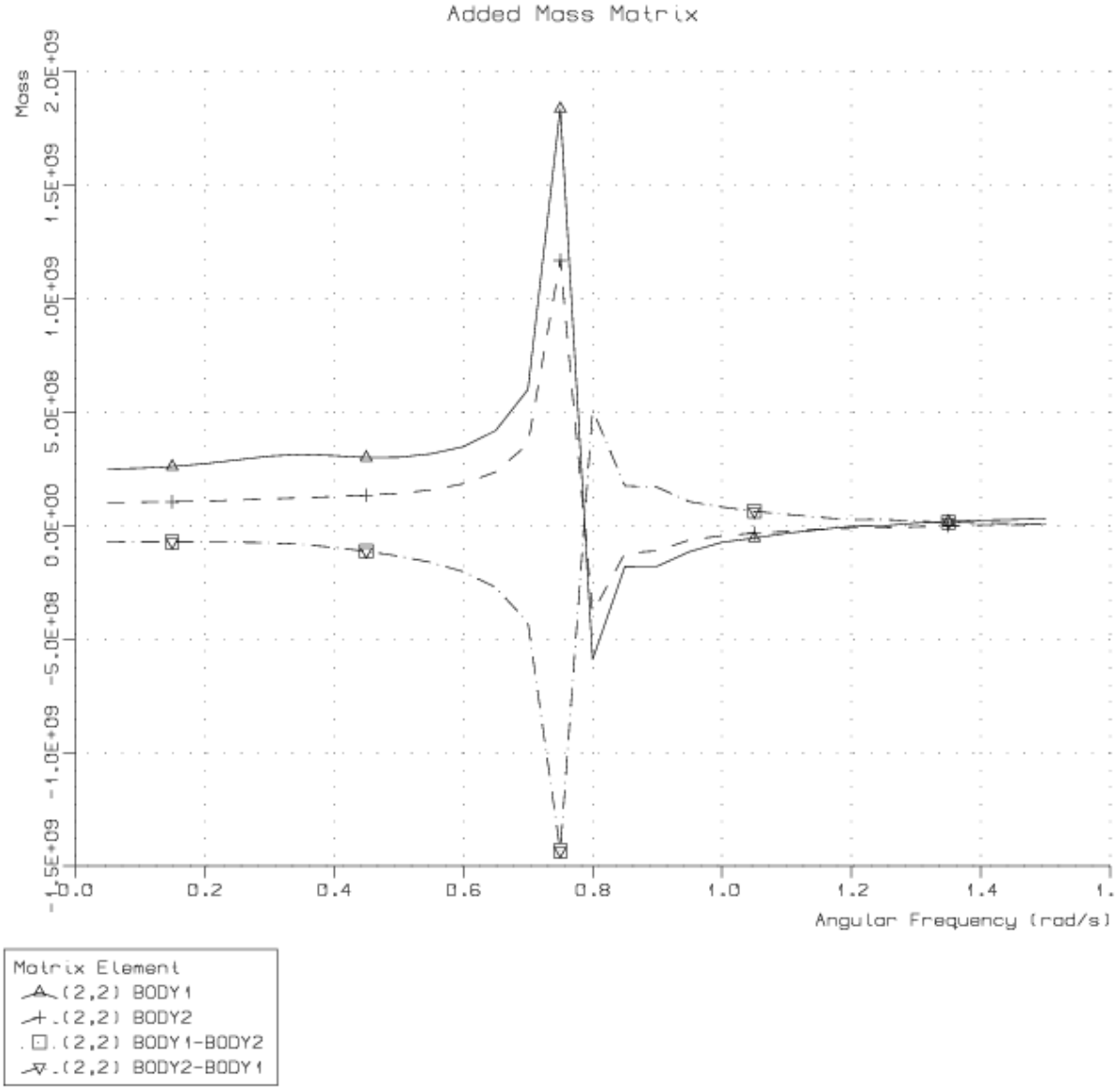

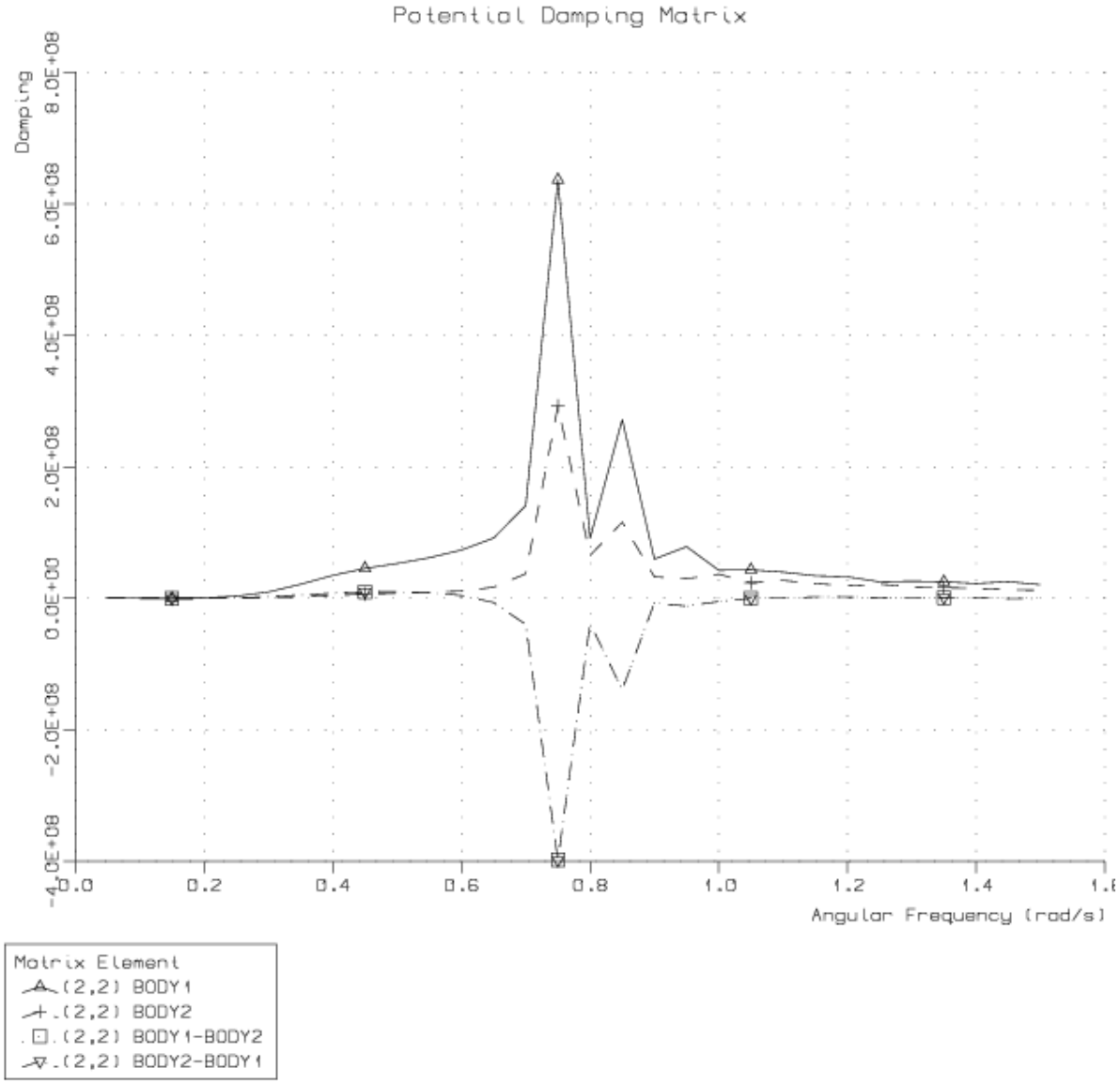

Figure 5-23 Hydrodynamic Coefficients (Added Mass and Potential damping)

5.6.4 Global Motion

The coupled retardation function is evaluated using impulse theory to include memory effect of fluid. The hydrostatic stiffness obtained in the frequency domain analysis comprises of the coupling between the wave frequency and low frequency motion. A sensitivity analysis for the linear damping is calculated from the frequency domain is and also compared with experimental study conducted by Zhao et al. (2014) on FLNG-LNGC system.

Table 5-8 Linear damping FLNG

Surge KN s/m	Sway KN.s/m	Heave KN.s/m	Roll KN.s.m	Pitch KN.s.m	Yaw KN.s.m
1.59E+03	2.43E+03	2.19E+04	3.92E+05	5.73E+09	6.00E06

Table 5-9 Linear Damping LNGC

Surge KN s/m	Sway KN.s/m	Heave KN.s/m	Roll KN.s.m	Pitch KN.s.m	Yaw KN.s.m
1.29E+03	2.27E+03	1.69E+04	3.02E+05	3.73E+09	7.00E06

The FLNG and LNGC global motion in the six degrees of freedom are predicted in the time domain analysis, the results are given in the plots and tables. The offloading arm distance are maintained, and the coupled vessel motion is observed to be realistic with the vessel sway and yaw motion following each other during the simulation duration. There is a stable oscillatory wave frequency motion for the roll, pitch, and heave due to the hydrostatic restoring forces involved. A statistical analysis has been done to obtain the time series, and statistical parameters listed in Table 5-10

It can be observed from Figure 5-24 that the LNGC displays a larger motion response compared to the FLNG, particularly the surge, heave, roll and pitch motions. This can be attributed to the general parameters of the LNGC which is much smaller than those of the FLNG vessel. As observed in Figure 5-24 the surge motion of the LNGC is slightly larger than the FLNG vessel. The roll response motion of the FLNG is smaller than that of the LNGC it can be negligible. This observation can be explained through the fact that the geometry of the FLNG is rectangular in shape, which induces a large added mass in waves. Also, the FLNG vessel mass is large than the LNGC.

Static Calculation: The static calculation analyses the initial equilibrium of the whole system without the effect of environmental forces. It is used to check the pretensions on the hawsers and mooring lines.

Dynamic Calculation: The dynamic analysis calculates the equation of motion in the time domain with effect of environmental forces taken into consideration. The realisation of ocean is obtained by using 5 wave seed number and the spectrum is done through the Fast Fourier Transformation (FFT).

Table 5-10 Mean Global motion for the FLNG and LNGC (Test Case 1)

Motion	Max Amplitude	Test Case No
Mean Surge_FLNG [m]	-18.209	4
Mean Sway_FLNG [m]	1.083	3
Mean Yaw_FLNG [m]	-3.3799	3
Mean Surge_LNGC [m]	-16.839	4
Mean Sway_LNGC [m]	1.4622	3
Mean Yaw_LNGC [m]	-3.4362	3

Global Motion FLNG and LNGC (Test case 1)

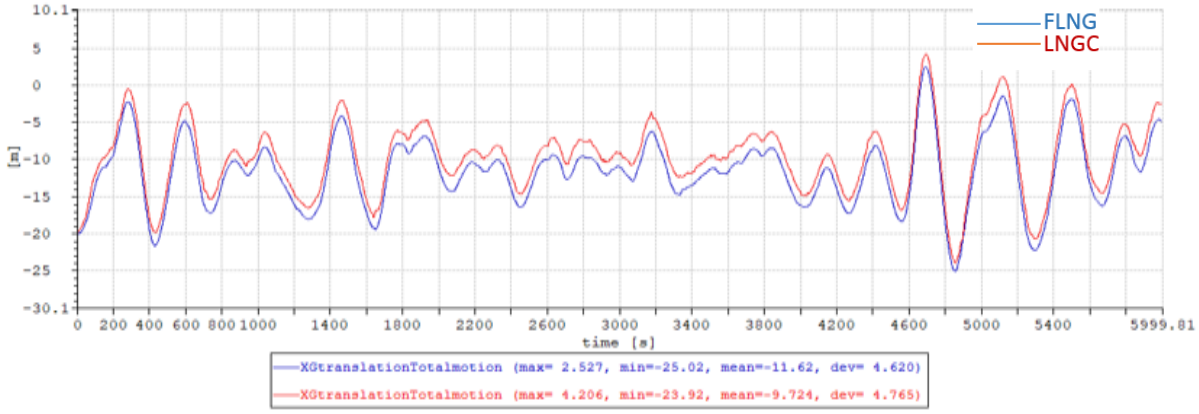

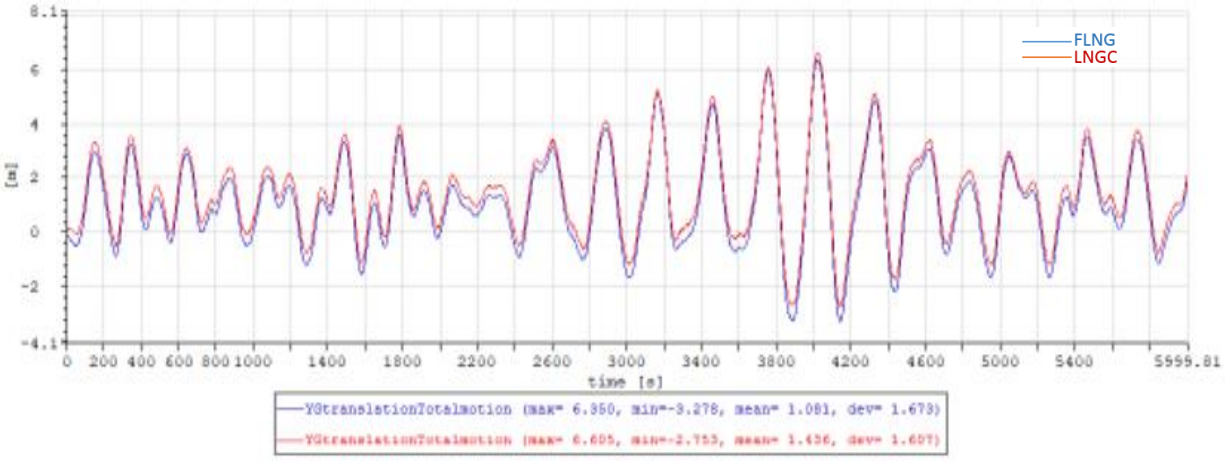

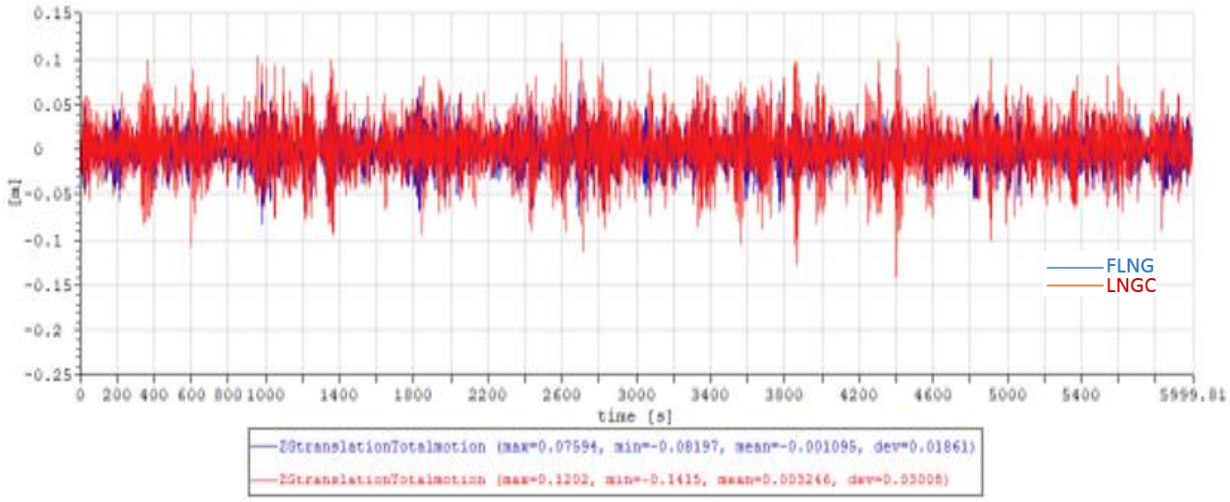
[m]
time [s]
FLNG
LNGC
ZGtranslationTotalmotion (max=0.07594, min=-0.08197, mean=-0.001095, dev=0.01861)
ZGtranslationTotalmotion (max=0.1202, min=-0.1415, mean=0.003246, dev=0.03008)

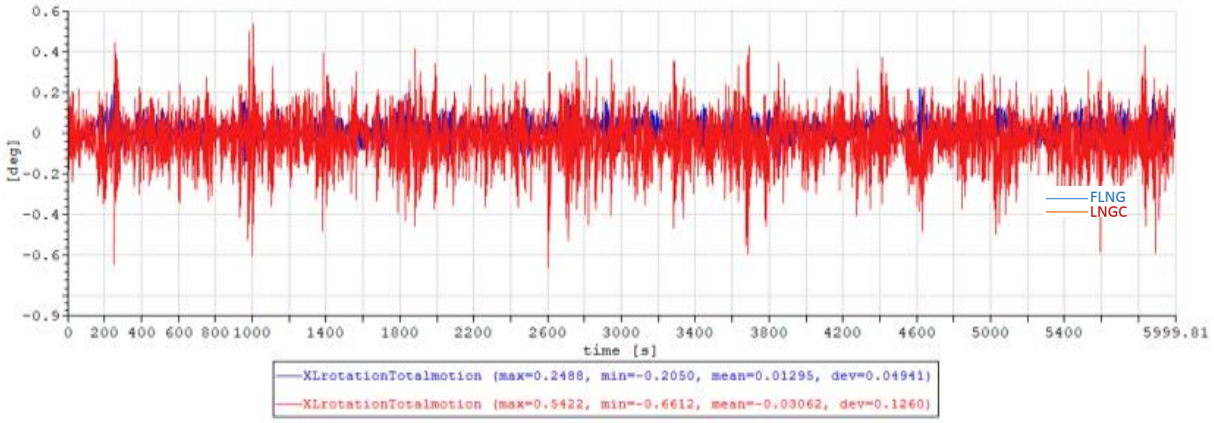
[deg]
time [s]
FLNG
LNGC
XLrotationTotalmotion (max=0.2488, min=-0.2050, mean=0.01295, dev=0.04941)
XLrotationTotalmotion (max=0.5422, min=-0.6612, mean=-0.03062, dev=0.1260)

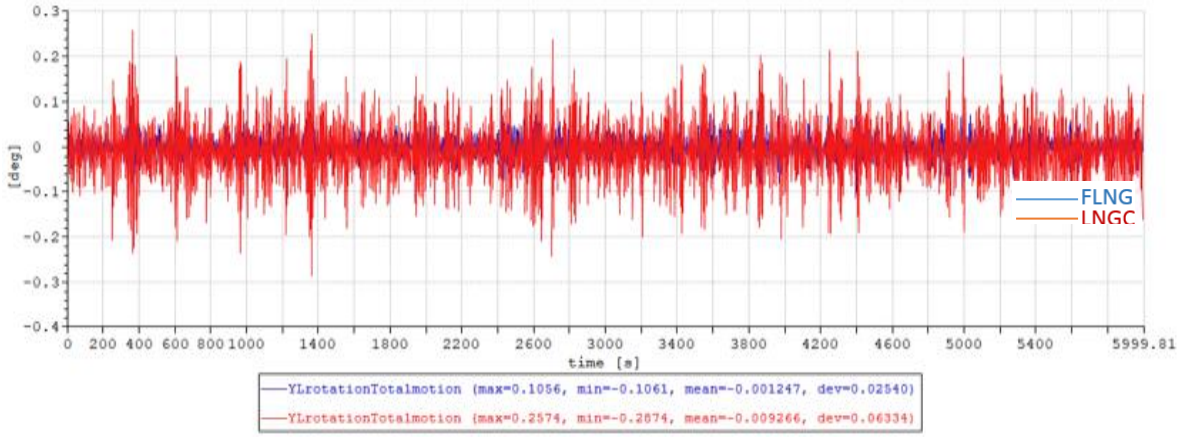
[deg]
time [s]
FLNG
LNGC
YLrotationTotalmotion (max=0.1056, min=-0.1061, mean=-0.001247, dev=0.02540)
YLrotationTotalmotion (max=0.2574, min=-0.2674, mean=-0.009266, dev=0.06334)

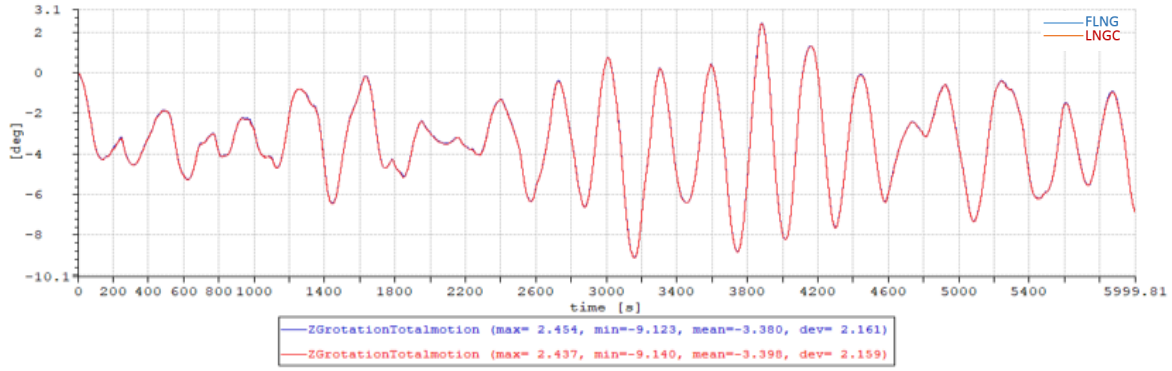

Figure 5-24 Global motion for FLNG and LNGC (Test Case 1)

The FLNG global acceleration is specifically important to the design of the sea fastening for the heave topside. The maximum roll for the FLNG is found to be 0.2 deg. A more detailed comparison of the FLNG and LNGC motions is shown in Figure 5-25. The three scenarios for the different environmental conditions are displayed in Figure 5-16 and the test cases are in Table 5-7.

Test Case 4 is observed to have the maximum mean surge motion for the FLNG and LNGC as the wind and current in heading sea and wave in oblique sea. In test case 4 the FLNG has the least displacement with only 10% loaded. However, the maximum mean sway motion of 1.4622m found for test case 3 that has a 50% loaded capacity condition for the FLNG and LNGC. For both test case 3 and 4 the wind and current are in heading sea while the wave is in oblique sea. The maximum mean yaw motion is also observed at test case 3. These motions may be due to the unsymmetrical multibody, the environmental loading due to the directional of the propagating wave which can cause the vessels to weathervane and the loading conditions, with the FLNG having the lowest loaded capacity in test case 4 and a 50% capacity in test case3.

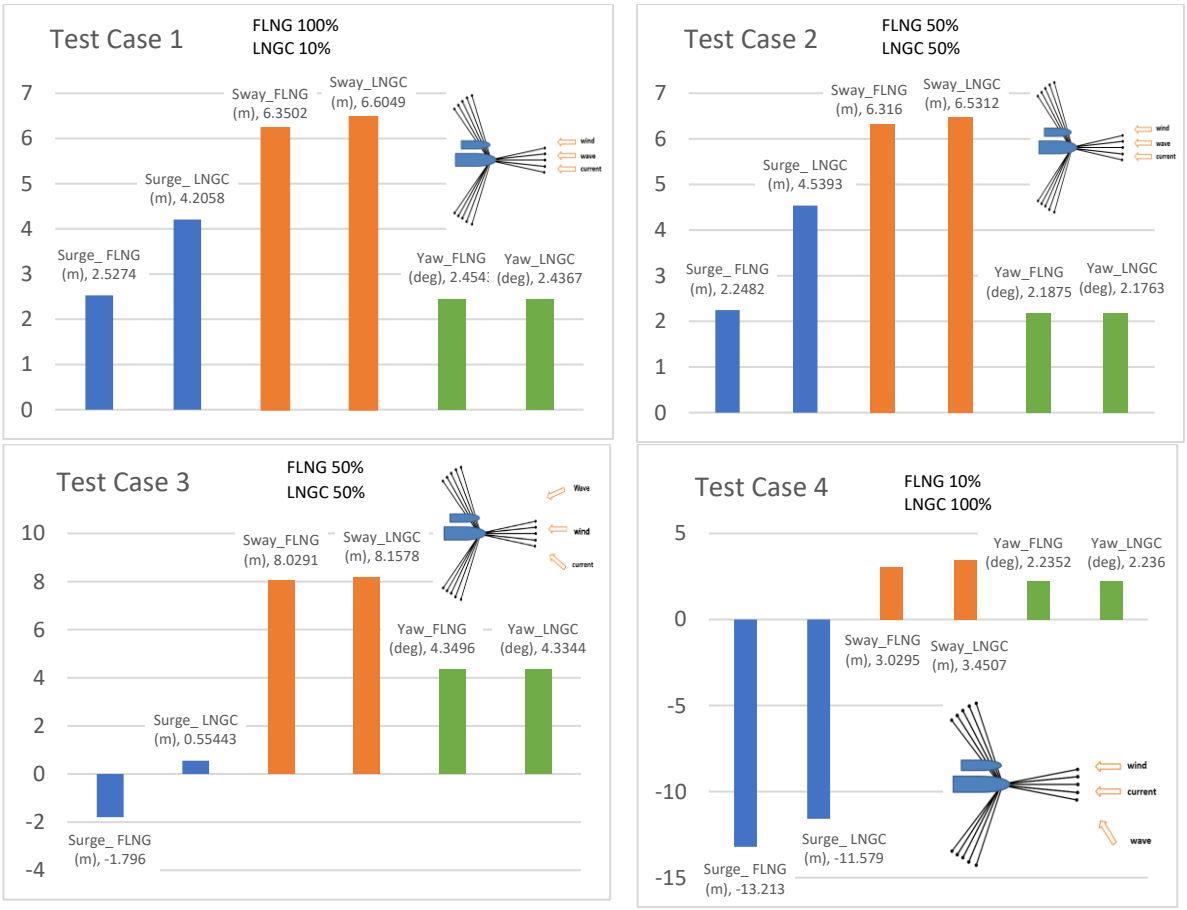

Figure 5-25. Comparison of Low frequency motion for FLNG and LNGC

Table 5-11. Global Motion FLNG and LNGC case 1

	Max.	Min.	Mean	Standard deviation
Surge_ FLNG (m)	2.52	-25.01	-11.61	4.61
Surge_ LNGC (m)	4.20	-23.91	-9.72	4.76
Sway_FLNG (m)	6.35	-3.27	1.08	1.67
Sway_LNGC (m)	6.60	-2.75	1.43	1.60
Heave_FLNG (m)	0.075	-0.08	-0.01	0.018
Heave_LNGC (m)	0.12	-0.14	0.003	0.03
Roll_FLNG (deg)	0.24	-0.20	0.012	0.04
Roll_LNGC (deg)	0.54	-0.66	-0.03	0.12
Pitch_FLNG (deg)	0.10	-0.10	-0.001	0.02
Pitch_LNGC (deg)	0.25	-0.28	-0.009	0.06
Yaw_FLNG (deg)	2.45	-9.12	-3.379	2.16
Yaw_LNGC (deg)	2.43	-9.14	-3.398	2.15

Table 5-12. Global Motion FLNG and LNGC case 2

	Max.	Min.	Mean	Standard deviation
Surge_ FLNG (m)	2.24	-23.45	-11.62	4.420
Surge_ LNGC (m)	4.53	-22.21	-9.79	4.562
Sway_FLNG (m)	6.31	-3.94	1.06	1.776
Sway_LNGC (m)	6.53	-3.41	1.42	1.707
Heave_FLNG (m)	0.06	-0.067	-0.001	0.017
Heave_LNGC (m)	0.15	-0.11	0.003	0.029
Roll_FLNG (deg)	0.21	-0.17	0.012	0.045
Roll_LNGC (deg)	0.46	-0.64	-0.03	0.119
Pitch_FLNG (deg)	0.12	-0.13	-0.001	0.028
Pitch_LNGC (deg)	0.30	-0.33	-0.009	0.069
Yaw_FLNG (deg)	2.18	-9.23	-3.362	2.311
Yaw_LNGC (deg)	2.17	-9.24	-3.379	2.307

Table 5-13. Global Motion FLNG and LNGC case 3

	Max.	Min.	Mean	Standard deviation
Surge_ FLNG (m)	-1.79	-21.63	-12.67	3.556
Surge_ LNGC (m)	0.55	-20.39	-10.87	3.634
Sway_FLNG (m)	8.029	-5.17	1.083	2.439
Sway_LNGC (m)	8.15	-4.51	1.462	2.342
Heave_FLNG (m)	0.083	-0.094	-0.001	0.024
Heave_LNGC (m)	0.16	-0.15	0.003	0.038
Roll_FLNG (deg)	0.35	-0.29	0.015	0.085
Roll_LNGC (deg)	0.81	-0.96	-0.029	0.175
Pitch_FLNG (deg)	0.14	-0.13	-0.001	0.035
Pitch_LNGC (deg)	0.32	-0.35	-0.015	0.086
Yaw_FLNG (deg)	4.34	-10.99	-3.418	2.952
Yaw_LNGC (deg)	4.33	-11.007	-3.436	2.948

Table 5-14. Global Motion FLNG and LNGC case 4

	Max.	Min.	Mean	Standard deviation
Surge_ FLNG (m)	-13.21	-22.55	-18.20	1.53
Surge_ LNGC (m)	-11.57	-21.56	-16.83	1.64
Sway_FLNG (m)	3.02	-2.11	0.139	0.93
Sway_LNGC (m)	3.45	-1.58	0.615	0.91
Heave_FLNG (m)	0.07	-0.07	-0.001	0.02
Heave_LNGC (m)	0.12	-0.13	0.001	0.023
Roll_FLNG (deg)	0.32	-0.32	-0.011	0.089
Roll_LNGC (deg)	0.43	-0.40	0.015	0.14
Pitch_FLNG (deg)	0.16	-0.17	-0.002	0.04
Pitch_LNGC (deg)	0.28	-0.30	0.001	0.06
Yaw_FLNG (deg)	2.23	-2.77	-0.35	1.01
Yaw_LNGC (deg)	2.23	-2.78	-0.35	1.01

5.6.5 Comparative Analysis

A comparative analysis is conducted for the six degrees of motion for the FLNG-LNGC system. Comparison investigation for the numerical analysis with experimental results show a good relationship with wave frequency motion but not a good relationship with low-frequency motion. As seen in Figure 5-24 the surge, sway and yaw motions are dominated by low frequency component while the heave, roll and pitch are dominated motions are dominated by wave frequency component.

Table 5-15 Comparative Analysis (Test Case 4)

	Max.	Min.	Mean	Standard deviation
Surge_ FLNG (m)				
Experiment	-20.59	-27.09	-23.73	1.62
Simulation	-13.21	-22.55	-18.20	1.53
Sway_FLNG (m)				
Experiment	3.30	-4.72	0.67	2.21
Simulation	3.02	-2.11	0.139	0.93
Heave_FLNG (m)				
Experiment	0.14	-0.15	0.00	0.05
Simulation	0.07	-0.07	-0.001	0.02
Roll_FLNG (deg)				
Experiment	0.14	-0.09	0.02	0.03
Simulation	0.32	-0.32	-0.011	0.089
Pitch_FLNG (deg)				
Experiment	0.09	-0.09	-0.01	0.03
Simulation	2.23	-2.77	-0.35	1.01
Yaw_FLNG (deg)				
Experiment	1.45	-1.87	-0.17	0.94
Simulation	0.16	-0.17	-0.002	0.04
Surge_ LNGC (m)				
Experiment	-20.30	-31.07	-24.73	1.62
Simulation	-11.57	-21.56	-16.83	1.64
Sway_LNGC (m)				
Experiment	3.44	-8.35	-2.76	2.44
Simulation	3.45	-1.58	0.615	0.91
Heave_LNGC (m)				
Experiment	0.38	-0.38	0.00	0.05
Simulation	0.12	-0.13	0.001	0.023
Roll_LNGC (deg)				
Experiment	0.54	-0.48	0.05	0.15
Simulation	0.43	-0.40	0.015	0.14
Pitch_LNGC (deg)				

Experiment	0.43	-0.34	0.01	0.11
Simulation	0.28	-0.30	0.001	0.06
Yaw_LNGC (deg)				
Experiment	1.96	-2.39	-0.22	1.03
Simulation	2.23	-2.78	-0.35	1.01

The low-frequency motion is plotted for the surge, sway and yaw motions in Figure 5-26 obtained through simulation and experimental data in (Jin et al., 2019). As can be seen in Figure 5-26, the sway good agreement with the experimental data for the FLNG while the sway and yaw show good agreement for the LNGC. From the graph below, the FLNG numerical model underpredicts the surge and yaw motions while the LNGC numerical model underpredicts the surge motion. The variations is this study is due to a type of equivalent linearization of the damping, whilst much of the damping is nonlinear in nature. This could explain the discrepancy of the results between the experiment and simulation.

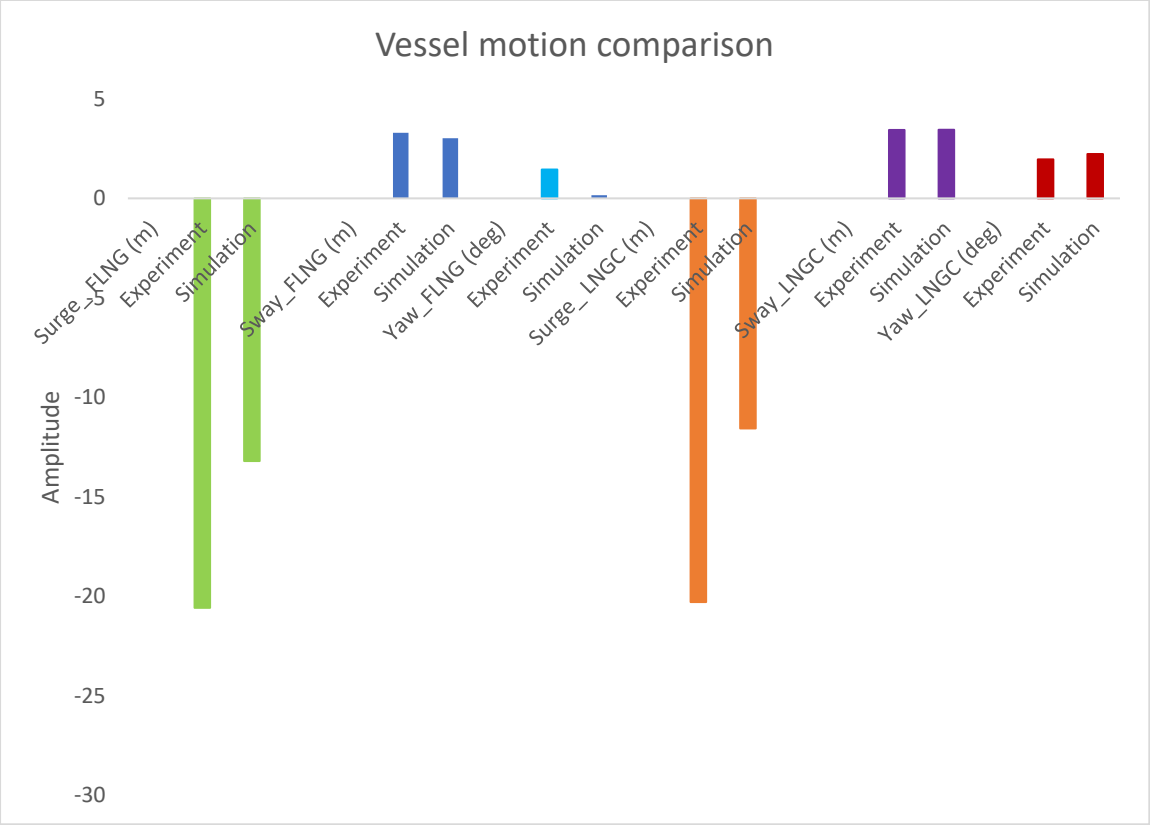

Figure 5-26 Comparison of literature and simulation results

5.6.6 Mooring Analysis

Mooring Loads Test case 1

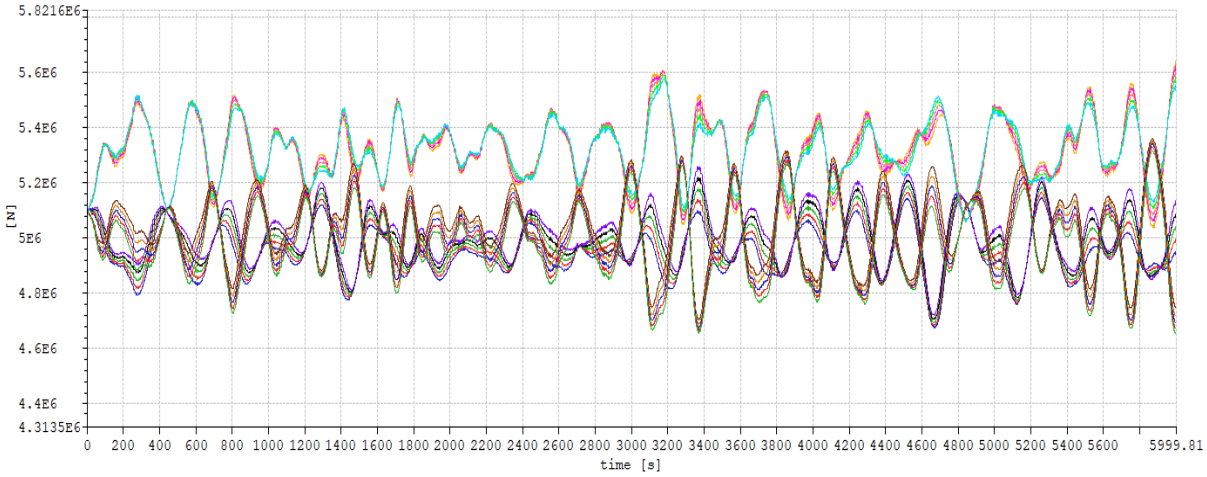

Mooring Loads Test case 2

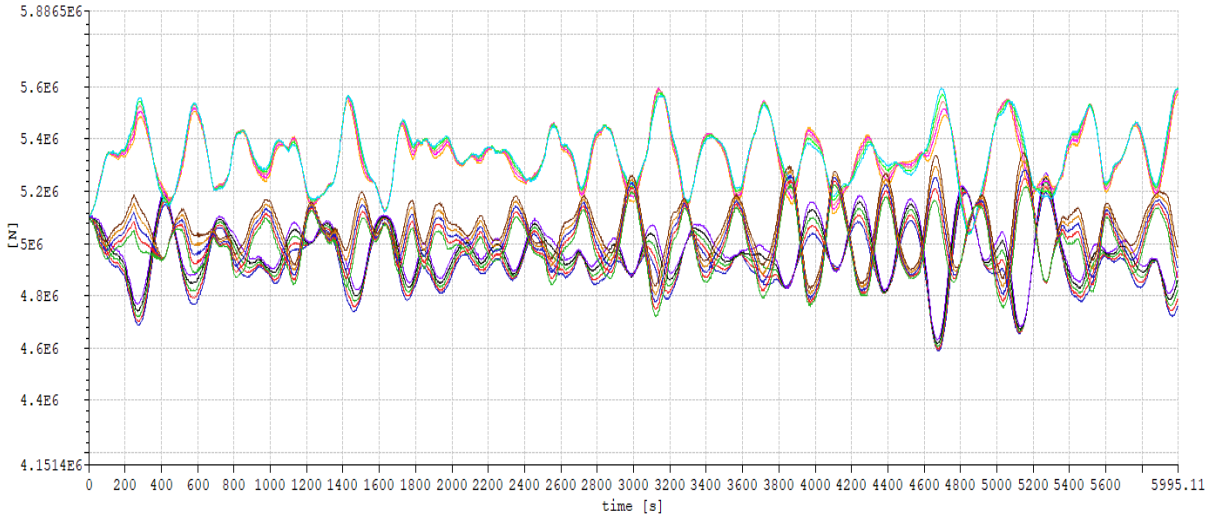

Mooring Loads Test case 3

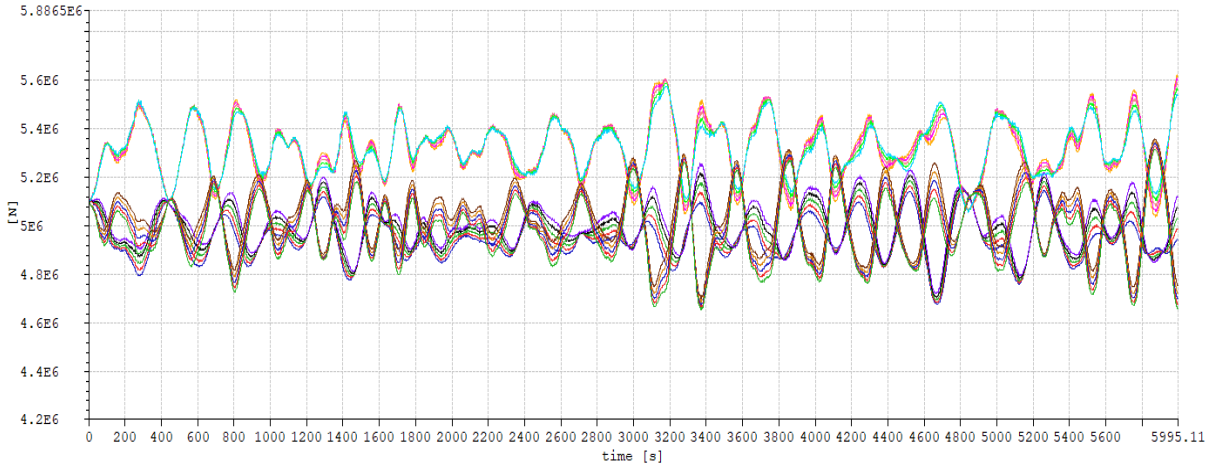

Mooring Loads Test case 4

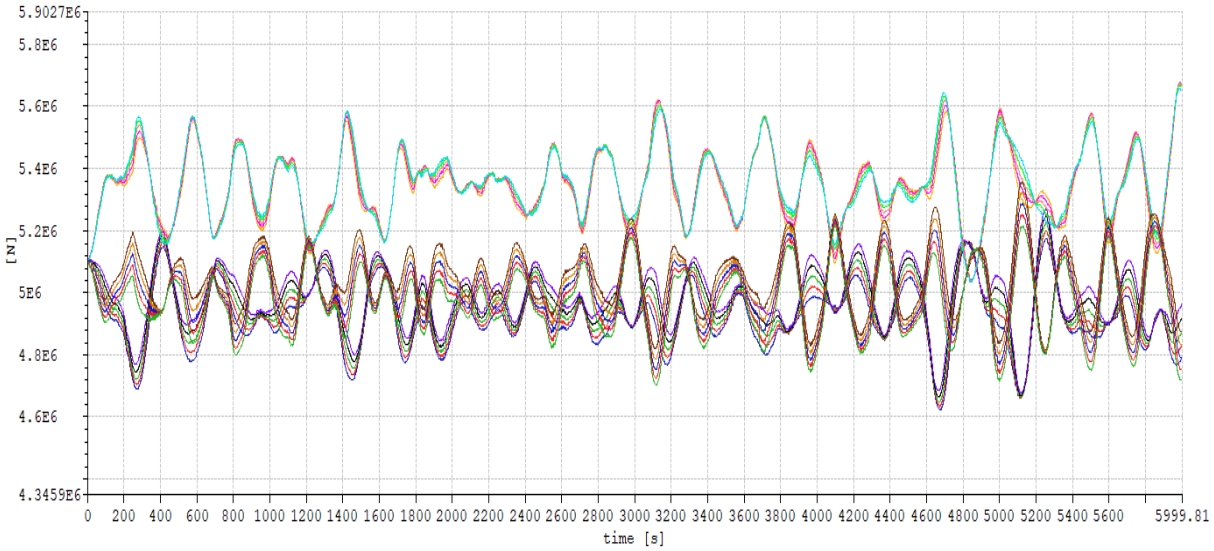

Figure 5-27. Mooring Loads

Table 5-16. Mooring Loads Case 1

	Maximum	Minimum	Mean	Standard Deviation
MooringLine1	524.64	458.2	491.7	11.04
MooringLine2	525.72	459.11	493.06	11.01
MooringLine3	526.69	460.36	494.56	10.96
MooringLine4	527.53	461.94	496.18	10.89
MooringLine5	528.24	463.83	497.91	10.80
MooringLine6	559.71	509.32	532.28	10.28
MooringLine7	561.24	509.48	532.94	10.43
MooringLine8	562.33	509.38	533.43	10.59
MooringLine9	562.98	508.07	533.74	10.74
MooringLine10	563.34	506.5	533.87	10.88
MooringLine11	534.85	478.46	506.36	9.84
MooringLine12	533.18	476.87	504.33	9.75
MooringLine13	531.33	475.53	502.34	9.68
MooringLine14	529.31	474.45	500.41	9.63
MooringLine15	527.16	473.64	498.56	9.61

Table 5-17. Mooring Loads Case 2 (tons)

	Maximum	Minimum	Mean	Standard Deviation
MooringLine1	519.73	458.88	491.75	10.44
MooringLine2	521.72	459.56	493.11	10.39
MooringLine3	523.63	460.43	494.61	10.33
MooringLine4	525.43	461.63	496.22	10.28
MooringLine5	527.12	463.15	497.94	10.23
MooringLine6	559.37	505.01	532.2	10.63
MooringLine7	559.22	504.52	532.86	10.69
MooringLine8	559.1	504.07	533.34	10.75
MooringLine9	559.28	503.65	533.65	10.79
MooringLine10	559.38	503.29	533.78	10.83
MooringLine11	534.63	482.52	506.4	9.98
MooringLine12	531.56	480.54	504.37	9.99
MooringLine13	528.33	477.53	502.39	10.01
MooringLine14	524.97	474.75	500.47	10.04
MooringLine15	522.58	472.29	498.62	10.09

Table 5-18. Mooring Loads Case 3

	Maximum	Minimum	Mean	Standard Deviation
MooringLine1	514.61	467.59	494.55	8.52
MooringLine2	516.55	468.31	495.98	8.68
MooringLine3	518.74	469.28	497.51	8.92
MooringLine4	521.93	470.5	499.14	9.23
MooringLine5	525.8	471.98	500.86	9.59
MooringLine6	563.96	503.59	531.47	11.86
MooringLine7	562.51	505.85	531.87	11.47
MooringLine8	560.61	505.76	532.11	11.05
MooringLine9	559.02	505.69	532.17	10.62
MooringLine10	557.65	505.66	532.08	10.19
MooringLine11	535.91	470.09	504.28	12.57
MooringLine12	535.11	468.48	502.44	12.81
MooringLine13	534.11	467.13	500.67	12.98
MooringLine14	532.93	466.05	498.97	13.10
MooringLine15	531.59	465.26	497.35	13.16

Table 5-19. Mooring Loads Case 4

	Maximum	Minimum	Mean	Standard Deviation
MooringLine1	517.76	492.29	505.86	3.90
MooringLine2	518.18	491.5	505.97	4.00
MooringLine3	518.54	490.86	506.12	4.10
MooringLine4	518.84	490.36	506.3	4.20
MooringLine5	519.07	490	506.5	4.29
MooringLine6	523.79	501.65	513.19	3.79
MooringLine7	523.69	502	513.45	3.71
MooringLine8	523.48	502.41	513.69	3.64
MooringLine9	523.18	502.88	513.89	3.58
MooringLine10	523.38	503.4	514.07	3.54
MooringLine11	527.39	499.49	511.24	4.68
MooringLine12	526.42	499.29	510.87	4.66
MooringLine13	525.33	499.17	510.49	4.63
MooringLine14	524.12	499.13	510.11	4.59
MooringLine15	522.8	499.14	509.73	4.53

A statistical table describing the maximum, minimum and mean load of the mooring line loads for test cases 1, case 2, case 3 and case 4 are shown in Table 5-16,Table 5-17, Table 5-18 and

Table 5-19respectively. While Figure 5-27 shows the mooring line load. The mooring lines are pretension by their self-induced weights and influenced by low frequency force component. The positional configuration of the mooring system under observation also effects the dynamic mooring loads. The maximum mooring loads is found to be 563 tons for test case 3. The mooring lines utilizes only 30% of the breaking load which means the mooring lines are effectively designed for the giving duration of the side-by-side operation. The over design is because to the long-life cycle of the FLNG and for the worst environmental condition compared to the calm environment during the side-by-side offloading operation. The lower values for the standard deviation showed that the there is a uniform distribution of the loads on the whole mooring system, therefore the mooring configuration is quite efficient. The Fast Fourier transformation (FFT) loads on the connecting system has low frequency

components; thus, the low frequency motions of surge, sway and yaw of the vessels are critical for the mooring load analysis.

5.6.7 Hawser Loads

The hawser loading for test case 1, 2, 3 and 4 are given in Table 5-20, Table 5-21, Table 5-22 and Table 5-23. The largest hawser loading is observed to occur for test case 1 which has collinear environment and reduces slightly with the change of environmental factors (wind, wave and current). The maximum hawser load is found to be on hawser 7 (707.34kN, 704.12kN, 706.45 and 634.75kN correspondingly) for the four test cases. The mean value of the hawser loads have the largest change from Test case 1 and test case 4 where we have the maximum differential in vessel displacement with the FLNG 100% and LNGC 10% loaded for test case 1 and FLNG 10% and LNGC 100% loaded for test case 4 which shows the effect of vessel displacement for on hawser loads, which is consistent with the trend for the relative motion in Figure 5-25.

The tension loads on the hawser calculated for the test cases 1 and 4 in Figure 5-29 Nwafor (2022) shows the mean load distribution on the hawser lines that are most affected. It can be observed that the hawser lines at the forward spring line (6, 7, 8 and 9) and the aft breast line (13, 14 and 15) are most affected. Upon careful investigation on the test case 1 and 4, it can be observed that the highest surge motion recorded for both vessels for all the test cases. Therefore, the spring line and aft breast lines might have influence on the relative surge motion of the vessels. Further investigation on the hawser loads should be carried out.

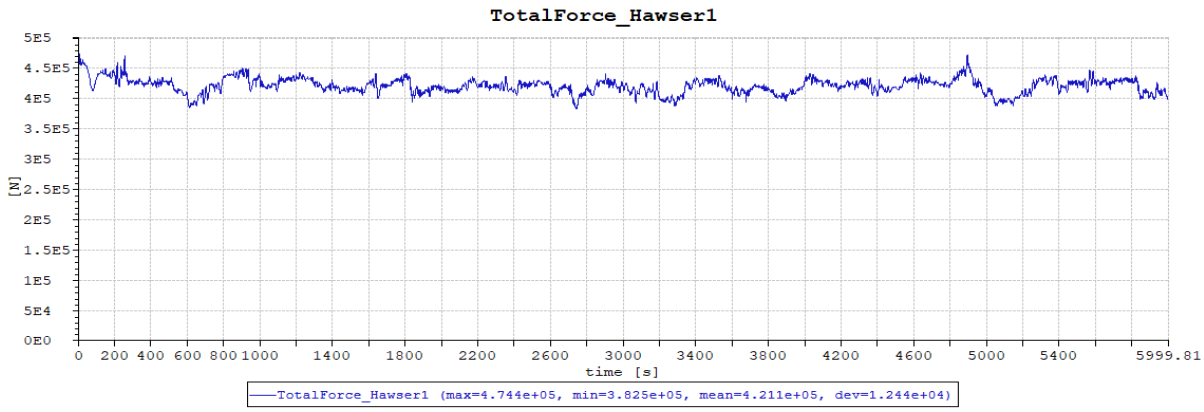
TotalForce_Hawser1
5E5
4.5E5
4E5
3.5E5
3E5
2.5E5
2E5
1.5E5
1E5
5E4
0E0
[N]
0 200 400 600 800 1000 1400 1800 2200 2600 3000 3400 3800 4200 4600 5000 5400 5999.81
time [s]
TotalForce_Hawser1 (max=4.744e+05, min=3.825e+05, mean=4.211e+05, dev=1.244e+04)

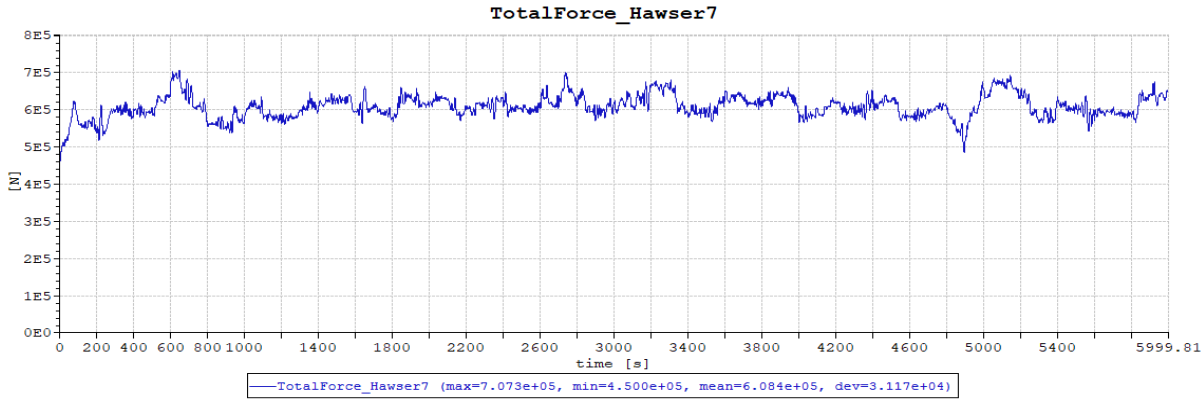
TotalForce_Hawser7
8E5
7E5
6E5
5E5
4E5
3E5
2E5
1E5
0E0
[N]
0 200 400 600 800 1000 1400 1800 2200 2600 3000 3400 3800 4200 4600 5000 5400 5999.81
time [s]
TotalForce_Hawser7 (max=7.073e+05, min=4.500e+05, mean=6.084e+05, dev=3.117e+04)

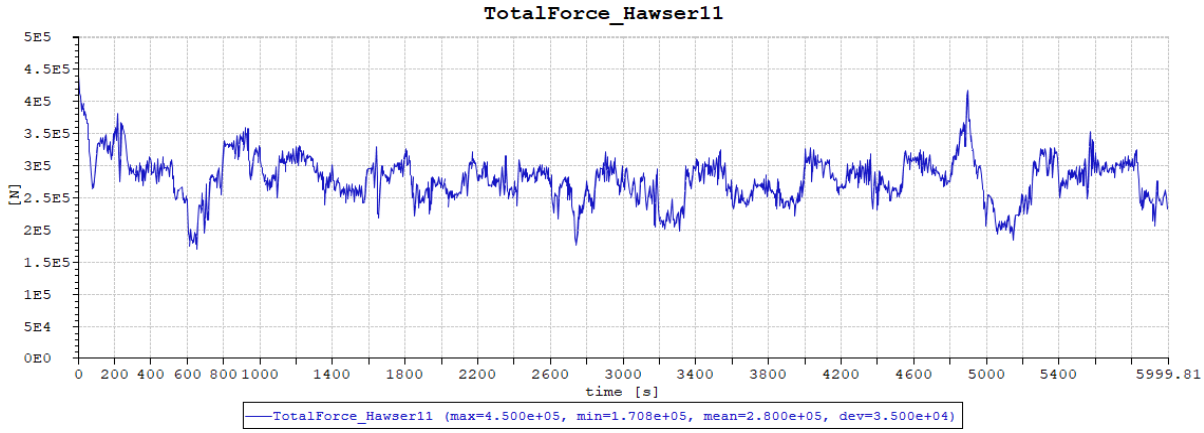
TotalForce_Hawser11
5E5
4.5E5
4E5
3.5E5
3E5
2.5E5
2E5
1.5E5
1E5
5E4
0E0
[N]
0 200 400 600 800 1000 1400 1800 2200 2600 3000 3400 3800 4200 4600 5000 5400 5999.81
time [s]
TotalForce_Hawser11 (max=4.500e+05, min=1.708e+05, mean=2.800e+05, dev=3.500e+04)

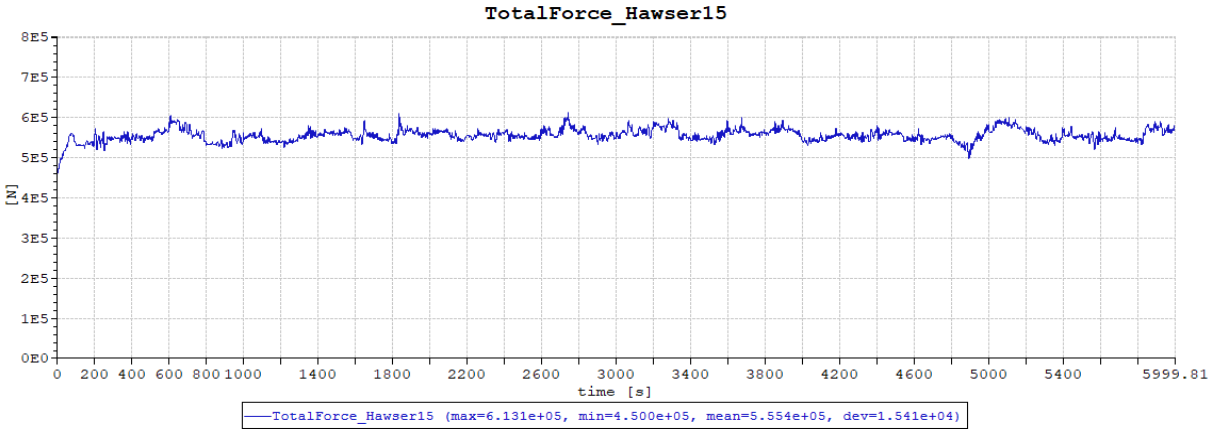

Figure 5-28. Time series of the forces on hawsers loads (Test Case 1)

Table 5-20. Hawser Load Case 1

Hawser line	Max (KN)	Min (KN)	Mean (KN)	Standard deviation
Hawser1	474.38	382.47	421.14	12.45
Hawser2	464.81	340.84	392.17	17.25
Hawser3	463.52	328.91	384.12	18.62
Hawser4	453.30	253.02	332.45	26.81
Hawser5	452.32	238.34	322.21	28.35
Hawser6	707.29	450.00	608.43	31.08
Hawser7	707.34	450.00	608.45	31.17
Hawser8	706.69	450.00	607.84	31.53
Hawser9	706.63	450.00	607.85	31.53
Hawser10	450.00	199.37	297.61	31.47
Hawser11	450.00	170.76	280.04	35.00
Hawser12	450.02	201.16	299.68	31.34
Hawser13	450.02	201.31	299.87	31.32
Hawser14	592.30	450.00	539.09	12.44
Hawser15	613.08	450.00	555.39	15.41
Hawser16	620.86	450.00	560.67	16.42

Table 5-21. Hawser Load Case 2

Hawser line	Max (KN)	Min (KN)	Mean (KN)	Standard deviation
Hawser1	488.86	385.95	424.04	11.64

Hawser2	483.49	343.38	395.80	16.20
Hawser3	481.66	331.14	387.95	17.50
Hawser4	468.20	254.01	337.36	25.32
Hawser5	465.42	239.04	327.30	26.79
Hawser6	704.05	450.00	603.42	29.61
Hawser7	704.12	450.00	603.42	29.68
Hawser8	703.75	449.83	602.67	29.99
Hawser9	703.70	449.89	602.68	29.99
Hawser10	455.32	202.14	302.85	29.91
Hawser11	455.45	173.88	285.87	33.27
Hawser12	456.97	204.00	304.90	29.81
Hawser13	457.10	204.18	305.09	29.79
Hawser14	602.42	450.00	537.44	12.08
Hawser15	621.23	450.00	553.15	14.76
Hawser16	627.30	450.00	558.23	15.68

Table 5-22. Hawser Load Case 3

Hawser line	Max (KN)	Min (KN)	Mean (KN)	Standard deviation
Hawser1	549.69	361.70	427.11	19.55
Hawser2	524.77	328.53	399.07	20.33
Hawser3	520.69	318.67	391.28	20.91
Hawser4	497.76	259.09	340.54	25.81
Hawser5	491.17	245.27	330.41	26.86
Hawser6	707.39	448.34	601.24	28.60
Hawser7	706.45	447.59	601.20	28.67
Hawser8	701.09	443.33	600.28	29.00
Hawser9	700.90	443.31	600.29	29.00
Hawser10	462.55	207.16	305.62	28.90
Hawser11	463.39	179.23	288.91	32.15
Hawser12	463.06	207.74	307.79	28.75
Hawser13	463.04	207.69	308.00	28.73
Hawser14	643.13	450.00	539.67	18.98
Hawser15	665.46	450.00	554.96	20.69
Hawser16	672.73	450.00	559.89	21.31

Table 5-23. Hawser Load Case 4

Hawser line	Max (KN)	Min (KN)	Mean (KN)	Standard deviation
Hawser1	495.34	410.77	439.88	8.30
Hawser2	480.64	380.93	417.27	10.41
Hawser3	477.10	372.45	410.99	11.07

Hawser4	454.44	316.19	369.51	15.31
Hawser5	452.74	305.57	361.03	16.11
Hawser6	635.27	450.00	568.16	18.04
Hawser7	634.75	450.00	568.00	18.06
Hawser8	631.45	450.00	566.56	18.12
Hawser9	631.31	450.00	566.55	18.11
Hawser10	450.03	274.56	338.86	18.03
Hawser11	450.01	254.37	325.91	20.06
Hawser12	450.06	275.09	340.55	18.02
Hawser13	450.06	275.10	340.69	18.02
Hawser14	569.29	450.00	521.67	8.82
Hawser15	585.73	450.00	533.43	10.03
Hawser16	590.90	450.00	537.23	10.47

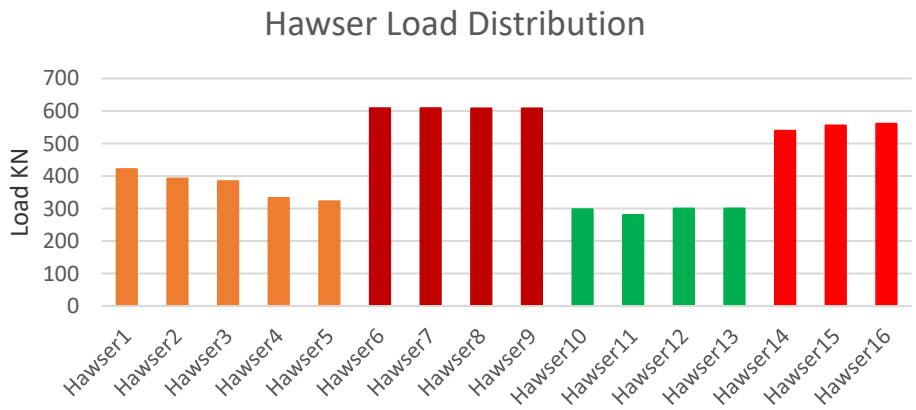

Figure 5-29. Hawser Load Distribution

5.6.8 Fender Loads

Table 5-24. Configuration of fender

Diameter (m)	Length (m)	Design deformation	Maximum reaction force (kN)
4.5	10.5	60%	5690

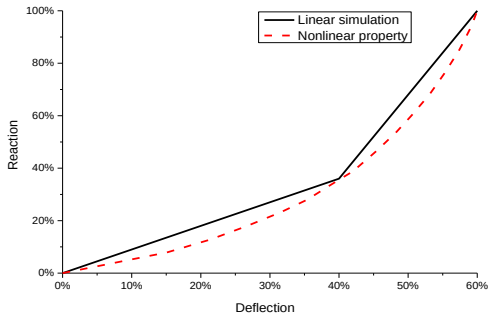

Figure 5-30. Deformation property and model of fender

Table 5-25. Location of fenders on FLNG

Number of fender	X(m) (From midship)	Y(m)	Z(m)
1	64	30.5	16.65
2	42	30.5	16.65
3	20	30.5	16.65
4	-20	30.5	16.65
5	-42	30.5	16.65
6	-64	30.5	16.65

The Fender deliver prevention measures against collision impact between the two vessels during the offloading operation and when the LNGC is approaching and departing from beside the FLNG. When the initial gap distance between the two vessels are maintained, the fender loads are negligible and throughout the offloading operation the fender experiences a pulsating squash compression force as shown in Figure 5-31. The study of the compressive loads and their frequency of occurrence are of interest for the strength assessment for the FLNG and LNGC. The fender compression is of equal and opposite load acting on each vessel.

The maximum fender load is found to be 3026kN for test case 3 which is less than the 60% design deformation of 3414kN in Table 5-24. This is due to the largest sway motion observed in this test case. The large sway motions of the vessels might be attributed to the environmental factors with both the wind and propagating waves in oblique wave for that test case.

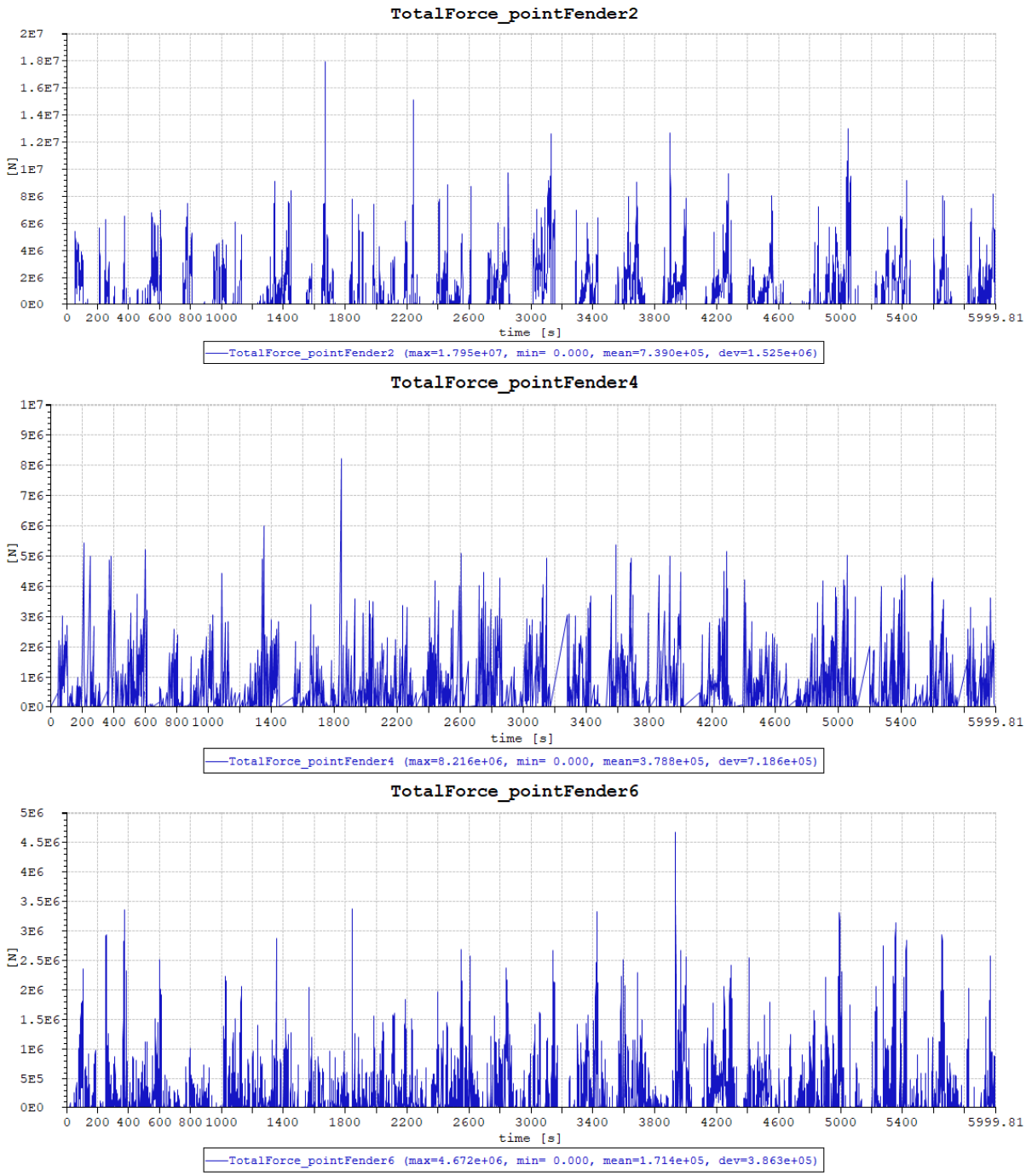

Figure 5-31. Fender Reaction (Test Case 1)

Table 5-26. Fender Reaction Case 1

Fender ID	Max (KN)	Min (KN)	Mean (KN)	Standard deviation
Fender1	2686	0	113	243
Fender2	1795	0	74	153
Fender3	1081	0	61	117
Fender4	822	0	38	72
Fender5	534	0	26	51
Fender6	467	0	17	39

Table 5-27. Fender Reaction Case 2

Fender ID	Max (KN)	Min (KN)	Mean (KN)	Standard deviation
Fender1	2569	0	100	215
Fender2	1747	0	63	135
Fender3	1137	0	52	106
Fender4	919	0	34	69
Fender5	750	0	25	53
Fender6	506	0	18	43

Table 5-28. Fender Reaction Case 3

Fender ID	Max (KN)	Min (KN)	Mean (KN)	Standard deviation
Fender1	3026	0	102	229
Fender2	1277	0	63	136
Fender3	1080	0	51	105
Fender4	979	0	34	68
Fender5	713	0	25	52
Fender6	583	0	18	44

Table 5-29. Fender Reaction Case 4

Fender ID	Max (KN)	Min (KN)	Mean (KN)	Standard deviation
Fender1	2335	0	108	192
Fender2	1145	0	64	109
Fender3	851	0	52	91
Fender4	719	0	43	74
Fender5	691	0	42	68
Fender6	1222	0	50	81

5.6.9 Relative Plane Motion

The time history plots of the FLNG and LNGC horizontal plane motion for the different test cases with varying loading conditions and environmental forces is shown in Figure 5-32. It can be observed that the trajectory of the LNGC is more sensitive to the

different loading conditions compared to that of the FLNG. This is because of the smaller displacement of the LNGC compared to the FLNG which brings about a lower inertia value, damping and restoring forces and moments. Another consideration is the fact that the turret mooring system is not directly connected to the LNGC. The LNGC is expected to have less damping, restoring force and moment, therefore for a given loading condition the LNG vessel tends to have more active motion than the FLNG.

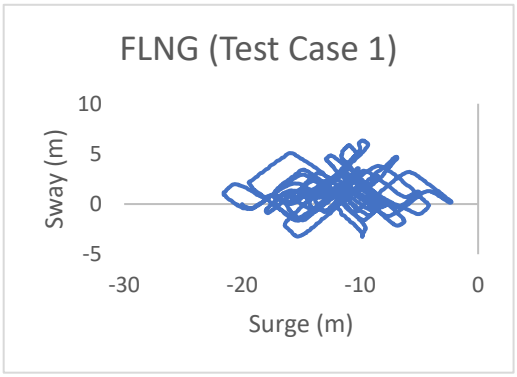

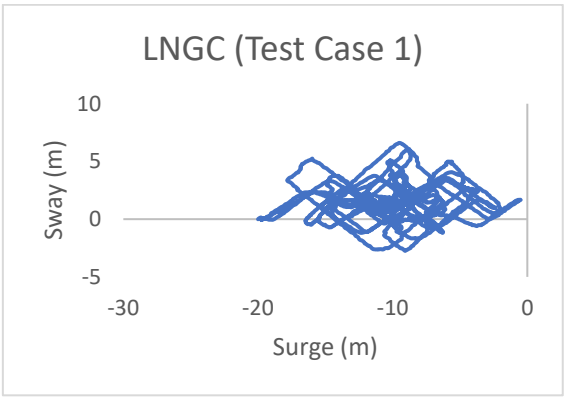

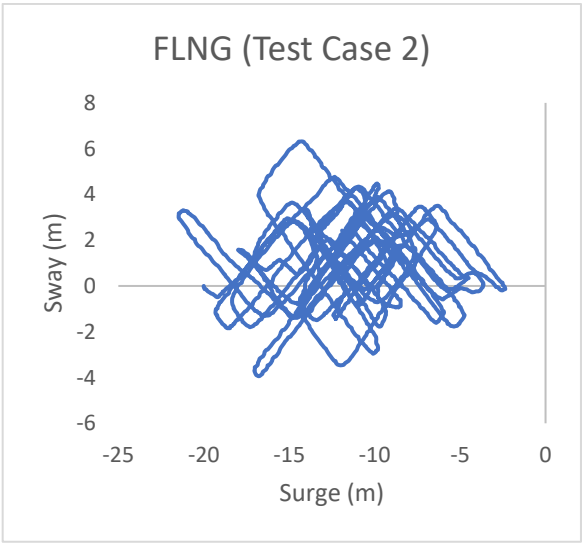

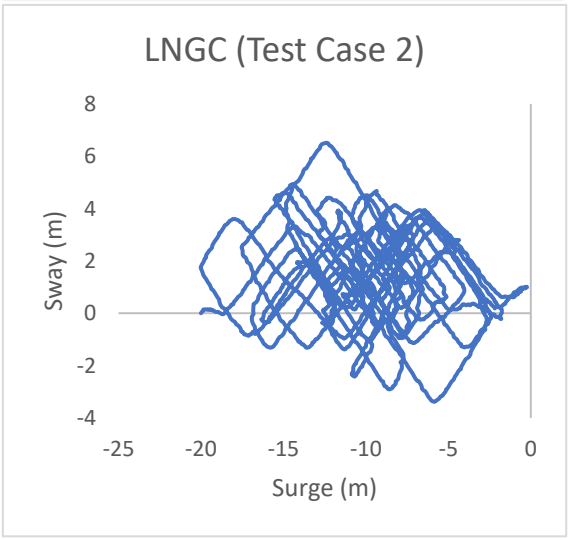

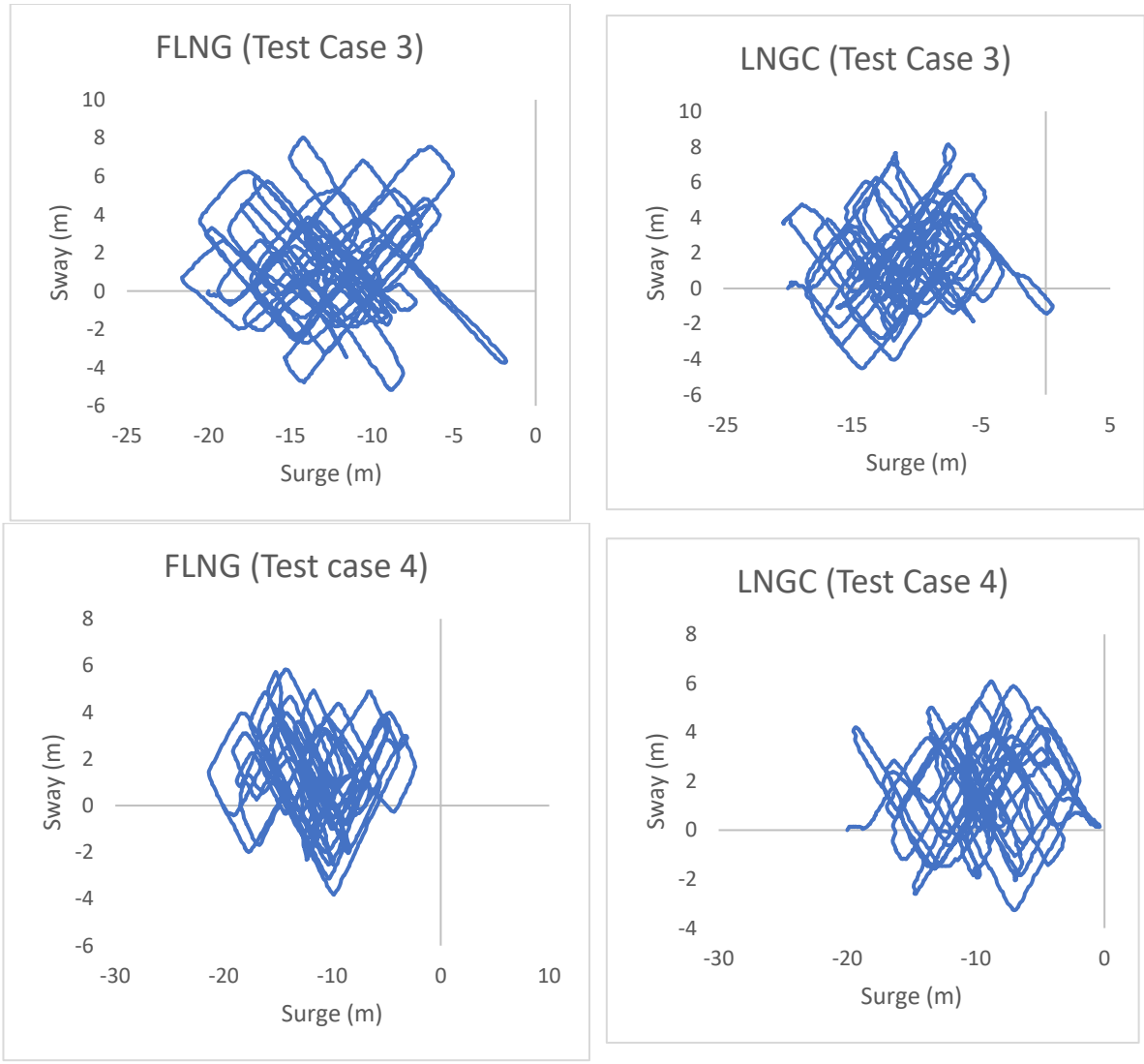

Figure 5-32. Horizontal plane motions of the FLNG and LNGC at different loading conditions

The relative deck height of the FLNG and LNGC is analysed to better understand the maximum level difference which affect the offloading arm which is important for safe offloading of floating LNG platform (Soares et al., 2015). This data is specifically vital to study the moment generated on the loading arm base

This data is specifically vital to study the moment generated on the loading arm base because of the level difference. However, the heave and pitch motion is observed to be small based on the numerical analysis given in Table 5-11, Table 5-12, Table 5-13 and Table 5-14. Hence the level difference in deck height does not make much disturbance on the loading arm during the side-by-side offloading operation unless the phenomenon of gap resonance induces large vessel motions.

Chapter 6. RESULTS AND DISCUSSIONS

6.1 Resonance frequency

In this section, we investigate the resonant modes in a narrow gap between side-by-side configured models. The same combination of fixed rectangular models with round bilges are simulated. The configuration of the side-by-side barges at model scale are given in Table 3-2. The incident wave considered are 180 degrees i.e heading sea and 135 degree oblique sea. The panel model for the two vessels is shown in Figure 5-2(a). For the study we stick to a fine mesh of 3m, for the large and small vessels we have 1328 and 862 quadrilateral panels generated respectively while the free surface mesh panels are 2950 shown in Figure 5-2(b).

The model test results in regular wave are carried out initially with the data collection done in calm waters before the waves are generated by the wave maker.

Only steady state part of the data is analysed before the reflected waves occurs to reduce their influence.

The comparison between the gap resonance RAOs of the model test data and the gap resonance RAOs of the numerical simulation is carried out in this section. The linear potential flow solver was used to introduction a calibrated free surface damping lid.

The Newtonian cooling method is used to introduce an external viscous damping effect of the fluid in the long narrow gap region. The damping coefficients are set as constants with the kinematic boundary condition modified to include the damping term which is applied on the free surface in the gap as shown in equ (4-22). This method is implemented in the potential solver. The artificial damping is a pure mathematical character and has no basis in physic. The physical damping can differ depending on the geometry, gap distance, vessel drafts and sea state hence the various test cases conducted.

The numerical simulation has similar arrangement as those of the experimental model test conducted in the hydrodynamic lab with the exact same parameters. The equations describing the theory for the damping method is discussed in section 4.8.

The RAOs are obtained for the regular wave case with the 10 wave frequencies shown in Table 3-3, and incident wave amplitude for all frequencies at 4mm. The Fast Fourier Transform (FFT) algorithm is used to analyse the frequency content from the time history of the water surface elevation in the gap for the three different gap widths.

It can be observed from the RAOs that at specific frequencies where resonance occurs for the three gap distances 33mm, 53mm and 67mm, spikes can be seen in the graph shown in Figure 6-1, with a damping factor of 0.03 used to suppress the extreme wave elevation. Table 3 shows the resonance frequencies for the 3 gap distances. The results confirm the ability of the potential flow solver to analyse gap resonance response.

Table 6-1**:** Resonance frequencies for different gap distances

Frequencies (rad/s)	33mm	53mm	67mm
0.337	-	-	-
0.478	-	-	-
0.615	-	-	-

0.759	-	-	-
0.901	-	✓	-
1.045	✓	-	✓
1.18	✓	✓	✓
1.331	✓	-	-
1.475	-	-	✓
1.618	-	-	-

(A)

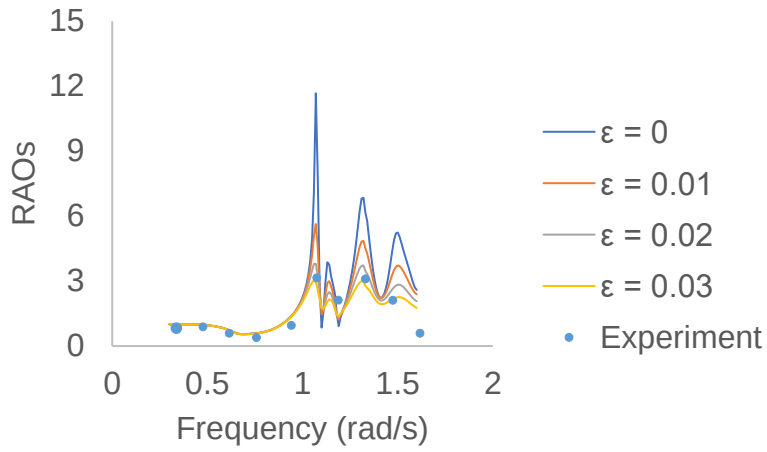

(B)

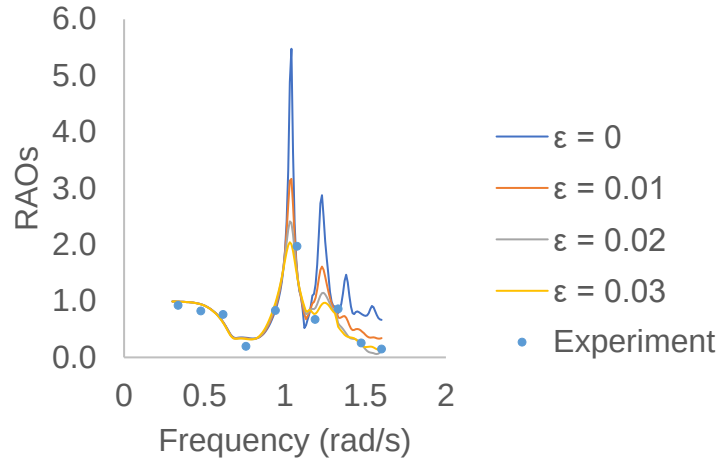

(C)

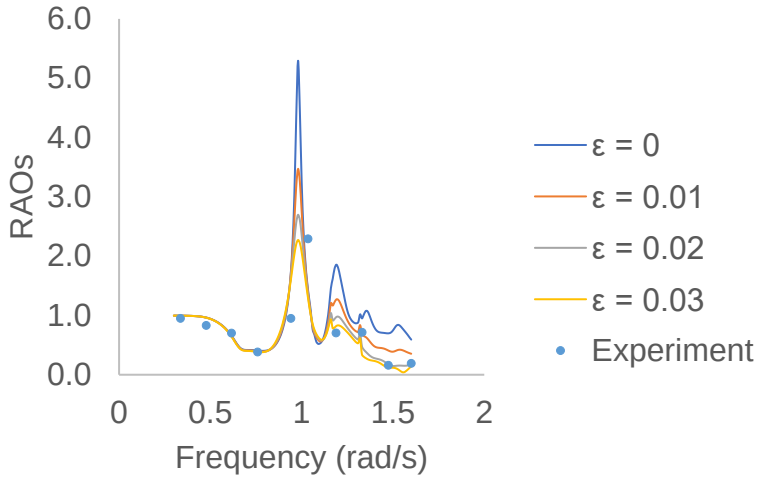

Figure 6-1**:** RAO at gap width for beam sea case (a) 33mm (b) 53mm and (c) 67mm at 3.3m 5.3m and 6.7m full scale respectively with different damping lids

Table 6-2 Resonance frequencies for different gap distances for oblique sea

Frequencies (rad/s)	33mm	53mm	67mm
0.337	-	-	-
0.478	-	-	-
0.615	-	-	-
0.759	-	-	-
0.901	-	✓	-
1.045	✓	-	✓
1.18	-	✓	-
1.331	✓	-	✓
1.475	✓	-	-
1.618	-	-	-

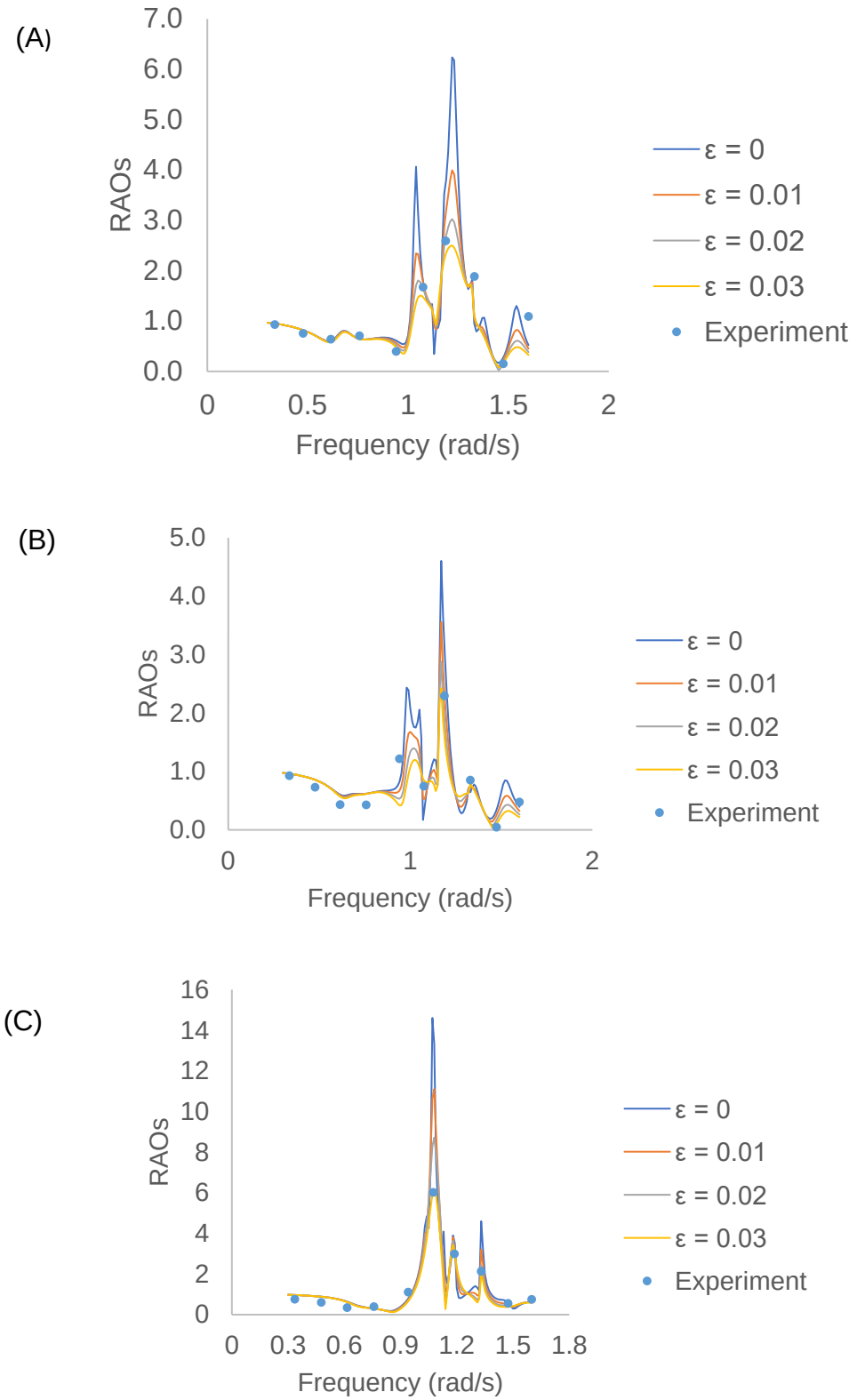

Figure 6-2 RAO at gap width for Oblique Sea case (a) 33mm (b) 53mm and (c) 67mm at 3.3m 5.3m and 6.7m full scale respectively with different damping lids

Table 6-2 and Table 6-3shows the frequency range where resonance responses occur for the two incident wave directions as 0.901rad/s, 1.045rad/s, 1.18 rad/s, 1.33 rad/s and 1.47rad/s, they correspond to mode 1, mode 2 and mode 3.To have a direct illustration of the resonance modes, an internal view of the model test is seen in the Figure 6-3, Figure 6-4 and Figure 6-5.

The piston mode (zeroth mode) and mode 1 with large wave excitation in the gap are generally more critical than the others. For the beam sea case the piston mode for gap distance 33mm, 53mm and 67mm correspond to 1.045 rad/s, 0.901 rad/s and1.045 rad/s respectively while for the oblique sea the piston mode for gap distances 33mm, 53mm and 67mm correspond to 1.045rad/s, 0.901rad/s and 1.045 rad/s respectively. The maximum elevation near the midship in the gap at the piston mode is over five times that of the incident wave amplitude.

For from Table 6-3, Table 6-4 and Table 6-5 a wave amplification for the different test cases were found which is the ratio of the incident wave amplitude (wave gauge 1) and the gap wave amplitude for the three wave gauges 3, 4 and 5 respectively shown Figure 3-4.

For the beam sea test case with first vessel drafts, the gap distances 33mm 53 mm and 67 mm experience amplification between (≈3 and ≥6) of 4 ,5 and 2 times. While beam sea test case with second vessel drafts, the gap distance 33mm 53 mm and 67 mm experience amplification between (≈3 and ≥6) of 6 ,4 and 5 times. And finally for oblique sea test case with second vessel drafts, the gap distance 33mm 53 mm and 67 mm experience amplification between (≈3 and ≥6) of 8 ,8 and 7 times. The intermediary gap distance of 53 had the most wave amplification followed by gap distance 67mm and 33mm, thus for the frequency range studied the closes gap distance has the less amplification while the largest gap distance saw a reduction in the wave amplification. This show that gap distance affects the resonance elevation, The vessels cannot be extremely close or far apart due to the minimum distance the offloading arm can operate and in order to prevent collision. Analysing the data from the wave direction, it is clearly seen that the oblique sea had the most wave amplification compared to the beam sea case with 23 compared to 11 and 15 respectively. Thus, wave direction can also affect the resonance response. The FLNG has a turret mooring system hence able to manoeuvre around the turret depending on the wave direction.

It is visible that the movement of the water surface in the gap, oscillates like a flexible plate as seen in Figure 6-3 and Figure 6-4. It is predictable that higher resonant modes (resonant wave elevation are low and of less interest). Though, nearly everywhere in the open ocean, there is the possibility of a long-period swell from distance storms. In engineering practice these swells could not drive considerable surface motion linearly in the gap region, due to the very low frequency (long period) to couple to the lowest gap mode. Nonetheless, there is a possibility which has been demonstrated experimentally that quadratic frequency doubling can and couple to the gap resonance (Zhao et al., 2017b). Hence, such interactions should be under consideration when planning side-by-side offloading operations.

Internal camera view of different modes

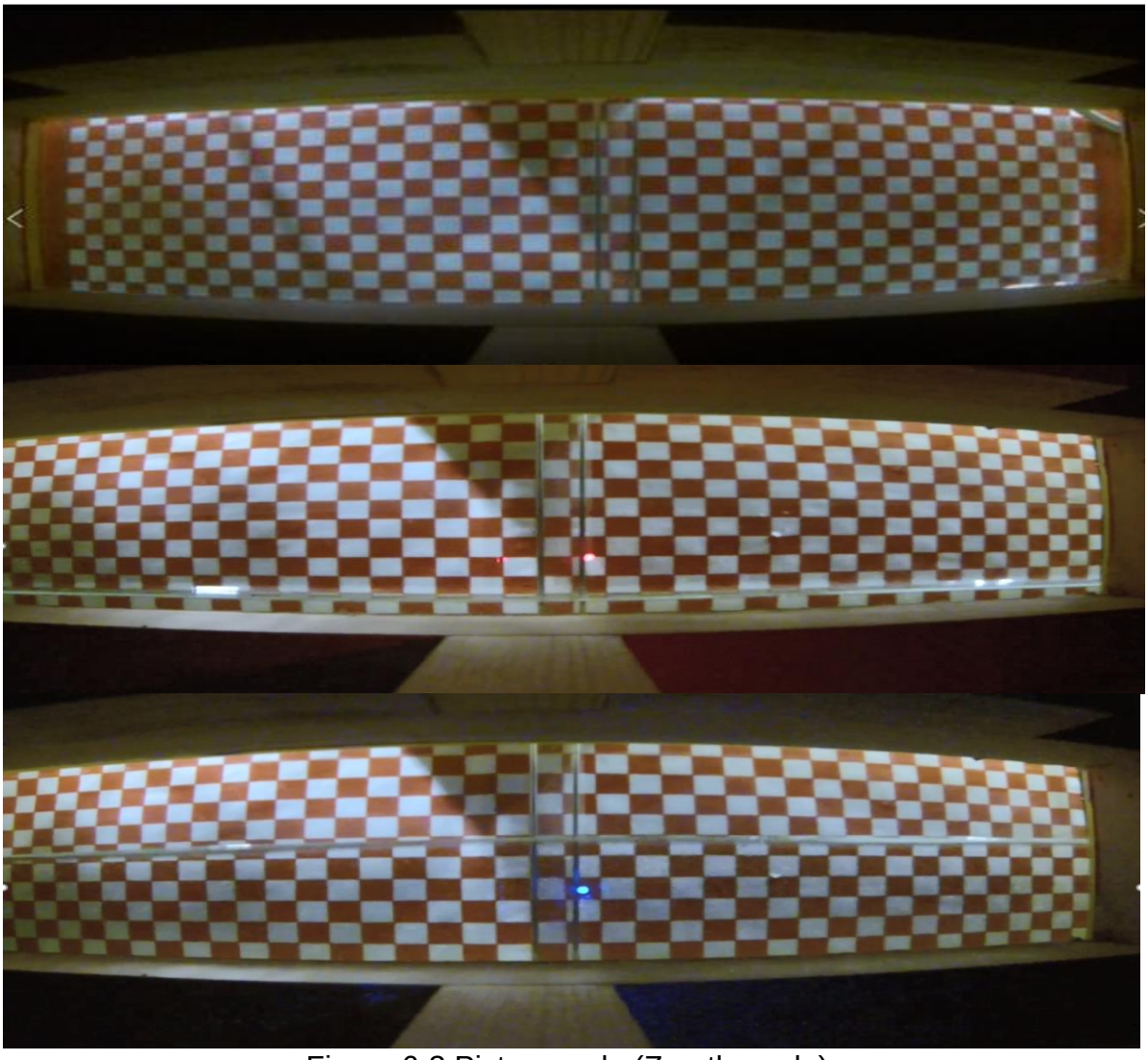

Figure 6-3 Piston mode (Zeroth mode)

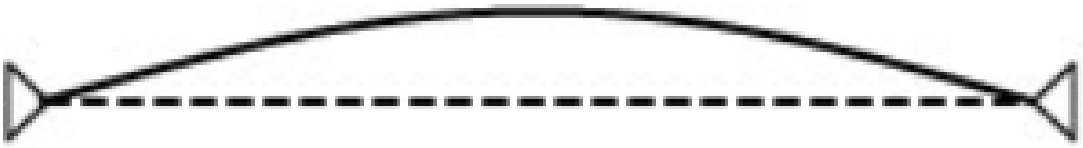

fundamental mode (n = 1)

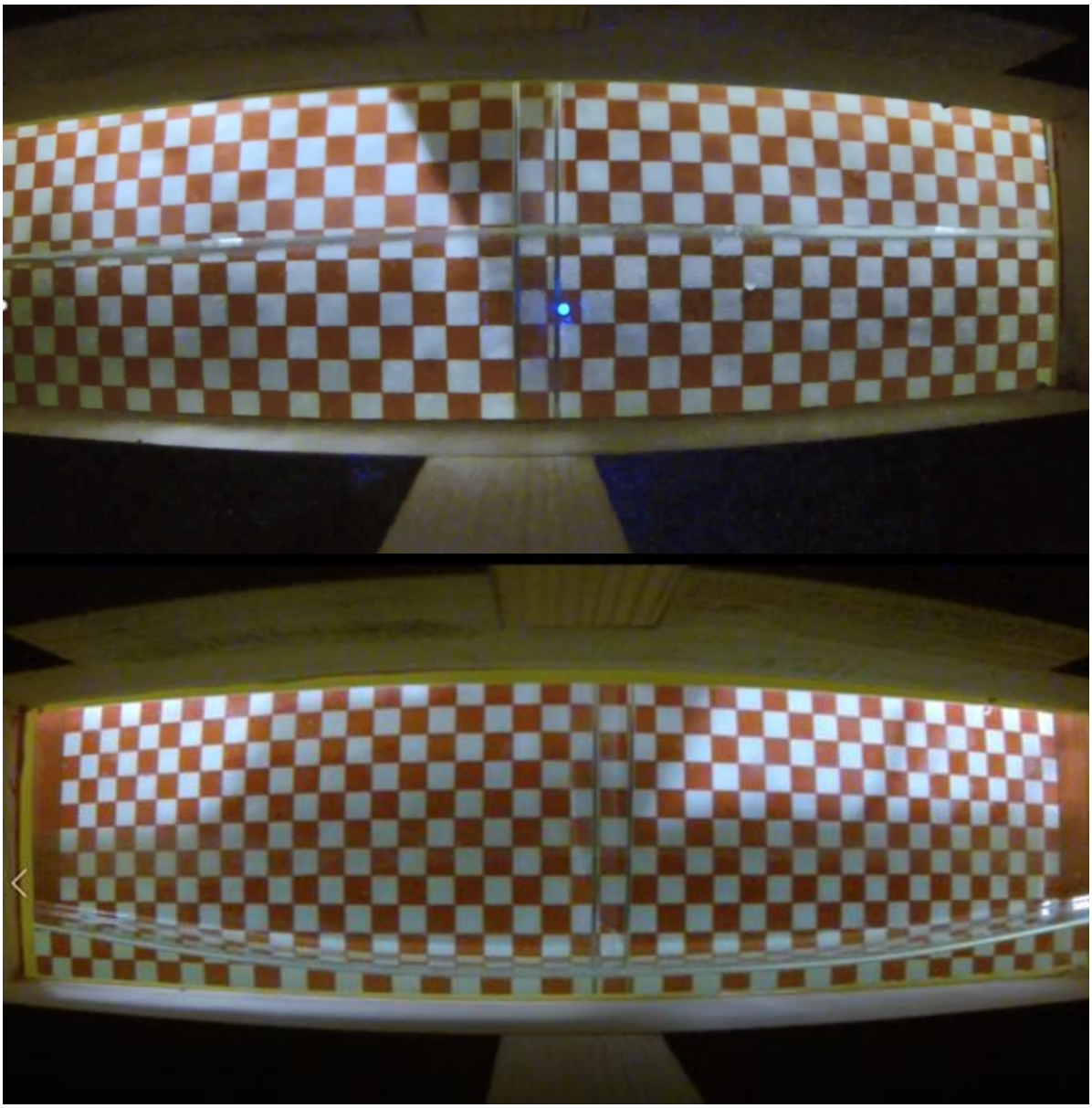

Figure 6-4 Fundamental mode (mode 1)

first harmonic (n = 2)

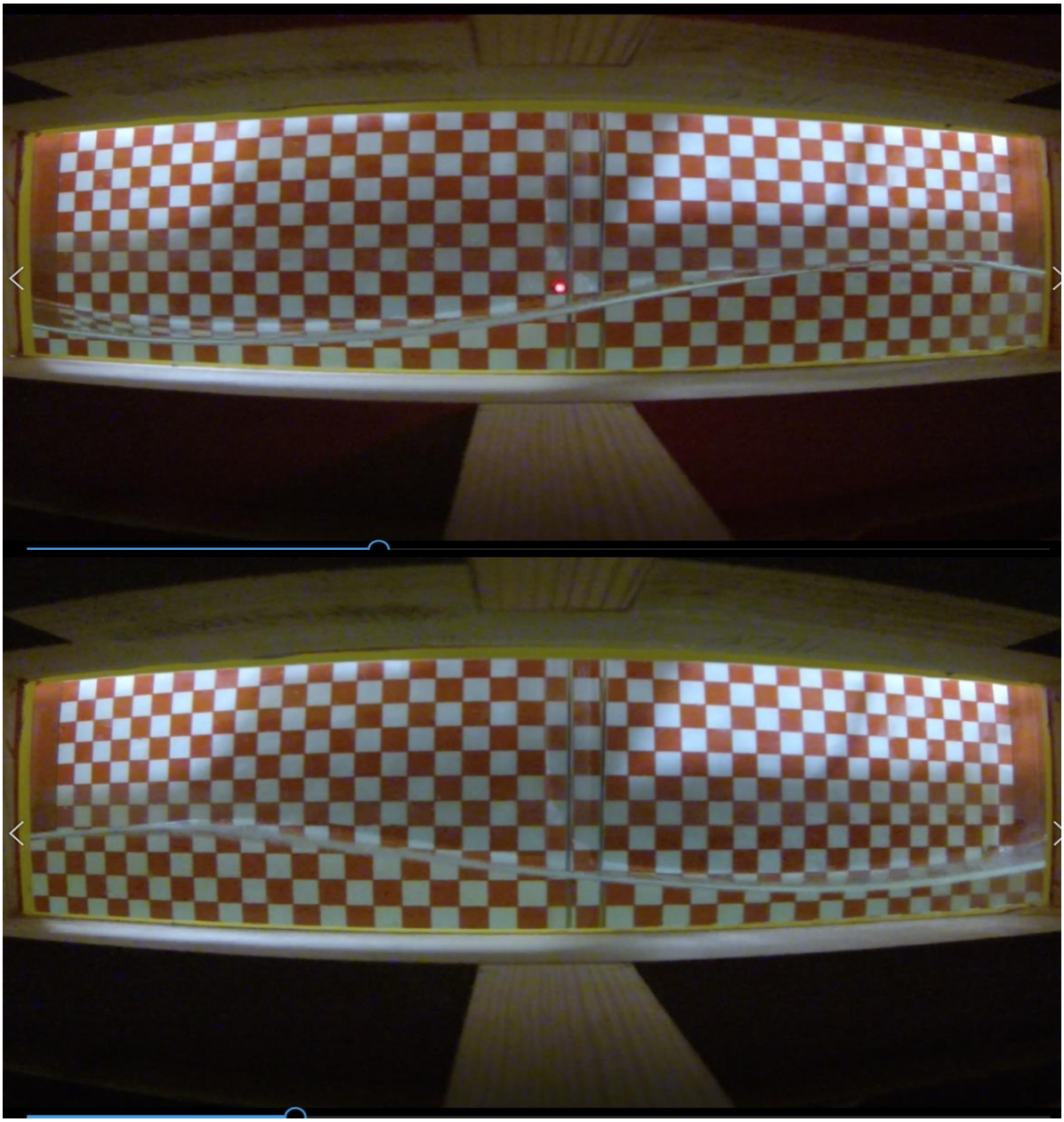

Figure 6-5 Mode 2

Table 6-3 Statistical description for draft 1 in beam sea

Wave elevation Beam Sea, Draft 1												
	33mm				53mm				67mm			
	Max	Min	Mean	STD	Max	Min	Mean	STD	Max	Min	Mean	STD
WG3	8.70	2.62	3.91	1.78	8.74	2.91	4.89	1.66	11.96	2.66	4.86	2.47
WG4	10.38	2.67	5.45	2.78	9.81	3.65	6.27	2.24	14.45	3.61	6.08	3.25
WG5	14.99	5.03	7.94	3.08	15.18	5.01	7.69	2.74	18.63	5.15	8.03	3.78

Table 6-4 Statistical description for draft 2 in beam sea

Wave elevation Beam Sea, Draft 2												
	33mm				53mm				67mm			
	Max	Min	Mean	STD	Max	Min	Mean	STD	Max	Min	Mean	STD
WG3	15.17	2.73	6.12	3.83	9.62	3.19	5.01	2.03	15.90	3.25	5.98	3.51
WG4	16.49	2.18	7.03	5.03	10.24	3.32	6.74	2.72	18.79	2.91	7.17	4.37
WG5	20.69	4.81	9.59	5.96	16.74	5.14	8.02	3.53	22.29	5.59	12.41	5.83

Table 6-5 Statistical description for draft 2 in oblique sea

Wave elevation Oblique Sea, Draft 2												
	33mm				53mm				67mm			
	Max	Min	Mean	STD	Max	Min	Mean	STD	Max	Min	Mean	STD
WG3	15.86	1.92	6.85	4.56	12.57	2.11	6.60	4.05	20.57	2.11	7.50	5.47
WG4	22.76	2.20	8.07	6.71	16.02	2.15	6.71	4.13	28.48	3.03	8.27	7.30
WG5	22.29	5.59	12.41	5.83	22.65	5.72	11.97	6.00	26.44	6.27	12.20	6.31

6.1.1 Wave Amplification Factor

The wave amplification factor is the ratio of the gap resonance amplitude to the incident wave amplitude.

Table 6-6 Wave amplification for draft 1 in beam sea.

Wave Amplification (Beam Sea, Draft 1)										
Gap Distances →		33mm			53mm			67mm		
Frequency	Incident wave	WG3	WG4	WG5	WG3	WG4	WG5	WG3	WG4	WG5
0.34	4.58	0.9	1.1	1.8	1.1	1.4	1.5	1.1	1.4	2.0
0.48	6.66	0.8	1.0	1.7	0.9	0.9	1.3	0.9	0.9	1.5
0.62	6.12	0.6	0.7	1.2	1.0	1.1	1.6	0.9	1.0	1.5
0.76	5.74	0.7	0.7	1.4	1.1	1.0	1.7	1.2	0.9	1.9
0.90	5.32	0.8	0.9	1.5	1.3	1.3	2.1	1.5	1.6	2.3
1.05	8.77	0.9	0.9	1.8	1.4	1.5	2.4	1.8	2.2	2.8
1.19	3.19	4.4	5.3	7.7	2.8	3.6	3.8	2.2	2.5	2.6
1.33	3.64	1.5	2.3	4.5	2.2	3.0	3.5	1.5	2.0	2.4
1.47	4.60	1.6	2.7	2.8	1.8	3.2	2.2	1.7	3.5	1.9
1.62	4.73	0.8	2.7	2.3	1.0	2.3	2.1	0.9	1.8	3.3

Table 6-7 Wave amplification for draft 2 in beam sea

Wave Amplification (Beam Sea, Draft 2)										
Gap Distances →		33mm			53mm			67mm		
Frequency	Incident wave	WG 3	WG 4	WG 5	WG 3	WG 4	WG 5	WG 3	WG 4	WG 5
0.34	4.58	1.1	1.0	1.9	1.1	1.3	1.7	1.5	1.5	2.4
0.48	6.66	0.8	0.8	1.2	0.7	0.8	1.1	0.9	0.6	1.1
0.62	6.12	0.8	0.9	1.3	0.8	1.0	1.3	0.8	1.0	1.2
0.76	5.74	0.9	0.6	1.5	1.0	0.8	1.6	1.1	1.0	1.7
0.90	5.32	1.0	1.0	1.5	1.1	1.4	1.7	1.2	1.3	1.9
1.05	8.77	1.2	1.0	1.9	1.4	1.5	2.5	2.0	2.3	2.8
1.19	3.19	5.5	6.0	7.4	2.5	3.6	3.2	3.0	3.5	3.9
1.33	3.64	2.1	3.3	4.4	1.9	2.6	3.1	1.2	1.8	2.1
1.47	4.60	2.5	2.7	1.8	2.0	3.5	1.9	2.0	3.0	1.1
1.62	4.73	1.3	2.7	3.4	1.0	2.4	2.9	1.1	2.0	3.1

Table 6-8 Wave amplification for draft 1 in Oblique Sea.

Wave Amplification (Oblique Sea, Draft 2)										
Gap Distances →		33mm			53mm			67mm		
Frequency	Incident wave	WG 3	WG 4	WG 5	WG 3	WG 4	WG 5	WG 3	WG 4	WG 5
0.34	4.58	1.3	1.5	2.4	1.3	1.3	2.0	1.1	1.0	1.9
0.48	6.66	1.0	1.2	2.8	0.7	0.9	1.9	0.9	1.0	2.0
0.62	6.12	0.6	0.7	1.5	0.7	0.7	1.5	0.5	0.7	1.7
0.76	5.74	0.8	0.6	1.4	0.8	0.6	1.6	0.7	0.7	1.5
0.90	5.32	0.3	0.4	1.0	0.4	0.6	1.2	0.5	0.7	1.5
1.05	8.77	1.0	1.1	2.6	1.7	2.2	4.2	5.3	7.3	6.8
1.19	3.19	2.8	4.0	3.5	3.2	2.6	5.2	2.5	2.1	4.3
1.33	3.64	3.7	6.1	7.2	4.4	5.6	8.0	3.0	3.5	5.0
1.47	4.60	3.4	2.4	4.6	2.8	2.8	4.4	2.2	2.6	2.8
1.62	4.73	2.3	2.0	4.5	3.0	2.1	3.7	2.6	1.6	3.1

Table 6-9 Wave Amplification (Beam Sea, Draft 1)

Gap Distances →	33mm	53mm	67mm	Total
Wave Amplification ≈3	0	5	2	7
Wave Amplification ≈4	2	0	0	2
Wave Amplification ≈5	1	0	0	1
Wave Amplification ≥6	1	0	0	1
Total	4	5	2	11

Table 6-10 Wave Amplification (Beam Sea, Draft 2)

Gap Distances →	33mm	53mm	67mm	Total
Wave Amplification ≈3	2	4	5	11
Wave Amplification ≈4	1	0	0	1
Wave Amplification ≈5	1	0	0	1
Wave Amplification ≥6	2	0	0	2
Total	6	4	5	15

Table 6-11 Wave Amplification (Oblique Sea, Draft 2)

Gap Distances →	33mm	53mm	67mm	Total
Wave Amplification ≈3	3	2	2	7
Wave Amplification ≈4	3	3	1	7
Wave Amplification ≈5	0	2	2	4
Wave Amplification ≥6	2	1	2	5
Total	8	8	7	23

6.1.2 Surface elevation at different location in the gap (Model test)

In the analysis of the wave elevation at different locations in the gap, we had wave gauges positioned at three locations in the gap as shown in Figure 3-3

The results in Figure 6-6show the different wave amplitudes when the maximum gap resonance occurred for beam sea and oblique sea test cases. It can be observed that the wave gauge 5 (WG5) shown in Figure 3-3 which was closer to the big vessel had the highest wave amplification compared to the other wave gauge locations while the wave gauge close to the small vessel experienced the smallest amplification.

This could be due to the slamming effect brought about by the different sizes of the models, the model geometry which is box shape, and the direction of wave propagation. The large model is longer and has a larger draft, it is directly impacted by the incident wave. This could bring about the slamming effect during gap resonance and might be the reason why wave gauge 5 experiences the highest wave amplification.

This observation highlights the variation of resonance response at different locations in the gap region, due to the difference in vessel sizes. The vessel draft is also an important parameter that needs further investigation because in practice, it is constantly changing during the offloading operation.

(A)

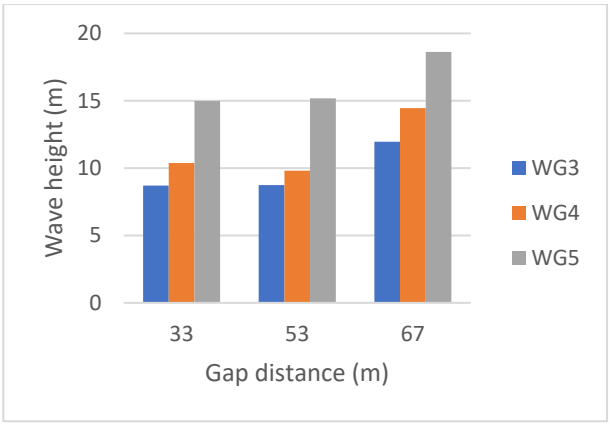

(B)

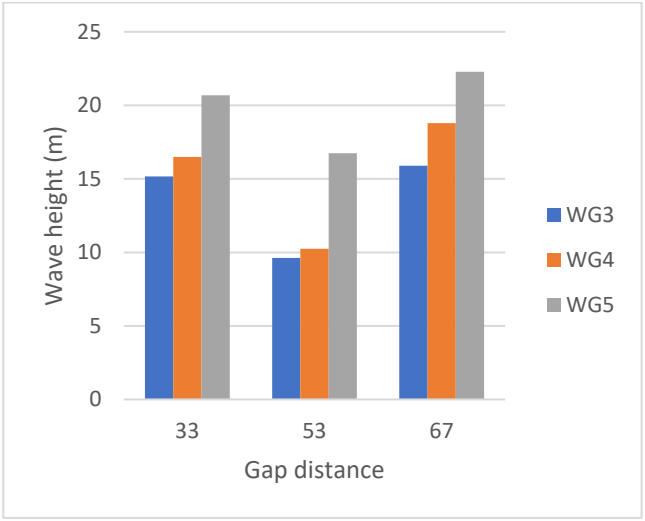

(C)

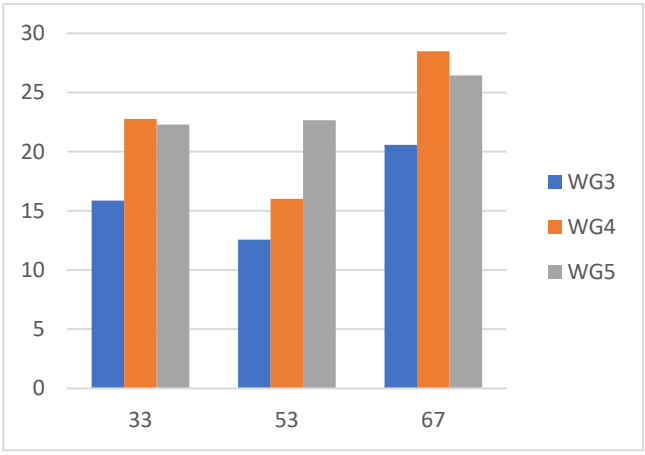

Figure 6-6: Wave height in extreme condition at the gap at different wave gauge locations (a) Beam sea draft 1 (b) Beam sea Draft 2 (c) Oblique sea draft 1

Chapter 7. GAP RESONANCE PREDICTION

7.1 Nonlinear curve fitting modelling

The dimensionless model depends on various parameters which are properly selected based on model test specification. The reference database used in practice for the FLNG side-by-side offloading does not have its entire range of conditions covered for which the model will be evaluated. The capability of the mathematical model to predict future variations in conditions are evaluated. The relevant input independent variables which are included in the model for this prediction analysis are the wave frequency, gap distance, vessel draft, max incident wave amplitude, and the dependent variable resonance responses in the gap region.

The statistical model was fitted to a dataset which includes 10 wave frequencies, 3 gap distances, 2 vessel drafts for the two models which totalled to a dataset of 90 observations for the occurrence of gap resonance and a total data of 540 used for the prediction.

For the development of the mathematical model, the coefficients of the ploynomials X_1, X_2, X_3, have to be determined. The mathematical model is developed with a 95% confidence level. The extent to which the control variable affects the resonance responses quantitatively was evaluated using the values of the regression coefficients. A hypothesis test of significance for individual parameter is carried out to eliminate the less significant coefficients without affecting much of the accuracy of the model. The rejection rule implies that we reject the null hypothesis if the p-value is less than or equal to a = 0.05, a calculated p-value > 0.05 exceeds the tabulated value for desired confidence limit, the coefficient thus becomes significant. After obtaining the significant coefficients using the data analysis tool in MatLab, the final mathematical model is developed using only the significant coefficients.

The mathematical model for gap resonance response (Y) is developed based on calculated coefficients determined using Matlab software:

Where X_1 is the coded value of (Gap distance/Vessel draft) × wave frequency, X_2 is (Incident wave height × wave frequency) and X_3, is (amplification factor × wave frequency).

The most significant coefficients are identified by analysing the mathematical model. The p-value (p <0.05) indicates the probability of getting our results. The final mathematical model after analysing the p-value of p < 0.05 probability criteria without affecting the accuracy is given in:

The parameters of wave frequency F, gap distance G, vessel draft D, Incident wave height I, amplification factor A and resonance response R are subsituted for X_1, X_2, and X_3 and simplified.

$$R = 13.909 - F^2\left(3.649\frac{I}{F} - 2.317\frac{A}{F} - 12.601\left(\frac{G}{D}\right)^2 + 0.289I^2 + 0.381A^2 + 0.527\frac{GI}{D}\right) \quad (7\text{-}1)$$

The predicted resonance response obtained using Eq. (7-1) are compared with the actual mesured gap resonance response.

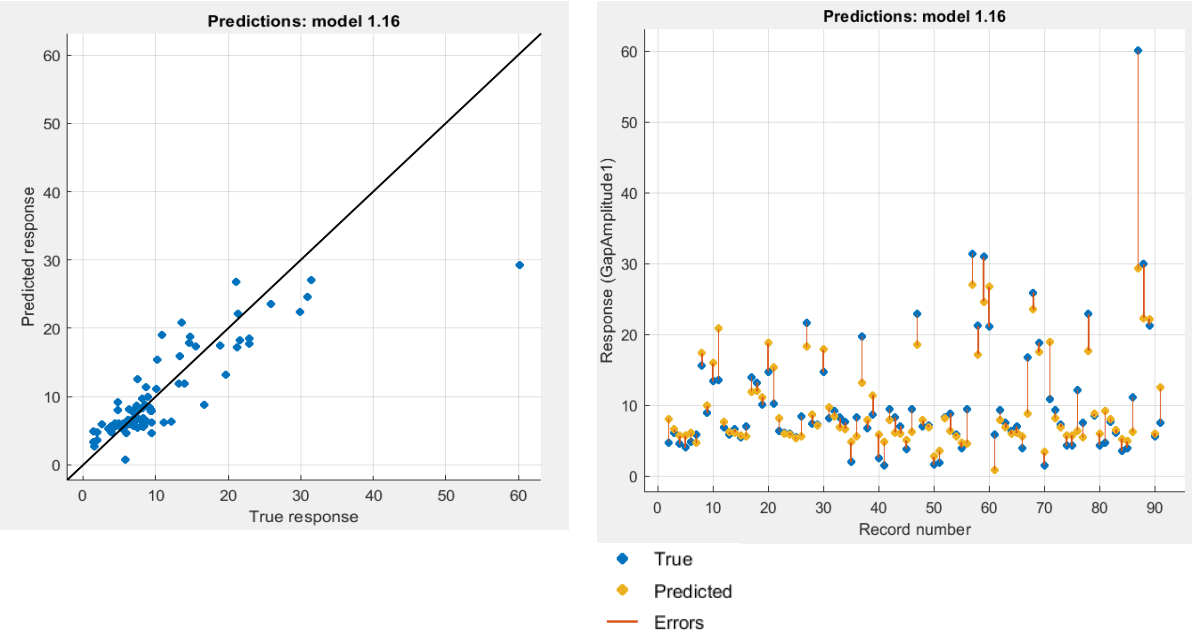

Figure 7-1 (a)

7.2 Empirical analysis

The existence of numerical and empirical method to predict and assess the gap resonance between two side-by-side floating vessels i.e FLNG_LNGC system is analysed in this section. The models in the experiment are modified and fixed to the gantry to focus on the wave amplification in the gap with the design parameters as *vessel length, gap distances, vessel drafts, wave frequency and wave direction*. Some of the parameters further combined to obtain *FLNG Length-Draft ratio (L/D), LNGC Length-Draft ratio (L/D) and gap distance-Draft ratio (G/D)* to enable the scaling up and application on different vessel sizes.

Table 7-1 Model parameters

Parameters	m
FLNG Length L1	150
LNGC Length L2	120
Gap Distance G1	3.3
Gap Distance G2	5.3
Gap Distance G3	6.7
FLNG Draft (D1)	12
LNGC Draft (D2)	7.4
FLNG Draft (D3)	10
LNGC Draft (D4)	6.4

Majority of statistical methods are based upon regression analysis on systematic series of results, resulting from an extensive range of wave basin experiments and actual ship data. Thus, they have characteristic applicable limitation as model test results. The empirical methods are based upon ‘the rule of thumb’ combined with empirical equations that express the relation occurring between performance of the wave excitation (gap resonance) prediction variables derived from the model test. The results used for the empirical analysis to estimate the resonance response has been validated with numerical simulation and the model experiment data.

This study analysis series of test cases conducted on two rigid models that are fixed during the model test, setting up a pure diffraction problem. With the numerical simulation, the same damping coefficient is applied for the different gap resonance modes for simplicity, bring about a satisfactory agreement with the model test data for the test cases of interest.

The approach is to fit an empirical equation to the data of the maximum wave amplitude when resonance occurs with the initial incident wave frequency and amplitude. The dataset used are the frequencies where the amplification is above a factor of 3 as shown in Table 6-6, Table 6-7and Table 6-8

A series of regular, irregular and focused waves were generated shown in Figure 3-7, Figure 3-9 and Figure 3-14 with the corresponding time histories, and the focused wave is given by the general equation for a gaussian with one dimensional input:

$$f(x) = \frac{1}{\sigma\sqrt{2\pi}} exp\left(-\frac{((x-\mu)^2)}{2\sigma^2}\right) \tag{7-2}$$

Where x is the input μ is the mean and σ is the standard deviation. This produces the bell-shaped curve, which has the centre at the mean μ.

To investigate the gap resonance response,the principal amplitude spectrum of the generated waves is gaussian and given by

$$S(f) = \frac{H_s^2}{16}\frac{1}{\delta\sqrt{2\pi}} exp\left(-\frac{\left((f-f_p)^2\right)}{2\delta^2}\right) \tag{7-3}$$

Where, H_s is significant wave height, f_p is the peak frequency of the spectrum and $\delta = 0.0775Hz$. The gap distance for the test case is 66mm and the frequency of the first mode gap resonance is 1.045rad/s shown in Table 6-1 (Zhao et al., 2018b).

An assumption that excitation forces are harmonic based and on the linear diffraction theory, hence the solution for the wave excitation in the gap are also harmonic.

The linearised component of the of the incident wave and the corresponding gap resonance response from the wave-structure interaction may be describes by stokes second-order wave theory for surface waves expanded to the second order in linear component amplitude A.

$$\eta(\theta) = A\eta_{11}\cos(\theta) + A^2(\eta_{20} + \eta_{22}\cos 2\theta) + O(A^5) \tag{7-4}$$

Where η_{ij} are the expansion coefficients and θ is the phase function. Taking an example with irregular waves the second-order free surface expansion in kA can be given as (Fitzgerald et al., 2014)

$$\eta = \sum_{n=1}^{N} A_n cos(\theta_n) + \sum_{n=1}^{N}\sum_{m=1}^{N}[A_n A_m B_{nm}^{+}\cos(\theta_n + \theta_m) + A_n A_m B_{nm}^{-}\cos(\theta_n - \theta_m)] \tag{7-5}$$

A_n is the amplitude of the free surface component, $\theta_n = k_n x - \omega_n t$ is the phase, $\omega = 2\pi f$. and B_{nm}^{+} and B_{nm}^{-} describe the wave-wave interaction.

With the assumption of a narrowband spectrum, the stokes expansion can be generalised for the focused wave group. Hence a free surface elevation up to the second order at the target position around the focused time is given by

$$\eta(\theta) = A(t)\cos(\omega_0 t + \epsilon_0) + A^2(t)[B^{+}\cos 2(\omega_0 t + \epsilon_0) + B^{-}] \tag{7-6}$$

Where B^{+} is the second-order sum coefficient and B^{-} is the second order difference coefficients both at peak frequency ω_0 and ϵ_0 is the phase of the peak frequency component.

7.3 ANN Model for prediction of gap resonance

In this section the ANN modelling is described including the experimental conditions and the choice of the input data. One of the most important components for a successful execution of the ANN model is the dataset, which is critical for ANN model learning. This section shows how ANN can produce good predictions for different test

cases. It is suitable for dealing with complex nonlinear problems, such as gap resonance for effective classification, mining and forecasting of given data.

The standard back propagation (BP) neural network is a multilayer feedforward neural network, and its application is conducted in this study The most important characteristics are the forward transmission and error back propagation which includes input, hidden and output layers respectively (Rumelhart et al., 1985) shown in Figure 7-2.

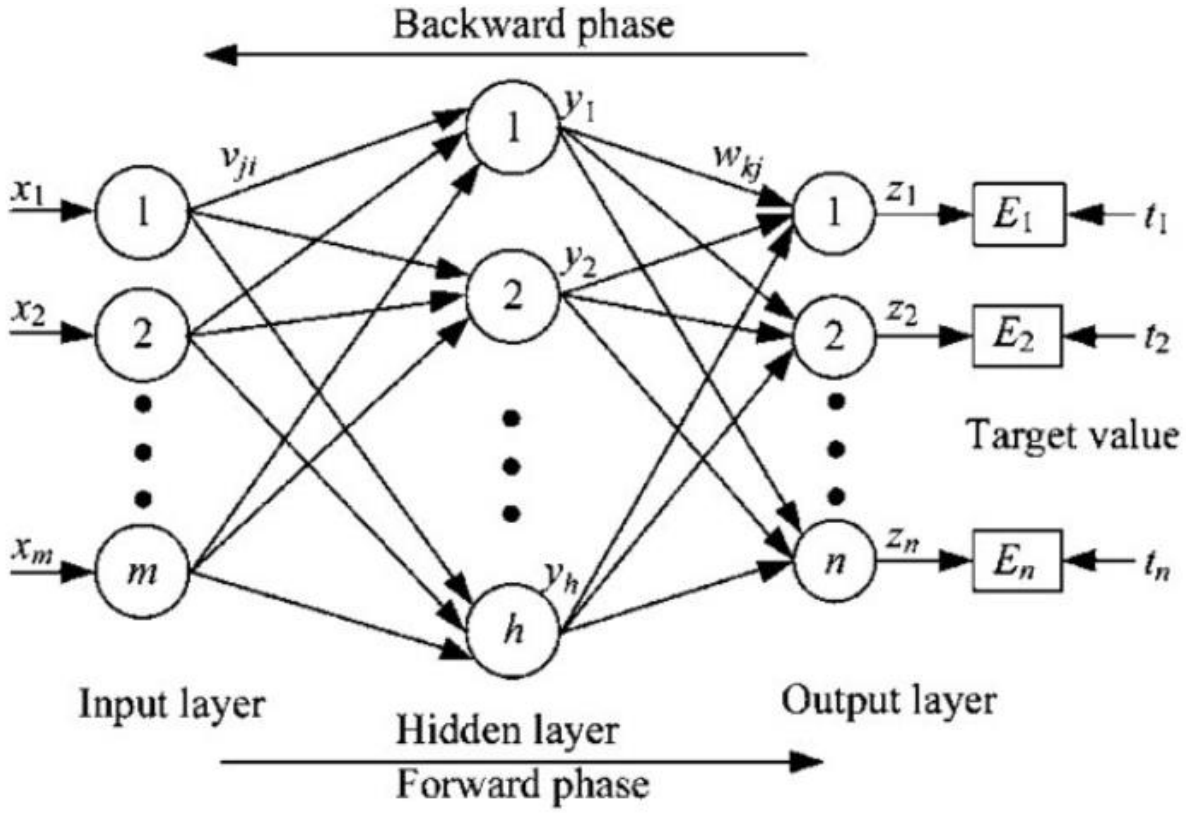

Figure 7-2 BP neural network with single hidden layer (Rumelhart et al., 1985)

ANNs can be described as simplified models that are formed by layers consisting of neurons, amongst the layers being interconnected by identical weight sets. The information which is given as the initial input goes through the input layer as neurons, after which the different transfer functions can be used to generate the output. The transfer function used in the study are expressed as

a. Log sigmoid transfer-function

$$f(x) = logsig(n) = \frac{1}{1 + e^{-n}} \tag{7-7}$$

b. Tan sigmoid transfer function

$$f(x) = tansig(n) = \frac{2}{1 + e^{-n}} - 1 \tag{7-8}$$

The interconnection between the weights in the learning process are adjusted in the input values, and this process is important in the ANN model. The algorithm of BP was adopted for training of the model. The hidden layer(s) is responsible for error reduction of the network by back propagation of the data from the output to the input in a sequential practice known as “incorporation”, until the target output is achieved by the network.

Hence, the objective is the application of specific inputs in the network to get accurate outputs using an error function, expressed as

$$E = \frac{1}{n}\sum (Dx - 0x)^2 \tag{7-9}$$

In the model test, the gap resonance response was simulated with the numerical simulation using a simplified vessel geometry shown in Figure 5-2 and Figure 5-3. Artificial neural network can efficiently setup a multilayer nonlinear network using transfer functions to optimize the numerical results from the different testing conditions. Using adaptive processing of the data and performing parallel processing of self-learning, the weights and thresholds in the neural network model can be obtained. (Walczak, 2018).

The weights and thresholds are adjusted by the network based on the prediction error. It has the ability to learn and store lots of input and output numbers for model mapping, hence it is not necessary to pre-set the model’s transfer function and mathematical equations. The general procedure for backward propagation network training is provided by Wang (2005).

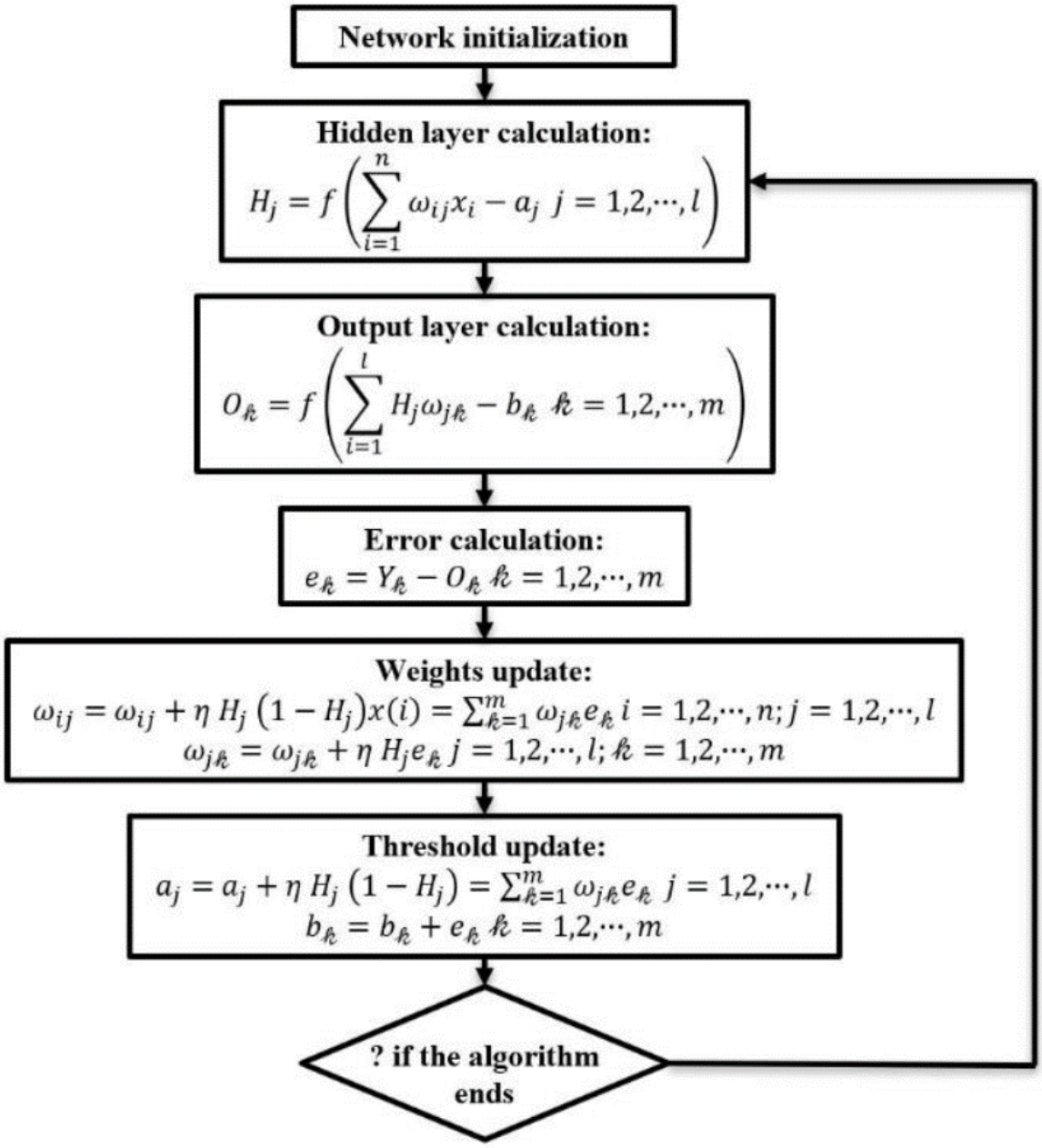

Figure 7-3 ANN calculation steps flow chart (Wang, 2005)

7.3.1 Backward phase algorithm and data selection

The backwards propagation is used to train a network via pairs of inputs and outputs till a function is created by the network (Haykin and Network, 2004). Different functions with constant architectural structure comprising of [(input-hidden layers-output) (2-20-2)] were trained using the LOGSIG and TANSIG functions in the input layer and LOGSIG function used in the output layer for the end results.

The preferred network structure design can be gotten by choosing various number of neurons in one or more hidden layers where the minimum number of neurons can be found using (7-10)

$$Number\ pf\ Hidden\ layers\ (HN) = Number\ of\ Input\ layers\ (IN) + 1 \quad (7\text{-}10)$$

The most important component for a successful execution of an ANN model is the dataset, which is important for ANN model learning. MATLAB is used to implement the algorithm based on BP neural network theory. The multi hidden layer structure is adopted for the algorithm to increase the accuracy.

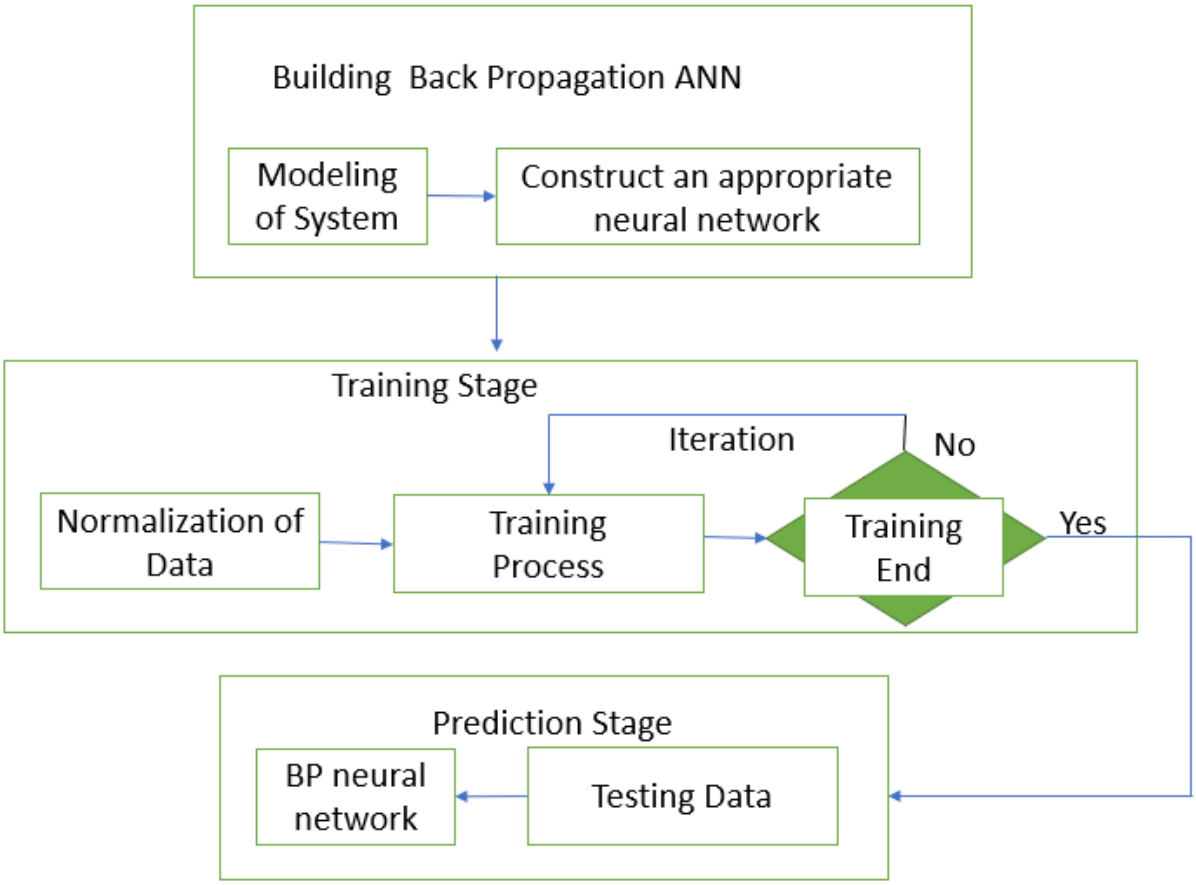

Figure 7-4 Algorithm flowchart of Backward propagation ANN

The data set for the side-by-side configuration based on gap distance, vessel draft, wave direction and wave frequency for the gap resonance response with a total of 450

data from the model test and 1800 from the simulation. The results from SIMA and experiment will be utilized as the primary data. The specific classification is shown in Table 7-2. While Table 7-3 is a additional explanation of Table 7-2, which shows the key parts of input and output data.

Table 7-2 ANN data selection

Test Cases	Total set	Training input data	Training output data	Test input data	Test output data
9	540	1-480	1-480	481-540	481-540

Table 7-3 ANN data

Test case	Input data	Output data
9	Wave frequency, wave direction, gap distance, vessel draft	Gap wave elevation

In the test cases, the training set there was a random selection of data. By disrupting the data, the input data can satisfy the independent distribution condition. It also enables convergence of the model. The data is normalised before training, which is all data is converted to 0 and 1. The min-max normalization is used with the MATLAB function mapminmax.

$$x_k = \frac{(x_k - x_{min})}{(x_{max} - x_{min})} \tag{7-11}$$

x_{max} is the largest number in the data sequence, x_{min} is the smallest number of the data sequence. The data normalisation is to reduce the large network prediction error, hence the different order of magnitudes are removed in the input and output data.

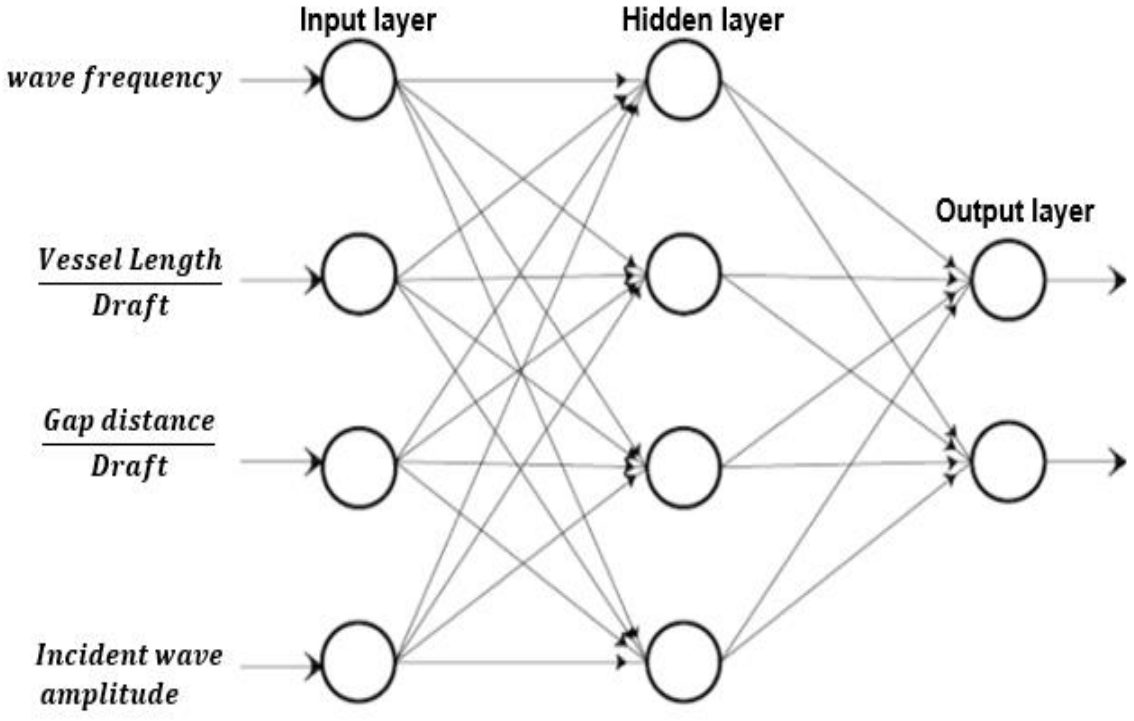

Figure 7-5 Construction of proposed ANN model

As mentioned, the adopted training algorithm that was implemented was the resilient BP (back propagation) with maximum epochs number in the simulation used which was 150; the ANN model was established within the MATLAB environment.

7.3.2 ANN prediction and Error Analysis

From Figure 7-6, Figure 7-7and Figure 7-8 it can be seen that numerical results after optimization by ANN maintain the same pattern as the model test with some points not relatively accurate.

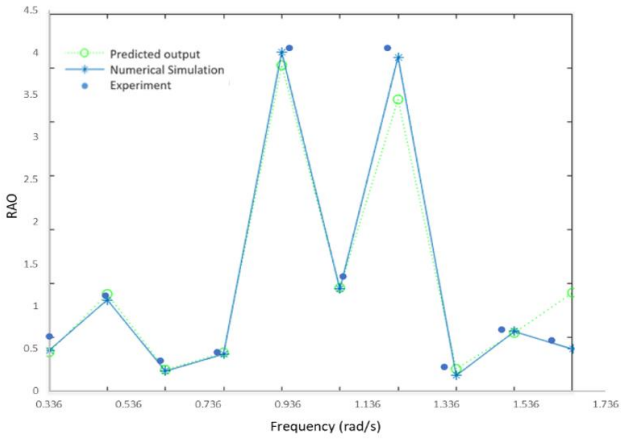

Figure 7-6 ANN, Numerical and Experimental prediction 33mm gap distance

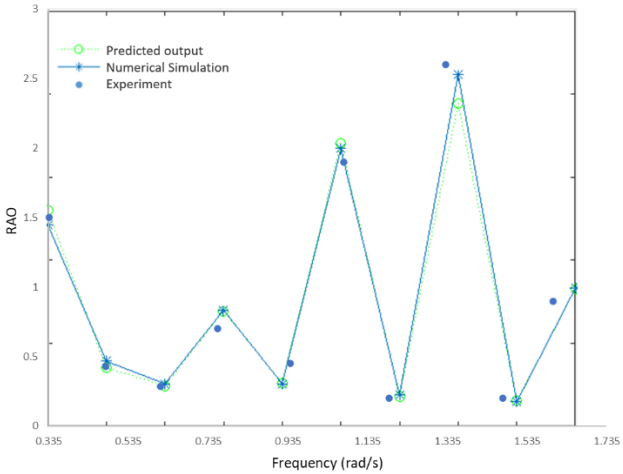

Figure 7-7 ANN, Numerical and Experimental prediction 67mm gap distance

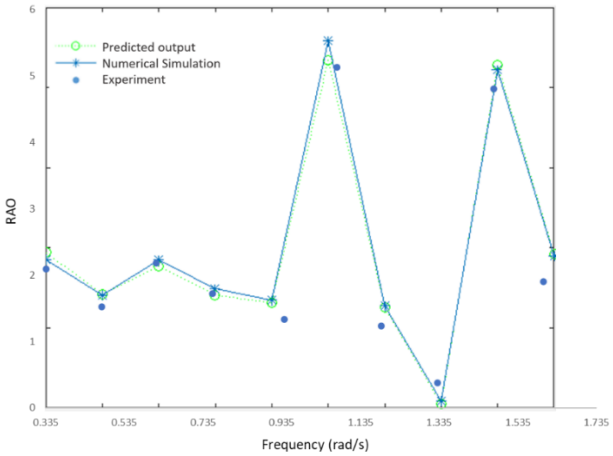

Figure 7-8 ANN, Numerical and Experimental prediction 67mm gap distance

Table 7-4 predicted resonance frequencies

Frequencies (rad/s)	33mm	53mm	67mm
0.337	-	-	-
0.478	-	-	-
0.615	-	-	-
0.759	-	-	-
0.901	✓	-	-
1.045	-	✓	✓
1.18	✓	-	-
1.331	-	✓	-
1.475	-	-	✓
1.618	-	-	-

The maximum resonance response occurs for a gap distance of 67mm at a frequency of 1.045rad/s with a wave amplitude of 5.75mm, followed by the gap distance of 33mm at a resonance frequency of 0.901rad/s and wave amplitude of 4.25mm. While the gap distance of 53mm experienced the least resonance response of wave amplitude of 2.5mm. From the observation of the graph the resonance frequencies comparison for the ANN and numerical and experiment have few minorities large prediction error. The frequencies of the resonance response are similar to that of the model test and numerical simulation results, hence the ANN method which is suitable for nonlinear multi-layer prediction is acceptable for our case study.

7.3.3 Error Analysis

Table 7-5, Figure 7-9, Figure 7-10 and Figure 7-11 gives a comparison of the percentage error of the gap amplitude which allows a better intuitive comparison of the differences between the ANN and the numerical simulation potential flow theory. It can be observed that the percentage error of the numerical simulation results after optimization by ANN is reduced at some of the wave frequencies. ANN sometimes over predicts and underpredicts the response amplitude in the gap. With the largest overpredicted amplitude at 34.21% for the gap distance 53mm and the largest underpredicted amplitude at 28.94% at gap distance 53mm. However, the magnitude of the wave elevation is small.

The percentage error for few frequencies are high but the actual amplitude difference between the ANN and numerical simulation results is small. However, the results of the ANN may be further optimized, to significantly reduce the error.

Table 7-5 ANN and Numerical Comparison

Frequency	Gap distances					
	33mm		53mm		67mm	
	ANN	Num	ANN	Num	ANN	Num
0.337	0.64	0.624	1.5	1.49	2.09	2.10
0.478	1.13	1.14	0.43	0.44	1.52	1.48
0.615	0.36	0.461	0.284	0.27	2.185	2.186
0.759	0.46	0.596	0.7	0.63	1.72	1.692
0.901	3.95	4.083	0.45	0.249	1.33	1.242
1.045	1.35	1.371	1.9	2.210	5.13	5.144
1.18	3.45	4.073	0.2	0.304	1.235	1.118
1.331	0.28	0.261	2.6	2.215	0.38	0.199
1.475	0.73	0.656	0.2	0.250	4.807	4.709
1.618	0.60	0.847	0.9	0.80	1.9	1.85

Table 7-6 Average error comparison (%)

Frequency	% error 33mm	% error 53mm	% error 67mm
0.337	-2.56	-0.67	0.48
0.478	0.88	2.27	-2.70
0.615	21.91	-5.19	0.05
0.759	22.82	-11.11	-1.65
0.901	3.26	-28.94	-7.09
1.045	1.53	14.03	0.27
1.180	15.30	34.21	-10.47
1.331	-7.28	-17.38	-22.98
1.475	-11.28	20.00	-2.08
1.618	29.16	-12.50	-2.70
Average	4.95	0.80	-5.13

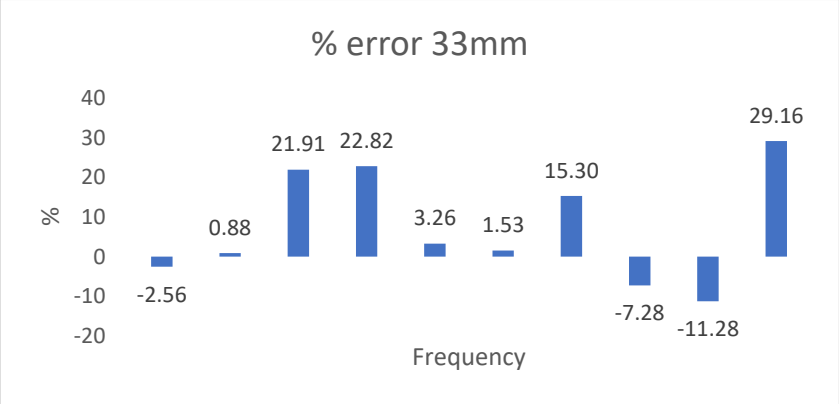

Figure 7-9 Average error comparison (%) with ANN and Numerical simulation for gap distance 33mm

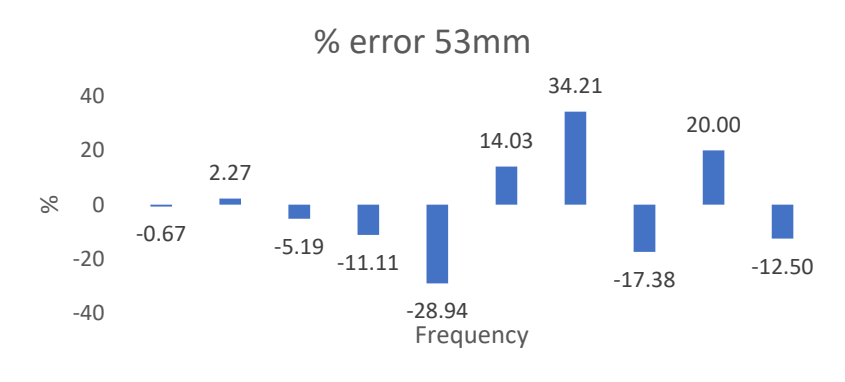

Figure 7-10 Average error comparison (%) with ANN and Numerical simulation for gap distance 53mm

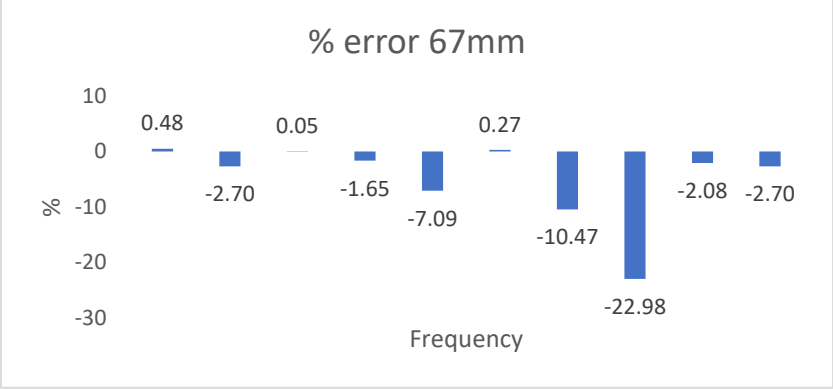

Figure 7-11 Average error comparison (%) with ANN and Numerical simulation for gap distance 67mm

Chapter 8. CONCLUSION

This research presents the novel approach of using artificial neural network ANN to predict the gap resonance response for the FLNG side-by-side offloading with training data obtained from the model test, using a new combination of models with different sizes and numerical simulation done with a potential flow solver. For gap resonance prediction using ANN, a feed forward back propagation network that comprises of different transfer functions (log and tan sigmoid) including one hidden layer made of a limited range of neurons was used. Model test was initially conducted with different test case parameters including wave frequency, gap distance, vessel draft and wave direction and numerical simulation was carried out using the potential flow solver HydroD and SIMA. Artificial damping was introduced to add a viscous damping effect in the potential flow solver and the calibrated damping factor was obtained when the comparisons between the gap RAOs were made and numerical data showed satisfactory agreement with the experiment for our test cases

Nonlinear curve fitting method and a simplified semi-empirical analysis was also carried out to predict the gap resonance. The curve fitting enabled us to obtain correlation coefficients for the model. While an empirical analysis was conducted for the focused wave group where the amplitude spectrum for the wave group is gaussian in nature.

Finally, a numerical analysis was carried out to analyse the hydrodynamic performance to the side-by-side offloading operation via frequency domain analysis after which an integrated time domain analysis was done to include the connecting system, the reliability of the result was done using comparative analysis.

The primary aim of better understanding the phenomenon of gap resonance was achieved and a further analysis of the hydrodynamic performance of a side-by-side FLNG system was done. The following points summarize the research with additions to the existing body of knowledge:

1. An extensive set of model test was carried out using a new combination of fixed rectangular hulls sizes under the excitation of regular waves, irregular waves and focused waves. it was observed that for the variation of gap distances in regular wave the amplification factor increases as the gap

distance reduces. There was also an increase in wave amplification in oblique sea cases compared to the beam sea case during resonance frequencies. We observed that due to the difference in model sizes, the gap RAOs at different location in the gap varied both along and across the gap. A phenomenon of slamming effect was noticed on the wave gauge located at the weatherside of the larger model when directly impacted by the propagating wave during gap resonance.

2. The results for the nonlinear curve fitting using the model test and numerical data are relatively reliable which can be considered as standard with a 95% confidence level. The p-value was used to evaluate the correlating coefficients with p-values>0.05 becoming insignificant. A nonlinear model was proposed but more work need to be done on the practical implementation in ocean waves.
3. An ANN model method for prediction of gap resonance is a new approach. It was established and tested. The provided results can be acceptable for engineering practice and within the average range of correlation coefficient R^2 92% -97%. The input layer parameters of $\frac{\text{Vessels Length}}{\text{Draft}}$ and $\frac{\text{gap distance}}{\text{Draft}}$ for both the FLNG and LNGC model which can be adjusted to suit the vessels sizes. Although this method does not capture the complex curvature of vessels, it can give us an approximate of gap resonance with the addition of the other parameters, wave frequency and direction.
4. An semi-empirical formula for calculating the gap resonance response amplitude operator (RAO) of a side-by-side configured FLNG-LNGC system is formulated in this study. The analysis of the focused wave with gaussian spectrum was carried out, where the equation for amplitude spectrum is used as the governing equation and the incident wave frequency, which is one of the key parameters that governs the amplitude spectra criterion, is obtained from its analytically of model test data. The analytical formula was then modified based on both physical considerations and laboratory data.
5. The gap resonance modes have spectra shapes that are very spiky hence a small change in the frequency from the gap resonance will bring about a significant reduction of the response. A numerical fit to the model test data gives linear damping coefficients for each test case and for each resonance

mode. It clearly shows that the artificial damping introduced matches the experimental data and a damping coefficient of 0.03 was selected to suppress the over-predicted gap resonance response.

6. A description of spatial variation of the water surface elevation in the gap region between the models was illustrated. For the irregular wave analysis, probability of exceedance curves was plotted and used to calculate the return period for the different wave gauge location to analyse which position along the gap region is most likely to experience more resonance wave amplification, from the investigation wave gauge 5 has a lower return period therefore the likelihood of resonance is higher for that location. This can indicate the most dangerous areas within the gap region where equipment like fender can be placed.

8.1 Recommendations and Further Work

While the present study has added to the current knowledge for gap resonance prediction and the hydrodynamic characteristics for the FLNG system in side-by-side configuration, there was time constraints due to the impact from the COVID-19 pandemic, other interesting assessments relating to this research could not be explored. Hence, the following have been recommended for further work.

- The development of an alternative technique to the feed-forward backpropagation artificial neural network, such as radial basis function network (RBF) and support vector machines (SVMs). These techniques can provide a broader array of options for engineering practice.
- The empirical can be expanded theoretically to include a wider option of vessel types.
- The hydrodynamic characteristic of the vessel and the connecting system can include modelling of the offloading arm and internal sloshing in the FLNG and LNGC tanks.

References

ABLOW, C. & SCHECHTER, S. 1983. Numerical simulation of undersea cable dynamics. *Ocean engineering,* 10**,** 443-457.

BAI, X.-L., YANG, K.-Y. & WANG, W.-Y. 2001. Large deformation contact analysis of incompressible hyperelastic material. *JOURNAL-SICHUAN UNIVERSITY ENGINEERING SCIENCE EDITION,* 33**,** 16-19.

BEARMAN, P. W. 1984. Vortex shedding from oscillating bluff bodies. *Annual review of fluid mechanics,* 16**,** 195-222.

BERG, T. E. & BAKKE, J. 2008. Ship-to-ship {LNG} transfer in Artic waters. *Proceedings of the ASME 27th International Conference on Offshore Mechanics and Arctic Engineering, OMAE2008, Estoril, Portugal.*

BUCHNER, B., VAN DIJK, A. & DE WILDE, J. 2001. Numerical multiple-body simulations of side-by-side mooring to an FPSO. *The Eleventh International Offshore and Polar Engineering Conference.* International Society of Offshore and Polar Engineers.

BUNNIK, T., PAUW, W. & VOOGT, A. 2009. Hydrodynamic Analysis For Side-by-Side Offloading. *The Nineteenth International Offshore and Polar Engineering Conference.* Osaka, Japan: International Society of Offshore and Polar Engineers.

CAI, Y. & CHEN, S. 1994. Dynamics of elastic cable under parametric and external resonances. *Journal of engineering mechanics,* 120**,** 1786-1802.

CALLAN, M., LINTON, C. & EVANS, D. 1991. Trapped modes in two-dimensional waveguides. *Journal of Fluid Mechanics,* 229**,** 51-64.

CHA, D. F., ZHANG, H. & BLUMENSTEIN, M. 2011. Prediction of maximum wave-induced liquefaction in porous seabed using multi-artificial neural network model. *Ocean engineering,* 38**,** 878-887.

CHAKRABARTI, S. K. 1987. *Hydrodynamics of offshore structures*, WIT press.

CHAKRABARTI, S. K. 2001. Response due to moored multiple structure interaction. *Marine structures,* 14**,** 231-258.

CHAKRABARTI, S. K. & COTTER, D. C. 1979. Motion analysis of articulated tower. *Journal of the Waterway, Port, Coastal and Ocean Division,* 105**,** 281-292.

CHEN, G.-R. & FANG, M.-C. 2001. Hydrodynamic interactions between two ships advancing in waves. *Ocean Engineering,* 28**,** 1053-1078.

CHEN, X.-B. Hydrodynamic analysis for offshore LNG terminals. Proceedings of the 2nd International Workshop on Applied Offshore Hydrodynamics, Rio de Janeiro, 2005a.

CHEN, X.-B. 2005b. Hydrodynamic analysis for offshore LNG terminals. *Proceedings of the 2nd International Workshop on Applied Offshore Hydrodynamics, Rio de Janeiro.*

CHITRAPU, A. S. M., MORDFIN, T. G. & CHANCE, H. M. 2007. Efficient time-domain simulation of side-by-side moored vessels advancing in waves. *ASME 2007 26th International Conference on Offshore Mechanics and Arctic Engineering.* American Society of Mechanical Engineers.

CHUA, K. H., DE MELLO, P., MALTA, E., VIEIRA, D., WATAI, R., RUGGERI, F., EATOCK TAYLOR, R., NISHIMOTO, K. & CHOO, Y. S. Irregular seas model experiments on side-by-side barges. The 28th Intl Offshore Polar Engng Conf., ISOPE, 2018.

CHUA, K. H., EATOCK TAYLOR, R. & CHOO, Y. S. Hydrodynamics of side-by-side fixed floating bodies. International Conference on Offshore Mechanics and Arctic Engineering, 2016. American Society of Mechanical Engineers, V007T06A060.

CLAUSS, G. F., DUDEK, M. & TESTA, D. Gap effects at side-by-side LNG-transfer operations. International Conference on Offshore Mechanics and Arctic Engineering, 2013. American Society of Mechanical Engineers, V001T01A042.

DEBOECK, G. & KOHONEN, T. 2013. *Visual explorations in finance: with self-organizing maps*, Springer Science & Business Media.

DEO, M. C., JHA, A., CHAPHEKAR, A. & RAVIKANT, K. 2001. Neural networks for wave forecasting. *Ocean engineering,* 28**,** 889-898.

DIBIKE, Y. B. 2002. Developing generic hydrodynamic models using artificial neural networks. *Journal of Hydraulic Research,* 40**,** 183-190.

DONG-YING, W. 2009. Finite element analysis of structure improved of rubber fender front panel. *Shanxi Architecture,* 9.

EVANS, D. & PORTER, R. 1997. Near-trapping of waves by circular arrays of vertical cylinders. *Applied Ocean Research,* 19**,** 83-99.

FALTINSEN, O. 1990. Sea loads on ships and ocean structures. *Cambridge University, Cambridge, UK*.

FALTINSEN, O. M., ROGNEBAKKE, O. F. & TIMOKHA, A. N. 2007. Two-dimensional resonant piston-like sloshing in a moonpool. *Journal of Fluid Mechanics,* 575**,** 359-397.

FENG, X. & BAI, W. 2015. Wave resonances in a narrow gap between two barges using fully nonlinear numerical simulation. *Applied Ocean Research,* 50**,** 119-129.

FENG, X., BAI, W., CHEN, X. B., QIAN, L. & MA, Z. H. 2017. Numerical investigation of viscous effects on the gap resonance between side-by-side barges. *Ocean Engineering,* 145**,** 44-58.

FITZGERALD, C. J., TAYLOR, P. H., TAYLOR, R. E., GRICE, J. & ZANG, J. 2014. Phase manipulation and the harmonic components of ringing forces on a surface-piercing column. *Proceedings of the Royal Society A: Mathematical, Physical and Engineering Sciences,* 470**,** 20130847.

FRENCH, M. N., KRAJEWSKI, W. F. & CUYKENDALL, R. R. 1992. Rainfall forecasting in space and time using a neural network. *Journal of hydrology,* 137**,** 1-31.

FU, L. 1999. Knowledge discovery based on neural networks. *Communications of the ACM,* 42**,** 47-50.

GIACOSA, A., MAURIES, B. & LAGARRIGUE, V. Joining Forces to Unlock LNG Tandem Offloading Using 20? LNG Floating Hoses: An Example of Industrial Collaboration. Offshore Technology Conference, 2016. Offshore Technology Conference.

GRACZYK, M. & MOAN, T. 2008. A probabilistic assessment of design sloshing pressure time histories in LNG tanks. *Ocean Engineering,* 35**,** 834-855.

GRUBERT, J. P. 1995. Prediction of estuarine instabilities with artificial neural networks. *Journal of Computing in Civil Engineering,* 9**,** 266-274.

HARICHANDAN, A. B. & ROY, A. 2012. Numerical investigation of flow past single and tandem cylindrical bodies in the vicinity of a plane wall. *Journal of Fluids and Structures,* 33**,** 19-43.

HAYKIN, S. & NETWORK, N. 2004. A comprehensive foundation. *Neural networks,* 2**,** 41.

HEO, J.-K., PARK, J.-C., KOO, W.-C. & KIM, M.-H. 2014. Influences of vorticity to vertical motion of two-dimensional moonpool under forced heave motion. *Mathematical Problems in Engineering,* 2014.

HONG, H., SHENG, Y. & WANG, H. 2000. The Measurement System of the Mechanical

Parameters for the Rubber Fender. *Electronic Measurement Technology*.

HONG, S. Y., KIM, J. H., CHO, S. K., CHOI, Y. R. & KIM, Y. S. 2005. Numerical and experimental study on hydrodynamic interaction of side-by-side moored multiple vessels. *Ocean Engineering,* 32**,** 783-801.

HONG, S. Y., KIM, J. H., KIM, H. J. & CHOI, Y. R. 2002. Experimental study on behavior of tandem and side-by-side moored vessels. *The Twelfth International Offshore and Polar Engineering Conference.* International Society of Offshore and Polar Engineers.

HU, J., KHAN, F. & ZHANG, L. 2021. Dynamic resilience assessment of the Marine LNG offloading system. *Reliability Engineering & System Safety,* 208**,** 107368.

HUIJSMANS, R. H. M., PINKSTER, J. A. & DE WILDE, J. J. 2001. Diffraction and radiation of waves around side-by-side moored vessels. *The Eleventh International Offshore and Polar Engineering Conference.* International Society of Offshore and Polar Engineers.

HURTADO, J., LONDONO, J. & MEZA, M. 2001. On the applicability of neural networks for soil dynamic amplification analysis. *Soil Dynamics and Earthquake Engineering,* 21**,** 579-591.

INOUE, Y. & ISLAM, M. R. 1999. Comparative study of numerical simulation and the experimental results for a parallely connected FPSO and LNG in waves. *The Ninth International Offshore and Polar Engineering Conference.* International Society of Offshore and Polar Engineers.

INOUE, Y. & KAMRUZZAMAN, M. 2005. Numerical simulation on mooring performance of LNG-FPSO system in realistic seas. *ASME 2005 24th International Conference on Offshore Mechanics and Arctic Engineering.* American Society of Mechanical Engineers.

ISLAM, M. R. & MURAI, M. 2013. Dynamic interaction of parallel moving ships in close proximity. *Journal of Marine Science and Application,* 12**,** 261-271.

JEAN-ROBERT, F., NACIRI, M. & XIAO-BO, C. 2006. Hydrodynamics of two side-by-side vessels experiments and numerical simulations. *The Sixteenth International Offshore and Polar Engineering Conference.* International Society of Offshore and Polar Engineers.

JIN, Y., CHAI, S., DUFFY, J., CHIN, C. & BOSE, N. 2019. Hydrodynamics of a conceptual FLNG system in side-by-side offloading operation. *Ships and Offshore Structures,* 14**,** 104-124.

JOHN, F. 1950. On the motion of floating bodies II. Simple harmonic motions. *Communications on pure and applied mathematics,* 3**,** 45-101.

KASHIWAGI, M., ENDO, K. & YAMAGUCHI, H. 2005. Wave drift forces and moments on two ships arranged side by side in waves. *Ocean engineering,* 32**,** 529-555.

KASPERKIEWICZ, J., RACZ, J. & DUBRAWSKI, A. 1995. HPC strength prediction using artificial neural network. *Journal of Computing in Civil Engineering,* 9**,** 279-284.

KIM, C., BAE, G., HONG, S., PARK, C., MOON, H. & SHIN, H. 2001. Neural network based prediction of ground surface settlements due to tunnelling. *Computers and Geotechnics,* 28**,** 517-547.

KIM, M. S., HA, M. K. & KIM, B. W. 2003. Relative Motions between LNG-FPSO and Side-by-Side positioned LNG carrier in Waves. *The Thirteenth International*

Offshore and Polar Engineering Conference. International Society of Offshore and Polar Engineers.

KIM, Y.-B. 2003. *Dynamic analysis of multiple-body floating platforms coupled with mooring lines and risers*, Texas A&M University.

KODAN, N. 1984. The motions of adjacent floating structures in oblique waves. *Journal of energy resources technology,* 106**,** 199-205.

KOKKINOWRACHOS, K. & ZIBELL, H. Wave interaction with multiple cross-sections in finite water depth. Proc. of the 3rd Int. Conf. on Offshore Mechanics and Arctic Engineering, New Orleans, 1984a. 144-157.

KOKKINOWRACHOS, K. & ZIBELL, H. Wave interaction with multiple cross-sections in finite water depth. Proc. 3rd International Symposium on Offshore Mechanics and Arctic Engineering (OMAE), 1984b.

KOO, B. J. & KIM, M. H. 2005. Hydrodynamic interactions and relative motions of two floating platforms with mooring lines in side-by-side offloading operation. *Applied Ocean Research,* 27**,** 292-310.

KORSMEYER, F., LEE, C., NEWMAN, J. & SCLAVOUNOS, P. The analysis of wave effects on tension-leg platforms. 7th International Conference on Offshore Mechanics and Arctic Engineering, Houston, Texas, 1988. 14.

KRISTIANSEN, T. & FALTINSEN, O. 2008. Application of a vortex tracking method to the piston-like behaviour in a semi-entrained vertical gap. *Applied Ocean Research,* 30**,** 1-16.

KRISTIANSEN, T. & FALTINSEN, O. 2010. A two-dimensional numerical and experimental study of resonant coupled ship and piston-mode motion. *Applied Ocean Research,* 32**,** 158-176.

KRISTIANSEN, T. & FALTINSEN, O. M. 2012. Gap resonance analyzed by a new domain-decomposition method combining potential and viscous flow DRAFT. *Applied Ocean Research,* 34**,** 198-208.

KUBAT, M. 1995. Neural networks and fuzzy systems: A dynamical systems approach to machine intelligence by Bart Kosko, Prentice Hall, Englewood Cliffs, NJ, 1992, pp 449,£ 24.96, ISBN 0-13-612334. *The Knowledge Engineering Review,* 10**,** 219-220.

KUZNETSOV, N. & MCIVER, P. 1997. On uniqueness and trapped modes in the water-wave problem for a surface-piercing axisymmetric body. *Quarterly Journal of Mechanics and Applied Mathematics,* 50**,** 565-580.

KYOZUKA, Y. & YOSHIDA, K. 1981. On wave-free floating-body forms in heaving oscillation. *Applied Ocean Research,* 3**,** 183-194.

LEE, C.-H. 1995. *WAMIT theory manual*, Massachusetts Institute of Technology, Department of Ocean Engineering.

LEE, D. H. 2002. Nonlinear stability analysis and motion control of tandem moored tankers. *PhD diss., Ph. D. dissertation. Seoul: Naval Architecture and Ocean Engineering, Seoul National University*.

LEE, H., CHOI, H.-S., LEE, D., KIM, B. & SHIN, Y. S. 2010. A motion analysis of two floaters in shallow water using Boussinesq equations. *The Twentieth International Offshore and Polar Engineering Conference.* International Society of Offshore and Polar Engineers.

LEE, I.-H., PARK, M.-K., MOON, J.-S., SIM, W.-S. & SHIN, H.-S. Experimental and Numerical Investigations Into the Station Keeping and the Offloading Performances of Hyundai LNG-FPSO. International Conference on Offshore Mechanics and Arctic Engineering, 2013. American Society of Mechanical Engineers, V001T01A033.

LEE, S. C., PARK, S. K. & LEE, B. H. 2001. Development of the approximate analytical model for the stub-girder system using neural networks. *Computers & Structures,* 79**,** 1013-1025.

LEE, T., TSAI, C., JENG, D. & SHIEH, R. 2002. Neural network for the prediction and supplement of tidal record in Taichung Harbor, Taiwan. *Advances in Engineering Software,* 33**,** 329-338.

LIANG, H., CHUA, K. H., WANG, H. C. & CHOO, Y. S. 2021. Numerical and experimental investigations into fluid resonance in a gap between two side-by-side vessels. *Applied Ocean Research,* 111**,** 102581.

LU, L., CHENG, L., TENG, B. & SUN, L. 2010. Numerical simulation and comparison of potential flow and viscous fluid models in near trapping of narrow gaps. *Journal of Hydrodynamics, Ser. B,* 22**,** 120-125.

LU, L., TENG, B., CHENG, L. & LI, Y. Numerical simulation of hydrodynamic resonance in a narrow gap between twin bodies subject to water waves. The Eighteenth International Offshore and Polar Engineering Conference, 2008. OnePetro.

LU, L., TENG, B., SUN, L. & CHEN, B. 2011. Modelling of multi-bodies in close proximity under water waves—Fluid forces on floating bodies. *Ocean Engineering,* 38**,** 1403-1416.

MAIER, H. R. & DANDY, G. C. 1997. Modelling cyanobacteria (blue-green algae) in the River Murray using artificial neural networks. *Mathematics and Computers in Simulation,* 43**,** 377-386.

MAIER, H. R. & DANDY, G. C. 2000. Neural networks for the prediction and forecasting of water resources variables: a review of modelling issues and applications. *Environmental modelling & software,* 15**,** 101-124.

MAKARYNSKYY, O., MAKARYNSKA, D., KUHN, M. & FEATHERSTONE, W. 2004. Predicting sea level variations with artificial neural networks at Hillarys Boat Harbour, Western Australia. *Estuarine, Coastal and Shelf Science,* 61**,** 351-360.

MANIAR, H. & NEWMAN, J. 1997. Wave diffraction by a long array of cylinders. *Journal of fluid mechanics,* 339**,** 309-330.

MARKENG, K., VADA, T. & PAN, Z. Y. Investigation of free surface damping models with applications to gap resonance problems. ASME 2017 36th International Conference on Ocean, Offshore and Arctic Engineering, 2017. American Society of Mechanical Engineers Digital Collection.

MCCORMICK, M. E. 2009. *Ocean engineering mechanics: with applications*, Cambridge University Press.

MCIVER, M. 1996. An example of non-uniqueness in the two-dimensional linear water wave problem. *Journal of Fluid Mechanics,* 315**,** 257-266.

MCIVER, M. & PORTER, R. 2002. Trapping of waves by a submerged elliptical torus. *Journal of Fluid Mechanics,* 456**,** 277-293.

MCIVER, P. 2005. Complex resonances in the water-wave problem for a floating structure. *Journal of Fluid Mechanics,* 536**,** 423-443.

MCIVER, P. & MCIVER, M. 2006. Trapped modes in the water-wave problem for a freely floating structure. *Journal of Fluid Mechanics,* 558**,** 53-67.

MCIVER, P. & MCIVER, M. 2007. Motion trapping structures in the three-dimensional water-wave problem. *Journal of Engineering Mathematics,* 58**,** 67-75.

MCIVER, P. & NEWMAN, J. 2003. Trapping structures in the three-dimensional water-wave problem. *Journal of Fluid Mechanics,* 484**,** 283-301.

MOLIN, B. 2001. On the piston and sloshing modes in moonpools. *Journal of Fluid Mechanics,* 430**,** 27-50.

MOLIN, B. 2017. On natural modes in moonpools with recesses. *Applied Ocean Research,* 67**,** 1-8.

MOLIN, B., REMY, F., CAMHI, A. & LEDOUX, A. 2009. Experimental and numerical study of the gap resonances in-between two rectangular barges. *13th congress of international maritime association of mediterranean.*

MOLIN, B., REMY, F., KIMMOUN, O. & STASSEN, Y. 2002. Experimental study of the wave propagation and decay in a channel through a rigid ice-sheet. *Applied ocean research,* 24**,** 247-260.

MOLIN, B., ZHANG, X., HUANG, H. & REMY, F. 2018. On natural modes in moonpools and gaps in finite depth. *Journal of Fluid Mechanics,* 840**,** 530-554.

MORADI, N., ZHOU, T. & CHENG, L. 2015. Effect of inlet configuration on wave resonance in the narrow gap of two fixed bodies in close proximity. *Ocean Engineering,* 103**,** 88-102.

MORILHAT, E. 2019. FLNG Offloading for Real Verdict from the Field. *International Conference & Exhibition on Liquefied Natural Gas*.

MOTULSKY, H. & CHRISTOPOULOS, A. 2004. *Fitting models to biological data using linear and nonlinear regression: a practical guide to curve fitting*, Oxford University Press.

NACIRI, M., WAALS, O. & DE WILDE, J. 2007. Time Domain Simulations of Side-by-Side Moored Vessels: Lessons Learnt From a Benchmark Test. *ASME 2007 26th International Conference on Offshore Mechanics and Arctic Engineering.* American Society of Mechanical Engineers.

NAM, B. W., KIM, Y. & HONG, S. Y. 2015. Hydrodynamic interaction between two barges during berthing operation in regular waves. *Ocean Engineering,* 106**,** 317-328.

NEWBY, M. A. & PAUW, W. SS-Safe Transfer of Liquefied Gas in the Offshore Environment. Offshore Technology Conference, 2010. Offshore Technology Conference.

NEWMAN, J. 1977. Marine hydrodynamics. 1st. The MIT Press.

NEWMAN, J. 1999. Radiation and diffraction analysis of the McIver toroid. *Journal of Engineering Mathematics,* 35**,** 135-147.

NEWMAN, J. Progress in wave load computations on offshore structures. Invited Lecture, 23th OMAE Conference, Vancouver, Canada, http://www. wamit. com/publications, 2004.

NEWMAN, J. & SCLAVOUNOS, P. The computation of wave loads on large offshore structures. BOSS'88, 1988. 605-622.

NEWMAN, J. N. 2001. Wave effects on multiple bodies. *Hydrodynamics in ship and ocean engineering,* 3**,** 3-26.

NING, D., ZHU, Y., ZHANG, C. & ZHAO, M. 2018. Experimental and numerical study on wave response at the gap between two barges of different draughts. *Applied Ocean Research,* 77**,** 14-25.

NWAFOR, J. C. Numerical Investigation on Coupling Dynamic Performance of FLNG and LNG Carriers. The 32nd International Ocean and Polar Engineering Conference, 2022. OnePetro.

NWAFOR, J. C. & HU, Z. 2021. An Experimental and Numerical Analysis of Gap Resonance Applicable for FLNG Side-by-Side Offloading. *ASME 2021 40th International Conference on Ocean, Offshore and Arctic Engineering.* American Society of Mechanical Engineers Digital Collection.

OCIMF 1994. Prediction of wind and current loads on VLCCs. *2nd ed.*

.

PATRICK, A. R., COLLINS, W. G., TISSOT, P. E., DRIKITIS, A., STEARNS, J., MICHAUD, P. R. & COX, D. T. 2003. USE OF THE NCEP MESOETA DATA IN A WATER LEVEL PREDICTING NEURAL NETWORK.

PAUW, W. H., HUIJSMANS, R. H. M. & VOOGT, A. 2007. Advances in the hydrodynamics of side-by-side moored vessels. *ASME 2007 26th International Conference on Offshore Mechanics and Arctic Engineering.* American Society of Mechanical Engineers.

PERIĆ, M. & SWAN, C. 2015. An experimental study of the wave excitation in the gap between two closely spaced bodies, with implications for LNG offloading. *Applied Ocean Research,* 51**,** 320-330.

PERKINS, N. C. 1992. Modal interactions in the non-linear response of elastic cables under parametric/external excitation. *International Journal of Non-Linear Mechanics,* 27**,** 233-250.

PIANC 2002. Guidelines for the design of fender systems. Pianc Brussels, Belgium.

POLDERVAART, L., OOMEN, H. & ELLIS, J. Offshore lng transfer: A worldwide review of offloading availability. Offshore Technology Conference, 2006. Offshore Technology Conference.

PORTER, R. & EVANS, D. 2008. Examples of trapped modes in the presence of freely floating structures. *Journal of Fluid Mechanics,* 606**,** 189-207.

RHO, J.-B., KOROBKIN, A. A., JUNG, J.-J., SHIN, H.-S. & LEE, W.-S. Coupled analysis of deepwater floating system including VIV in time domain. ASME 2007 26th International Conference on Offshore Mechanics and Arctic Engineering, 2007. American Society of Mechanical Engineers, 639-649.

RUMELHART, D. E., HINTON, G. E. & WILLIAMS, R. J. 1985. Learning internal representations by error propagation. California Univ San Diego La Jolla Inst for Cognitive Science.

SAITOH, T., IWATA, H., TAKAHASHI, Y., MIAO, G. & ISHIDA, H. 2006. CHARACTERISTICS AND APPEARANCE CONDITIONS OF FLUID RESONANCE IN NARROW GAPS OF VERY LARGE FLOATING STRUCTURE COMPOSED OF RECTANGULAR MODULES. *PROCEEDINGS OF CIVIL ENGINEERING IN THE OCEAN,* 22**,** 845-850.

SHANMUGANATHAN, S. 2016. Artificial neural network modelling: An introduction. *Artificial neural network modelling.* Springer.

SHIPWAY, B. & EVANS, D. 2003. Wave trapping by axisymmetric concentric cylinders. *J. Offshore Mech. Arct. Eng.,* 125**,** 59-64.

SIMON, M. & URSELL, F. 1984. Uniqueness in linearized two-dimensional water-wave problems. *Journal of Fluid Mechanics,* 148**,** 137-154.

SINTEF, O. 2017. RIFLEX 4.10. 0 Theory Manual. *Trondheim, SINTEF Ocean.[Online]*

SOARES, C. G., TAYLOR, R. E. & EWANS, K. 2015. Safe offloading from floating LNG platforms. *Applied Ocean Research***,** 252-254.

STANDARD, B. 1991. Maritime structures. Part.

SUN, L., TAYLOR, R. E. & TAYLOR, P. H. 2010. First-and second-order analysis of resonant waves between adjacent barges. *Journal of Fluids and Structures,* 26**,** 954-978.

TAJALI, Z. & SHAFIEEFAR, M. 2011. Hydrodynamic analysis of multi-body floating piers under wave action. *Ocean Engineering,* 38**,** 1925-1933.

TAN, L., LU, L., TANG, G.-Q., CHENG, L. & CHEN, X.-B. 2019. A viscous damping model for piston mode resonance. *Journal of Fluid Mechanics,* 871**,** 510-533.

TEIGEN, P. & NIEDZWECKI, J. A Computational Study of Wave Effects Related to Side-by-Side LNG Offoading. The Sixteenth International Offshore and Polar Engineering Conference, 2006. OnePetro.

THIRUMALAIAH, K. & DEO, M. 1998. River stage forecasting using artificial neural networks. *Journal of Hydrologic Engineering,* 3**,** 26-32.

TUSIANI, M. D. & SHEARER, G. 2007. *LNG: a nontechnical guide*, PennWell Books.

URSELL, F. Trapping modes in the theory of surface waves. Mathematical Proceedings of the Cambridge Philosophical Society, 1951. Cambridge University Press, 347-358.

VAN DER VALK, C. A. C. & WATSON, A. 2005. Mooring Of LNG Carriers To A Weathervaning Floater--Side-By-Side Or Stern-To-Bow. *Offshore Technology Conference.* Offshore Technology Conference.

VAN OORTMERSSEN, G. 1976. The motions of a moored ship in waves. H. Veenman en Zonen nv.

VAN OORTMERSSEN, G. 1977. The behaviour of moored ships in waves. *Offshore Technology Conference.* Offshore Technology Conference.

VASSALOS, D., HUANG, S. & KOUROUKLIS, A. Experimental investigation of snap loading of marine cables. The Fourteenth International Offshore and Polar Engineering Conference, 2004. OnePetro.

VOOGT, A. J. & BRUGTS, H. SS: LPG & LNG offshore operations: Numerical simulations to optimize offshore offloading operations. Offshore Technology Conference, 2010. Offshore Technology Conference.

WADAM, D., SESAM USER MANUAL 2017. Wave Analysis by Diffraction and Morison theory. Ver.

WALCZAK, S. 2018. Artificial neural networks. *Encyclopedia of Information Science and Technology, Fourth Edition.* IGI Global.

WANG, K. 2005. *Applied computational intelligence in intelligent manufacturing systems*, Advanced Knowledge International Pty.

WEHAUSEN, J. V. & LAITONE, E. V. 1960. Surface waves. *Fluid Dynamics/Strömungsmechanik.* Springer.

WEI, Y., RAFIEE, A., HENRY, A. & DIAS, F. 2015. Wave interaction with an oscillating wave surge converter, Part I: Viscous effects. *Ocean Engineering,* 104**,** 185-203.

WOLGAMOT, H. A., TAYLOR, P. H., TAYLOR, R. E., VAN DEN BREMER, T., RABY, A. & WHITTAKER, C. 2016. Experimental observation of a near-motion-trapped mode: free motion in heave with negligible radiation. *Journal of Fluid Mechanics,* 786.

XU, T.-J., ZHAO, Y.-P., DONG, G.-H., LI, Y.-C. & GUI, F.-K. 2013. Analysis of hydrodynamic behaviors of multiple net cages in combined wave–current flow. *Journal of Fluids and Structures,* 39**,** 222-236.

YAN, S., MA, Q. W. & CHENG, X. 2009. Fully nonlinear hydrodynamic interaction between two 3D floating structures in close proximity. *The Nineteenth International Offshore and Polar Engineering Conference.* International Society of Offshore and Polar Engineers.

YU, X., LAKHOTIA, C. & FALZARANO, J. M. 2009. Development of a multi-body vessel dynamics simulation tool. *ASME 2009 28th International Conference on Ocean, Offshore and Arctic Engineering.* American Society of Mechanical Engineers.

ZANUTTIGH, B. & VAN DER MEER, J. W. 2008. Wave reflection from coastal structures in design conditions. *Coastal engineering,* 55**,** 771-779.

ZHAO, D., HU, Z. & CHEN, G. 2017a. Experimental investigation on dynamic responses of FLNG connection system during side-by-side offloading operation. *Ocean Engineering,* 136**,** 283-293.

ZHAO, W.-H., YANG, J.-M. & HU, Z.-Q. 2012. Hydrodynamic interaction between FLNG vessel and LNG carrier in side by side configuration. *Journal of Hydrodynamics, Ser. B,* 24**,** 648-657.

ZHAO, W., MILNE, I. A., EFTHYMIOU, M., WOLGAMOT, H. A., DRAPER, S., TAYLOR, P. & TAYLOR, R. E. 2018a. Current practice and research directions in hydrodynamics for FLNG-side-by-side offloading. *Ocean Engineering,* 158**,** 99-110.

ZHAO, W., PAN, Z., LIN, F., LI, B., TAYLOR, P. H. & EFTHYMIOU, M. 2018b. Estimation of gap resonance relevant to side-by-side offloading. *Ocean Engineering,* 153**,** 1-9.

ZHAO, W., TAYLOR, P. H., WOLGAMOT, H. A. & TAYLOR, R. E. 2018c. Linear viscous damping in random wave excited gap resonance at laboratory scale—

NewWave analysis and reciprocity. *Journal of Fluids and Structures,* 80**,** 59-76.

ZHAO, W., WOLGAMOT, H. A., TAYLOR, P. H. & EATOCK TAYLOR, R. 2017b. Gap resonance and higher harmonics driven by focused transient wave groups. *Journal of Fluid Mechanics,* 812**,** 905-939.

ZHAO, W., YANG, J., HU, Z. & TAO, L. 2014. Prediction of hydrodynamic performance of an FLNG system in side-by-side offloading operation. *Journal of Fluids and Structures,* 46**,** 89-110.

ZHAO, W., YANG, J., HU, Z. & XIE, B. 2013. Hydrodynamics of an FLNG system in tandem offloading operation. *Ocean engineering,* 57**,** 150-162.

ZHU, H.-R., ZHU, R.-C. & MIAO, G.-P. 2008. A time domain investigation on the hydrodynamic resonance phenomena of 3-D multiple floating structures. *Journal of Hydrodynamics, Ser. B,* 20**,** 611-616.

8 Appendix

Governing equations

The governing equations used to describe the motions of the fluid flow is given by mass conservation (equation of continuity). We consider a small amplitude progressive wave interacting with a rigid floating body. Then the body will experience simple harmonic oscillation described by the displacement of the body from its equilibrium position. In the development of the potential flow theory, we assumed incompressibility and continuity of flow. The fluid motion is also irrotational. Thus, as a result, the fluid velocity can be represented as a gradient of a scalar potential Φ satisfying the Laplace's equation in the fluid domain (Lee, 1995).

$$\nabla^2\Phi = 0 \tag{8-1}$$

The dynamic quantities are taken as harmonic and time dependent, such that Φ may be expressed as a complex velocity potential ϕ;

$$\Phi = \mathrm{Re}(\phi\, e^{\mathrm{i}\omega\mathrm{t}}) \tag{8-2}$$

Where Re represents the real part and ω denotes the frequency of the incident wave and *t* is time. The associated BVP is expressed in terms of the complexed velocity potential ϕ and the physical values is the real part of the product be between the complex amplitude and the time factor $e^{\mathrm{i}\omega\mathrm{t}}$. The linearized form of the free surface elevation as ζ and defined as,

$$\zeta = \mathrm{Re}(\eta\, \mathrm{e}^{i\omega t}) \tag{8-3}$$

Two boundary conditions are applied on the free surface, that is the *kinematic* and *dynamic*. The kinematic boundary condition states that a particle lying on the free surface at one moment in time will continually remain on the free surface and thus must have the same velocity of the free surface itself.

$$\frac{\partial\eta}{\partial t} = \frac{\partial\Phi}{\partial z} \tag{8-4}$$

The dynamic free surface condition is derived from Bernoulli equation, on the assumption that the atmospheric pressure outside the fluid is constant (McCormick, 2009).

$$\left\{\frac{\partial \Phi}{\partial t} + g\eta + \frac{1}{2}V^2\right\}\Big|_{z=\eta} = 0 \tag{8-5}$$

Equation (8-5) is nonlinear due to the squared velocity term. For small values of wave steepness, the nonlinear velocity term in Equation (8-5) can be neglected.

$$\frac{\partial \Phi}{\partial t} + g\eta = 0 \tag{8-6}$$

From Equation (8-6) the linearized dynamic free-surface condition can be expressed by

$$\eta = -\frac{1}{g}\left(\frac{\partial \Phi}{\partial t}\right) \tag{8-7}$$

The two free surface boundary conditions may be combined into one by eliminating one of the unknowns, ζ, as follows (Chakrabarti, 1987):

$$\frac{\partial^2 \Phi}{\partial t^2} + g\frac{\partial \Phi}{\partial z} = 0 \tag{8-8}$$

We take the time derivative and eliminate the time factor, now the boundary condition in terms of the time independent potential φ is described as

$$-\frac{\omega^2}{g}\varphi + \frac{\partial \varphi}{\partial z} = 0 \tag{8-9}$$

In the presence of a fixed body in waves, the fluid velocity at the body boundary described by the direction normal, *n*, must be zero,

$$\frac{\partial \Phi}{\partial n} = 0 \tag{8-10}$$

For the floating body, the water particle at the body boundary, has its velocity equal to the velocity of the body at that point.

$$\frac{\partial \Phi}{\partial n} = U \cdot n + \Omega \cdot (r \times n), \tag{8-11}$$

Where n represents the normal vector, r denotes the radius vector from the centre of rotation, U is the body translational velocity and Ω is the body angular velocity. For our initial 2-dimensional problem 3 degrees of freedom is considered i.e., sway, heave and roll while for the 3-dimensional problem six degrees of freedom are considered, the components of the body velocity are

$$U_j = \mathrm{Re}\{\mathrm{i}\omega\xi_j \, \mathrm{e}^{i\omega t}\} \qquad j = 1, 2, \ldots\ldots, 6 \tag{8-12}$$

ξ_j represents the complex amplitude, and j is the vessel motion with 1, 2, ….,6 as the surge, sway, heave, roll, pitch, yaw respectively. While for the two-dimensional analysis the relevant degree of freedoms is j = 2,3,4.

The hydrodynamic problem in regular waves is normally dealt with as sub problems namely radiation and diffraction potential respectively and super position principle used to sum them up,

$$\Phi = Re\{(\varphi_R + \varphi_D) \, \mathrm{e}^{i\omega t}\} \tag{8-13}$$

The radiation potential is gotten from the oscillation of the body and the diffraction potential is due to the incident wave and the wave scattering due to the presence of the body. The contributions of each degree of freedom makes up the radiation potential, for the three-dimensional motion we have,

$$\varphi_R = \sum_{j=1}^{6} \xi_j \varphi_j, \qquad j = 1,2,\ldots,6 \tag{8-14}$$

And j = 2,3,4 for 2-dimentional motion and j =0 for a fixed structure.

ξ_j represents the complex displacement amplitude. The boundary condition on the body for the radiation potential is gotten from (8-11)

$$\begin{aligned} \frac{\partial \varphi_j}{\partial n} &= i\omega n_j \qquad && j = 1,2,3 \\ \frac{\partial \varphi_j}{\partial n} &= i\omega (r \times n)_{j-3} \qquad && j = 4,5,6. \end{aligned} \tag{8-15}$$

The diffraction potential be made up of the velocity potential due to the incident wave φ_0 with amplitude A, and velocity potential due to the wave scattered (or diffracted) from the surface of the structure, φ_s.

$$\varphi_D = A(\varphi_0 + \varphi_S), \tag{8-16}$$

Where φ_0 is,

$$\varphi_0 = \frac{ig}{\omega} e^{ky - ikx}, \tag{8-17}$$

For a fixed body we refer to (4.8), the body surface-boundary condition may be rewritten as follows:

$$\frac{\partial \varphi_s}{\partial n} = -\frac{\partial \varphi_0}{\partial n} \tag{8-18}$$

Which shows that the body surface normal velocity from the incident wave is equal and opposite to the normal velocity from the scattered wave.

For a floating body we have φ_j and φ_s, with this the wave radiates outwards from the body, this is the radiation condition, which is essential for the boundary value problem. In three-dimension we have,

$$\varphi_j \, \alpha \, R^{-1/2} e^{-ikR}, \qquad as \, R \to \infty \qquad J = 1,2,\ldots,6,s \tag{8-19}$$

R represents the radial distance from the body. The two-dimension radiation condition is,

$$\varphi_j \, \alpha \, R^{-1/2} e^{-ikR}, \qquad as \, R \to \infty \qquad J = 1,2,\ldots,6,s \tag{8-20}$$

The boundary conditions problem described by(8-1), (8-9), (8-15), (8-18) , and will be referred to as the basis problem.

Table 8-1 FLNG mass model Beam properties full loading condition

Beam	Original Density	Volume	Density	Mass	LCG	CM
Beam 1	1293004	12.5	1316420	16455248	-152	-2.5E+09
Beam 2	363203.3708	44.5	386619.2	17204554	-136	-2.3E+09
Beam 3	281087.8261	57.5	304503.6	17508960	-120	-2.1E+09
Beam 4	265831.4145	60.8	289247.2	17586232	-104	-1.8E+09
Beam 5	264959.8361	61	288375.7	17590915	-88	-1.5E+09
Beam 6	264959.8361	61	288375.7	17590915	-72	-1.3E+09
Beam 7	264959.8361	61	288375.7	17590915	-56	-9.9E+08
Beam 8	264959.8361	61	288375.7	17590915	-40	-7E+08
Beam 9	264959.8361	61	288375.7	17590915	-24	-4.2E+08
Beam 10	264959.8361	61	288375.7	17590915	-8	-1.4E+08
Beam 11	264959.8361	61	241544	14734185	8	1.18E+08
Beam 12	264959.8361	61	241544	14734185	24	3.54E+08
Beam 13	264959.8361	61	241544	14734185	40	5.89E+08
Beam 14	264959.8361	61	241544	14734185	56	8.25E+08
Beam 15	264959.8361	61	241544	14734185	72	1.06E+09
Beam 16	264959.8361	61	241544	14734185	88	1.3E+09
Beam 17	265831.4145	60.8	242415.6	14738868	104	1.53E+09
Beam 18	281087.8261	57.5	257672	14816140	120	1.78E+09
Beam 19	363203.3708	44.5	339787.5	15120546	136	2.06E+09
Beam 20	1293004	12.5	1269588	15869852	152	2.41E+09
				3.23E+08	-5.613	-1.8E+09
					-5.613	

Table 8-2 LNGC mass model Beam properties full loading condition

Beam	Original Density	Volume	Density	Mass	LCG	CM
Beam 1	991005	5	990920.3	4954601	-133	-7E+08
Beam 2	278372.191	17.8	278287.5	4953517	-119	-6E+08
Beam 3	160877.435	30.8	160792.7	4952415	-105	-5E+08
Beam 4	129037.109	38.4	128952.4	4951771	-91	-5E+08
Beam 5	108188.319	45.8	108103.6	4951144	-77	-4E+08
Beam 6	108188.319	45.8	108103.6	4951144	-63	-3E+08
Beam 7	108188.319	45.8	108103.6	4951144	-49	-2E+08
Beam 8	108188.319	45.8	108103.6	4951144	-35	-2E+08
Beam 9	108188.319	45.8	108103.6	4951144	-21	-1E+08
Beam 10	108188.319	45.8	108103.6	4951144	-7	-3E+07
Beam 11	108188.319	45.8	108273	4958906	7	3E+07
Beam 12	108188.319	45.8	108273	4958906	21	1E+08
Beam 13	108188.319	45.8	108273	4958906	35	2E+08
Beam 14	108188.319	45.8	108273	4958906	49	2E+08
Beam 15	108188.319	45.8	108273	4958906	63	3E+08
Beam 16	108188.319	45.8	108273	4958906	77	4E+08
Beam 17	129037.109	38.4	129121.8	4958279	91	5E+08
Beam 18	160877.435	30.8	160962.2	4957635	105	5E+08

Beam 19	278372.191	17.8	278456.9	4956533	119	6E+08
Beam 20	991005	5	991089.7	4955449	133	7E+08
				99100500	0.036	4E+06
					0.036	

Gap resonance training data

F	(L/D)_FLNG	(L/D)_LNGC	(G/D)_FLNG	(G/D)_LNGC	I_W	DAF	G_A
0.337	0.08	0.0062	0.275	0.446	4.232	1.118	4.732
0.477	0.08	0.0062	0.275	0.446	6.154	1.001	6.158
0.616	0.08	0.0062	0.275	0.446	6.277	0.726	4.556
0.758	0.08	0.0062	0.275	0.446	5.875	0.681	4.000
0.901	0.08	0.0062	0.275	0.446	5.263	0.926	4.876
1.045	0.08	0.0062	0.275	0.446	6.808	0.867	5.901
1.188	0.08	0.0062	0.275	0.446	2.935	5.305	15.569
1.331	0.08	0.0062	0.275	0.446	3.836	2.323	8.911
1.475	0.08	0.0062	0.275	0.446	4.948	2.700	13.359
1.617	0.08	0.0062	0.275	0.446	5.090	2.669	13.586
0.337	0.08	0.0062	0.442	0.716	4.859	1.405	6.829
0.477	0.08	0.0062	0.442	0.716	6.857	0.854	5.856
0.616	0.08	0.0062	0.442	0.716	5.900	1.114	6.571
0.758	0.08	0.0062	0.442	0.716	5.607	0.976	5.471
0.901	0.08	0.0062	0.442	0.716	5.275	1.331	7.022
1.045	0.08	0.0062	0.442	0.716	9.502	1.471	13.977
1.188	0.08	0.0062	0.442	0.716	3.677	3.595	13.216
1.331	0.08	0.0062	0.442	0.716	3.386	2.967	10.047
1.475	0.08	0.0062	0.442	0.716	4.642	3.168	14.705
1.617	0.08	0.0062	0.442	0.716	4.553	2.255	10.267
0.337	0.08	0.0062	0.558	0.905	4.650	1.359	6.318
0.477	0.08	0.0062	0.558	0.905	6.984	0.865	6.039
0.616	0.08	0.0062	0.558	0.905	6.182	0.966	5.974
0.758	0.08	0.0062	0.558	0.905	5.740	0.942	5.406
0.901	0.08	0.0062	0.558	0.905	5.428	1.551	8.418
1.045	0.08	0.0062	0.558	0.905	9.997	2.167	21.665
1.188	0.08	0.0062	0.558	0.905	2.959	2.476	7.327
1.331	0.08	0.0062	0.558	0.905	3.702	1.951	7.224
1.475	0.08	0.0062	0.558	0.905	4.218	3.473	14.650
1.617	0.08	0.0062	0.558	0.905	4.546	1.803	8.195
0.337	0.0667	0.0053	0.330	0.516	3.897	2.370	9.238
0.477	0.0667	0.0053	0.330	0.516	6.036	1.365	8.238
0.616	0.0667	0.0053	0.330	0.516	5.709	1.333	7.608
0.758	0.0667	0.0053	0.330	0.516	5.944	0.329	1.956
0.901	0.0667	0.0053	0.330	0.516	5.655	1.469	8.308

1.045	0.0667	0.0053	0.330	0.516	9.065	2.174	19.707
1.188	0.0667	0.0053	0.330	0.516	4.151	1.621	6.727
1.331	0.0667	0.0053	0.330	0.516	7.016	1.228	8.614
1.475	0.0667	0.0053	0.330	0.516	4.976	0.515	2.563
1.617	0.0667	0.0053	0.330	0.516	4.746	0.310	1.473
0.337	0.0667	0.0053	0.530	0.828	4.693	2.021	9.487
0.477	0.0667	0.0053	0.530	0.828	6.923	1.200	8.306
0.616	0.0667	0.0053	0.530	0.828	6.185	1.132	6.999
0.758	0.0667	0.0053	0.530	0.828	6.076	0.628	3.815
0.901	0.0667	0.0053	0.530	0.828	5.777	1.643	9.491
1.045	0.0667	0.0053	0.530	0.828	####	2.253	22.900
1.188	0.0667	0.0053	0.530	0.828	3.721	1.891	7.038
1.331	0.0667	0.0053	0.530	0.828	5.631	1.269	7.148
1.475	0.0667	0.0053	0.530	0.828	4.342	0.368	1.597
1.617	0.0667	0.0053	0.530	0.828	4.739	0.400	1.897
0.337	0.0667	0.0053	0.670	1.047	4.473	1.838	8.222
0.477	0.0667	0.0053	0.670	1.047	7.007	1.262	8.843
0.616	0.0667	0.0053	0.670	1.047	6.495	0.903	5.864
0.758	0.0667	0.0053	0.670	1.047	5.950	0.659	3.921
0.901	0.0667	0.0053	0.670	1.047	6.174	1.537	9.487
1.045	0.0667	0.0053	0.670	1.047	####	2.573	31.438
1.188	0.0667	0.0053	0.670	1.047	3.754	5.643	21.185
1.331	0.0667	0.0053	0.670	1.047	6.686	4.635	30.992
1.475	0.0667	0.0053	0.670	1.047	4.413	4.779	21.090
1.617	0.0667	0.0053	0.670	1.047	4.411	1.334	5.885
0.337	0.0667	0.0053	0.275	0.446	4.776	1.946	9.294
0.477	0.0667	0.0053	0.275	0.446	5.769	1.305	7.528
0.616	0.0667	0.0053	0.275	0.446	6.866	0.930	6.385
0.758	0.0667	0.0053	0.275	0.446	5.858	1.203	7.045
0.901	0.0667	0.0053	0.275	0.446	9.289	0.423	3.934
1.045	0.0667	0.0053	0.275	0.446	6.567	2.545	16.712
1.188	0.0667	0.0053	0.275	0.446	8.516	3.043	25.915
1.331	0.0667	0.0053	0.275	0.446	4.634	4.067	18.848
1.475	0.0667	0.0053	0.275	0.446	5.208	0.285	1.485
1.617	0.0667	0.0053	0.275	0.446	5.935	1.838	10.907
0.337	0.0667	0.0053	0.442	0.716	4.842	1.913	9.263
0.477	0.0667	0.0053	0.442	0.716	5.692	1.281	7.291
0.616	0.0667	0.0053	0.442	0.716	6.489	0.663	4.301
0.758	0.0667	0.0053	0.442	0.716	5.265	0.812	4.273
0.901	0.0667	0.0053	0.442	0.716	8.771	1.385	12.147
1.045	0.0667	0.0053	0.442	0.716	6.249	1.192	7.452
1.188	0.0667	0.0053	0.442	0.716	5.771	3.970	22.912
1.331	0.0667	0.0053	0.442	0.716	4.269	1.992	8.504
1.475	0.0667	0.0053	0.442	0.716	4.475	0.975	4.362
1.617	0.0667	0.0053	0.442	0.716	5.433	0.873	4.742
0.337	0.0667	0.0053	0.558	0.905	5.041	1.510	7.610

0.477	0.0667	0.0053	0.558	0.905	6.117	0.993	6.073
0.616	0.0667	0.0053	0.558	0.905	6.782	0.512	3.471
0.758	0.0667	0.0053	0.558	0.905	6.172	0.636	3.924
0.901	0.0667	0.0053	0.558	0.905	9.403	1.182	11.112
1.045	0.0667	0.0053	0.558	0.905	5.833	6.889	40.183
1.188	0.0667	0.0053	0.558	0.905	6.900	4.341	29.951
1.331	0.0667	0.0053	0.558	0.905	4.878	4.368	21.308
1.475	0.0667	0.0053	0.558	0.905	5.188	1.072	5.563
1.617	0.0667	0.0053	0.558	0.905	5.920	1.269	7.511

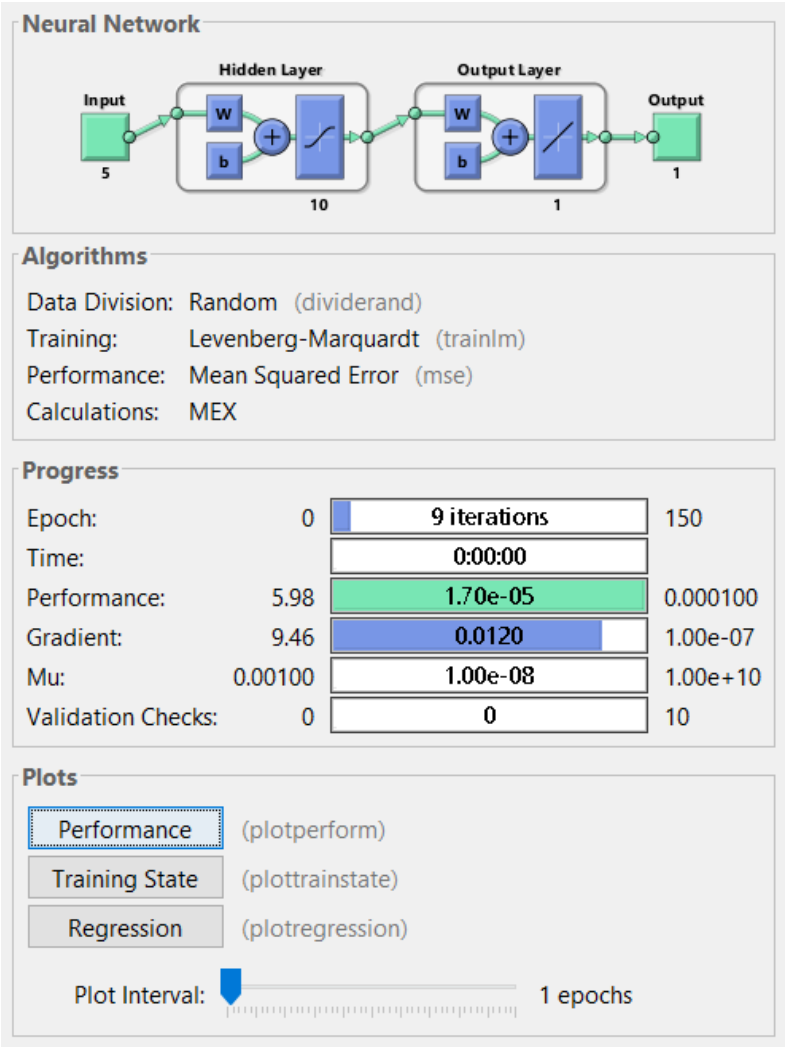

MATLAB ANN flow chart